Understanding enhanced oil recovery (EOR) in sandstone reservoirs: the role of redox changes in clay minerals on wettability

NIKOLAOS ANTONIOS APEIRANTHITIS

Understanding enhanced oil recovery (EOR) in sandstone reservoirs: the role of redox changes in clay minerals on wettability

PhD Thesis

Nikolaos Apeiranthitis

Supervisors:

Prof. H. Chris Greenwell
Prof. Cédric Carteret
Dr. Anke Neumann

Advisor:

Dr. Ian Collins (BP)

The Layered Mineral Geochemistry Group
Department of Earth Sciences
University of Durham
United Kingdom

September, 2021

Understanding Enhanced Oil Recovery (EOR) in sandstone reservoirs: the role of redox changes in clay minerals on wettability

Nikolaos Apeiranthitis

Submitted for the degree of Doctor of Philosophy
September 2021

Abstract

A great body of research has been focused on understanding enhanced oil recovery in mature sandstone reservoirs. The benefit of further producing such mature fields is indisputable, since the natural-driven oil recovery of the oil initially in place can vary from <5% to 50%, at the best case scenario. The enhanced oil recovery methods, such as CO_2 injection, steam injection, surfactant injection etc., have been established through the years, with researches proposing mechanisms that can explain the additional oil recovery. The following pages of this thesis explore in more detail the low salinity waterflooding (LSWF), a method that has gained significant ground the recent years, due to the low costs of implementation. Many mechanisms have been proposed since the 1950's, when first observations were made, with more light being shed since the late 1990's, continuously to present day.

The experimental work of this PhD project focused on examining reduction-oxidation (redox) processes during oil recovery upon EOR implementation. This was approached by using iron-bearing clay minerals, with various iron content, as proxies of iron phases present in the reservoir rock. First, the wettability of those clay minerals, such as natural occurring nontronite and illite, was explored via clay mineral films, measuring the contact angle of crude oil and DI water, under reduced and oxidised conditions, with reduced clay films, exhibiting more water-wet surfaces. Then, the hydration and structural changes of a nontronite clay mineral was established with infrared spectroscopy (IR). At these experiments, the saturating cation was manipulated by clay mineral treatment, acquiring homoionic Na^+, Ca^{2+} and K^+ samples of nontronite, allowing the isolation of hydration effects and other clay mineral / cation interactions. Those IR measurements revealed a more hydrated state under partial reduction, and stronger clay mineral/ cation interaction under (partially) reduced conditions (N-IR, M-IR). Significant spectral alterations were also observed at the F-IR range, upon clay mineral reduction, with minimum effects due to cation saturation and relative humidity induced. Lastly, the thermodynamics of cation exchange reactions, using two Na^+-saturated nontronites and a Na^+-saturated montmorillonite, was attempted to be quantified. Two different reactions were considered for all three minerals: clay mineral- Na→Ca and Na→K. These experiments, conducted under fully reduced conditions, showed that the inverse of the Na→Ca reaction is favoured (Ca favoured with $\Delta G < 0$), which supports the basic theory of LSWF, as sodium is considered a key factor for LSWF positive effect, but also how cation exchange, under such redox conditions, are exhibiting hysteresis, a key observation for better understanding such processes on clay minerals, across disciplines.

Declaration

The work in this thesis is based on research carried out at the Greenwell Group, the Department of Earth Sciences, Durham University, England. No part of this thesis has been submitted elsewhere for any other degree or qualification and it is all my own work unless otherwise stated in the text.

How to Cite

Apeiranthitis, Nikolaos. *Understanding enhanced oil recovery (EOR) in sandstone reservoirs: the role of redox changes in clay minerals on wettability*, Department of Earth Sciences, Durham University, United Kingdom, 2021

Acknowledgements

First of all, I would like to thank my supervisor, Prof. H. Chris Greenwell. Since the beginning of my time at Durham University, he was very supportive, his office always open to ask questions and very helpful and thoughtful of all his students' well-being. Personally, I am happy for the opportunity he gave me to work on a subject I knew little, to collaborate with people of high expertise on their field and to allow me to explore my research capabilities freely. That led to collaborating with Prof. Cédric Carteret from Lorraine University and Anke Neumann from Newcastle University. I would like to thank Cédric for all his support during my limited time in his labs. He was always willing to answer my questions and I am pleased that we managed to produce nice results, pending publication. Anke provided her labs, too, where I got valuable experimental training for all my work during these four years. Pablo Cubillas, although not directly involved in my project, was always happy to discuss and to introduce me on the initial experiments I undertook.

Special thanks are to be given to NERC CDT of oil & gas for providing all the necessary funding for this project, as well as the extensive training. John Underhill, Lorna Morrow and Anna Clark were always very active, reassuring the highest quality of all courses, trips and conferences for all students' benefit. In my opinion, however, the most important outcome of this CDT was the sense of community that gave us, the students, and the friendships that were formed during our trips around the UK and beyond. I had great times with Abraham and Mike, sometimes tolerating my black humour, Elliot, Sam, Bastian and Max, always happy to share rooms, Callum, Claire, Lily, Edoardo, Zoe and Sophi, for the pints and pool games we had together, Lauren and Sam for the nice morning runs, Chrises, Louis for the nights out; you all helped me fill like home and acclimatise faster in the British traditions!

Of course, I can't forget all the people I've met in Earth Sciences department. I shared great moments with Juan and Nuno, eating together, drinking beers at Durham's local brewery or playing basketball, Erin, Sean, Chris, Tim, Kate, Liz, Craig, Josh and many more, for the Newcastle and Durham nights out or playing football, Simon and Ilaria, the most frequent guest in my house, eating or playing music. I want to thank my office mates, Tara and Claire, who welcomed me the best way possible, happy to help me with anything. Nipada and Catriona, great lab trainers, and friends, in conferences and trips in France. Ashleigh and Emma, smoking shisha on Saturdays. Daud, with who I enjoyed sharing my oriental experiences or having a coffee together. Diego and Hector, my Mexican friends, who I got to know them better towards the end, but really enjoyed every moment with them, cooking or training together! I want to thank all these people and others that I met more briefly, as these longer or shorter interactions helped me realise myself better.

The people I spent most of my time with, and reminded me of home were, of course, Dimitris M. the "oldest" in the department, who introduced me in the Durham life, Dimitrios, with who I was flatmate and had each other's support in good and bad, Pavlos, the best running coach ever,

and Christos, who I have shared my food with, my inner thoughts, my happier or sad moments, had the deepest and most meaningful conversations and who was always present to support me as a friend. Special to me were and still are Nicholas, Emmanuela and Emmelia, who supported me during my PhD, by being friends and family at the same time, and learnt so many things from them.

Last but not least, huge appreciation and love to all my family, my parents and siblings. They have supported me unconditionally, all the years of studying and especially during the last four. They were always available to chat with me and hear the difficulties I had to face, offering their help, but most importantly, I want to thank them for being happier and prouder than me, for what I have achieved so far.

Thank you all!

Dedicated to

My parents and siblings

Contents

List of Figures

List of Tables

Chapter 1

Introduction and Thesis outline

1.1 Introduction

Energy demands are constantly rising and the energy sector along with governmental bodies are trying to make a change towards low greenhouse emission options of producing energy. Wind energy, solar energy, green (and blue) hydrogen technologies are gaining momentum, in a swiftly changing world during this year of 2021. However, fossil fuels still provide and can provide a stable and secure energy background for developing and meeting net-zero targets set by many major oil companies.

In this landscape, improved or enhanced oil recovery methods come into play, as capital investments towards new exploration lessens or new drilling legislation makes oil production from new fields challenging, and able to maximise economic recovery and to provide this energy security our society needs for further progress in our standard of living.

Future projections estimate that by 2035 more than 50% of global energy generation will come from renewable sources, with peak oil demand placed in the late 2020's and peak gas demand in the late 2030's. (McKinsey Global Energy Perspective 2021). At the same time, in the long term and for a successful energy transition, new oil is expected to be produced from new fields. (Global oil outlook to 2040, McKinsey 2021).

Figure 1.1 shows a projection of the primary energy production mixture to 2050. Renewables have the greatest share, with traditional fossil fuels being in a constant decline.

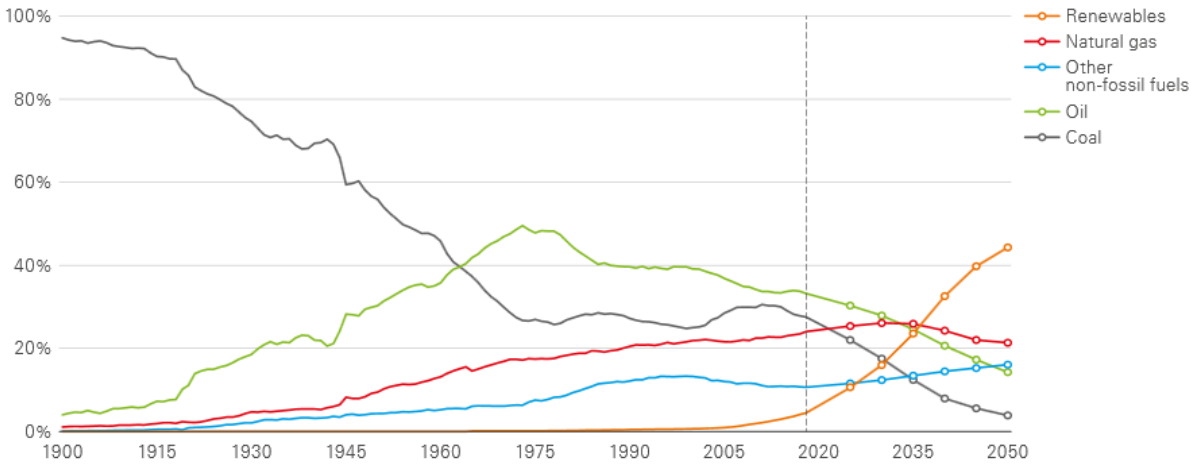

Figure 1.1: Shares of primary energy production projected to 2050. Data extracted by BP's Energy Outlook 2020.

Hydrocarbons are produced in three production stages: (i) primary recovery, due to the natural drive / pressure in the reservoir, (ii) secondary recovery, which involves mainly waterflooding. The first two stages can deliver between 20%-40% of the original oil in place (OIP). (iii) Tertiary recovery, involving many different enhanced oil recovery (EOR) methods, able to reach a total oil recovery of >70% or OOIP, Figure 1.2.

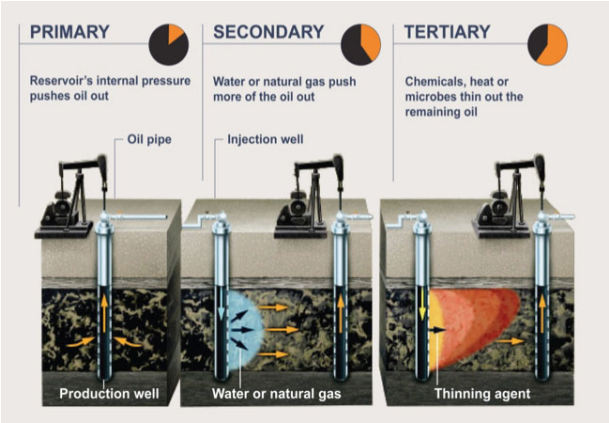

Figure 1.2: Schematic represenation of recovery stages of an oil reservoir. Taken from https://petgeo.weebly.com/thereservoir.html

Enhanced oil recovery methods have been implemented for many years, making mature reservoirs economical to produce, with lower cost than exploring for new reservoirs. EOR methods can be utilised during secondary or tertiary recovery of an oil reservoir, all with the main pur-

pose to produce more hydrocarbons. These methods include water injection in the reservoir, alkaline-surfactant-polymer (ASP) injection, gas injection or even various well completions, such as gas lift methods. So, EOR methods can be mechanical, chemical or both, varying at the scale of implementation.

Focusing on the waterflooding method, it is, at first sight, a mechanical method (classified as secondary recovery, Figure 1.2) which helps the reservoir keep its pressure high enough, and so the hydrocarbons can be produced. Also, water flooding sweeps oil away from the injection well and towards the production well, Figure1.3. However, the chemical implications of water flooding and effects on the three phase rock/oil/brine system, in the reservoir can be very high. The interfaces of these three components in the reservoir have been close to thermodynamic equilibrium for very long time, so any perturbation to the environment will change and shift this equilibrium, which needs to be understood better. Until relatively recent years, waterflooding was predominantly implemented by using brine formation or sea water, of high-salinity (HS) water, re-injected in the reservoir. This way, the disturbance to the system is at a minimum. In terms of hydrocarbon production, it has been shown that secondary recovery has a positive effect and can extend the reservoir life for many years.

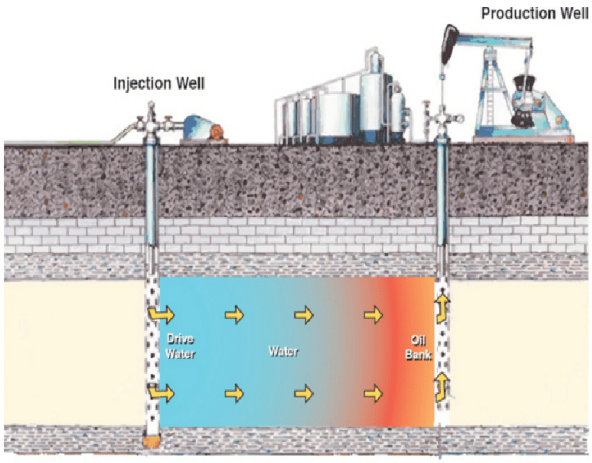

Figure 1.3: Schematic representation of a waterflooding operation. Water is injected through the injection well, pushing the oil towards the production well. Taken from www.nap.edu

Yet, in systematic studies some authors (Lager et al., 2008; McGuire et al., 2005; Tang, Morrow, 1999) reported an enhanced positive effect on the oil recovery by using water of lower salinity than that of the reservoir brine (when using water of similar salinity). The first results regarding low-salinity waterflooding came out during the 1960s by Bernard (1967); Wagner,

Leach (1959) and more extensively the 1990's by Tang, Morrow (1999), who used core flood experiments and described the observed effects of a method where lower salinity water floods were employed. Since then, numerous authors have tried to better understand and constrain the underlying geochemical basis of low salinity water flood EOR, often using core flood experiments, to establish the necessary conditions, and suggesting possible mechanisms in order to interpret any changes observed at the rock surface or the chemical composition of the effluents. In addition, there have been some field-scale implementations of low-salinity waterflooding, showing positive results after evaluation with single-well tracer test (SWTT)[1].

Most of the experiments were trying to emulate a secondary-recovery state of the reservoir, having been flooded already with brine formation water. As such, the cores were first injected with high salinity (HS) water (secondary recovery), the oil recovery measured, and then injected with low-salinity water (tertiary recovery), in order to examine the potential of this method in terms of extending a reservoir's life. There were also some researchers that were trying to compare low-salinity flooding as a secondary recovery method with low-salinity flooding as tertiary recovery (Siyambalagoda Gamage, Thyne, 2011; Zhang, Morrow, 2006; Winoto et al., 2012; Fjelde et al., 2013; Nasralla, Nasr-El-Din, 2012). Low-salinity secondary recovery would give better insights into how low-salinity can affect the chemical equilibrium in the reservoir and if this can be more beneficial in terms of oil recovery. The pressure / temperature conditions of these experiments are most of the times at ambient conditions, not taking into account the higher pressure of the reservoir.

Another important factor that has least been explored and taken into account is the redox (reduction-oxidation) state of the reservoir before commencing water flooding operations. Prior to production, the reservoir would be in a highly reduced state owing to hydrocarbon conversion processes consuming available oxygen. When water enters the reservoir during production, though generally de-oxygenated to avoid corrosion, it may contain sufficient oxidation potential that causes changes in the reservoir system. These changes are particularly related to the changes in redox state and hence mineral surface charges, which impacts on wettability alteration and fines migration.

To conclude this introductory section, the work presented in this thesis aims to examine the

[1]SWTT invloves injection of certain oil/water partitioning chemicals. These chemical react with the reservoir brine, and the non-partitioning products of the reaction, along with the initial chemicals are back-produced. The time difference that the peak concentration of each chemical is recorded at the well-head determines the residual oil - S^{or} and can evaluate the EOR method performance. See Seccombe et al. (2010) for example

effects of redox state of the reservoir and the possible effect of oxidation on the rock forming mineral surfaces, as well as the implications created on various parts of our chemical system such as rock/oil/water interaction, mineral hydration and cation exchange, and to evaluate the differences of low-salinity water flooding in secondary and tertiary recovery.

1.2 Thesis Outline

Chapter 2: Literature review

This chapter presents some geological and physico-chemical principles that govern a sandstone hydrocarbon reservoir, as well as it presents an extensive literature review on low-salinity water-flooding (LSWF), from proposed mechanisms to simulation and modelling of this EOR technique, redox implications on oil adsorption and hydrocarbon production.

Chapter 3: Materials, Methodology and Analytical techniques

In this chapter, the materials used within the experiments are described, with parts dedicated to clay mineralogy, clay mineral groups description, the main Fe^{3+} reduction theory and the structural changes manifested on clay minerals. Then, all the clay mineral treatment procedures utilised for this PhD study are given, along with mineral characterisation techniques such as X-ray diffraction (XRD), mineral surface chemical characterisation, and Mössbauer spectroscopy. Afterwards, the main experimental methodologies are given, with more details on those, at the specific experimental chapters, and lastly, analytical techniques principals are explained such as infrared spectroscopy and inductively coupled plasma - atomic emmision spectroscopy (ICP-AES).

Chapter 4: Contact angle measurement - Redox depedancy of wettability on clay minerals

Contact angle (CA) measurements are presented, using two different clay minerals, under oxidised and reduced conditions. The CA involves, crude oil and deionised (DI) water static and/or dynamic sessile drop measurement on clay (mineral) films. Several studies have already explored different settings with this kind of measurements, but never under reduced conditions. Conclusions and discussion are given, setting new questions on the actual changes the reservoir

undergoes during production and during EOR methods implementation.

Chapter 5 and Chapter 6: Infrared Spectroscopy studies - Clay mineral hydration and spectral alterations upon iron reduction

With this integrated study, completed in Laboratoire de Chimie Physique et Microbiologie pour les Matériaux et l'Environnement (LCPME) part of Lorraine University, and CNRS, France. Using infrared (IR) Spectroscopy, the clay mineral cation-induced hydration was examined, as well as various structural changes manifested, upon reduction, in all IR ranges, at Near- Mid- and Far- IR. Again, oxidised and reduced samples were prepared accordingly, giving new perspectives on the hydration process, especially under reduced conditions. Along with the IR studies, water vapour adsorption isotherms are presented, for quantifying clay mineral's hydration.

Chapter 7: Cation exchange reaction studies

Utilising cation exchange isotherm studies, two parameters can be studied; first, the thermodynamics of cation exchange on a clay mineral surface (and interlayer), and second, the clay mineral cation selectivity, in respect to the cations studied. These experiments were done under fully reduced conditions only, using two Na-saturated nontronites and a Na-saturated montmorillonite, examining these two parameters for the Na→Ca and Na→K exchange reactions. In conjunction with the previous IR studies, it became evident that cation hydration and cation selectivity/exchange are inter-related and correlated subjects.

Final synthesis

The final synthesis discusses all the findings of this PhD study with the current literature, giving new perspectives and suggesting new hypotheses worth testing for the petroleum and the surface geochemistry scientific field, overall.

Chapter 2

Theoretical Background and Literature review of Low-Saliniry waterflooding

2.1 Introduction

In this chapter, the scientific background and context of this work is given, which includes basic sandstone reservoir properties, dealing with rock wettability, capillary pressure and relative permeability, the rock/brine/oil system established within the rock, some reservoir production aspects and an extensive low-salinity water-flooding (LSWF) literature review.

First, let's consider a petroleum system which consists of the source rock, providing the hydrocarbons, the reservoir, which provides the place the hydrocarbon will migrate to and be stored, the sealing rock formation, and finally the trap, which ensures that the reservoir is properly sealed and the hydrocarbon will not leak at the surface, Figure 2.1. Such a petroleum system exist upon the correct sequence of events, e.g., deposition of source rock, deposition of reservoir, deposition of sealing, and proper timing, e.g., oil migration after trap formation (Gluyas, Swarbrick, 2021). The following pages details the fundamental processes taking place in the reservoir rock, e.g., wettability, capillary pressure but also reviews the low salinity waterflooding enhanced oil recovery.

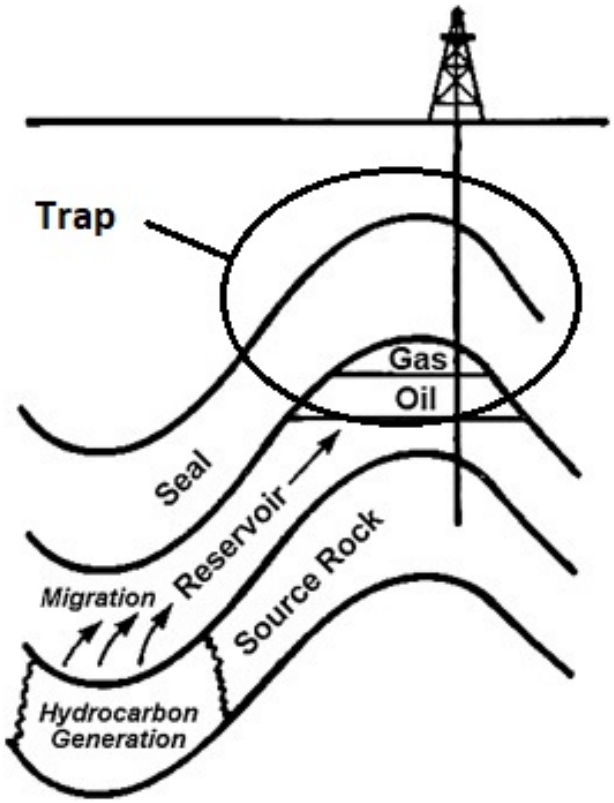

Figure 2.1: Elements of a petroleum system. The source rock, reservoir rock, seal, and hydrocarbons are depicted, as well as the migration process, as hydrocarbons are expelled from the source rock and leached into the reservoir, eventually trapped in the anticline, noted as Trap. Modified after Dembicki, Jr. (2017)

2.2 Fundamentals of sandstone reservoir properties

Wettabillity

Wettability is the characteristic of a solid surface that exhibits a preference in contacting with one liquid- the wetting liquid- in comparison to another one. This difference among liquids for a specific solid can be quantified by measuring the contact angle of the liquid on this surface. In the case of a reservoir rock the liquids are the formation water and the petroleum. A reservoir rock can be water-wet, oil-wet or mixed-wet, when surfaces have different preference, or intermediate-wet when there is no particular preference, Figure 2.2, (Abdallah et al., 2007). When the contact angle, θ, of a water droplet is $< 90^o$ then the surface is water-wet and oil-wet when the angle is $> 90^o$, Figure 2.3. Factors that affect the reservoir preference to a wetting liquid include the pressure, the temperature, the mineralogy, the pH and the formation water composition.

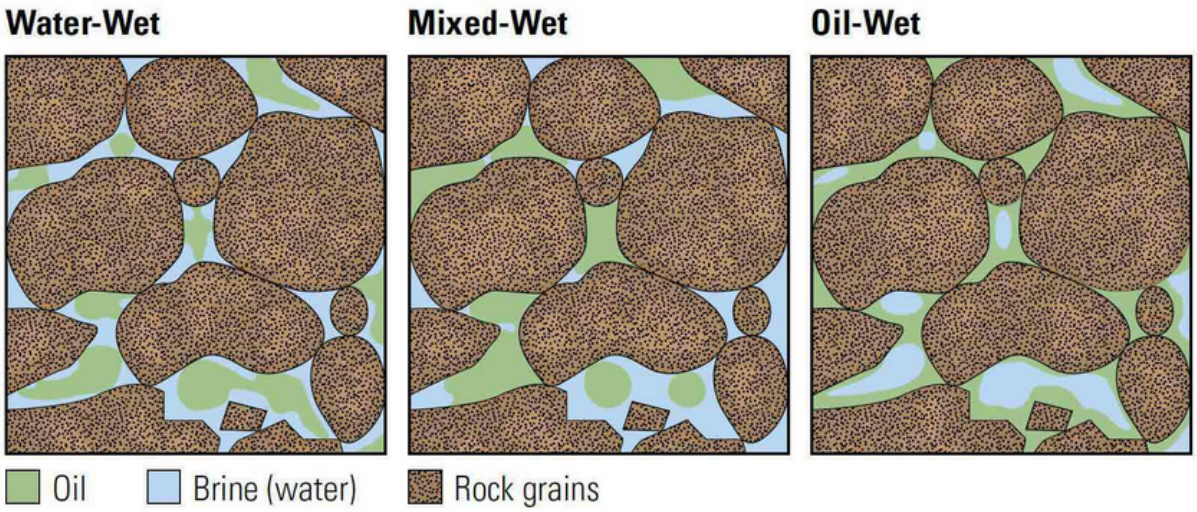

Figure 2.2: Reservoir rock wettability depiction. Grains can be water-wet (left), with oil remaining in the centre of the pores. When grain are oil-wet, the opposite occurs (right), with water in the centre of the pores, while when grains are mixed-wet, both liquids can adhere on the grain surfaces at different grains/ parts of the pores. Taken from www.slb.com

From a thermodynamic point of view, when the surface and the two liquids come in contact there will be a three-interface contact point, Figure 2.3. The distance separating the three phases is a thermodynamic variable. However, there are various disjoining forces that tend to separate again to an infinite distance the interfaces. A positive disjoining force separates the interfaces, while a negative disjoining force attracts the interfaces. The conditions for equilibrium of a system like this are equality of temperature and chemical potential between the phases and the

augmented Young-Laplace equation (Equation 2.1) (Hirasaki, 1991),

$$p^{\alpha} - p^{\gamma} = \Pi + 2H^{\alpha\gamma} * \sigma^{\alpha\gamma} \tag{2.1}$$

where $H^{\alpha\gamma}$ = mean curvature, $\sigma^{\alpha\gamma}$ = interfacial tension (IFT) and $p^{\alpha} - p^{\gamma}$ = Laplace pressure or capillary pressure P_c.

Another theoretical aspect of the wettability regards the expression of the contact angle in relation to the interfacial energies according to the Young equation (Equation 2.2) (Drummond, Israelachvili, 2002)

$$\gamma_{SO} = \gamma_{SW} + \gamma_{OW} * \cos\theta \tag{2.2}$$

where γ_{SO} is the surface or interfacial energy of the solid-oil interface, γ_{SW} is the interfacial energy of the water interface, and γ_{OW} the interfacial energy of the oil-water inteface, as shown in Figure 2.3.

Despite these two equations and the thermodynamic aspect above, hysteresis is observed during θ angle measurements. It is proposed that the volume of the droplet being measured plays a role, as well as the surface roughness, which is difficult to measure, and/or chemical heterogeneity of the solid surface. In addition, adsorption and desorption time on surfaces modify surface energies and complicate the solution of the above Equations 2.1 and 2.2, (Drummond, Israelachvili, 2002).

Drummond, Israelachvili (2002) conducted experiments measuring the wettability of a brine/oil/mica system, producing a wettability map, Figure 2.4. The completely water-wetting regime, with sodium solutions as brine, appears when the pH is high, and the sodium concentration is low, as well as at intermediate to low pH and high salinities. Also, it was observed that at high pH values the repulsive electrostatic double-layer forces, (see Chapter 3, section 2.5.3), between the oil and the mica dominate, as well as in high salt concentrations. At this regime water-wetness is strongly promoted. In the intermediate regime, the negative charges of the mica surface are lower, (edge sites more affected by the pH), so the repulsion is less. At this state the mica surface is not completely wetted by either of the liquids and hysteresis in the contact angle is observed. The oil-wet regime occurs at high pH and high salinity, Figure 2.4. Oil adhesion is promoted which is not expected by the DVLO (Derjaguin-Landau-Verwey-Overbeek) theory, (Drummond, Israelachvili, 2002). This observation, however, stands for the particular system with the specific

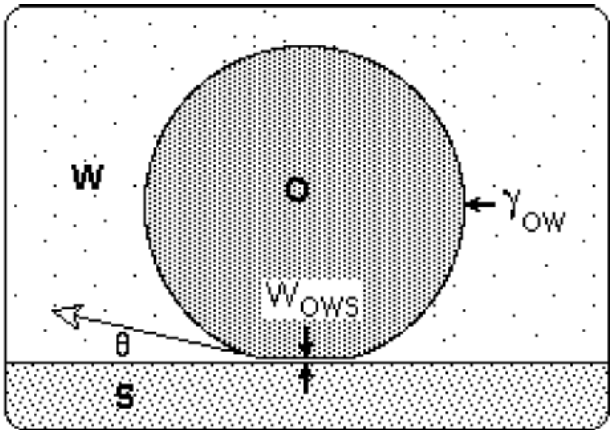

Figure 2.3: Schematic representation of a drop of oil O in water W on a solid substrate S. The relationships between θ, γ and W given by Eq.2.2. Taken from Drummond, Israelachvili (2002)

brine composition (NaCl and $NaNO_3$); for other brines different wetting maps are valid. Nevertheless, this particular adhesion map is a good example on how low-salinity waterflooding can create favourable wetting condition- more water-wet- to deliver a higher oil recovery.

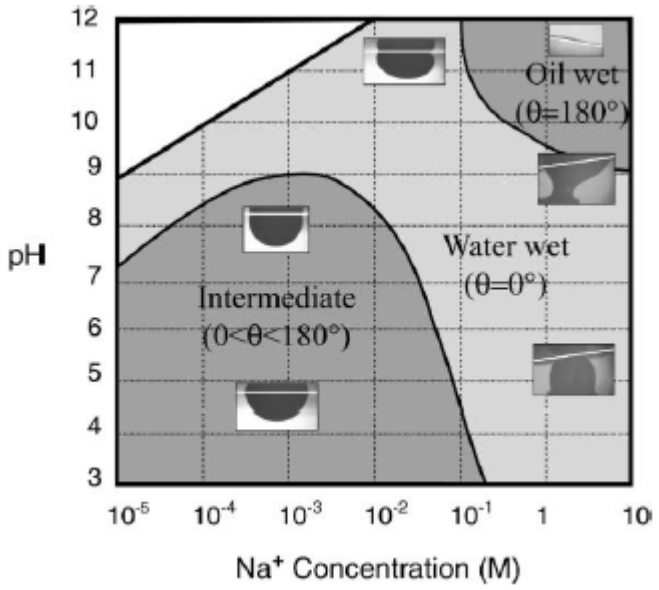

Figure 2.4: Wettability map for crude oil in aqueous solutions of NaCl and $NaNO_3$. Static contact angles show three regimes; water-wet 0^o, intermediate-wet $0^o - 180^o$ and 180^o oil-wet. Taken from Drummond, Israelachvili (2002)

On the practical side of defining the wettability of a sandstone reservoir, relative permeability curve studies are useful. In this kind of study, the relative permeability of water and oil is measured in order to access the wetting phase, by flowing these fluids through a rock core plug.

Depending which liquid phase is produced the least, that would be the wetting phase. Example of relative permeability curves are shown in Figure 2.5, where on the left side of the figure a water-wet case is depicted, with blue curve and green curve representing the water and the oil phase. As can be seen, in this water-wet situation, as the water saturation % increases (x axis) the oil permeability decreases, reaching at a final point of about 80% water to 20% oil. That saturation would be the residual oil saturation and is the target oil for the EOR methods as it cannot be produced directly by water flooding alone. In a oil-wet environment, the permeability curves will have the opposite trends while for the mixed-wet it is shown on the right-hand side of the same graph, Figure 2.5.

Capillary Pressure

Using a definition by the Society of Petroleum Engineers (SPE) capillary pressure is "the pressure differential between two immiscible fluid phases occupying the same pores caused by interfacial tension between the two phases that must be overcome to initiate flow." Capillary pressure can be calculated by Laplace's equation (Equation 2.3),

$$P_{cow} = p_o - p_w = \sigma_{ow} \left(\frac{1}{R_1} + \frac{1}{R_2} \right) \tag{2.3}$$

where P_{cow} is the capillary pressure between oil and water phases, which can be related to the principal radii of the curvature R_1 and R_2 of the shared interface and the interfacial tension σ_{ow} for the water/oil interface.

In a transition zone, depending on the wetness of the surface, the capillary curve in a diagram of capillary pressure vs water saturation will have a different shape due to the difference in wettability, as shown in Figure 2.6.

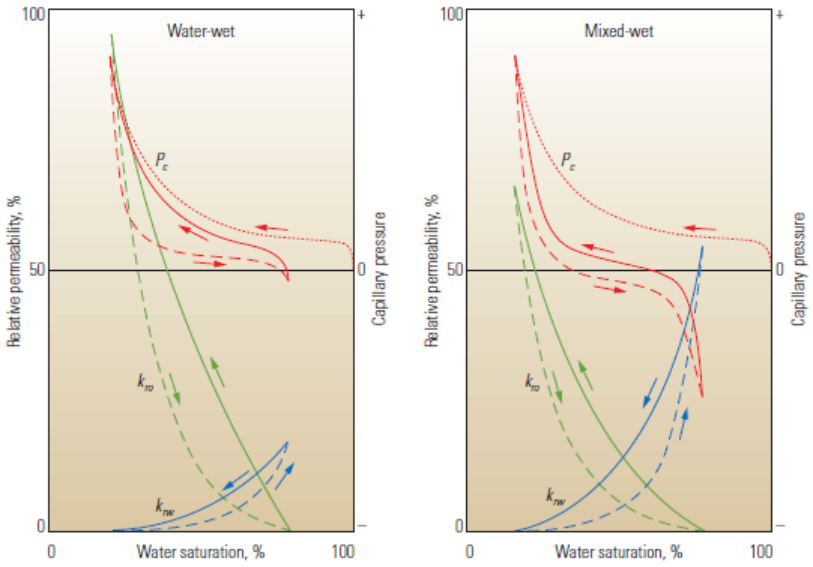

Figure 2.5: Schematic representation of Capillary Pressure curves along with relative permeability curves for water-wet and mixed-wet conditions. The dotted red line indicates a certain required pressure in the oil phase before displacement of water can take place; "Primary drainage P_c curve". The same line is for the mixed-wet conditions. The dashed red line indicates increase in water phase; imbibition process, while the solid line indicates increase in oil phase; drainage process. In water-wet conditions the capillary pressure takes only positive values, while in mixed-wet can take negative values, suggesting that some parts of the surface imbibe water and others oil. Taken from Abdallah et al. (2007)

When producing a reservoir, the capillary curves are not unique as there is dependence on the production stage. Primary production, of a water-wet reservoir, can be referred to as an spontaneous imbibition process which increases the wetting phase saturation, i.e. water. Whilst drainage processes refer to an increase in the non-wetting phase, the oil. These two processes will have different capillary curves.

In the case of producing a water-wet reservoir, after water saturation has increased, water will occupy pores/throats that formerly were filled with oil. In such case, some pores containing oil will be cut off, trapping the oil from the main displacement flow path. The pressure that keeps this oil trapped is the capillary entry pressure, which needs to be overcome in order to recover this oil. This can be achieved with EOR methods, which reduce the interfacial tension between the oil/water interface or change the contact angle. Both processes will result in the reduction of the capillary entry pressure. In case of a mixed-wet reservoir, the oil phase is continuous, and the water cannot snap-off (trap in pores) the oil; which may seem a more favourable wetting state for an oil reservoir (Abdallah et al., 2007).

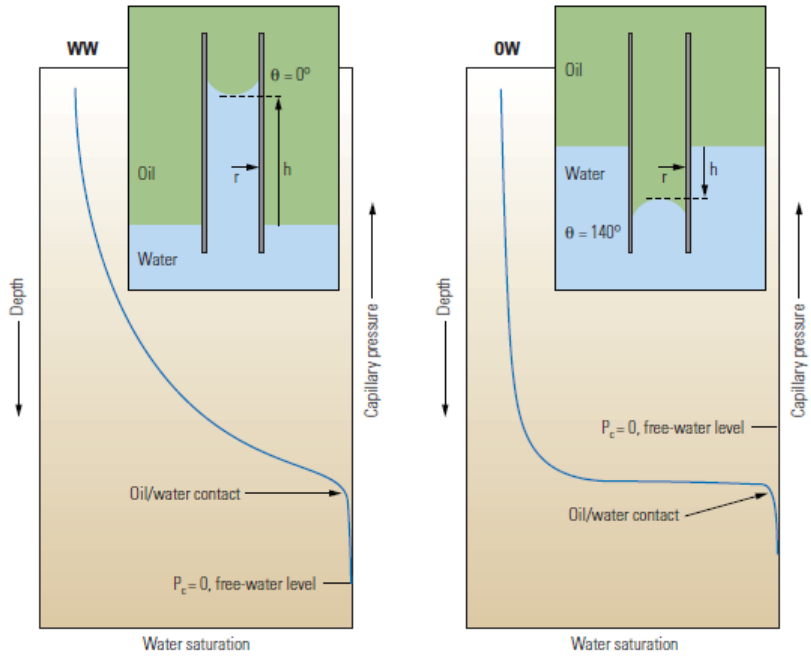

Figure 2.6: Capillary curves in oil/water transition zones for different wettability states; water-wet **ww** and oil-wet **ow**. Illustration of the two different wettabilities in tubes, representing pores of the rock. Taken from Abdallah et al. (2007).

Rock/Oil/Brine System

Rock

Sandstones have several characteristics that will define their behaviour during hydrocarbon production. These characteristics are the porosity, as the cumulative space between the rock grain constituents, the permeability, as the pore network that allows fluid flow, and the mineralogy. Porosity can be <40%, although permeability is most important in terms of hydrocarbon production. Chemical composition and mineralogy of a reservoir rock will define partly the wettability preference, once the oil has migrated. The main mineral assemblage of such rocks is quartz, feldspars, clay minerals and micas, with other minerals in much lower abundance (Kareem, 2017).

Quartz is the most common mineral in sandstones, as it is mechanically durable, very abundant in crystalline rocks (source of sedimentary rocks). It appears with different polymorphs, but in sandstones the main representative is monocrystalline quartz with no inclusions. Inclusions tend to reduce the strength of a mineral grain, due to discontinuities in the structure. So, during compaction many such grains do not survive, (Blatt, 1992).

Although feldspars are very common in crystalline rocks, in sandstones they are unstable relative to quartz, within the prevailing pressure and temperature conditions in such sedimentary rocks. Due to the high variability in their chemical composition (tertiary solid solution) and structure they can appear with many alterations, especially to forming clay minerals, via processes of kaolinization, montmorillonization, illitization. These alterations can take place either during diagenesis or during weathering of the rock, (Blatt, 1992)

Clay minerals can be more abundant than feldspars, as most of the latter have been altered through diagenesis. However, there can be clay minerals formed by precipitation from solution (Eslinger, 1988). In addition, clay mineral can occur as grain coatings, which play a significant role on the permeability preservation of the reservoir rock, (Charlaftis et al., 2021).

Apart from quartz and clays that tend to affect the wettability of the reservoir rock, exhibiting an initial negative charge on their surface, it has been shown that the presence of iron particles, and the redox state of the system, can affect the wettability as well (Fjelde et al., 2017). There can be several minerals that contain iron and exist in an oil reservoir rock, depending on the overall geochemistry of the formation. These are micas such as biotite, clay minerals such as, nontronite, montmorilonite, chamosite (Fe-rich cholite mineral), berthierine (Fe-rich mineral in sperpentine subgroup), glauconite (Fe-rich mica) and pyrite (Mu et al., 2015; Hornibrook, Longstaffe, 1996). Various iron oxides can also be present with other minerals, like quartz hosting hematite or hematite coating quartz and feldspars.

Oil

Petroleum is a mixture of liquid, gas, and solid constituents of hydrocarbon components. The main chemical components of hydrocarbons are C and H, as well as traces of O, N, S, and metals, Na, Ca, Mg, Al, Fe, Ni, V. Carbon is relatively in constant concentration and it is the other components that would give different characteristics in hydrocarbon accumulations (Speight, 2006).

Petroleum can be classified by hydrocarbon resources and by chemical composition.

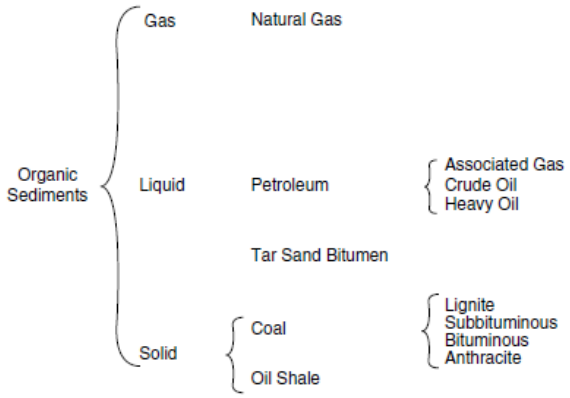

Figure 2.7: Organic sediments and hydrocarbon classification. Taken from Speight (2006)

Hydrocarbon can occur as a gaseous phase, as liquid phase as well as within the solid phase. While the gas and liquid phases are extracted naturally, the hydrocarbon from solids are extracted after treatment, Figure 2.7. Natural hydrocarbons that contain only carbon and hydrogen, can be classified into paraffins, straight or branched chains, naphthenes, saturated hydrocarbons containing one or more rings and aromatics, hydrocarbons that contain aromatic molecules such as, benzene, naphthalene etc.

A fractionation method of oil characterization is called SARA, after Saturates, Aromatics, Resins, Asphaltenes. In saturates, the paraffins and the naphthenes are included, while in resins and asphaltene molecules with high molecular masses containing hetero-atoms like sulphur, nitrogen and oxygen or metals such as nickel and vanadium, are included. (Speight (2006), Schlumberger Definition of SARA).

Hydrocarbons will affect the wettability of a reservoir rock. In a crude oil there will be oil molecules that tend to be adsorbed on the mineral faces. These molecules are often the basic and acidic members with high molecular masses. Denekas et al. (1959) presented how fractions of crude oil can affect the wettability. They concluded that fractions with high boiling temperature, have greater effect on the wettability - towards oil-wet - than the lower boiling temperature fractions, Figure 2.8. Furthermore, crude oil will have similar effect on the wettability as the distillation residue. Fractions with high boiling point are heavy oil molecules, including acidic and basic members. These exhibit a certain polarity due to their structure by containing nitrogen-, oxygen- and sulphur- based functional groups. Organic bases are usually with nitrogen, which will have greater effect on basic surfaces of limestones. Sandstones, although they have more acidic surfaces they don't exhibit any specific sensitivity on basic or acidic components. However,

certain fractions from residual oil can have a great oil-wetting effect on sandstone, (Denekas et al., 1959).

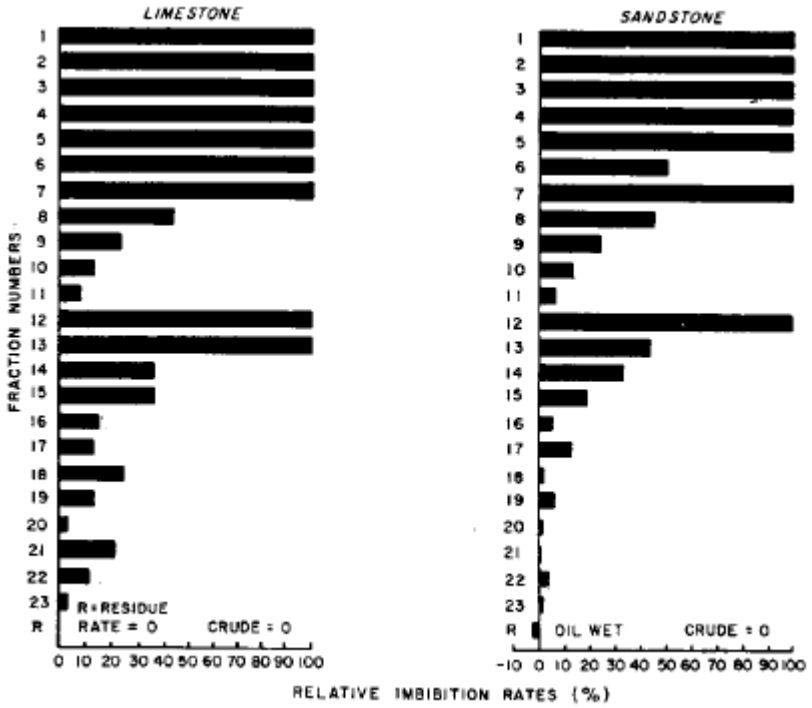

Figure 2.8: Effects of distillation fraction on wettability. Fraction were acquired during a distilation process not exceeding 200°C. These crude oil fraction although broad, were considered to sufficielty represent different molecular classes of crude oil components. Taken from Denekas et al. (1959)

Brine

Formation water or reservoir brine plays a significant role for the rock/oil/brine system as it is a dynamic factor which from the deposition of a sedimentary rock to the creation of a reservoir rock has a great impact. Water will transfer the sediments, minerals will be precipitated during diagenesis from water under various pressure and temperature conditions, which will constitute the reservoir rock. From formation water much information can be extracted, as it is a conveyor of the geochemistry of the rock, rock/water interactions, hydraulic connectivity and how the reservoir can be expected to react during hydrocarbon production.

2.3 Stages of Reservoir Production and the Residual oil issue

Once the production well or wells are completed, the reservoir starts to produce hydrocarbons due to the pressure difference between the reservoir and the bottom hole well pressure, as one of the key mechanisms. This mechanism of production uses the natural driving force of the formation itself. This pressure may originate from the aquifer below the hydrocarbons and /or the gas cap, above the hydrocarbons. After this pressure difference has become small, the formation cannot produce oil sufficiently using the residual pressure gradient. At this point, where primary recovery ceases, the oil recovery can vary from <5% to> 50% of STOOIP (stock tank original Oil-In Place), depending on varius natural drive mechanisms participation (Gluyas, Swarbrick, 2021)

Secondary recovery is the stage at which water, or gas, is injected in the reservoir via injection well(s) to provide supplementary pressure to the formation and further boost the production. The pressure difference is thus increased, and more oil can be recovered. The oil recovery varies from 15% to 40% OOIP following primary and secondary recovery. (Schlumberger Oil Field Glossary).

Although a significant amount can be produced from these two stages, tertiary recovery occurs where EOR techniques are deployed, which have multiple impacts on the reservoir formation and not just supplying extra pressure for oil production. EOR techniques, on top of primary and secondary recovery, can account for more than half of the OOIP (Nwidee et al., 2016).

EOR techniques span a wide variety of technologies and disciplines and can be coarsely classified as: thermal, chemical, gas injection or microbial EOR. Each of these classes may be further subdivided, with specific techniques such as alkaline or polymer flooding for chemical EOR, *in-situ* combustion or steam injection for thermal EOR, etc. (Nwidee et al., 2016). The aim of all these EOR implementations is to make inaccessible oil, or residual oil, easier to be produced by either changing the viscosity of the oil, reducing the interfacial tension between the oil/water interface, achieving wettability alteration on the rock formation to a more favourable state, or a combination of these.

However, in this thesis the proven low-salinity waterflooding (patented as the LoSal® process by BP) EOR method will be studied, which has manifold impacts on the reservoir formation and it does not give just extra pressure. Many possible mechanisms have been postulated, as discussed later, that show the multiple effects of this type of water flooding.

2.4 Low-Salinity Waterflooding - Overview

2.4.1 Working Conditions

It is widely accepted, after numerous research efforts, that low-salinity waterflooding (LSWF) has a positive effect on oil recovery, either when deployed at the secondary or tertiary stage. The first authors that reported a systematic study of the low salinity effect were Tang, Morrow (1999), who described oil recovery through fines migration, where the oil adhered to fine particles that became mobilised as the salinity was changed. After that, authors observed different effects of low-salinity waterflooding suggesting various mechanisms may be operating, such as, multicomponent ion exchange (Lager et al., 2008), alkaline-like flooding effects (McGuire et al., 2005), local pH increases (Austad et al., 2010), etc. Along with these core flood-experiment based research, many other measurements have been conducted so far in order to understand the mechanisms underpinning the LSWF effects. These measurements include contact-angle measurements, atomic force microscopy (AFM) measurements, adhesion maps, imaging techniques, cation exchange capacity and zeta potential studies (Jackson et al. (2016) and therein). The bottom line of all this work is the observed necessary factors that should be present in a rock/brine/oil system of a reservoir rock, to display low-salinity effects and consequently further oil recovery are the presence of

- Clay minerals.
- Formation water, containing divalent cations.
- Polar oil, containing acidic and basic molecules.
- A high salinity difference created by the injected water.

Each of the above factors/conditions contributes to creating the environment where low-salinity water will have the effect of releasing more oil. The effect of each of these is now considered in turn.

Presence of Clay Minerals

Clay minerals are aluminosilicate layered minerals, typically with anisotropic morphology and typically less than 2 μm in diameter. Clay minerals have been identified as a key condition

needed in order to observe the LSWF EOR effect. The capacity of clay minerals to exchange cations on their surface, is one of the underlying mechanisms thought to be key in promoting LSWF EOR effects. Clay minerals undergo cation exchange with the injected brine and also are mobilised as migrating fines during low salinity water floods. The total amount of cations that can be exchanged by a given clay mineral is termed the cation exchange capacity (CEC) and is dependent on the structure of the clay mineral, as well as pH and for redox active clay minerals, Eh. Generally, CEC varies in the order of kaolinite < mica/illite < montmorillonite and the CEC (meq/100g). However, even if kaolinite exhibits lower CEC than other clay films, it is believed that it can better facilitate the exchange between cations and oil molecules on its surface, as described by the multi-ion exchange mechanism (see below Section 2.4.2), (Seccombe et al., 2008; Lager et al., 2008). Important to note that other lattice asymmetries and edge site pH-dependency can affect the cation exchange on clay mineral surfaces. Other treatments, that would inhibit clay minerals to exchange cations include firing and acidising (Tang, Morrow, 1999). This way, the clay minerals become more stable on the solid substrate. Fines migration phenomenon can be observed even if the clay mineral volume/mass percentage is low in a rock, through the presence of various thin coatings (clays, iron oxides) on the quartz surface. On the other hand, no or little work has been conducted on clay mineral-free rocks, as after Tang, Morrow (1999), every researcher took the presence of clay minerals as a starting condition (Jackson et al., 2016) for LSWF EOR floods.

Formation Brine

Formation brine containing elevated concentrations of divalent cations is reported to be needed initially, in core flood tests, in order to observe low salinity (LS) effects (Lager et al., 2008; Tang, Morrow, 1999). Divalent cations can promote oil adhesion onto clay minerals through forming ion bridges and lead to mixed-wet wettability in the reservoir. It is considered that initially mixed-wet rock can give higher oil recovery after LSWF, (Jadhunandan, Morrow, 1995; Jackson et al., 2016).

Polar Oil

In addition to the above condition, polar oil should be present. Significant number of acidic and basic molecules should exist in the crude oil. These will use the divalent cations of the formation

brine to aid binding onto minerals, or binding onto clay minerals free surface, directly. Again, the rock will move towards exhibiting a mixed-wet state.

Apart from the presence of polar oil that has an effect on establishing the reservoir rock wettability, another factor is the retention time of crude oil in pores along with local characteristics of the porous media. These parameters, described below by Mugele et al. (2014, 2016), will play a role during low-salinity water flooding.

The retention of oil on the substrate is a matter of different factors, such as the interfacial tension among the rock, oil and brine, as well as the geometry and the morphology of the substrate. The final minimum-energy point, which these three interfaces will reach, is not unique and exhibits hysteresis. When low-salinity water is introduced in the system, some of these low energy points will become unstable, releasing the adhered oil. In order to examine this process, the time that oil is released in the pores, a set of experiments were conducted by Mugele et al. (2014, 2016), revealing some interesting results.

For oil drops, having $<90^\circ$ contact angle with the solid, entrapped in a gap, they are stable; however when the substrate becomes water-wet, the oil drop is adhered weakly on the substrate $>90^\circ$, and easily can be swept by a water stream. Contact-angle hysteresis, also plays significant role on the oil drop release. From a 2° contact angle hysteresis to 5° can be enough in order to inhibit oil release from that substrate.

Regarding the transport of the released oil drop, experiments have been carried out in microfluidic channels with various states of wettability and different geometries (Mugele et al., 2014, 2016). When the walls of the channels were covered with a thin film of oil, the drop could be transported with minimum effect from droplet - surface defect interactions or large topographic structures, even for large oil drops. On the other hand, if the drop is in direct contact with the substrate, it will be strongly adhered to it. In order for this drop to be released, high flow rates are required, much larger than typical reservoir flow rates, which can be achieved when a pore is completely blocked (Mugele et al., 2014, 2016).

Injection Water/ Salinity shock

The injected water should have a salinity of 10 to 100 times diluted (or TDS$<$ 5000 ppm), relative to the formation brine (Jackson et al., 2016; Tang, Morrow, 1999) in order for a salinity shock to be created and change the equilibrium of the rock/oil/brine system. However, there is no

model predicting this optimum salinity for every potential system. Apart from that, it is well established that the injected water needs to contain very low amounts of divalent cations and be predominantly of monovalent cations. These cations have some affinity to clay minerals and at the end will be exchanged with oil components adhered on the clay minerals.

In summary, the initial rock/oil/brine system has come to a thermodynamic equilibrium after geological time, with specific characteristics as discussed above, for every member of this system, which can promote a low-salinity effect. Regarding core experiments, the main effect is wettability alteration, from strongly water wet to mixed-wet after aging in oil, and the wettability of the mineral surfaces to a more water-wet state (Jackson et al., 2016). Mechanisms that can promote mixed-wet conditions are oil components directly bonded onto clay minerals or through divalent cations bridging oil and clay surfaces with the same charges (Jackson et al. (2016) and therein). Evidence of wettability alteration to more water-wet state after LSWF are reported by measuring contact angles at the rock/oil/mineral interfaces, imaging clay-coated surfaces using scanning electron microscope (SEM) (Fogden et al., 2011), AFM mapping on silica and natural quartz surface suggesting decreasing oil adhesion under low-salinity conditions, (e.g., Hassenkam et al. (2011, 2012); Jackson et al. (2016)).

2.4.2 Proposed Mechanisms

There are numerous mechanisms proposed that could explain the LSWF effects. These mechanisms are, clay swelling and fines migration, pH increases and interfacial tension (IFT) decrease, multi ion exchange (MIE), double layer expansion, osmotic pressure, saponification, emulsification/snap off, etc. Many of them have as their end effect wettability alteration, however wettability alteration is considered separately as a mechanism by many authors. Here will be presented in more detail the main mechanisms of (i) MIE, (ii) pH increase, (iii) fines migration and (iv) double layer expansion.

Multi-Ion Exchange - MIE

Lager et al. (2008), reported a low-salinity effect by measuring the concentration of cations in the effluents of core plug experiments. Their observation was that Ca^{2+} and Mg^{2+} concentrations were lower than that of the injected brine. They concluded that divalent cations are necessary to exist in the formation brine in order to facilitate the oil adhesion onto clay minerals and also, that

oil components need to be adsorbed directly onto clay mineral surfaces. After the oil components are adhered on the clay minerals, various organo-clay components will be formed. Low-salinity sodium-rich water will cause exchange of the bridging divalent ions on the clay surfaces resulting in the release of these components.

In Figure 2.9 it is illustrated how crude oil can adhere on the mineral surface it is suggested that low-salinity water will cause these bonds to break, and oil molecules are released in the system. There is an affinity order of cations that can be adhered to the clay surface and facilitate this exchange of oil molecules. This affinity from high to low is $Li^+ > Na^+ > K^+ > H^+ > Mg^{2+} > Ca^{2+}$, in which the exact order can vary for different clay minerals. We can see that sodium cations have higher affinity than calcium cations. Eventually, due to an excess presence on sodium (Na^+) cations, the clay mineral surface will adsorb two of them in order to balance the divalent cations loss. Divalent cations in the low-salinity water is suggested that may act as substitutes to oil molecules directly bonded to the clay surface (Lager et al., 2008).

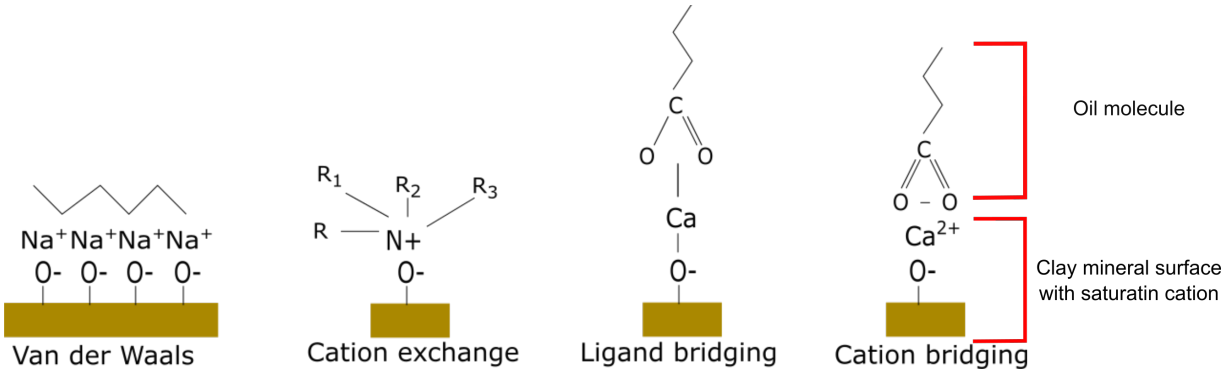

Figure 2.9: Adhesion mechanisms of crude oil on mineral surface. Clay mineral surface, with saturating cation and oil molecule are denoted. Modified after Lager et al. (2008)

pH increase and inter-facial tension (IFT) reduction

McGuire et al. (2005) suggested another mechanism for LSWF effect, after observation of the core flood effluent's pH values (Figure 2.10). They noted that the low-salinity water will cause an increase in pH of the reservoir mostly caused by carbonates, via a 2-step dissolution reaction:

$$CaCO_3 \leftrightharpoons Ca^{2+} + CO_3^{2-}$$

$$CO_3^{2-} + H_2O \leftrightharpoons HCO_3^- + OH^-$$

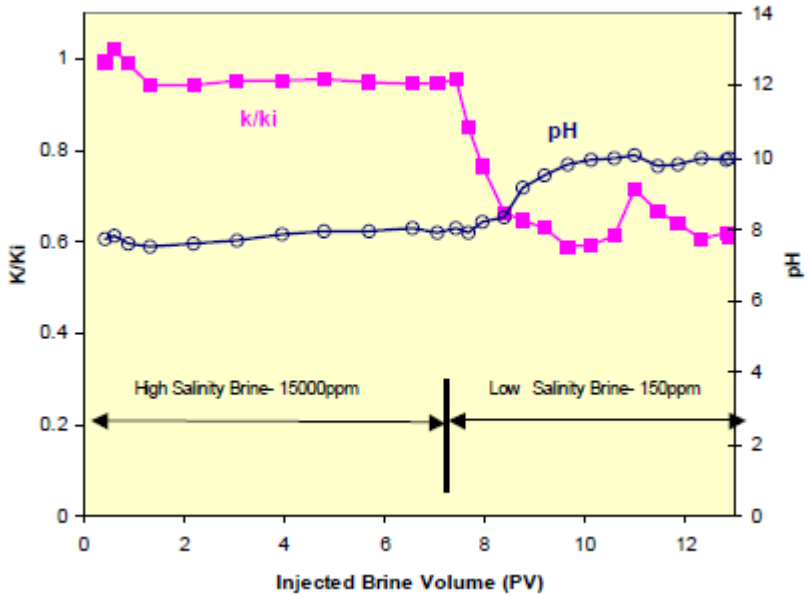

Figure 2.10: Change of pH after injection of low-salinity water. k/k_i represent injected water permeability. Taken from McGuire et al. (2005)

releasing hydroxyls in the system (Lager et al., 2008). Also this dissolution, is enhanced due to the under-saturation of injected water in divalent cations (e.g., Ca^{2+}), causing this carbonate dissolution. Another consequence of this increase in pH is the formation of surfactants, which will reduce the interfacial tension between the oil/water interfaces.

Supplementary to this first suggestion, Austad et al. (2010) suggested a mechanism of local pH increase due to reactive plagioclase. The reaction of the mineral with the low salinity water will lead to hydroxyl release and at the same time hydrogen ions will exchange cations on the clay surfaces bonded with oil molecules, according to the cation affinity order on clay minerals (Figure 2.11).

$$NaAlSi_3O_8 + H_2O \leftrightharpoons HAlSi_3O_8 + Na^+ + OH^-$$

On the other hand, it is known that alkaline flooding is taking place under pH values > 11, which are not observed by any researcher for low-salinity waterflooding and additionally, there are acid gases, like CO_2, H_2S, which will buffer any change in bulk pH values. The local pH increase theory is difficult to be proved, but from a chemical perspective could theoretically be valid.

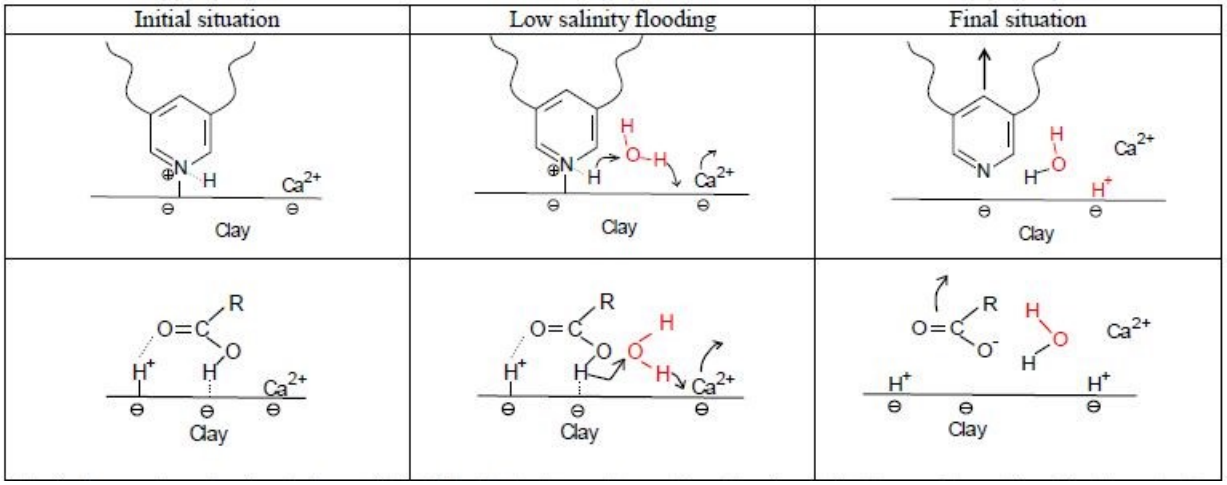

Figure 2.11: Mechanism of basic and acid oil molecules desorption by proton cations. Taken from Austad et al. (2010)

Fines migration

Tang, Morrow (1999) were the first that reported the effects of LSWF. In their experiments, they observed increases in pH values, and fines at the produced effluents. The production of fines is caused by the low salinity of the water. There is a threshold, which indicates at what salinity clay mineral fines will be desorbed from the main substrate (clay mineral flocculation). When the salinity is too low, clay minerals become unstable and are desorbed. Any oil component adhered to these fines will be consequently released, as well (Figure 2.12). This way the oil recovery is increased. It was observed that a pressure drop occurred during their experiments, indicating pore blocking and potential of formation damage. However, this formation damage can improve the sweep efficiency, as the injected water will be forced to travel through smaller pores, releasing trapped oil.

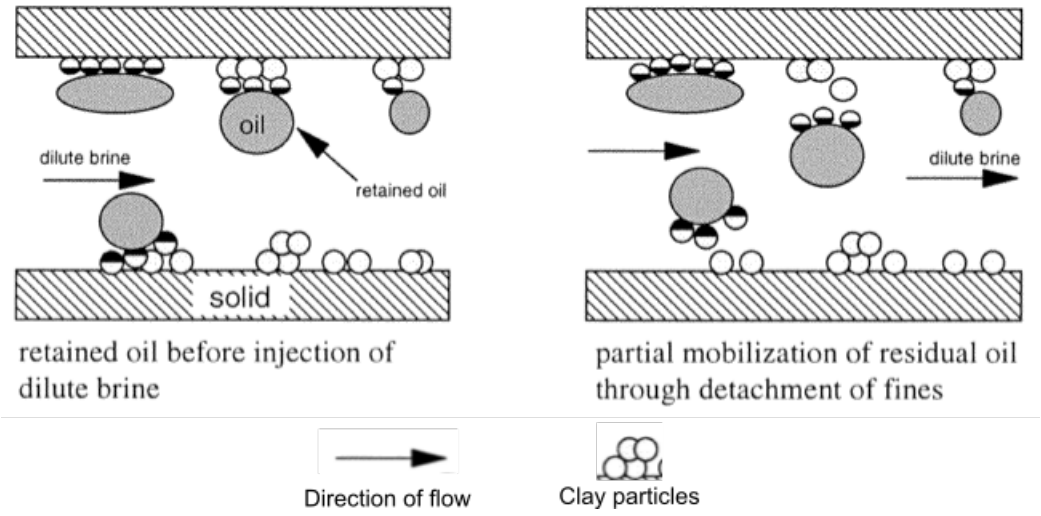

Figure 2.12: Fine mobilization during low-salinity waterflooding. Direction of flow, solid substrate, oil molecules,water-wet and oil-wet fines are depicted on this sketch. Taken from Tang, Morrow (1999)

Double Layer Expansion

Ligthelm et al. (2009) first suggested that double layer expansion (DLE) is the prime mechanism for LSWF rather than the cation exchange. Nasralla, Nasr-El-Din (2012) examined extensively the double layer expansion as a contributor to EOR, by a series of experiments.

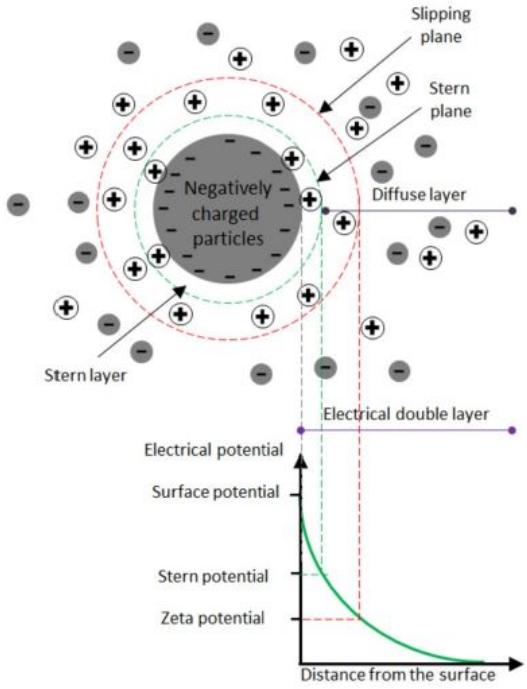

Figure 2.13: Double layer illustration, consisting of the Stern plane, a firrst layer of cations counterbalancing surface charges, and the diffuse layer, which reaches into the bulk composition of the solution. On the same graph, it is shown the relative distance of the stern plane and the zeta potential versus the surface potential. Taken from Nasralla, Nasr-El-Din (2014)

The underpinning theory behind this mechanism is associated with the double layer theory which is a combination of van der Waals attraction forces and electrostatic repulsion. Nasralla, Nasr-El-Din (2012) studied the effect of brine composition on zeta potential and pH on oil/rock/brine interfaces. Zeta potential - the repulsive inter-particle forces in a colloid suspension- defines the double layer thickness with consequences for water film stability. Increased film thickness results in a more stable water film and finally more water-wet rock. In addition, pH was controlled to avoid any other effects, like those via surfactant creation, and they concluded that at low pH injected water, the oil recovery was less for the same brine composition (Nasralla, Nasr-El-Din, 2012).

Other Mechanisms

Other mechanism reported by Pu et al. (2010) is mineral dissolution, who suggested low-salinity oil recovery due to dissolution of anhydrite. Again for this mechanism, fines or mineral mobilization is taking place, which will cause wettability alteration, to more water-wet state, by revealing

such rock surfaces, after mineral particles mobilisation, with adhered oil being detached. However, it is a mineralogy dependent mechanism, which can only be observed at specific examples.

A salt-in effect has been reported as well by RezaeiDoust et al. (2009), as a mechanism which describes that the solubility of oil components can be increased in the low-salinity water by decreasing the critical ionic strength of the water. Again, wettability alteration is associated with this mechanism, but it cannot explain the dependency on mineralogy, pH etc., (Sheng, 2014).

2.4.3 Implications and Mechanistic Gaps of Low-salinity Waterflooding

Mechanistic Gaps

In the review by Jackson et al. (2016), the evidence for low-salinity waterflooding EOR effects is described in detail. The authors describe the necessary conditions to have these LSWF EOR effects, the main mechanisms proposed with the experiments supporting these mechanisms and those that are contradictory. At the end, several things are pointed out regarding the possible connection of the mechanisms proposed.

Conditions necessary for low salinity enhanced oil recovery

Though the presence of clay minerals has generally been accepted to play a significant role for the low salinity(LS) effect, few experiments have tested clay mineral-free sandstones. Moreover, the type of clay mineral that has better LS effects seems to be controversial too, in the terms of CEC, as kaolinite has better results in flooding than others with higher CEC, which would suggest cation exchange/bridging may be less important than some postulate.

Regarding wettability alteration, it is mentioned that it is a consequence rather than a cause, as it is observed that alteration can be caused by many mechanism, such as MIE, pH changes, etc. Already, it has been said that the salinity must be less than 5000 ppm [1], there must be an optimum concentration of low-salinity water for every rock/oil/brine system that is examined at every time. This is not yet modelled. There are even cases where improved recovery was observed by increasing the salinity of the injected water (Sharma, Filoco, 2000).

Formation brine composition is also important for observing a LS effect with a formation brine, the presence of divalent cations necessary. In various studies, no LS effect has been

[1] Lager, Arnaud & Webb, KJ & Black, CJJ. (2007). Impact of Brine Chemistry on Oil Recovery. 10.3997/2214-4609-pdb.24.A24.

observed when the formation brine was absent, or contained no divalent cations (Jackson et al., 2016).

Mechanisms

Clay mineral swelling, subsequent detachment and fines migration is one suggested mechanism. Under low salinity, clay minerals can be detached from the base rock substrate revealing more water-wet surfaces. In some cases, fines are found in effluents after flooding events, while in other cases not (Soraya et al., 2009). Increased pressure drop is also mentioned as a consequence of fines migration, suggesting pore blocking, but this is not always associated with more oil recovery. pH increase and saponification is also suggested, but there are limits for saponification to occur at pH > 9, which does not seem to be observed during the LS effect. Also, the acidic number in the crude oil plays a significant role and has to be high enough (Jackson et al. (2016) and therein).

MIE is one of the main mechanisms proposed for the LS EOR effect. As clay minerals are cation exchange surfaces, they can exchange (divalent) cations existing in the low-salinity water with oil molecules directly absorbed on them, in order for the latter to be released (Lager et al., 2008). CEC capacity does not seem to be always a guide for the clay minerals showing stronger correlation for LS EOR in reservoir tests, as kaolinite is more closely associated with LS effect [2]. On the other hand, increase in pH contradicts the cation exchange mechanism according to Austad et al. (2010). As such, it can be concluded that MIE cannot explain the LS effect alone.

A local increase in pH was proposed by Austad et al. (2010), suggesting that protons exchange divalent cations on the surface of minerals, promoting local pH increase and sufficient enough to promote oil molecule desorption, Figure 2.11. However, any dissolved CO_2 buffers any pH increase and any local pH increase is difficult to prove experimentally.

Double layer expansion is associated with the electric double layer (EDL) and the attractive forces between the mineral phases and the water. At low to moderate salinity, the electric double layer depth increases. Zeta potential will also increase with decreased ionic strength, (Jackson et al., 2016). At low salinities the EDL thickness increases by its relation to the ionic strength, resulting in repulsion of adsorbed oil molecules. However, adhesion tests shows an opposite trend, where adsorption of oil is increased after low salinity at fixed pH (Buckley, Morrow, 1990). Also,

[2] Lager, Arnaud & Webb, KJ & Black, CJJ. (2007). Impact of Brine Chemistry on Oil Recovery. 10.3997/2214-4609-pdb.24.A24.

the LS effect is not always observed with reduced ionic strength (Jackson et al., 2016). Moreover, the double layer expansion is dependent on the ion species, in terms of how much it can expand.

Discussion

From the above, it can be noted that all the LS effects are an expression of microscopic changes in the rock/oil/brine interfaces. However, there is, as yet, no consensus on the exact mechanism of the LSW effect and several mechanisms may be operating together, or cooperatively, depending on the reservoir environment. These changes manifest themselves through, wettability alteration, IFT reduction, and increased oil solubility in the brine. A common factor across many of the observed changes is the change in zeta potential of the mineral/rock surface, as it is a parameter affected by many aspects, such as MIE, local pH increase due to changes in charges on mineral surfaces and decrease in ionic strength leading to DLE. However, the exact contribution of zeta potential to LS EOR is not fully understood. In addition, changes in pH and the mechanism of MIE seem to be in contradiction, as the former requires desorption of cations and release of protons, while the latter the opposite, i.e. adsorption of cations, exchanged with polar oil from the mineral surfaces, (Jackson et al. (2016) and therein).

Another mechanism, that of fines migration, needs swelling clay minerals and very low salinity, possibly with saponification in high total acidic number oils, conditions which are not always met. IFT reduction is associated to salinity decrease, but IFT drops to a minimum at a critical salinity.

In general, the main mechanisms so far postulated that lead to LS EOR are MIE, ΔpH and DLE, which all have an effect on the zeta potential. In addition, lab measurements such as AFM, SEM, and contact angles tend to be undertaken under ambient conditions, but should be conducted at reservoir temperature and pressure for direct comparison with the many core experiments reported at reservoir conditions.

Hamon (2016) tried to demonstrate several inconsistencies at the LS EOR core flooding experiments during secondary and tertiary recovery. The main points presented were the existence of a double saturation shock, the water phase dispersion, and the actual wettability alterations that govern the LS waterflooding. It was mentioned that lack of additional studies during waterflooding can cause misinterpretation of the results. These additional studies could include, relative permeability saturation analyses, ionic concentration after waterflooding, differential

pressure and wettability tests. These analyses can give significant information about the actual mechanism related to the low-salinity waterflooding either during secondary or tertiary recovery. Regarding the first point of the double shock, it was constrained between the salinity shock of high- and low- salinity water and the change of oil saturation, as the oil starts to be displaced, to residual oil saturation by high-salinity water, as it was suggested the viscosity ratio of oil/water (μ_o/μ_w) plays a big role on the success of the LS coreflooding, (Hamon, 2016).

As salinity should be decreased up to a certain threshold, dispersion of water in the core can decrease the incremental oil recovery during tertiary recovery. If high pore volumes of water are required for a specific core length in order to achieve the required salinity threshold, this situation is not realistic. This might explain late and slow oil recovery in many core flooding experiments, (Hamon, 2016).

Wettability changes during LS EOR wateflooding are considered to move towards more water-wet conditions. This is concluded after oil recovery by LSWF spontaneous imbibition compared with high-salinity water injection, with not being always the case, (Hamon, 2016). A better comparison of high and low salinity injection should be implemented during core flooding in order to see the wettability changes after low-salinity water has made contact with the reservoir rock.

2.4.4 Modelling and Simulation of LSWF

Jerauld et al. (2008), addressed the matter of modelling the LSWF events. In their model, they related salinity with capillary and relative permeability curves. As it was discussed above, there are salinity thresholds in terms of low salinity effects. It was considered that a 10% decrease of the initial salinity should give low-salinity effects, but there are cases where low-salinity effects was observed even with higher decreases in salinity, as well as other cases that no additional oil recovery was achieved. Here, it was assumed to be a linear correlation between the upper and low salinity threshold values. The salinity was modelled as a single-lumped component and the viscosity and density of the aqueous phase was salinity dependent. As the displacement of the injected low-salinity water was assumed to take place with some degree of mixing with the formation water, portions of connate water were made inaccessible to demonstrate the impact of banking of the connate water. Oil flow was modelled by taking into account hysteresis between imbibition and secondary-drainage water relative permeability. One other significant parameter

was the dispersion that occurs during low-salinity waterflooding. The dispersion can affect the result of the LSWF, as the mixing of the low-salinity water with the connate water created intermediate salinity water, which was less effective during the process. In laboratory experiments it may be easy to calculate the dispersion (2%-5% of the travelled distance), but in field scale this can be challenging, as dispersivity is affected by the heterogeneities and geometries of the reservoir. Single-well tracer tests, can give a good approximation for dispersion, as it involves injecting and producing from the same well; yet the distance is small (10 m) compared to field scale water-flooding (inter-well distances). However, the authors noted that in the case of secondary LSWF, the core experiment dispersion can be up-scaled to field scale implementation, as only low-salinity water is injected. However, in the case of tertiary LSWF, the injected water will mix with secondary (high) salinity water, so slugs of low-salinity water will acquire a different salinity, which will delay low-salinity positive effect on oil recovery. This may be the reason why in many core experiments reported, more incremental oil is observed only after many pore volumes of injected waters. For 1-D simulations it was concluded that as the grid-block size became smaller, smaller low-salinity slugs were optimum for achieving oil recovery of a given amount of low-salinity water. This showed that the estimation of the dispersion was essential to understand the optimal slug size (Jerauld et al., 2008). In 2-D simulations, the authors concluded that numerical dispersion was a good approximation to physical dispersion, without high grid-resolution being needed. In addition, the authors concluded simulations should be run in multiple dimensions, as the slug-size dispersion reacts different for 1-D and multidimensional flow.

Another contribution to modelling LSWF was made by Dang et al. (2013). Dang and co-workers developed a new model which comprised not only a multiphase multicomponent flow model, but also a wide range of other important factors that have great effect on the effects of LSWF such as an ion exchange model with geochemical processes including intra-aqueous and mineral reactions. This model can take into account physical and chemical events during LSWF, including mineral dissolution/precipitation, ion exchange and wettability alteration. The base line of this model is that wettability alteration occurs due to ion exchange between the aqueous phase and the mineral phase, from less water-wet to more water-wet state. The model was tested with the experiment results of other authors, as well as was compared to the compositional simulator PHREEQC for the ion-exchange model, giving successful validation. The studies

concluded that the "Ca^{2+} equivalent fraction on the exchanger, used as interpolant, is sufficient to provide a good match of experimental data" (Dang et al., 2013) . In other words, the adsorption of Ca^{2+} by the mineral phase has been shown as the main factor that alters the wettability to more water-wet. It was observed that as the salinity decreased, a specific factor on the model related to Ca^{2+}, increased, validating their assumption that adsorption of Ca^{2+} will shift the relative permeability curves, resulting in more oil recovery. Other conclusions were that many observations during experiments and field tests could be explained through this model, such as local pH increase, mineralogy contributions, a decrease in divalent effluent concentration and the influence of connate water/injected water compositions.

2.4.5 Comparison of Secondary and Tertiary Low-salinity Waterflooding

The majority of the core flood experiments hitherto carried out have been undertaken in either of two stages of oil recovery; secondary recovery with formation brine (high salinity water) and tertiary recovery with low-salinity water or controlled-salinity water. The rationale for this approach is the need to emulate the state of most of the reservoirs encountered during oil production, as these have already been water flooded with formation brine and then to examine the potential for low-salinity flooding at tertiary mode.

Yet, there are also experiments that try to compare a secondary LSWF to that of tertiary flooding. Zhang, Morrow (2006), in their work reported comparative experiments of different Berea cores, in terms of permeability, which were injected with various salinity waters. They concluded that a high difference in salinity between 'artificial' formation and injected brine gives better results in terms of incremental oil recovery. Also, the authors found a positive correlation between initial water saturation (S_{wi}) with improved oil recovery by low-salinity water. The higher the S_{wi}, the more improved oil recovery was observed. At the right hand side of Figure 2.14, we can compare results of low-salinity water flooding of the same core type, as distinguished by Zhang, Morrow (2006), with different initial water saturation. The highest oil recovery observed is achieved when $S_{wi} = 27.1\%$. Furthermore, improved oil recovery is successfully observed in both modes (secondary and tertiary), but more often for secondary recovery.

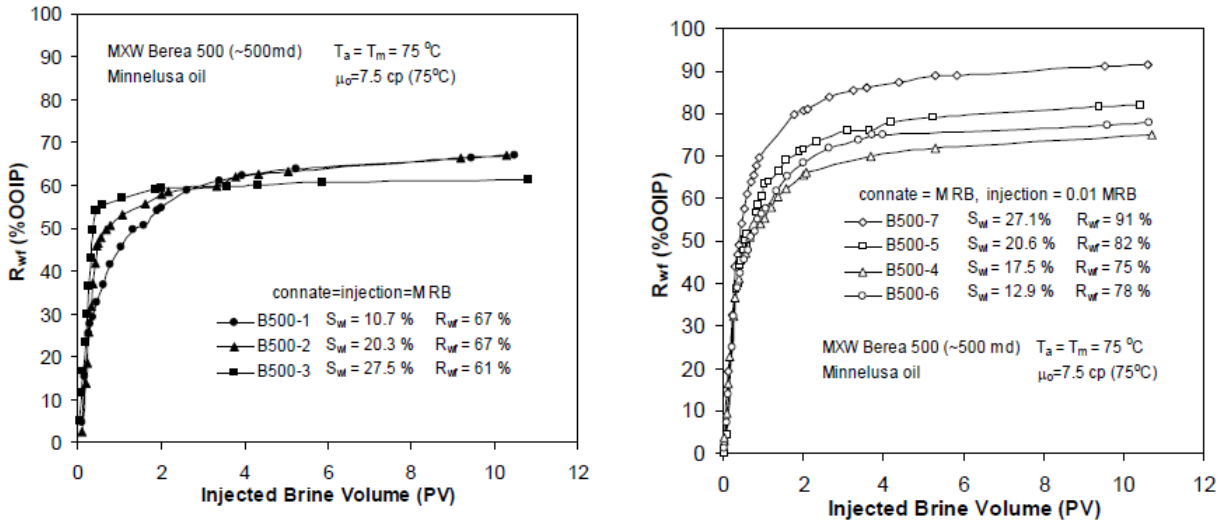

Figure 2.14: Comparison of high salinity and low salinity oil recovery during secondary waterflooding. Taken from Zhang, Morrow (2006)

Siyambalagoda Gamage, Thyne (2011) reported a series of experiments using Berea outcrop cores and Minnesula reservoir cores with two different crude oils - Raven Creek (RC) and Gibbs (GBS) oil - from Minnesula reservoirs. In their work single and two phase experiments were conducted. The former were undertaken to provide a baseline to evaluate the two phase experiments, measuring the pressure drop, pH values or observing fines in effluents. The two phase experiments included low-salinity waterflooding in tertiary and secondary mode. Briefly, in tertiary recovery the high salinity flooding recovered 40% oil with an extra of 4% after low-salinity injection (Berea cores with RC crude oil). For the same core/oil combination the secondary LSWF gave 51% oil recovery. Similar results were observed with Berea cores with GBS crude oil.

Regarding the pH variations and conductivity, from Figure 2.15, it can be seen that the absolute values for secondary low-salinity waterflooding are higher than in tertiary; with these being pH=9.4 and conductivity at around 7+ (mS/cm), and pH=8.4 and conductivity at around 6 (mS/cm), respectively. However, these differences are accounted as similar according to Siyambalagoda Gamage, Thyne (2011). For the reservoir cores with the two oils, similar results were acquired, showing higher low-salinity oil recovery in secondary mode than the tertiary mode delivered. Pressure drop was observed in every experiment and was associated with the low-salinity water injection.

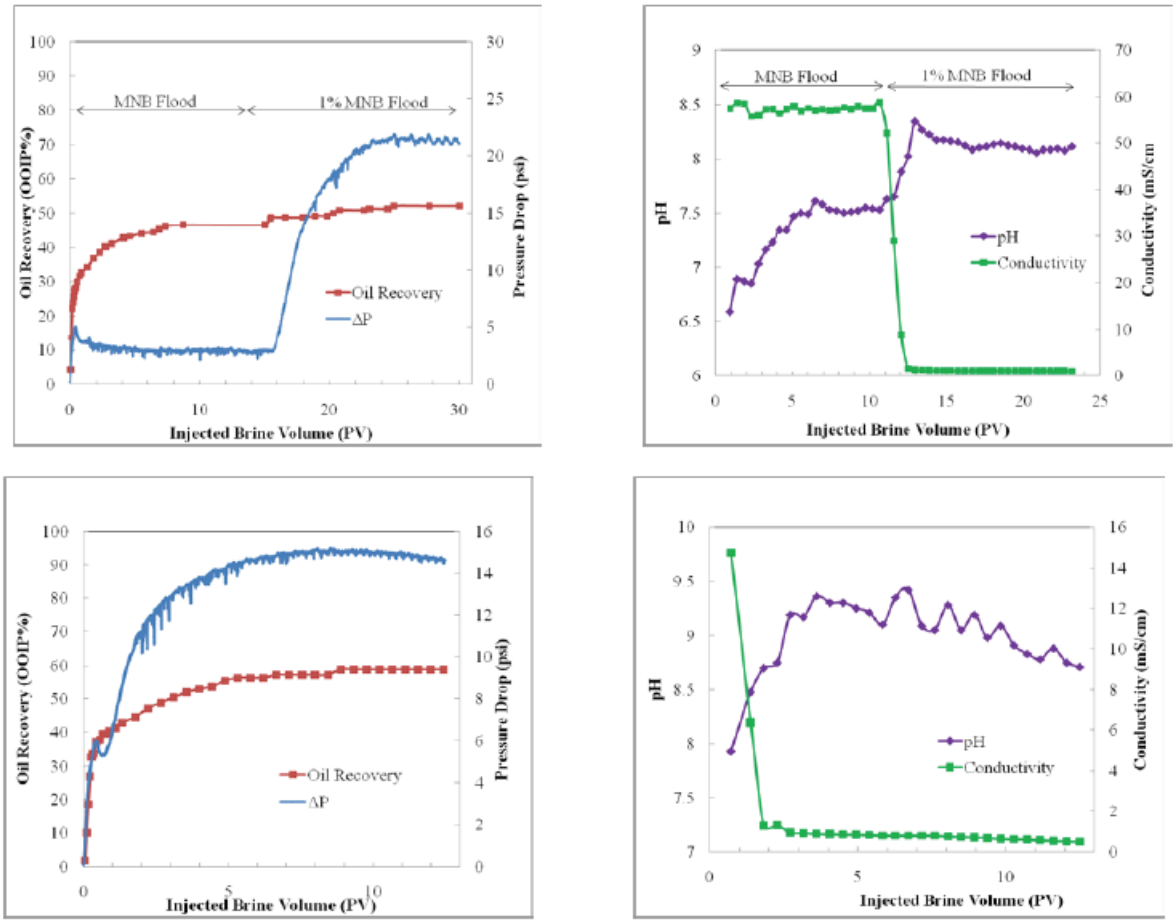

Figure 2.15: Comparison of tertiary (upper) and secondary (lower) low-salinity waterflooding. MNB stands for synthetic Minnelusa brine and 1% low salinite brine. Taken from Siyambalagoda Gamage, Thyne (2011)

In Figue 2.16, the comparative oil recovery diagrams are shown in relation to the brine salinity. At the left-hand side diagram low-salinity water flooding is implemented during tertiary recovery, with an extra oil recovery of 12.6 %. In the middle, low-salinity water flooding is implemented during secondary recovery, with total oil recovery of 75 %. In the right-hand side diagram the comparison of formation brine waterflooding and secondary low-salinity water flooding is shown, with an oil recovery difference at 29.2 %. Even if the 12.6% percent of tertiary low-salinity water flooding is excluded, the total extra oil recovery due to low-salinity water is 16.6%.

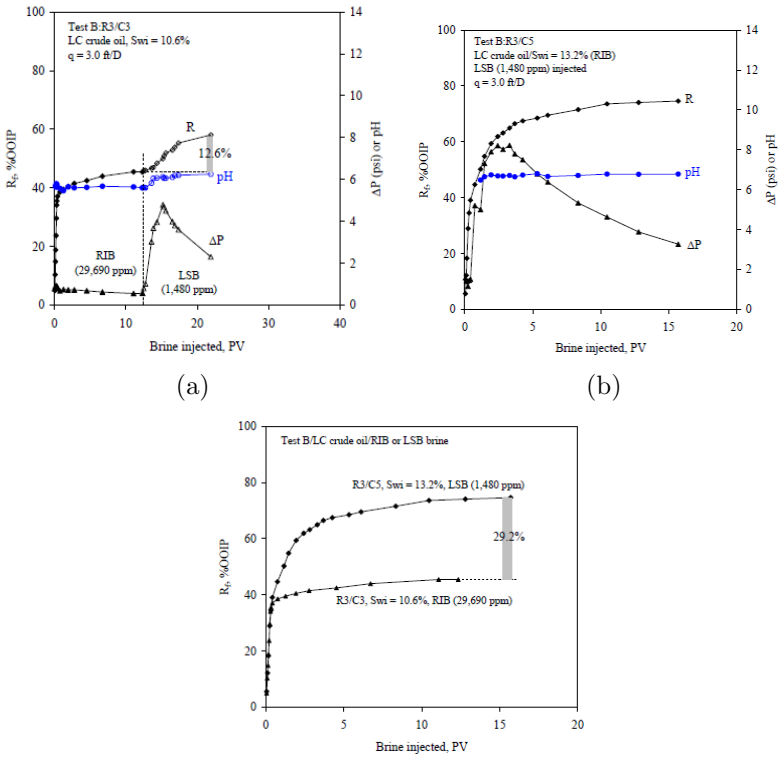

Figure 2.16: (a) Tertiary and (b) secondary oil recovery, and their difference (c), in respect of same ionic strength but different pH values of the low-salinity water. LC, WP are crude oils, RIB is the synthetic formation brine,LSB is the low salinity brine. R1, R2, C5 etc, are core restoration index and water resaturation index. Taken from Zhang et al. (2007)

Nasralla, Nasr-El-Din (2012) in their work examining the double layer expansion, along with the zeta potential charges, tested the effects of LSWF in secondary and tertiary mode. Better effects were observed during secondary mode, and with brine of lower ionic strength (NaCl vs $CaCl_2$), Figure 2.17. In addition, for the same low-salinity water solution but with different pH values, better oil recovery was achieved with higher water pH. During tertiary mode, the pressure-drop increased, with the authors attributing this to formation damage, with no extra oil recovered. So, it is concluded that the sweep efficiency improvement is not a always a LSWF recovery mechanism.

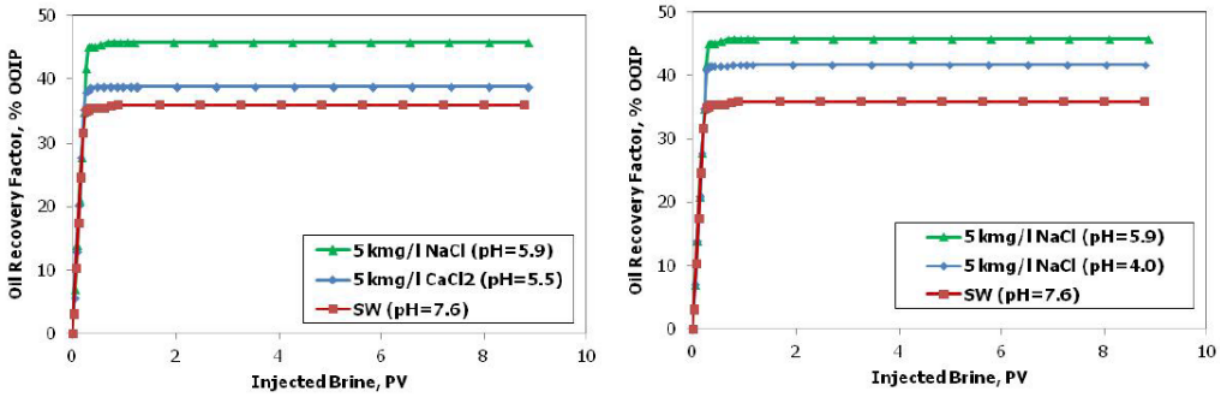

Figure 2.17: Comparison of secondary oil recovery, demonstrating the ionic effect of the low salinity water. SW stands for sea water. Taken from Nasralla, Nasr-El-Din (2012)

Fjelde et al. (2013) in an insightful work, presented a series of core flooding experiments coupled with chemical simulation. The experiments included LSWF in secondary and tertiary recovery mode, revealing useful data for improved understanding of the effects. For the selected cores, the LSWF resulted in less water-wet conditions, in secondary mode than that of high salinity water flooding. This caused earlier water breakthrough and a slower oil recovery (decreased oil relative permeability - k_{ro}). This wettability alteration can improve the microscopic sweep efficiency [3] In addition, the authors pointed out that both macroscopic and microscopic sweep efficiency should be considered and not just the total additional oil recovery achieved.

Another point underlined was that the effect of low-salinity water can be evaluated by considering the rock composition and formation brine composition. It is important to take into account any mineral dissolution, such as from carbonates, which will alter the LSWF-potential of the injected brine, causing a less favourable low-salinity effect. Through geochemical simulations, the authors wanted to evaluate the low-salinity water (LSW) composition that reduces the divalent cation concentration on the clay minerals. These concentrations during low-salinity waterflooding in secondary mode will depend on the initial rock/formation water composition, while during tertiary mode, the concentrations will depend on the high-salinity water prior to that, (Fjelde et al., 2013). In general during high-salinity waterfloods, the water used is formation water. There is no data implying any changes in divalent concentrations during such waterflooding. Nevertheless, LSW similar in composition, can give different wettability alterations and

[3] Microscopic sweep efficiency is when inaccessible pores of the reservoir start to contribute at the fluid flow. Changes in entry pressure of these pores can get the hydrocarbon mobilised.

production profiles, so it is important to simulate and optimise LSW for the most favourable composition according to the rock, formation and injection brines. In addition, the effectiveness of the LSW will be affected by any mineral dissolution in the reservoir. It was concluded that in order to make reliable predictions on LSWF, relative permeability, k_r and capillary pressure, P_c functions should be evaluated after LSWF experiments for the actual positive effect and the profitable potential of the flooding to be ascertained. Additional oil recovery reports alone can be misleading.

2.4.6 Oxidation-Reduction Implications

So far, reservoir redox state has not been taken into account during core flood experiments. Few researchers have addressed this matter, with a very small number of studies pointing out implications on wettability alteration and release of iron particles associated to the redox state changing. The following paragraphs address the redox effects related to the reservoir wettability while in Section 2.5.5 more details are given, regarding the direct redox effects on clay minerals.

Core handling seems to be an important factor for acquiring proper results during core experiments, when the preservation of the initial wettability is a matter of considerable ongoing study (e.g., Sripal, James (2018). In addition, as the underlying mechanism of low-salinity effects have not yet been fully understood, it is important to approach core experiments by replicating reservoir conditions in terms of pressure and temperature and, presumably, redox state, as well. It is shown that redox state plays a key role for oil adhesion on mineral surface (Wang, Guidry, 1994), which is also associated to the cation charges on these surfaces; iron has two commonly encountered oxidation states depending on the redox state of the environment - Fe(II) and Fe(III).

Reservoirs can be in an oxidizing or reducing environment during early stage deposition, depending on burial stage and bacteria presence, while the source rock will be under reducing conditions, such that orcanic matter can be preserved. So during oil migration, the state of the reservoirs will be a reducing environment already. Redox potential (Eh) is measured in mV, with negative values for a reducing environment and positive values for an oxidizing environment. Eh for oil reservoirs can vary either at positive values range (+200 mV to + 450mV) or negative values (-100mV to -200mV), with pH values 6-8. (Wang, Guidry (1994)and references therein).

Wang, Guidry (1994), in their work, conducted a series of experiments using Berea sandstones cores and Loudon reservoir core plugs. The Berea cores were treated in three different ways: a

conventional oxidising flooding, reducing and re-oxidising flooding, reducing and anaerobic flooding, in order to examine the wettability in relation to the redox state. Using sodium dithionite $Na_2S_2O_4$, reducing conditions were achieved. This condition was kept, or some plugs were oxidised again. The cores were initially strongly water-wet. Although, after the experiments, the cores remained at this wettability, iron was observed in the produced brine.

The mechanism suggested was that dithionite reduced some Fe^{3+} to Fe^{2+} at the most accessible mineral sites, creating an increased net negative charge at the surface of clays. In addition, ferric iron (Fe^{3+}), may have an oil-wetting effect on the mineral surface promoting oil adsorption. By reducing this ferric iron to ferrous iron, the water-wetness is kept on the clay surfaces. To avoid iron or other transition metal removal from mineral sites, Berea cores were also treated with gas-phase hydrogenation to achieve reducing conditions. The results are similar after 54 days of aging. The cores were water-wet; yet after 196 days of aging the wettability changed to mixed-wet. During the conventional flooding experiments mixed-wet wettability was observed after 54 days of aging, as well. Regarding these differences of the wettability alteration in these experiments two mechanisms were proposed: an adsorption site model and a catalytic oxidation model.

In the first (adsorption site) model, iron ions or other transition metals, play the role of adsorption sites on the mineral phase surfaces. When these ions are removed after dithionite treatment, the adsorption capacity of the minerals is reduced. At the end, the wettability of the mineral surface will stay the same (water-wet). On the other hand, the hydrogenated cores, kept their wettability in water-wet state after 54 days, like the dithionite-treated cores, but changed to mixed-wet after the 196 days. In these cores there was limited iron dissolution after treatment. The conclusion wass that adsorption of polar oil continued under reduced conditions but at a much lower rate.

In the second model for the particular experiments, ferric iron acts as a catalyst that oxidises oil components, such as carboxylic acids. These oil components tend to be critical in altering the wettability of the mineral surfaces by being adsorbed on ferrous iron, aluminium, calcium etc. The catalytic reaction reduces the Fe(III) to Fe(II) . Under aerobic flooding conditions ferric iron will be produced again by oxygen present in the solution, while in anaerobic conditions water may oxidized the ferrous iron at a much slower rate through the presence of alternative oxidants such as halides etc. The catalytic reaction will progress until all oil components susceptible to

oxidation are consumed.

The main conclusion of these two models was that oil adsorption was hindered under reducing conditions, with iron particles playing a key role on wettability alteration. However, these models explained the particular experiments carried out; so more work should be done to better understand the mechanism. In addition, it can be concluded that originally mixed-wet cores don't change wettability under reducing conditions, whereas water-wet will, under aerobic conditions, unless iron containing particles are removed from the system.

Ma et al. (2016) studied samples from the area of the Minhe Basin, China. Reservoir samples with oil seepages and two samples from different outcrops were analysed in terms of mineralogy and iron speciation.

Studying the iron speciation, the authors concluded that hydrocarbon invasion or bleaching in a reservoir may result in redox reactions and can enhance the rock porosity. It was observed that oil molecules were able to reduce ferric iron to ferrous iron. This was measured, as the concentration of para-Fe^{2+} species were elevated in oil bearing reservoir rock, relative to the non-oil contaminated rock. The iron promptly reduced was located in the hematite crystals and then the ferric iron on smectitic minerals. The reduction of iron species was correlated with total organic carbon (TOC), which showed a positive correlation (Fe^{2+} vs TOC). The authors concluded from these two observations that (1) hydrocarbon reduces iron and (2) the positive correlation of Fe and TOC can be an indicator of hydrocarbon migration into a reservoir. In relation to the previous work (Wang, Guidry, 1994), the hypothesis that acidic oil molecules can act as catalyst reducing iron is supported from another author, as now described.

Fjelde et al. (2017) conducted floatation experiments and core flooding to examine how Fe^{2+} and Fe^{3+} can affect the wettability of reservoir rocks. During lab core flooding experiments iron was produced after replacing formation water (FW) and sea water by low-salinity water, (100 times FW diluted). Even when low-salinity water is injected from initial water saturation, Fe is again produced, Figure 2.18.

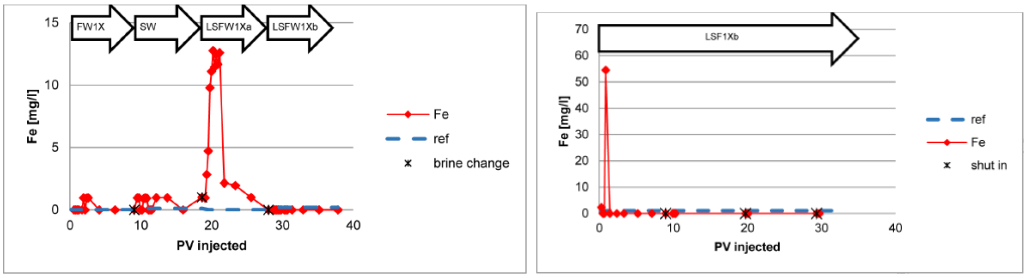

Figure 2.18: Fe production peaks after injections of different brines in the cores. FW1X= formation water, SW= sea water, LSFW1Xa 100 times FW diluted and LSFW1Xb 1000 times FW diluted. Taken from Fjelde et al. (2017)

During floatation experiments two oil/FW systems were used with different compositions of total acidic/basic oil molecules number and Fe concentration, respectively. Fe^{2+} was added in the brines and aged resulting in Fe oxidation, and for the particular floatation experiment, some Fe^{3+} was also introduced. Only one of the oil/brine system gave more oil-wet glauconite (iron rich mica mineral) particles, but when a certain amount of Fe^{3+} was added, both systems exhibited increase in the oil-wet mineral particles concentrations, even though the total acidic number was quite low. After geochemical simulation of these experiments, it was demonstrated that the concentration of multivalent cations on the clay surface was not changed. What affected the clay wettability was the precipitation of various Fe-oxides on the clay surface, as the solubility of Fe^{3+} was low under the particular experimental conditions.

On the other hand, no explanation was found to explain the fact that under low salinity waterflooding Fe^{3+} was produced from the reservoir rock. In relation to the work by Lager et al. (2011), who reported the composition of produced water after low-salinity waterflooding at a reservoir scale (Figure 2.20), a possible explanation for the Fe production was the presence of carboxylic acids in the formation water. After reaction with Fe, this results in the formation Fe-carboxylates, which are more soluble in the water and can be produced. In their experiments only in the native cores were such acids present, but not in the restored cores, which were cleaned and no Fe was detected after all brines were injected (Fjelde et al., 2017).

It was also underlined that the preservation of the original wettability of the rock samples must be carried out carefully. Removing oxygen can affect the prepared wettability of the rock, especially when containing Fe-bearing minerals. Chemicals, such as dithionite, used to achieve such reduced conditions have not been examined for how they can affect surface interactions of other minerals.

A first report of a field scale low-salinity waterflooding in tertiary mode was made by Seccombe et al. (2010), demonstrating the procedure and results of the inter-well BP (LoSal®) implementation in the Endicott field, in Alaska. After core flood experiments and single-cell tracer test in this field (Seccombe et al., 2008), a reservoir interval was chosen for LSWF. Injecting low-salinity water into the pilot injection well, a response was observed after three months at the associated production well. The main observations, when the low-salinity water kicked in, were that the water-cut [4] dropped from 95% to 92%. Also, after constantly measuring the ions concentration, a significant decrease was observed. However, iron (Fe) appeared in the produced water, which was not present during the high-salinity waterflooding or in the low salinity water injected. From a detection limit concentration of 0.2 ppm it rose to 2 ppm in two days, as shown in Figyre 2.19. This amount of iron produced was attributed to dissolution of iron oxides precipitated on the mineral grains. During the sandstone deposition of the particular reservoir, iron carbonates should have been dissolved after weathering. This carbonate saturated the connate brine, and after reaction with the low-salinity water, iron was exchanged on the mineral surfaces, and any oil molecule adhered to this iron was released into the system, which was explained by the multi-ion exchange mechanism (see above). As iron appeared at the same time as the incremental oil recovered, it was suggested that Fe acted as a bridge between polar oil compounds and the kaolinite present in the rock, (Seccombe et al., 2010).

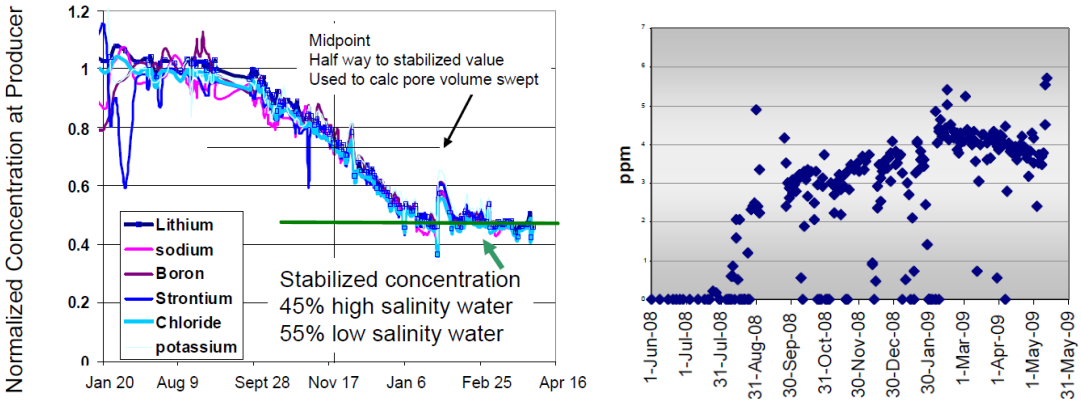

Figure 2.19: Ion changes in concentration during low-salinity waterflooding. On the left it is shown the decrease of the ions concentration and on the right the increase in iron concentration. The abrupt increase in Fe concentration denotes the first arrival of low-salinity water at the production well. Taken from Seccombe et al. (2010)

[4] water-cut term describes how much water in % is produced in respect to the oil produced.

The geochemical implications of the field scale implementation was examined by Lager et al. (2011). In addition to the above paragraph, it was observed that the produced water had a high-salinity water component from a nearby well, so at the end the low-salinity water had a 55% contribution to the produced water. Apart from that, a shut -in period of the production well occurred and when it was back online, little difference in the water composition was observed. This showed that no mineral dissolution happened during the waterflooding due to the low-salinity water, such as feldspar or other aluminosilicate minerals.

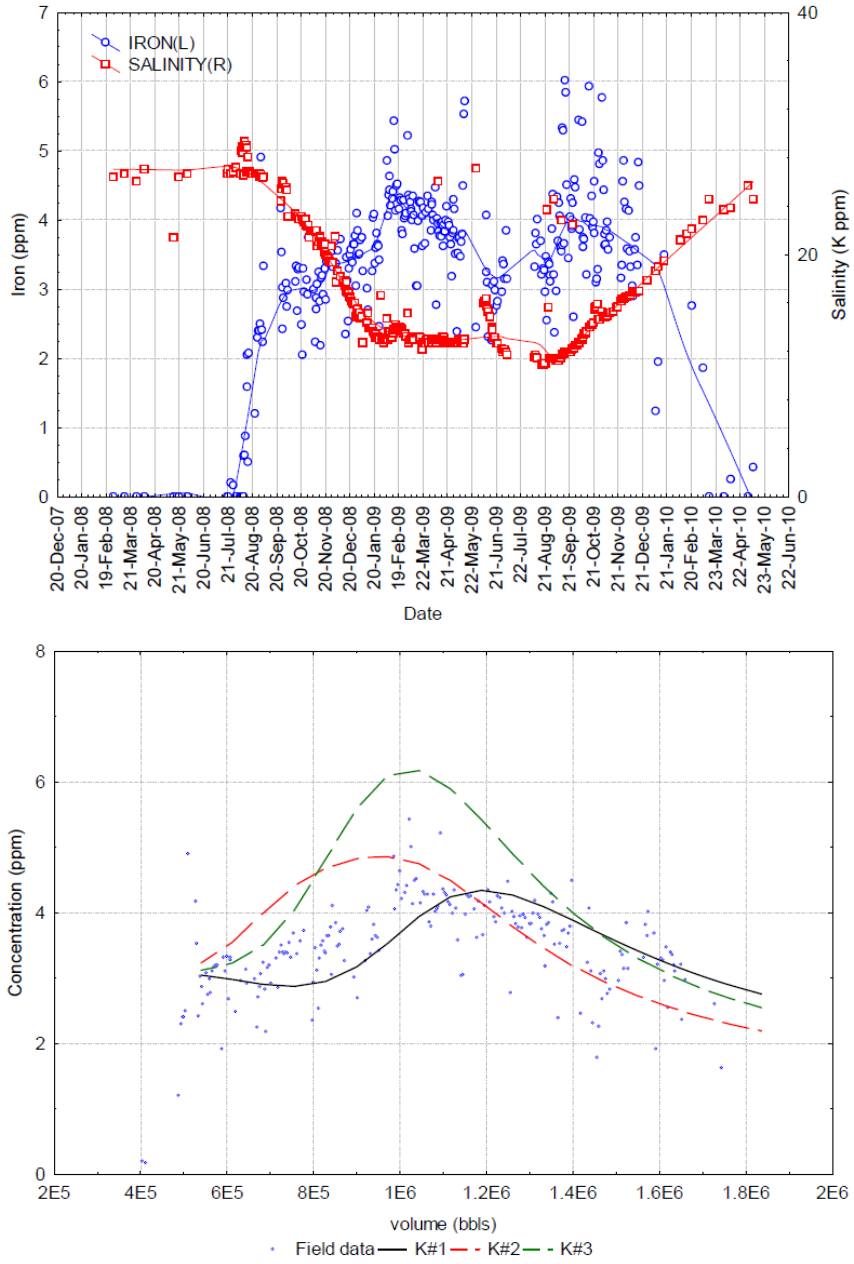

Figure 2.20: Production profile of iron production in relation to salinity from Endicott Field low-salinity waterflooding implementation (upper side graph). Produced iron matched data after geochemical model with organometallic complexes. Three different stabillity constants are used, K1, K2, K3, (lower side graph.) Taken from Lager et al. (2011)

As iron had increased concentration in the water produced, it was concluded that it was not from iron carbonate dissolution present in the reservoir as cement, but rather from the dissolution of iron oxides precipitated on the clay mineral surfaces (Lager et al., 2011; Seccombe et al., 2010).

In order to verify this hypothesis, i.e. that iron acted as bridges to oil compounds and clay

mineral surfaces, geochemical models were built by the authors (Lager et al., 2011), in order to match the production data of the iron composition in the produced water. When considering mineral dissolution of pyrite and/or siderite, as the main source of this iron, the model resulted in much higher concentrations of iron than the actual values observed. However, when allowing the model to create organo-metallic complexes with different stability constants K, varying independently, a better match of the iron concentration was achieved, Figure 2.20. This was due to removal of these complexes by the low-salinity water. After the complexes are removed, Fe ions are chelated and prevented from further interaction with the clay mineral surface (Lager et al., 2011).

2.5 Clay Mineralogy

In Section 2.2 a brief description of the reservoir rock and clay mineral content was given. In the following paragraphs a more detailed description will be given for clay minerals from different clay groups, in terms of structural characteristics, element substitutions, bonds, basal and surface charges and pH effects. In addition, effects of Fe^{3+} reduction will be described, by presenting the main reduction models in the literature.

2.5.1 Clay Minerals Description

Clay mineral building blocks

As clay minerals belong to the phyllosilicate mineral group, they have layered structure, consisting of tetrahedral and octahedral sheets packed together in two main ways: tetrahedron-octahedron (T-O) or one octahedron in between two tetrahedra (T-O-T). The tetrahedron consists of a silicon atom Si surrounded by four oxygen atoms O. Many tetrahedra of SiO_4^- will bond to form a tetrahedral sheet, Figure 2.21, while octahedron consists of a cation, typically Al^{3+}, surrounded by oxygen (O) and hydroxyls (OH), Figure 2.22. The main classification of clays is done by the type of layers that are formed, when tetrahedral and octahedral sheets are combined.

- 1:1 phyllosilicate clay minerals, like kaolinite, combine 1 octahedral and 1 tetrahedral sheet. The thickness of one layer is around 7 Å.

- 2:1 phyllosilicate clay minerals, like pyrophyllite, combine 2 tetrahedral sheets and 1 octahedral sheet in between. The thickness of one layer can be 10Å to 14Å.

Cation substitution can occur in both kind of layer sheets, inducing negative charge in the clay mineral structure; for tetrahedra, Si^{4+} is substituted by Al^{3+} while in octahedra other common divalent cations are Mg^{2+}, Fe^{2+} or trivalent Fe^{3+}.

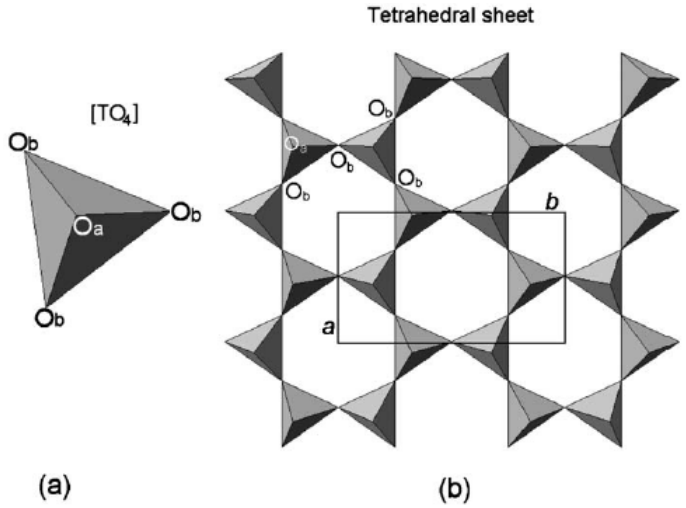

Figure 2.21: In (a) the tetrahedron is depicted. In (b) a tetrahedral sheet, with O_a and O_b for apical and basal oxygen atoms. a-b box stands for unit cell parameters. Taken from Brigatti et al. (2006)

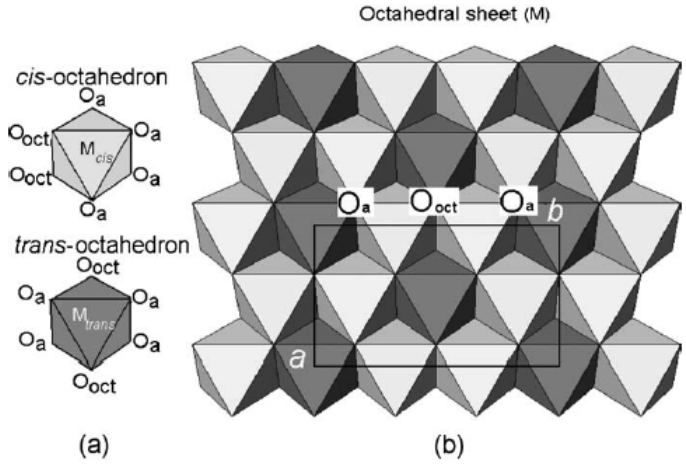

Figure 2.22: In (a) the basic octahedron configuration. O_{oct} is the position for the anions in the structure. In (b) octahedral sheet. a-b box for unit cell parameters. Taken from Brigatti et al. (2006)

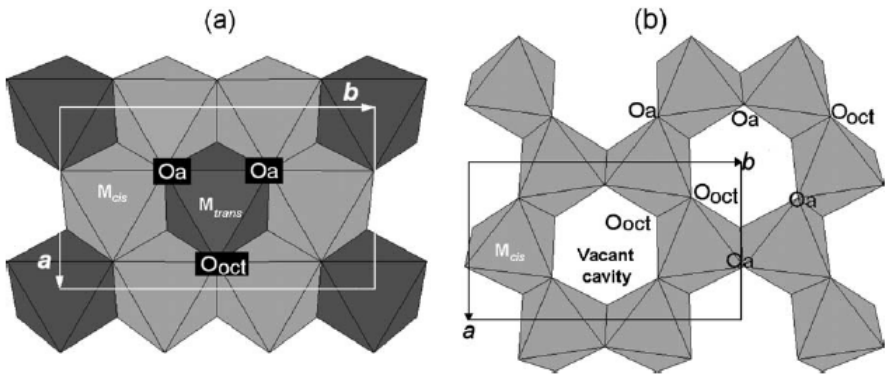

Figure 2.23: Configuration of (a) trioctahedral and (b) dioctahedral sheet. O_a for apical oxygen atoms and O_{oct} for anionic site. Taken from Brigatti et al. (2006)

2:1 clay minerals can further be distinguished in di-octahedral or gibbsite-like structure, with the form of $Al(OH)_6^{-3}$ as unit cell and in tri-octahedral or brucite-like structure, with the form of $Mg(OH)_6^{-4}$ as unit cell, Figure 2.23. Related substitution will be Al^{3+} to Mg^{2+} or Fe^{3+} for dioctahedral and Mg^{2+} to Fe^{2+} for trioctahedral, (Yariv, Cross, 2001; Eslinger, 1988; Ballah, 2017).

An important characteristic of clay minerals is the cation exchange capacity (CEC). The units used to measure this CEC capacity are milliequivalent per 100 grams (meq/100g) of clay. It takes into account the concentration of the unfixed cations in the diffuse layer (more in Section 2.5.2) depending on the magnitude of the total layer charge and pH values.

Clay mineral surfaces also exhibit acidic and basic behaviour. The acidity of the clay mineral surface is expressed as the ability to donate protons in various organic compounds and is affected by the exchangeable cations and their hydration energy. Frenkel (1974) concluded that the acidity of montmorillonites increases with decreasing interlayer water and, in addition, that substitutions taking place in the octahedral sheet amplifies the acidity of the mineral surface, for the particular method used in their work.

Regarding the basicity of clay mineral surfaces, it is located on the oxygen plane of the silicate layer. Oxygen atoms can donate nonbonding lone-pair electron to acidic compounds. In addition, basicity is related to tetrahedral substituion of Si for Al. Dioctahedral and trioctahedral will exhibit different basic strength with decreasing order of beidellite (dioctahedral) < vermiculite (tri-octahedral) < montmorillonite (dioctahedral) < saponite (trioctahedral) < laponite (trioctahedral), (Garfinkel-Shweky, Yariv (1997) and referenced within).

Smectite Group

Smectites are highly swelling clay minerals. Due to their structure, smectites are of 2:1 type, and the way the layers (tetrahedron-octahedron-tetrahedron) are interconnected, water molecules are integrated in the structure, creating the swelling effect. A schematic representation of a smectite can been seen in Figure 2.24, including the region where water molecules and exchangeable cations are integrated in the structure.

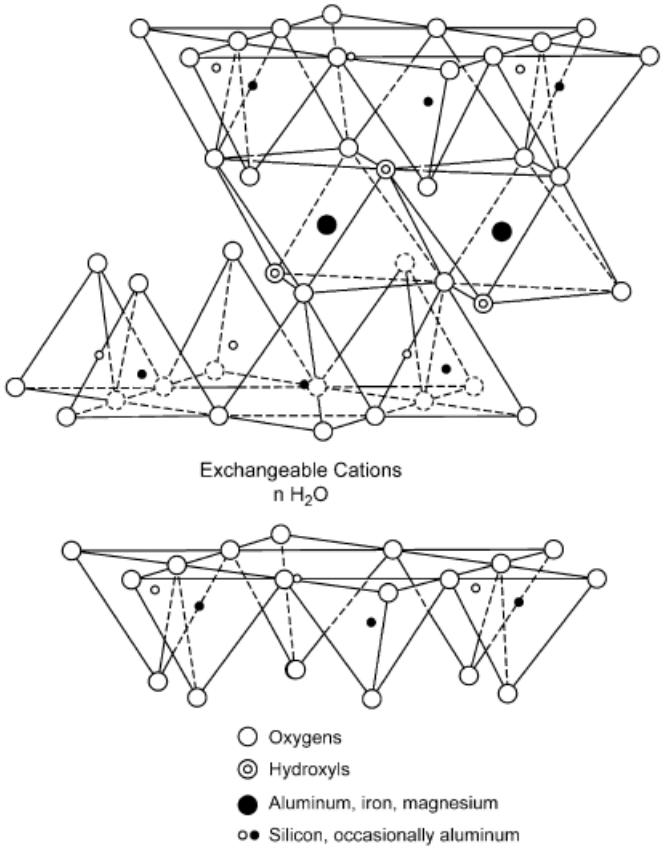

Figure 2.24: Structure of Smectite mineral group. Taken from Murray (2006)

The interlayer area is hydrophilic and can be directly hydrated in various degrees, depending on the identity of the interlayer cation present. However, not all smectites have the same swelling ability. Montmorillonite, for example, swells much more that nontronite. This phenomenon is attributed to the number of water layers that take part to the swelling and not the separation distance between the individual clay layers, (Stucki et al., 2002).

Illite Group

Illite mineral group is very similar to smectites, in terms of structure. Illite is a 2:1 type of clay mineral, meaning that one octahedral sheet is sandwiched by two tetrahedral sheets, forming that way an illitic particle. The layer-layer bonding is facilitated by K^+, which has low enthalpy of hydration, making the layer-layer bonding strong, as it prevents water occupying these positions. In Table 3.1, it can be seen that the illite sample IMt2 has the highest amount of potassium. As such, illites are generally termed non-swelling clays. In the schematic representation of the illite clay minerals in Figure 2.25, the position that potassium takes in the structure of the mineral is shown and it fits in the hexagonal rings that are formed by the oxygens of the adjacent silica tetrahedral sheets (Murray, 2006). Regarding structural elemental substitutions, Al^{3+} in the octahedral sheets can be substituted by Mg^{2+} and Fe^{2+}.

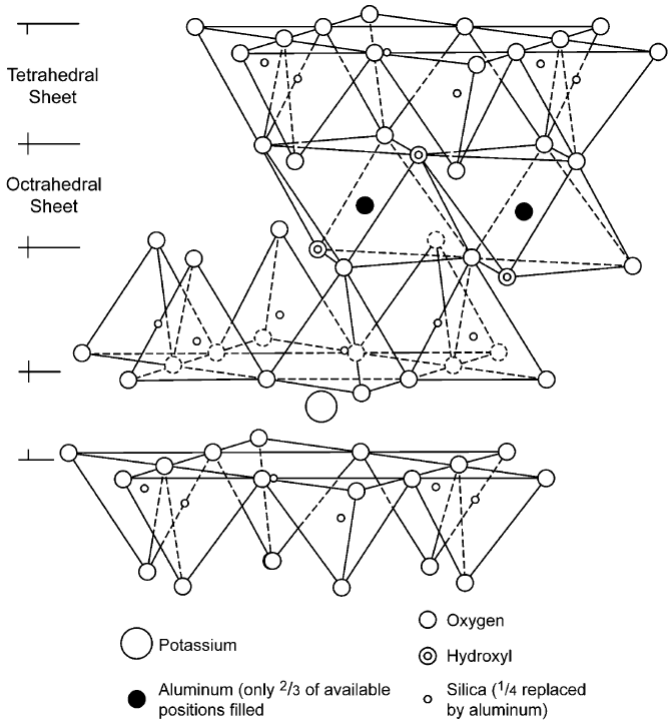

Figure 2.25: Structure of Illite mineral group. Taken from (Murray, 2006)

Chlorite Group

Chlorite minerals are 2:1 type of clay minerals that contain a brucite sheet in between the clay mineral layers with chemical composition ($Mg(OH)_2$). The substitutions that can occur in the octahedral sheet are Al^{3+} by Fe^{3+}, Mg^{2+} and Fe^{2+} and in the tetrahedral sheet Si^{4+} by Al^{3+}.

The total charges of the octahedral sheet will be dependent on the charges dominant in the tetrahedral sheet. When tetrahedral charge is <-1 , then octahedral charge is positive, and when it is >-1, then it's negative. The point of zero surface charge in chlorite occurs at pH=2.5, after zeta potential measurements with distilled water, (Hussain et al., 1996).

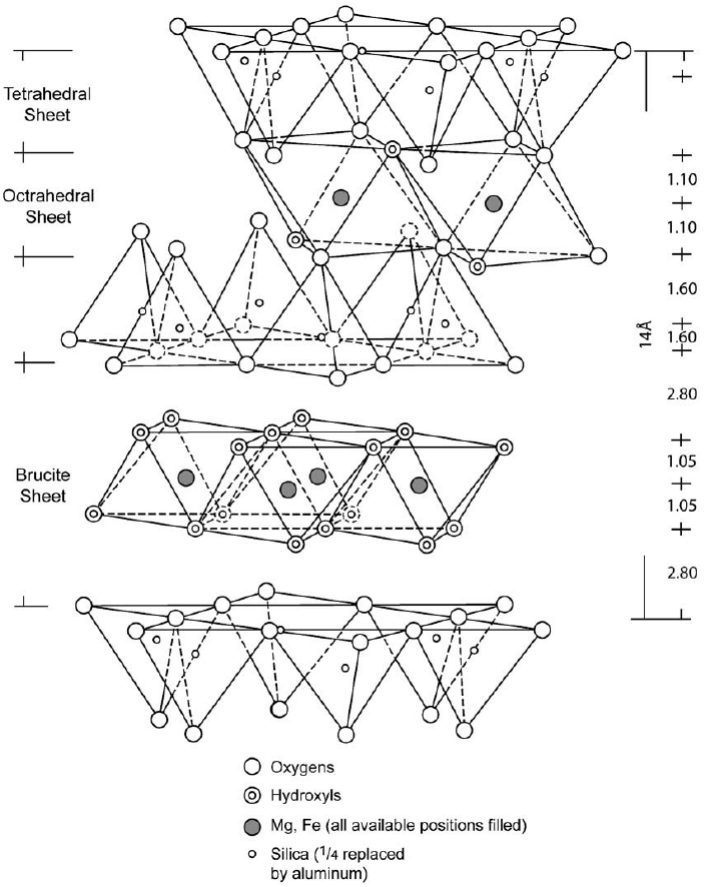

Figure 2.26: Structure of Chlorite mineral group. Taken from (Murray, 2006)

Sepiolite Group

Sepiolite is a 2:1 clay mineral type with inverted structure, as shown in Figure 2.27. This creates high internal surface area, with high sorptive capacity. The CEC of the mineral can be at 30-40 meq/100g, a value between kaolinites and calcium montmorillonites (Murray, 2006).

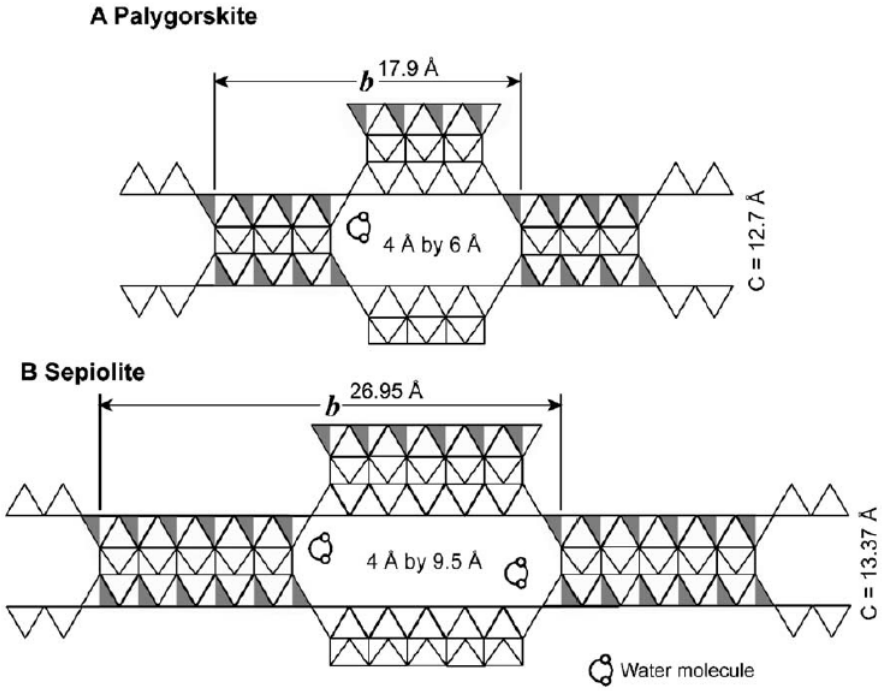

Figure 2.27: Structure of Sepiolite- Palygorskite minerals group. Taken from (Murray, 2006)

2.5.2 Surface Charge and Zero Point of Charge (ZPC)

Clay minerals exhibit two kinds of charges: structural or permanent charges which depend on the various substitutions at a structural level in tetrahedral (Al^{3+} for Si^{4+}) and octahedral sheets (Mg^{2+} or Fe^{2+} for Al^{3+}), and surface charges which are pH dependent. The surface charges originate on the basal surface area of tetrahedral sheets of 2:1 clays and on the basal of both tetrahedral and octahedral sheets for 1:1 clays, and along the edges of sheets for both kind of clays, (Eslinger, 1988). Broken bonds of Si-O and Al-OH at these surfaces can bond with free H^+ and create hydroxyls, which can act as acid or base and create positive or negative charges on the surface by further bonding of H^+, as shown below.

$$MOH + H^+ \rightarrow MOH^{2+}$$

$$MOH + OH^- \rightarrow MO^- + H_2O$$

The silicate structure, pH and salinity of the solution will determine the final charges of these reactions: positive or negative. At low pH values the surface will exhibit an anion exchange capacity, while at high pH values they will exhibit cation exchange capacity. For 2:1 clay minerals,

the surface charges account for less than 1% of the total charge, but for kaolinite this is not the case, as structural substitutions are uncommon, and surface charges have higher contribution to the net charge.

As the pH of the solution will affect the surface charges there is a value at which the charges are zero, point of zero charge - pzc or isoelectric point- IEP. The isoelectric point is at that pH value, which the zeta potential is zero, measured at the Helmholtz plane, Figure 2.28. These two terms can coincide, if no specific adsorption occurs, but there are cases which the pH value is different, Figure 2.28, (Alvarez-Silva et al., 2010; Hunter, 2013) For example, smectite clay mineral exhibit pH-dependence in zeta potential, due to the structural differences of the mineral itself and for that reason, pzc and IEP will have different values.

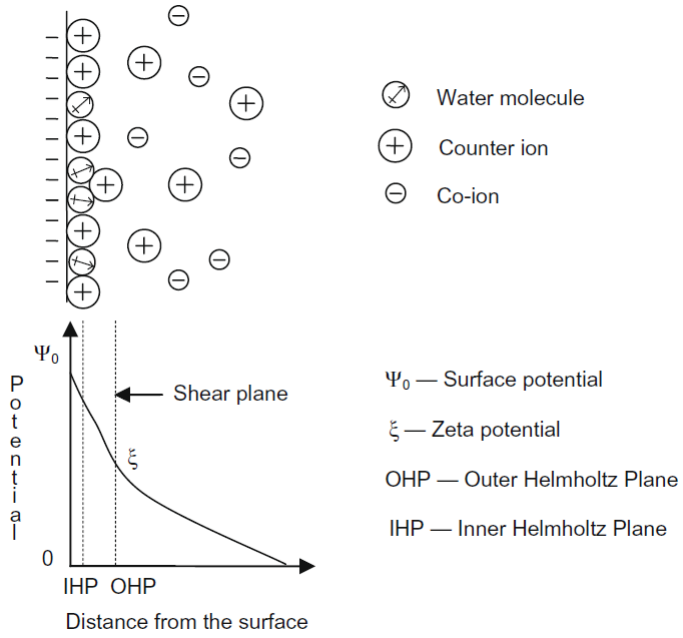

Figure 2.28: Representation of the double layer structure. Taken by (Alvarez-Silva et al., 2010)

Regarding the pzc, when the solution pH is lowered, then H^+ will bond on the surface and positive charge will result. On the other hand, when the pH is increased, OH^- will bond on the surface resulting in a shift to negative charge, Figure 2.29. Depending on the permanent charges of a clay mineral, the pzc can be at higher or lower than pH=7.

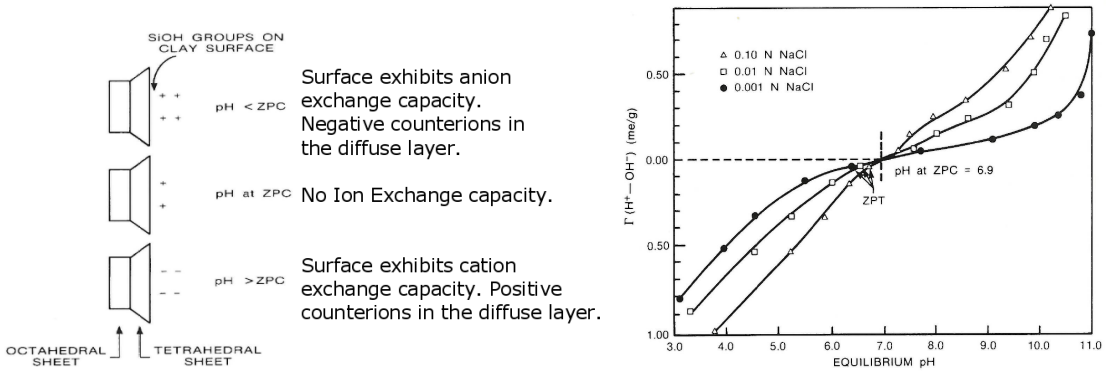

Figure 2.29: Surface charge changes depended on the pH values in relation to the zero point of charge (left graph). pH titration curve of iron oxides, showing zero point of charge at pH=6.9. Above that value the net charge of the oxides will be negative, and below that value will be positive (right graph). Taken from Eslinger (1988).

Zero point of charge is significant because this will determine at what pH values of solutions the minerals exhibit anion or cation exchange capacity. This will impact the behavior of the clay minerals along with other minerals in solution, and will control attraction or repulsion between mineral grains. This fact can be rather important from an oil-industry perspective, as clays can cause production difficulties and oil recovery impedance once mobilised through aggregation in and blocking fine pores. In addition, zpc will determine the pH range that a clay mineral suspension can be formed and the amount of water that a clay mineral can hold. The last two facts are explained below by the diffuse double-layer theory, (Eslinger, 1988).

2.5.3 Diffuse Double layer Theory and Models

The diffuse layer can be explained by the diffuse double layer theory, which describes the interactions among clay mineral surfaces, interlayer cations and water. Generally, clay minerals exhibit a negative charge on their surfaces. When they are mixed within a water solution, due to this charge, water will tend to attach on the surface, while at the same time cations from the surface will diffuse to a distance from the clay surface. A double layer is formed, as the negative layer is the clay mineral surface and the positive layer is the cation diffuse zone next to the clay mineral surface. There are three diffuse double layer models, the: Helmholtz Model, Gouy-Chapman Model, Stern Model, Figure 2.30, (Eslinger, 1988; Pilon et al., 2015).

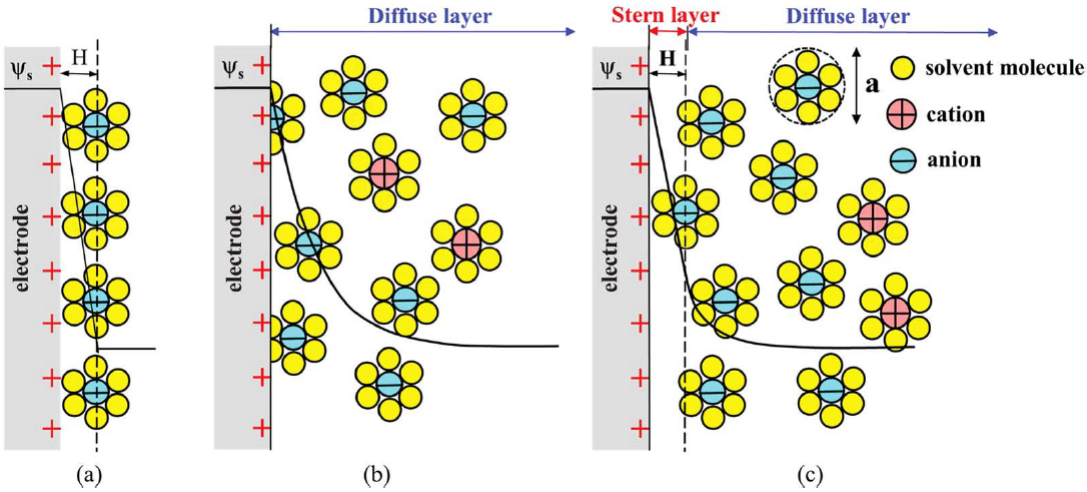

Figure 2.30: Schematic representation of different electic double layer model proposed by (a) Helmholtz, modified by Gouy-Chapman (b) and by Stern (c), incorporating the other two models. Taken from (Pilon et al., 2015).

The first who described the double layer theory was Helmholtz, suggesting a positively or negatively charged surface will repel ions of the same charge, when immersed in a solution, but will attract ions of the opposite charge. By this process two layers of ions will be formed, one close to the charged surface (attracted ions), while the other layer will be in the electrolyte, and near the charged surface (repelled ions). At this model a mono-layer is hypothesized for the attracted ions near the charged surface, which will define a plane of H distance between the surface and the counter-ions, Figure 2.30 (a), (Pilon et al., 2015).

The Gouy and Chapman modification of this model introduced the concept that the "ion distribution should be continuous in the electrolyte solution" (Pilon et al., 2015). The distribution of the ions around the charged surface will be dependent on the ion concentration in the solution. This distribution is result of an equilibrium situation, of electrostatic attraction and diffusion around the surface, in which the zone around the surface has a finite, but diffuse, thickness. The ion concentration will be higher close to the surface and will decrease at a distance from the surface until it reaches the concentration of the initial solution. As an example, at a smectite mineral, with a negatively charged surface, the double layer created is the negatively -charged clay surface and the diffuse positively charged zone next to that, Figure 2.30 (b), (Eslinger, 1988). In addition to this example, if the salinity gets higher, the diffuse layer gets thinner, with a certain point where the layers of the clay mineral particles overlap, resulting in flocculation or aggregation, (Eslinger, 1988).

The Stern model is a combination of the two previous models, describing two distinct areas around a charged surface. The first region is close to the surface, the Stern layer, where the ions are adjusted to the surface, not taking part in the diffuse layer, the second region of this model. The Stern model takes into account the finite size of ions in the electrolyte solution, Figure 2.30 (c), (Eslinger, 1988; Pilon et al., 2015).

2.5.4 Other Clay Mineral Characteristics

Some types of clay minerals tend to swell when in contact with water. Clay minerals that exhibit swelling are especially those of the 2:1 (TOT) type, as there is more space for the water to be attached on the surface at a region, between the tetrahedral sheets of two neighbouring clay particles, named as intra-particle swelling (Eslinger, 1988).

Another important characteristic of clay minerals is the cation exchange capacity (CEC). As already stated, this is the capacity of clay minerals to exchange cations from their surface. This capacity is dependent on the mobile cations in the diffuse layer. The diffuse layer thickness is controlled by the pH (solution salt concentration or surface charge), so CEC will be controlled by the pH of the environment. The CEC of clay minerals are reported at pH=7. In Table 2.1, the CEC of different clay minerals is presented (after Eslinger (1988)). Clay minerals have different cation exchange capacities, depending on the overall surface area, i.e. the external and internal available surface available from the clay mineral structure, but strongly governed by the layer charge.

Table 2.1: Cation Exchange Capacities of clay minerals

Clay Mineral	CEC in (meq/100g)
Smectite	80-150
Vermiculite	120-200
Illites	10-40
Kaolinite	1-10
Chlorite	<10

2.5.5 Effect of Redox State on clay mineral

In a series of papers by Stucki and co-workers and other authors, (Stucki, Roth, 1977; Stucki et al., 1984b,a; Stucki, Lear, 1990; Stucki et al., 1996; Manceau et al., 2000b,a; Stucki et al., 2002; Claire et al., 2002; Lee et al., 2006; Ribeiro Fabiana et al., 2009; Geatches et al., 2012) and many

more, oxidation - reduction mechanism and effects for structural iron in smectites (nontronite) have been examined through various experiments and molecular simulations.

Fe^{3+} reduction can be achieved either by using a reducing chemical agent such as sodium dithionite ($Na_2S_2O_4$) or using microbes. The reduction process differs between the two, (Lee et al., 2006), and hereafter only the chemical agent will be considered.

Initially, the reducing agent will give its free electron to the Fe^{3+} reducing it to Fe^{2+}. As this process goes on, the previously established negative charges, balanced by cations, will start to increase. That will cause a higher cation adsorption of cations to balancing this extra negative force, leading to increase of the cation exchange capacity (CEC) of the clay mineral (Stucki, Roth, 1977; Stucki et al., 1984a). At a second stage and higher degrees of reduction, the excess of charges will be balanced by de-hydroxylation from the mineral lattice, with concurrent $cis-$ to $trans-$ site Fe^{2+} migration and trioctahedral domain creation. This structural change would cause disturbance of the six-fold coordination of Fe^{3+}. Early research suggested that Fe^{2+} will have a five-fold coordination, but Manceau et al. (2000b,a), established that a six-fold coordination is kept for Fe^{2+}, too. That is achieved by re-protonation (H^+) of the under-saturated O_{ext} groups, creating hydroxyls eventually. These protons are readily available mainly from the interlayer water.

One key aspect of the reduction process is the increase of negative charges, which are depended by the initial iron content but are not increasing indefinitely. The relationship between reduction degree and negative charges appears linear at early reduction stages, but is curvilinear in total. It was established that the reduction is initiated by the reducing agent, but then continued by SO_2^- radicals, and at very high reduction degrees, electron delocalisation from other cations in the lattice (Al^{3+}), Stucki et al. (1996). So, no more electrons are induced in the lattice to cause further negative charges, but rather an electron redistribution, Figure 2.31.

Other important changes worth considering are the interlayer collapse and the interlayer dehydration. In addition, decrease of the specific surface area is studied as well as, minor Si, Al and Fe dissolution from the mineral lattice, which is not considered significant for altering the mineral to a high extent. This dissolution is caused by the dithionite-water solution, if not buffered properly, during the reduction, (Stucki et al., 1984b,a).

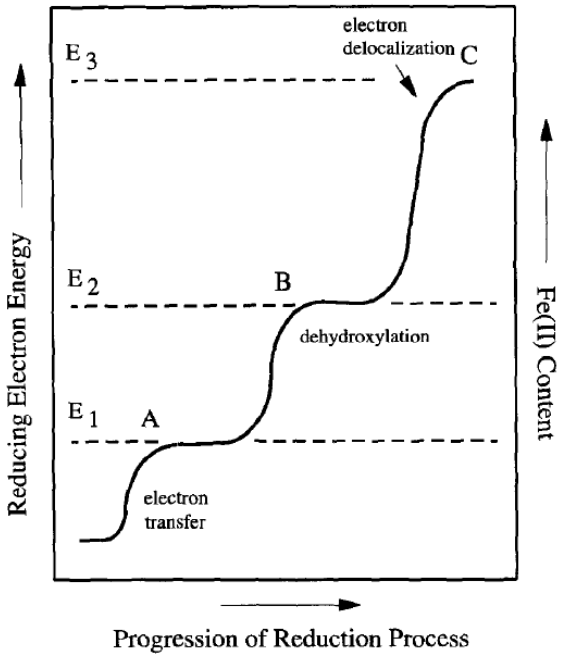

Figure 2.31: Reduction model suggested by Stucki et al. (1996) involving reducing electron energy, Fe(II) content and reduction process

The oxidation state of the clay mineral can affect the swelling behaviour of the mineral. In the oxidised state, smectites can hold more water in the vicinity of the exchangeable cation, in the presence of inorganic cations such as Na^+, than reduced smectites which are observed to hold less water (Stucki et al., 2002). Reduced Fe_{str} decreases the water-holding capacity of the clay mineral interlayer, causing layer collapse. On the other hand, when the interlayer space is occupied by organic cations the layer collapsing effect is lower in comparison with the inorganic cation case, Figure 2.32. Other important aspects of reduction process, will be discussed in relation to the experiments and the results acquired in this PhD project, at the following chapters.

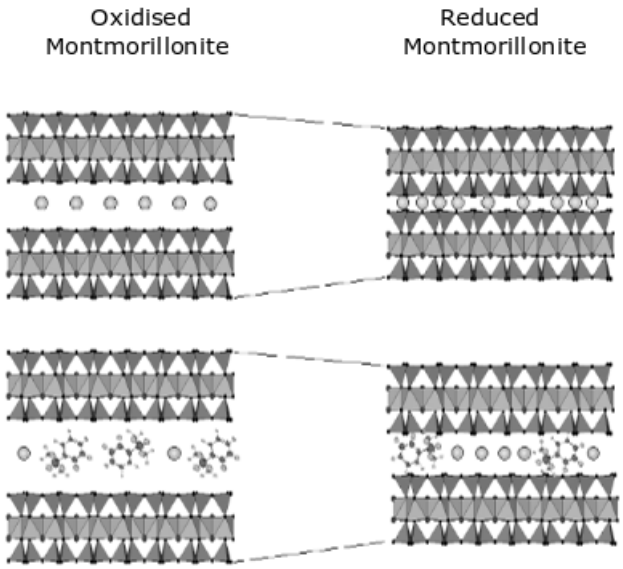

Figure 2.32: Inorganic (upper section) and organic cation (lower section) effect in smectites structure, upon reduction. Taken from (Stucki et al., 2002)

2.6 Conclusions and Project Aims

From the above review and analysis, it is apparent that low-salinity waterflooding is a rather promising EOR method for field scale application, but better understanding of the related mechanisms and the constraints of implementation need to be addressed. As more information is requested regarding how LSWF actually works, studies are focusing in greater detail on each mechanism to decipher the exact changes at the rock/oil/brine interfaces that cause the observed effects of greater oil recovery.

Redox state of the reservoir environment can determine many physicochemical processes on the constituent mineral surfaces, which govern the oil adsorption/desorption and all the interactions involved in this rock/oil/water system. The overall purpose of this research work in this thesis is to look how redox state can affect the aforementioned system by conducting fundamental experiments under reduced and oxidised conditions, deciphering the behaviour of clay minerals under these conditions in relation to the present liquids, of oil and water. Once that is better understood and constrained, then a better comprehension of the low-salinity waterflooding principles can be achieved, leading to optimising this EOR method for each reservoir case independently.

Thesis objectives

- Objective 1

  Understanding the wettability changes of clay minerals upon reduction. In Section 2.4.6, it was discussed the studies that have pointed out the effects of reduced iron, in clay mineral or as particle/element, have on the the rock surface when it comes into contact with crude oil. For that reason, wettability measurements are going to be shown, taken on iron reduced clay mineral films using contact angle measurement techniques.

- Objective 2

  Focusing on the multi-ion exchange mechanism (MIE), as per Section 2.4.2, and consequently to the above wettability studies, cation exchange processes were to be explored in more detail, for reduced clay minerals. Thus, (i) the clay mineral hydration is studied with infrared (IR) spectroscopy, under reduced and oxidised conditions, as well as the structural changes of iron-bearing clay minerals. Also, (ii) cation exchange reactions are considered, for these clay minerals, quantifying thermodynamically the relative selectivity of Na^+, Ca^{2+} and K^+ on the clay mineral surface. Nontronite and montmorillonite were first homoionised (Na-saturated) and purified, and then appropriate samples were prepared for each of the (i) and (ii) studies.

- Objective 3

  Utilise different structural iron reduction degrees, such as oxidised, partially and fully reduced state, for the above studies, in an attempt to propose a model of optimum low-salinity waterflooding implementation, during secondary or tertiary recovery.

Chapter 3

Materials - Methodology - Analytical Techniques

3.1 Introduction

As the wettability effects of Fe-minerals in relation to redox state of the reservoir is the subject of this PhD project studies, several ferruginous clay minerals will be used in various experimental set-ups to understand the effects of the different redox conditions. No core plugs will be used, as the rock compositions of such ferrous minerals can be low in model sandstone cores such as Berea or Castlegate (Kareem, 2017). Previous research has pointed out, the high molecular weight oil molecules will adhere preferentially on the mineral phases, especially those with acidic and basic functional groups (Buckley et al., 1989, 1997, 1998), for that reason, crude oil will be used to create a more-realistic representation of the clay mineral/oil/water environment. In this chapter, materials tested and used will be described, methodologies and experimental outlines will be defined and working principles of analytical techniques utilised are given, too.

3.2 Materials Used

For the experimental work of this PhD study, 7 different clay minerals were acquired from "The Clay Minerals Society" (CMS) Repository in the USA. The minerals supplied are two nontronites (NAu1, NAu2), Na-Montmorilonite (SWy3), the iron-bearing chlorite, Ripidolite (CCa2), illite (IMt2) and Sepiolite (SepSp1). At Table 3.1, the chemical composition of these minerals is given.

Table 3.1: Major Elements chemical composition of the clay minerals supplied from Clay Minerals Society. All information were taken from *www.clays.org*

Clay Minerals Chemical Composition						
Oxides	NAu1	NAu2	CCa2	IMt2	SWy3	SepSp1
SiO_2	53.33	56.99	26	49.3	62.9	52.9
Al_2O_3	10.22	3.4	20	24.25	19.6	2.56
TiO_2	0	0	0.476	0.55	0.09	0.001
Fe_2O_3	34.19	37.42	26.6	7.32	3.35	1.22
FeO	0	0	20.8	0.55	0.32	0.3
MnO	0	0	0.1	0.03	0.006	0.13
CaO	3.47	2.67	0.25	0.43	1.68	0.01
MgO	0.27	0.34	17.2	2.56	3.05	23.6
Na_2O	0.08	0.11	0.1	0	1.53	0.01
K_2O	0.03	0.02	0.2	7.83	0.53	0.05
P_2O_5	0	0	0.02	0.08	0.049	0.01
F	0	0	0	0	0.111	0
S	0	0	0	0	0.05	0
LOI	0	0	9.32	8.02	0	20.8

Initially, all clay mineral were tested, untreated, for clay film creation. As each mineral has different characteristics, and with the method used for clay film creation, (see Chapter 4), only nontronite-2 (NAu2), with high iron content, and illite (IMt2), with medium iron content, were considered stable enough for such clay film purposes, useful for contact angle measurement experiments. For the infrared spectroscopy measurements (Chapter 5 and Chapter 6), treated (Section 3.3.2) clay minerals, mainly nontronite-1 (NAu1) was used. NAu1 is frequently used in the literature, so it was considered a good model high-iron clay mineral. For the cation exchange experiment, (see Chapter 7) again treated NAu1, NAu2 and SWy3 were used.

The crude oil used for the contact angle measurements (Chapter 4) was provided by BP, with characteristics shown in Table 3.2 after gas chromatography (GC) analysis, (Kareem, 2017).

Table 3.2: Results of Gas chromatography (GC) analysis of crude oil constituents, physical characteristic and polar components concentration (provided by BP). Taken from (Kareem, 2017)

Hydrocarbon type (C < 36)	**wt %**	**Physical properties of C <36**	
Normal paraffins	12.27	Density (25°C)	0.8793
Isoparaffins	12.72	Viscosity (40°C	41.71
Aromatics	0.784		
Naphthenes (C17 < C < 25)	7.535	**Polar Components** (mg KOH /gr)	
Aromatics (C17 < C < 25)	10.22	Total Acidic Number (TAN)	1.2
Unknowns (C < 25)	14.36	Total Basic Number (TBN)	0.52
$C36^{+}$	36.77		

3.3 Clay mineral characterisation and treatment

3.3.1 X-ray diffraction

X-ray diffraction phenomenon was first described by Sir W.H Bragg and Sir W.L.Bragg with the following equation, known as Bragg's Law (n is an integer)

$$n\lambda = 2dsin\theta$$

.

This equation describes the interference of an X-ray beam with a crystal or a material. When the wavelength λ of the X-ray beam irradiate a material with a interplanar spacing d, the constructive interference or X-ray diffraction, can be observed at specific angles 2θ for the material under examination, Figure 3.1, ($https://ywcmatsci.yale.edu$). As each material will have a different interplanar spacing, then X-ray diffraction can be used to identify different mineral phases, in geological studies. In practise, the different mineral phases in an unknown sample, e.g., sandstone sediment, can be determined by mounting the sample on the holder, with X-ray beam and detector moving synchronised at different incidental (and refraction) angle. That enables the detector to record the constructive diffraction of interplanar spacing of the different phases, or in other words, the similarity of the X-ray beam in relation to the different crystal

lattices at the angle θ observed.

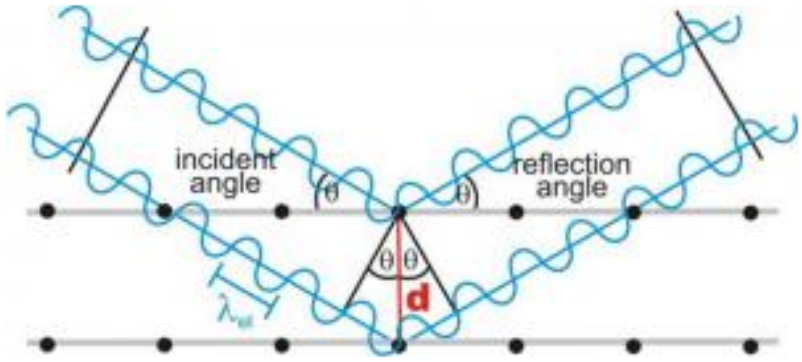

Figure 3.1: X-ray diffraction - Bragg's Law schematic representation. Taken from *https* : *//ywcmatsci.yale.edu*

X-ray diffraction (XRD) data were acquired for mineral characterisation. The instrument was a PANalytical X'Pert Pro MPD, powered by a Philips PW3040/60 X-ray generator and fitted with an X'Celerator[1] detector. Diffraction data is acquired by exposing powder samples to Cu-K X-ray radiation, which has a characteristic wavelength (λ) of 1.5418 $\mathring{A}$. X-rays are generated from a Cu anode supplied with 40 kV and a current of 40 mA. Air-dried samples were prepared for XRD analysis by back-loading approximately 200mg of dry powder into stainless steel sample holders. Data sets were collected over a range of $2-80°$ 2θ with a step size of 0.0167° 2θ and nominal time per step of 750 seconds, using the scanning XCelerator detector (hence the apparently long counting time per step) and a secondary graphite crystal monochromator in the diffracted beam path. Fixed divergence and anti-scatter slits of 1/2° and 1°, respectively, were used together with a beam mask of 10mm, soller slits of 0.04 radians and all scans were carried out in 'continuous' mode.

Comparing XRD data with the literature (Keeling et al., 2000; Hower, Mowatt, 1966; Borden, Giese, 2001; Wu, 2001; Mermut, Lagaly, 2001; Mermut, Cano, 2001; Gates, 2005) a strong consistency is found on the XRD patterns for all clay mineral below. More details on the XRD data regarding the mineral phases identified in these clay minerals can be found at the Appendix A.1.

[1]The XCelerator is an ultra-fast X-ray detector that uses RTMS (Real Time Multiple Strip) technology. It operates as an array of a hundred channels which can simultaneously count X-rays diffracted from a sample over the range of 2θ angles specified during a scan. The XCelerator is therefore able to produce high quality diffraction data in a significantly shorter time period than an older style diffractometer would require.

In addtion to Table 3.1, proposed structural formulae of these minerals are (clays.org, (Gates, 2005)):

Nontronite-1 - NAu1 :

$$M^{+}_{1.0}[Si_{7.00}Al_{1.00}][Al_{0.58}Fe_{3.38}Mg_{0.05}]O_{20}(OH)_4$$

Nontronite-2 - NAu2 :

$$M^{+}_{0.72}[Si_{7.57}Al_{0.1}Fe_{0.42}][Al_{0.52}Fe_{3.32}Mg_{0.7}]O_{20}(OH)_4$$

Ilite - IMt2 :

$$(Mg_{0.09}Ca_{0.06}K_{1.37})[Al_{3.37}Fe^{3+}_{0.16}Fe^{2+}_{0.1}MntrMg_{0.45}Ti_{0.02}][Si_{7.08}Al_{0.92}]O_{20}(OH)_4$$

with charges distribution : Octahedral= -0.44, tetrahedral= -1.23, interlayer= -1.68, unbalanced= 0

Montmorillonite - SWy3 :

$$(Ca_{0.12}Na_{0.32}K_{0.05})[Al_{3.01}Fe^{3+}_{0.41}Mn_{0.01}Mg_{0.54}Ti_{0.02}][Si_{7.98}Al_{0.02}]O_{20}(OH)_4$$

with charges distribution : octahedral= -0.53, tetrahedral= -0.02, interlayer= -0.55, unbalanced=0.05, cation exchange capacity (CEC) 76.4 meq/100g, with principle exchange cations Na and Ca.

XRD data

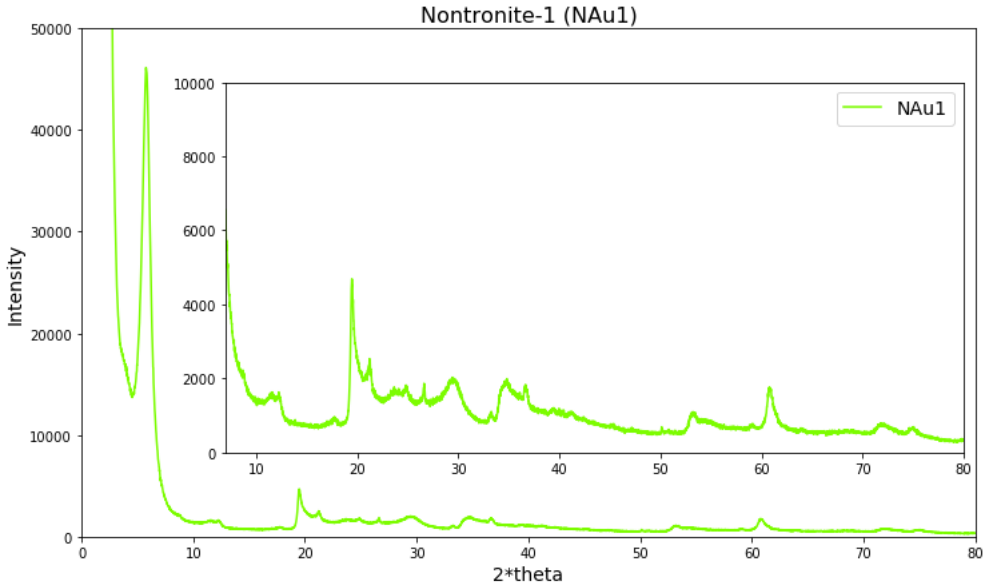

Figure 3.2: XRD data for nontronite-1 (NAu1).

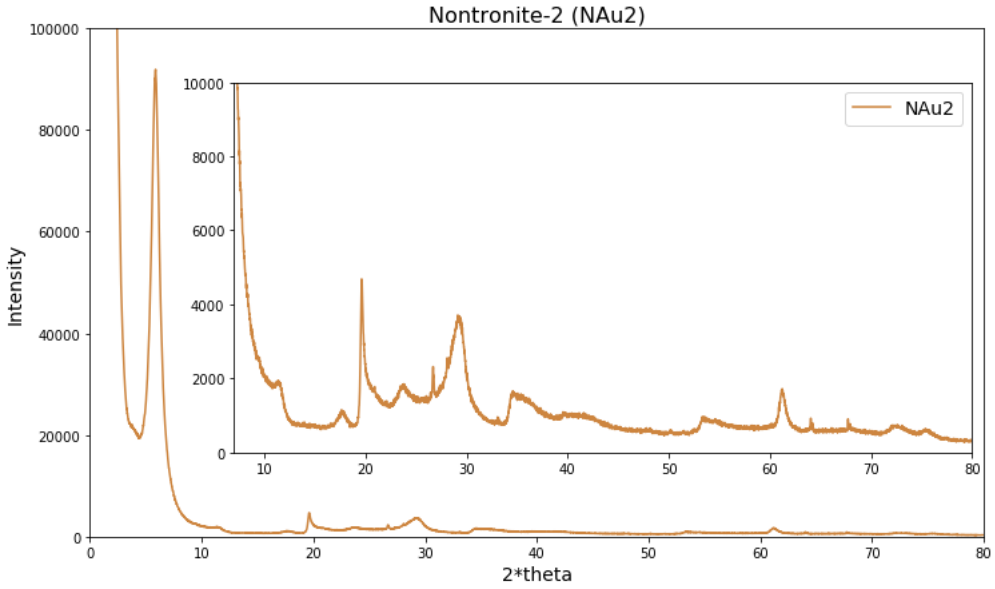

Figure 3.3: XRD data for nontronite-2 (NAu2).

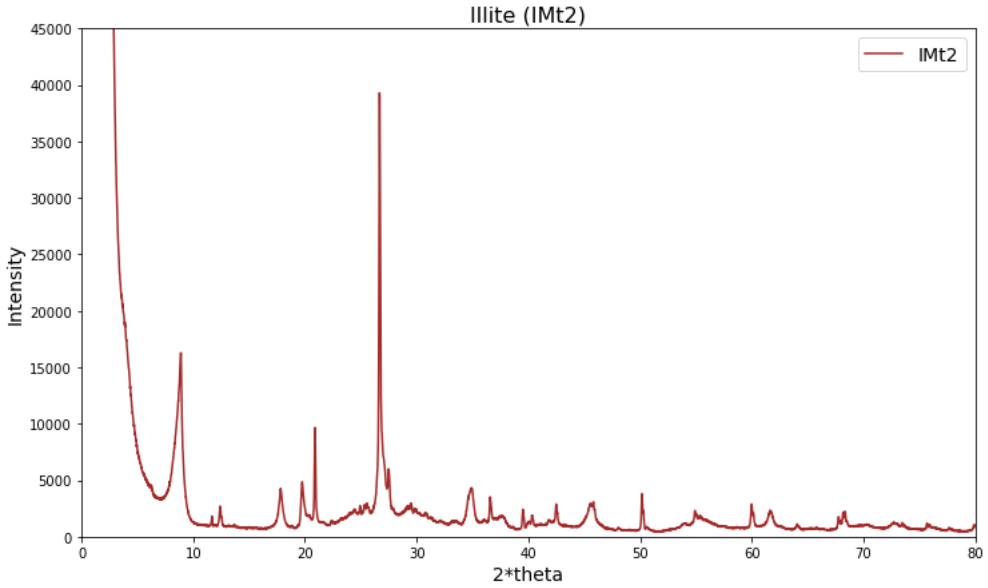

Figure 3.4: XRD data for Illite (IMt2).

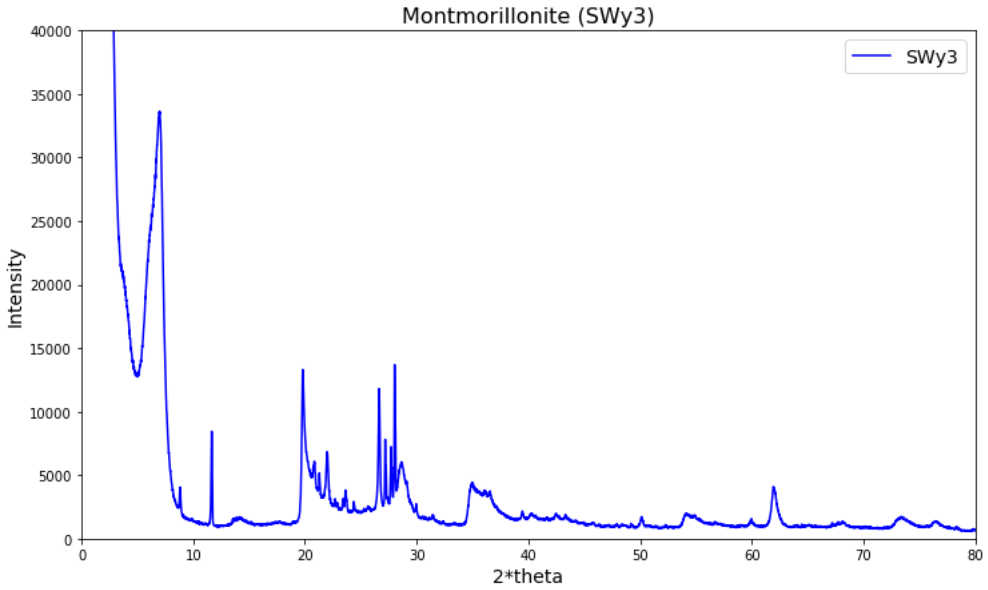

Figure 3.5: XRD data for montmorillonite (SWy3).

3.3.2 Size-fractionation, homo-ionization and purification of clay minerals

After the clay minerals were purchased from the Clay Mineral repository, they were ground to a fine powder, using a Retsch RM100, equipped with stainless steel mortar and pestle, for 10 min. Then, they were treated as described in Jackson Ml,(Soil Chemical Analysis: Advanced Course, 1956).

For size-fractionation, 15 g of clay mineral were weighted and suspended in 1 M NaCl for 24 h. After total centrifugation in a Thermoscientific Multifuge X3R using the FiberLite F14 rotor, at 10000 ppm, 10 °C and 15 min, the clay mineral solids were re-suspended in DI water for 24 h. In order to obtain the $< 2\mu$ m size fraction, the suspension was centrifuged in conical tubes, using the Thermoscientific 75003180 swing bucket rotor,at 500 rpm, 16 °C for 7 min 45 seconds. The mathematical relationship to calculate centrifugation speed and duration is:

$$T_m = \frac{6.3 * 10^9 * \eta log_{10}[\frac{R}{S}]}{N^2 D^2 \Delta s}$$

T_m: time for sedimentation, η: viscosity (in poise; temperature dependent, 0.01111 @ 16 °C), R: distance from the axis of rotation on top of sediment, S: distance from axis of rotation to top of suspension, N: revolutions per min (rpm), D: particle diameter, Δs: difference in density between solvated particle (2.65 g/cm^3) and suspension liquid (0.999 g/cm^3).

The supernatant from the fractionation was kept and NaCl was added to form 1 M of salt solution and left to saturate over night. Centrifugation (10000 rpm, 10 °C, 15 min) and re-suspension in 1 M NaCl was repeated for another 2 times, followed by 2 washes with DI water. The purpose of saturating the solids with NaCl was to have the same charge background on the clay mineral surfaces.

The purification process of the clay minerals involved multiple centrifugations at 8000 rpm, 10 ° C for 5 min with a FiberLite F14 rotor, DI water washes and re-suspension of the solids, until any impurities such as kaolin, Fe oxides, silica, quartz and carbonates are extracted of the clay mineral solids. The progress of the purification was tested using FTIR and looking for the diagnostic bands of the aforementioned impurities; Fe oxides at 720 cm^{-1}, carbonate at 2513, 1467, 1417 cm^{-1} and kaolin at 3700, 700 cm^{-1}.

At the end of this process, the purified clay mineral was centrifuged for an hour at maximum speed of 11000 rpm. The supernatant was discarded and the clay mineral gel was freeze-dried, acquiring the final clay mineral powder.

3.3.3 Clay mineral reduction

The clay mineral are reduced after an adapted version of the method suggested by Stucki et al. (1984b); Neumann et al. (2011).

The desired amount of clay mineral was reduced using sodium dithionite in a buffer solution

of 9 mM of sodium citrate and 0.22 M of sodium bicarbonate. The amount of dithionite used for the reduction was determined by 1:2 stoichiometry considering the reaction that takes place. For example 40 mg of dithionite will reduce 0.46 mmol of Fe. In the case that NAu1 was used, the clay mineral will be approximately reduced at 10%. Higher percentage of reduction can then be calculated. A quick rule for 100% reduction is to add three times the weight of the clay mineral of sodium dithionite. For other clay minerals with different iron content the required adjustment are made for dithionite mass calculation and reduction degrees.

The whole procedure was performed inside a glovebox, Figure 3.6, using de-oxygenated DI water. First, the clay mineral with the buffer solution was stirred overnight to achieve optimum clay dispersion. Then, the temperature of this suspension was raised at 70° C and the appropriate amount of dithionite was added in the solution. It was stirred at this temperature for 2-4 hours, when the heating was turned of. Once the solution was cooled enough, it was washed three times with NaCl and two times with DI water by centrifugation and re-suspension in 4 hours intervals. In order to avoid oxygen contamination, while using the centrifuge, bottles with o-rings and teflon tape were used.

Figure 3.6: NAu2 clay mineral solution during reduction. On the left-hand side, the clay solution is under reduction, upon adding dithionite, with the distinctive deep green colour, while at the right-hand side of the picture, an oxidised (natural) NAu2 solution is also depicted for colour contrast.

3.3.4 X-ray photoelectron Spectroscopy

X-ray Photoelectron Spectroscopy (XPS) analysis of treated NAu1 (NAu1-Na and NAu1-Ca) was conducted to assess exchanged-cation homogeneity onto clay mineral. The characterizations were

performed using a KRATOS Axis Ultra X-ray spectrometer (Kratos Analytical, Manchester, UK) equipped with a monochromated AlK X-ray source (h = 1486.6 eV) operated at 150 W. Samples were mounted on Cu tapes, passed into the spectrometer, through the oxygen-free preparation chamber. Data at Table 3.3 show the extent of homionisation upon clay treatment.

Table 3.3: XPS mass concentration % data of NAu1-Na and NAu1-Ca oxidised samples. C appearing in the analyses is part of data acquirement and not part of the mineral composition.

NAu1-Na		NAu1-Ca	
Peak	Mass Conc. %	Peak	Mass Conc. %
Si (2p)	22.5	Si (2p)	20.7
Al (2p)	4.5	Al (2p)	4.1
Fe (2p)	14.3	Fe (2p)	12.8
O (1s)	47.2	O (1s)	47.4
Na (2p)	3.0	Ca (2p)	2.0
C(1s)	8.5	C (1s)	13.0

3.3.5 Mössbauer Spectroscopy

Mössbauer Spectroscopy was discovered by Mössbauer in 1958 and is based on the resonant (or recoil-free energy) absorption of nuclear gamma rays in solids, when emitted by a radioactive decaying source. Using the Doppler effect, by which the radioactive source is moved reciprocally, with low velocity, relative to the absorbing material, it is possible to observe the small spread of energies between the nucleus and the surrounding electrons. (Goodman, 1994; Dyar et al., 2006)

The Mössbauer effect is well exhibited by the ^{57}Fe which occurs naturally in clay minerals c. 2%, and can be excited effectively by the ^{57}Co radioacive isotope. ^{57}Co isotope has a half-time life 270 days, and decays into an excited state equal to the first excited state of ^{57}Fe. This excitation of the iron atom is at 14.4 keV (in excitation steps) and has a half-time of 100 ns, Figure 3.7. After momentum conservation, when this gamma ray energy (recoiless) energy is released by the nucleus returning to its ground state, another ^{57}Fe nucleus will absorb that gamma ray energy having the same excitation effects. (Goodman, 1994)

When examining a Mössabauer spectrum of a material, there are three Mössbauer parameters, which are the isomer shift (IS), the quadrupole interaction (QS) and the magnetic splitting, composing the hyperfine interactions between the nuclei and the proximal electrons. The IS

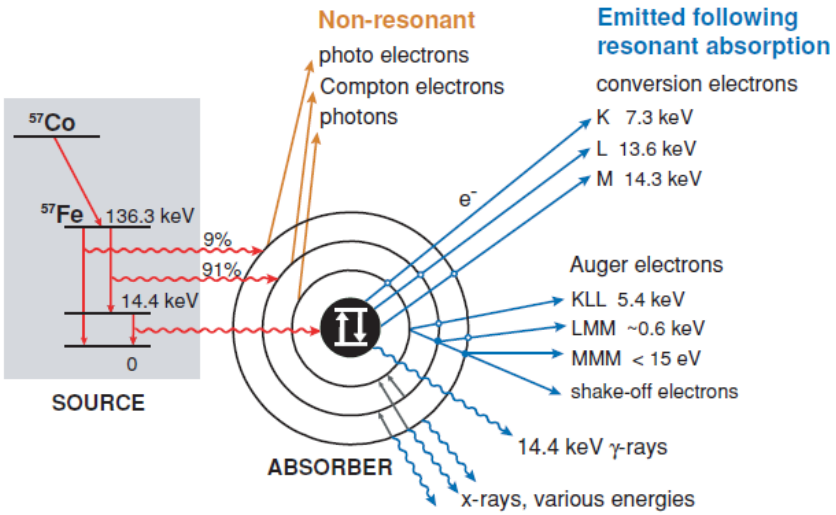

Figure 3.7: Schematic repreentation of the Mössbauer effect and the gamma rays energy that is radiated by the 'Source' (14.4 keV) and absorbed by the nucleus and re emmited as gamma rays at 14.4 keV. In this scheme other type of electromagnetic energies, such as x-rays, auger electrons, that fall in the resonant absorption spectroscopy category are depicted, which all can be used with proper apparatus modifiations for surface analysis to various depths in nm as well as the interior of the examined material. Taken from Dyar et al. (2006)

comes from the coulombic interactions of the nucleus and, mainly, the electron distribution of *s*- orbit charge density. The IS exhibited by a sample, is effectively the differential energy absorption when compared to a standard absorber, Figure 3.8 (blue spectrum). The QS results from the interaction of the ellipsoid nuclear charge density (quadrupole moment) and electric field gradient for the crystal. This interaction causes the splitting of the 3/2 nuclear spin level into two sub-levels, appearing in the spectrum as a doublet, with the center of the doublet being the IS, Figure 3.8 (red spectrum). The magnetic splitting is associated with the interaction of the ^{57}Fe magnetic moment and the presence of a magnetic field, which will cause a multiple splitting (hyperfine or magnetic splitting) of spin level forming a sextet spectrum, Figure 3.8 (green spectrum). (Dyar et al., 2006). Additionally, these three parameters can give information about the oxidation state, character of bond (by IS and QS), or electro-negativity of ligands (by IS) and molecular symmetry (by QS), while magnetic interaction can be given by the presence of the magnetic splitting. (online source: Lecture notes of P.Gutlich, University of Mainz) [2]

Mössbauer spectroscopy is a powerful analytical technique which can be used for many studies (as Figure 3.7 indicates). However, in the context of this piece of research, it is used as a clay

[2] $https://www.blogs.uni-mainz.de/fb09akguetlich/files/2017/11/Moessbauer_Lectures.pdf$

mineral oxidation state diagnostic tool. In Figures 3.9 and 3.10, the NAu1 partially and fully reduced spectra are presented with NAu2 and SWy3 shown in the Appendix A.2, Figures A.5 & A.6. The fitting parameters of the acquired Mössbauer data for the cases of NAu1 can be seen at Table 3.4, (See Appendix A.2 for NAu2 and SWy3, Table A.1).

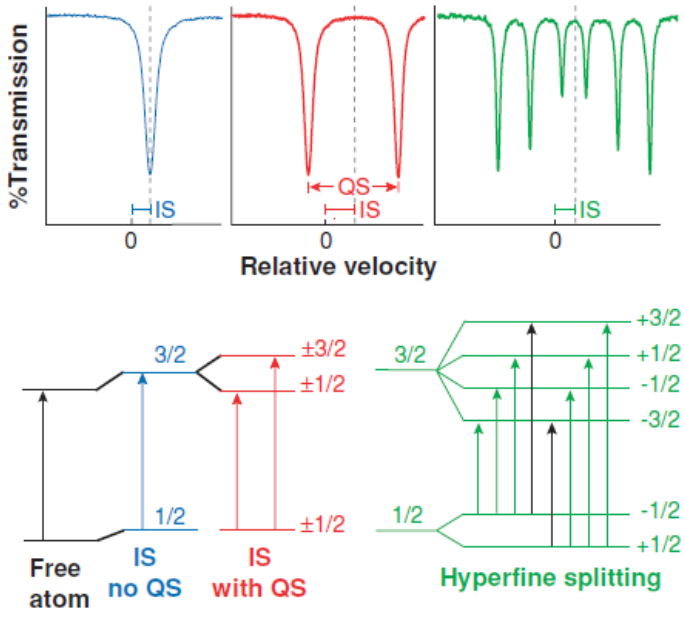

Figure 3.8: In the upper part of the graph, blue line represent the isomer shift (IS) of the absober when compared to the absorption of the standrad material. On the lower part, the isomer shift occurs when no energetic splitting occurs in the source and absorber atoms, but only the energetic level is different. The quadropole splitting (QS),in red lines, occurs when the nuclear quadropole moment and the electric field interact to split the I=3/2 nuclear spin level into to, forming a doublet, as shown in the lower and upper part respectivley. Similarly, the hyperfine or magnetic splitting, in greens lines, caused by the interaction of both nyclear spin I=1/2 and I=3/2 with the magnetic field, forming a sixtet and spin level splitting, as shown in the upper and lower part of the graph, respectively. Taken after Dyar et al. (2006).

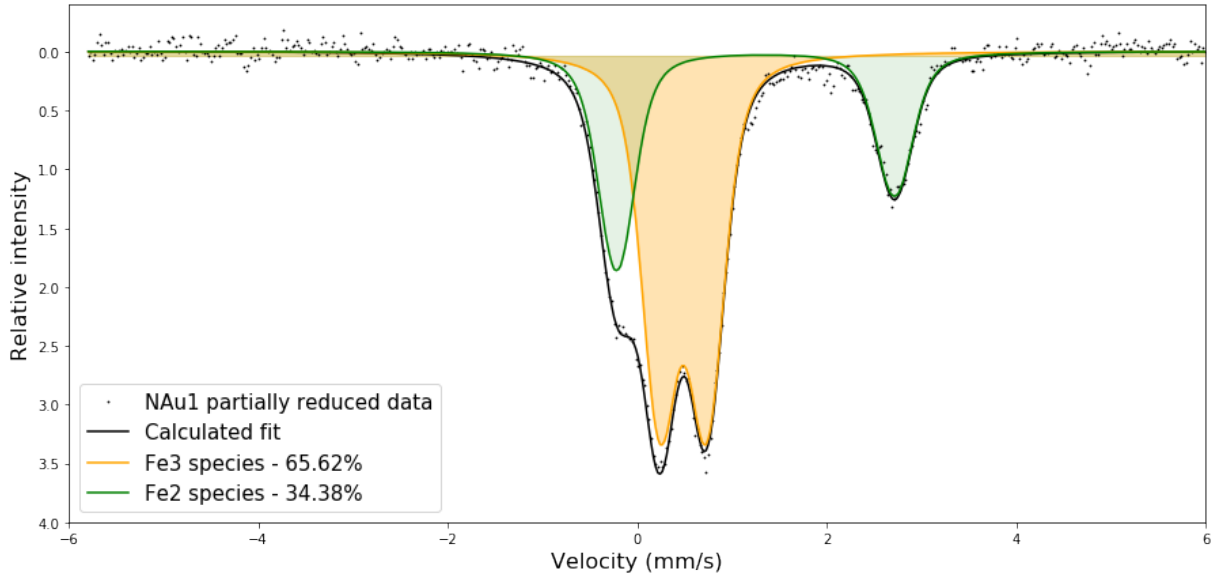

Figure 3.9: Mössbauer spectrum of NAu1 under partilly reduced conditions. Fe^{2+} species are denoted under the green area, with 34.68 % coverage, while Fe^{3+} species are denoted under the orange area, with 65.62% coverage, hence the reduction degree would be at 35%.

Table 3.4: Isomer shift (IS), quadrupole shift (QS), area and sigma fitting parameters of the Mössabuer data, for partially and fully reduced NAu1. Site population % denote the percentage of each species in the mineral and consequently the reduction degree.

NAu1	Fe species	IS (mm/s)	Area	QS (mm/s)	Sigma	Site population %
partially reduced	Fe^{2+}	1.25	25541	2.93	0.28	34.38%
	Fe^{3+}	0.485	48756	0.498	0.27	65.62%
fully reduced	Fe^{2+}	1.279	229361	2.98	0.51	85.66%
	Fe^{3+}	0.219	38400	0.47	0.47	14.34%

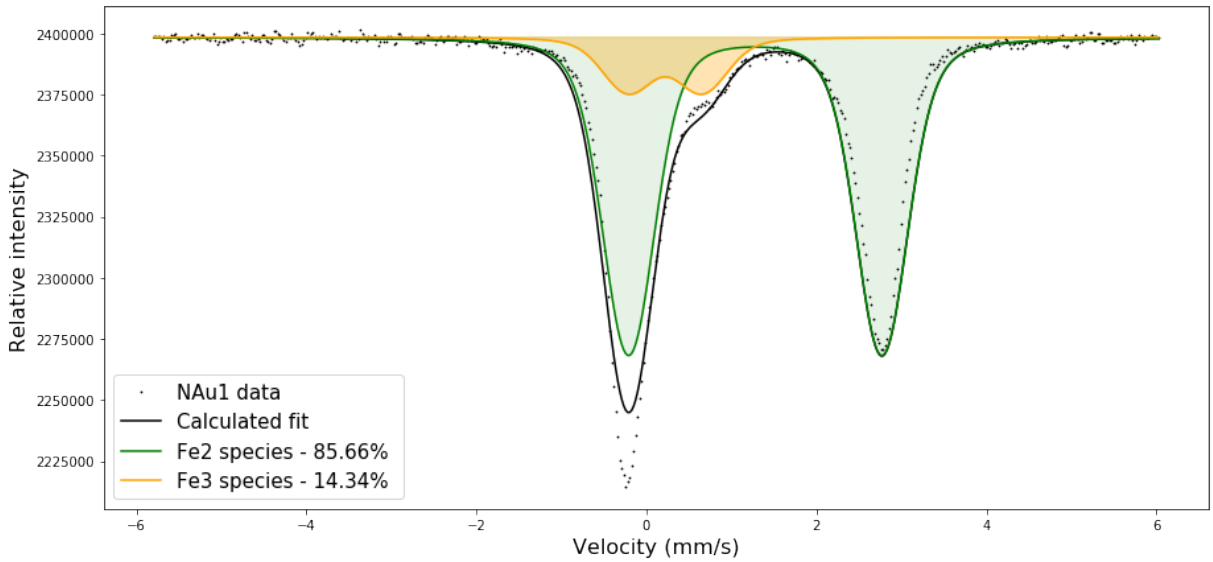

Figure 3.10: Mössbauer spectrum of NAu1 under fully reduced conditions. Fe^{2+} species are denoted under the green area, with 85.66 % coverage, while Fe^{3+} species are denoted under the orange area, with 14.34% coverage, ence the reduction degree would be at 86%.

3.3.6 HF digestion for Fe^{2+}/ Fe_{tot} determination

In order to determine Fe(II) and Fe(tot) in clay minerals, HF digestion was performed after Stucki et al. (1984a) and Amonette J. E. (1998), adapted to our purposes.

This method was used in both, oxidised and reduced samples, determining the initial Fe (Fe_{tot}) and the Fe^{2+} content in clay minerals and to analyse/verify the reduction extent, along with Mossbauer Spectroscopy.

The **solutions** used for this analysis were:

- 1,10 Phenathroline, 10% in Ethanol
- Sulfuric Acid H_2SO_4, 10%
- Boric Acid H_3BO_3, 5%
- Sodium citrate $Na_3C_3H_5(COO)_3$, 1%
- Hydroxylamine $NH_2OH \cdot HCl$, 1% in 1% sodium citrate

Digestion procedure:

- Prepared standard solutions of ethylenediammmonium sulfate (FES : $Fe_2SO_4 \cdot NH_3CH_2CH_2NH_3SO_4$ by weighing 10, 20, 30, 40, 50 mg in HDPE bottles.

- Prepared digestion solution in HDPE bottle, adding per sample to digest, 12 mL sulfuric acid, 2 mL phenathroline, 1 mL concentrated HF.
- Once samples (oxidised and reduced) for analysis were weighted in HDPE bottles, 15mL of the digestion solution was added, giving priority to the reduced samples.
- Shake all bottles overnight to ensure clay mineral digestion.
- After shaking was completed, 10 mL of boric acid was added in each sample, as well as 50 ml of DI water.
- A double set of 30 mL HDPE bottles were used for each sample, one, was for mixing 1 ml of digested clay mineral with sodium citrate and Fe^{2+} determination, and two, for mixing 1 mL digested solution with hydroxylamine for Fe_{tot} determination.
- Colour development in these solution acquired at least 4 hours, but overnight shaking was preferred.
- The absorbance at 512 nm of 1 mL of these solution was determined with colorimetry spectroscopy.

Calculations:

Detailed weighing measurements were taken during the whole procedure, (HDPE bottles, added clay mineral samples, added solutions, before and after shaking etc), because the calculations were based on the Amonette J. E. (1998) method, which uses the density of each solution and the mass of the added solution as well as the dilution factors. The calibration curve was derived from the standard solutions of FES using linear regression at Figure 3.11. Below, at Figures 3.12 and 3.13, data from fully reduced NAu1 and NAu2 clay mineral are shown, validating the reduction degree calculated from the reduction procedure described above.

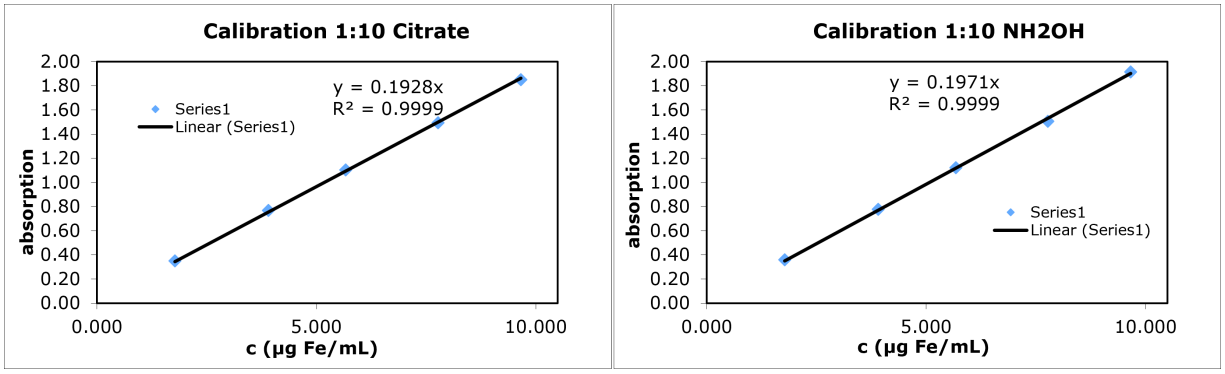

Figure 3.11: Citrate calibration regression line for Fe^{2+} determination (left), and Hydroxylamine calibration regression line for Fe_{tot} determination (right), after standard solution colorimetry spectroscopy, after standard solution colorimetry spectroscopy

		NAu-1, 100% red R1	NAu-1, 100% red R2	NAu-2, 100% red R1	NAu-2, 100% red R2
m(sample)	g	0.000	0.000	0.000	0.000
V(sample)	µL	7500.000	7500.000	7500.000	7500.000
absorption		0.627	0.629	0.586	0.591
c(Fe)	µg/mL	3.251	3.262	3.039	3.065
c(Fe)	**wt%**	**0.0**	**0.0**	**0.0**	**0.0**
c(sample)	mol/L Fe(II)	0.007	0.007	0.006	0.006
amount(sample)	µmol	50.562	51.233	47.852	48.092
Fe(II)/Fe(tot)	**%**	**94.4**	**94.8**	**90.6**	**86.9**
		AVG	**STD**	**AVG**	**STD**
Average amount(sample)	µmol	50.898	0.475	47.972	0.169
Average Fe(II)/Fe(tot)	%	94.581	0.312	88.743	2.614

Figure 3.12: Summary of Fe^{2+} determination calculations

In Figure 3.12, the result of the HF digestion shows that the Fe^{2+}/ Fe_{tot} ratio is at 94.5 for NAu1 and 88.7 for NAu2, meaning that the minerals are reduced at 94% and 88% according to the reduction procedure followed.

In Figure 3.13, Fe_{tot} is reported showing a bit higher iron content for NAu2 at 54 μmol in comparison to NAu1 at 53.8 μmol, as expected from the given chemical composition given previously.

		NAu-1, 100% red R1	NAu-1, 100% red R2	NAu-2, 100% red R1	NAu-2, 100% red R2
m(sample)	g	0.000	0.000	0.000	0.000
V(sample)	µL	7500.000	7500.000	7500.000	7500.000
absorption		0.679	0.678	0.661	0.695
c(Fe)	µg/mL	10.938	10.922	10.648	11.196
c(Fe)	**wt%**	**0.0**	**0.0**	**0.0**	**0.0**
c(sample)	mol/L Fe(tot)	0.007	0.007	0.007	0.007
amount(sample)	µmol	53.584	54.043	52.822	55.345
clay mineral concentration	**g/L**	**1.780**	**1.796**	**1.755**	**1.839**
		AVG	**STD**	**AVG**	**STD**
Average n(sample)	µmol	53.813	0.325	54.083	1.784
Average solid Fe content	wt%				

Figure 3.13: Summary of Fe_{tot} determination calculations

3.4 Experimental Methodologies

3.4.1 Contact Angle Measurement Methods

As wettability is explained in detail in Section 2.2, here some more fundamentals, in smaller scale, will be presented, as well as, the main methods that are reported and used in the literature for contact angle measurements.

The contact angle of a droplet on a surface will be defined by the tension between the liquid/solid interface and the liquid/vapour (air) interface, at the common point of these three phases (Yuan, Lee, 2013). Another fundamental factor that plays a role for the contact angle is the surface tension of the liquid itself (Yuan, Lee, 2013; Drelich et al., 1996). Due to intermolecular forces in the droplet of a liquid, the droplet has the tendency to have the smallest size possible for a specified volume. In conclusion, surface tension, external forces and the liquid/solid interface will determine the contact angle of a liquid on a solid surface.

Contact angle can also be dependent on the surface roughness and/or heterogeneity (Yuan, Lee, 2013). For this reason, it exhibits hysteresis which is equal to the difference between the advancing and the receding contact angle. The higher the hysteresis, the higher the roughness of the measured surface. The challenging fact about surface roughness is that, static contact angle can be greatly misleading, as it does not take into account the wettability at the very small scale. With dynamic contact angle measurements this can be eliminated to a certain extent. However, for very rough surfaces, other equations can be used in order to characterise a surface's wettability (Yuan, Lee, 2013). So, in any clay film experiments, the surface should be as smooth as possible, or any heterogeneity should be considered consistent across the clay film.

There are several methods for characterising wettability of surfaces by measuring contact angle, but for the purpose of this study, sessile static and dynamic drop methods are utilised, which are described below.

Sessile static droplet method

For static measurements, a droplet is dispensed on a solid surface, using a syringe needle. The apparatus in use, analyses the droplet and gives the contact angle of the droplet on the selected surface, Figure 3.14.

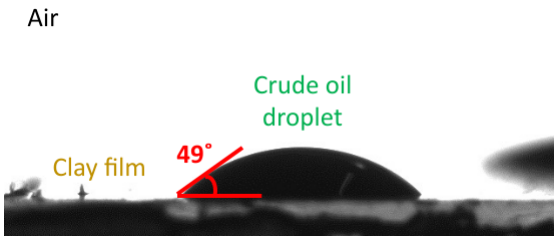

Figure 3.14: Droplet dispensed on clay film for contact angle measurement by static sessile drop method. Contact angle at 49°. Photo taken with Rame-Hart goniometer apparatus.

Sessile dynamic droplet method

For dynamic measurements, again a droplet is dispensed on a solid surface but this time the volume of the droplet is increased, at a preassigned rate, until it reaches a plateau. The angle at this point will be the advancing contact angle for the particular liquid droplet. When this measurement is taken, the volume of the droplet is then decreased to a minimum, which will give the receding contact angle, as shown in Figure 3.15, (Shang et al., 2008).

A second way of determining dynamic contact angles is by using tilted plate equipment, where the dispensed droplet exhibits two different angles due to the plate dip, as shown at Figure 3.16. The advancing angle is denoted as θ_{max} and the receding as θ_{min}, as per (Yuan, Lee, 2013). Dynamic contact angles for this PhD study were taken according to the first method, by changing the volume of the droplet using an automated dispense system.

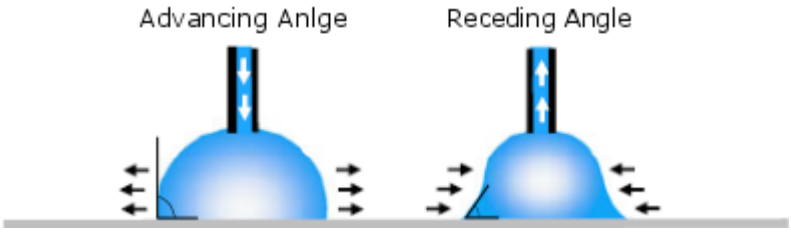

Figure 3.15: Advancing (left) and receding (right) contact angle of a liquid droplet. The difference of these two angles gives the contact angle hysteresis. Taken from (Yuan, Lee, 2013).

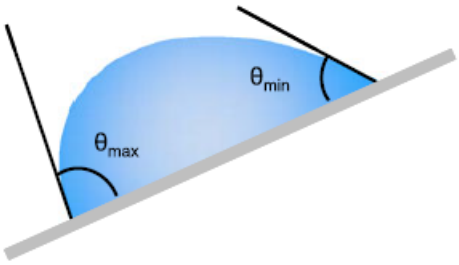

Figure 3.16: Tilted plate method for measuring dynamic contact angle, (Macdougall et al., 1942). θ_{max} advancing angle and θ_{min} receding angle. Taken from (Yuan, Lee, 2013).

The apparatus and set-up used is shown at Figure 3.17.

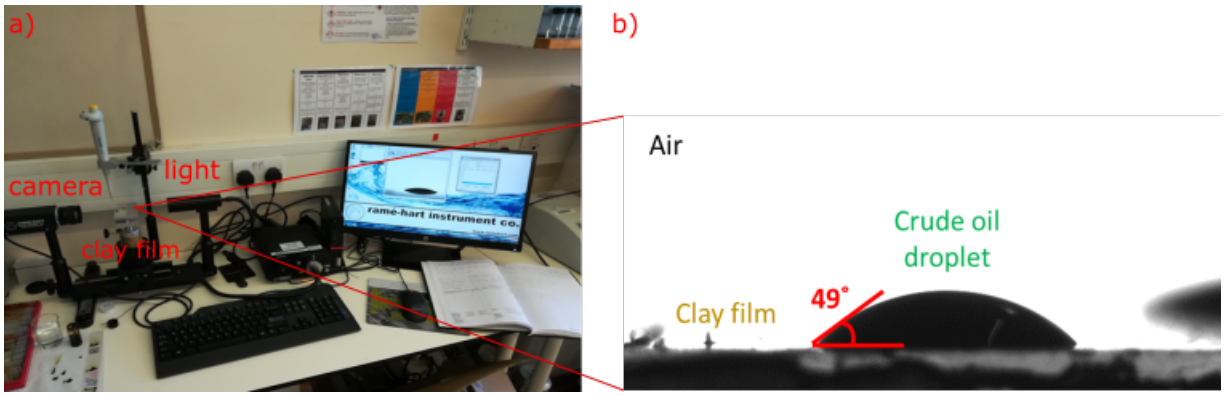

Figure 3.17: Goniometer apparatus (a) used for taking the contact angle measurements. (b) A capture of a oil droplet on a clay film surface as generated by the software.

3.4.2 Infrared (IR) Spectroscopy

For Infrared Spectroscopy there are many methods for preparing samples and acquiring data. For the particular studies conducted, clay mineral are diluted with KBr for the Mid-IR spectral range, while pure clay mineral powder is used for N-IR spectral range. The mode of measurements for these type of prepared samples was pseudo-Absorption, Log (1/R). In addition, clay deposits on silicon and PE (teflon) wafer were prepared for absorption mode measurements at Mid- and Far-IR spectral ranges. More on IR principles at few sections below.

In Figure 3.18 the FT- Infrared Spectroscopy apparatus is shown, along with the auxilliary equipment used, for relative humidity control and N_2 flow in the environmental chamber.

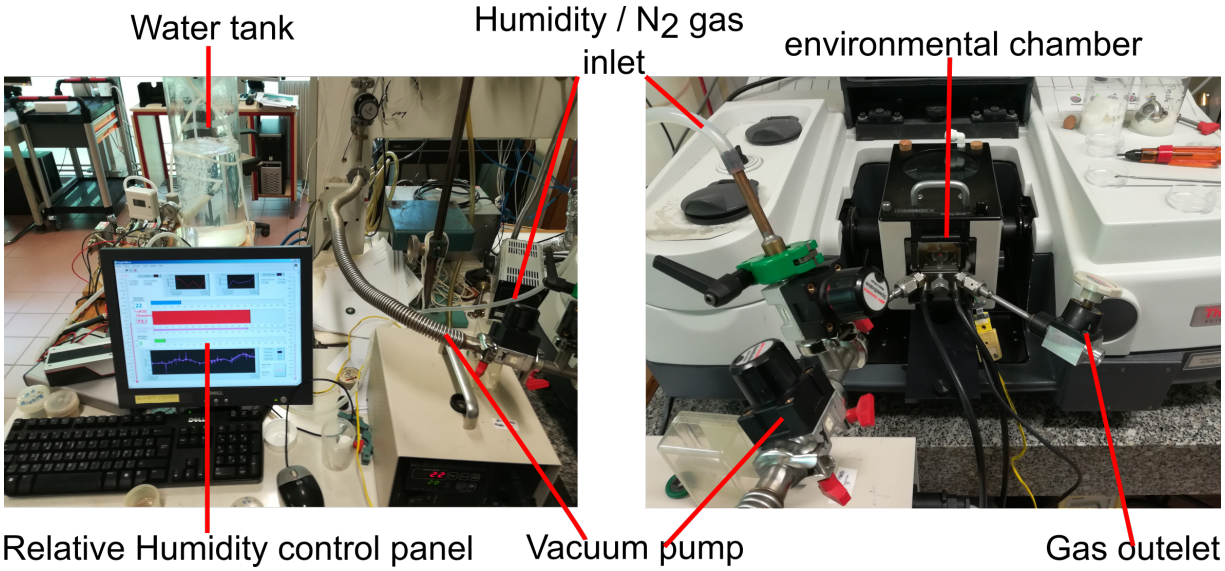

Figure 3.18: Infrared spectometer set-up. On the left, the relative humidity control panel is shown, with humidifier equipment shown at the back (water tank). On the right, the spectrometer with the environmental chamer are shown, with connection tubes, vacuum pump and gas outlet mounted on the chamber.

3.4.3 Cation Exchange

For the cation exchange experiments a combined method was formulated after Wada, Weerasooriya (1990); Shainberg et al. (1987). This method involves mixing of salts solutions, in various mixing ratios between the two salt (e.g. Na and Ca). The single cation-saturated clay mineral (e.g Na- saturated) is suspended in these mixing solutions so that the cation exchange reaction takes place. The resulted reacted solutions are kept for analysis, revealing how much non-saturating cation (e.g Ca) is adsorbed on the clay mineral. The clay mineral then undergoes a second exchange reaction with ammonium acetate, revealing, after analysis, the actual adsorbed amount of the non-saturating cation. More specifics on the method and reactions involved are given in the relevant chapter.

3.5 Analytical Techniques

3.5.1 Infrared (IR) Spectroscopy

The Infrared (IR) spectroscopy is a non-destructive method of material structural analysis. By utilising electromagnetic energy, in the infrared range of 10^2 - 10^4 cm^{-1}, Figure 3.19, the inter-

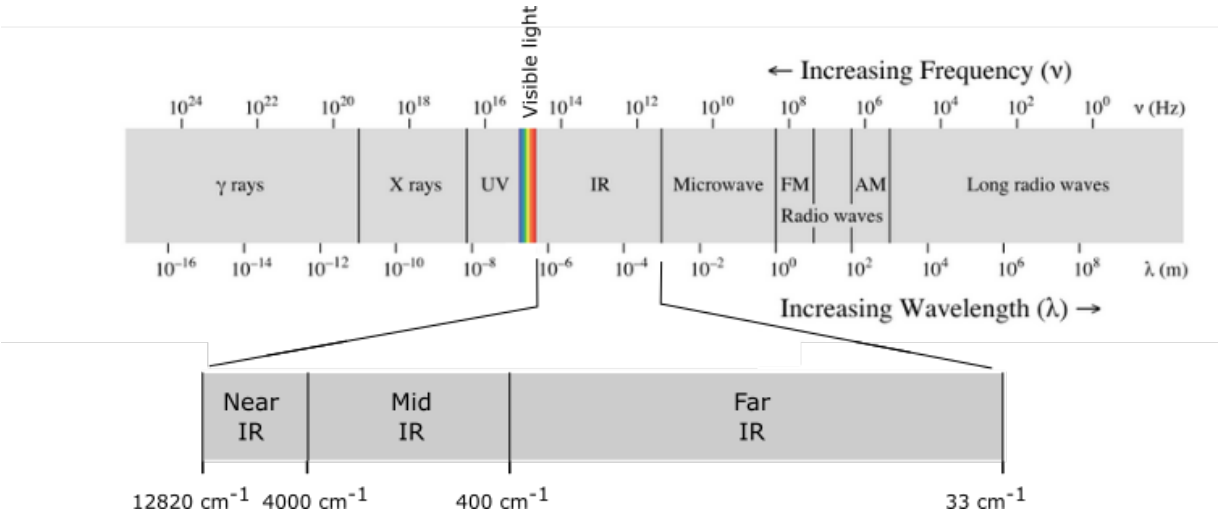

Figure 3.19: The electromagnetic spectrum with the Infrared (IR) range annotated and separated, arbitrarily, in Near-IR, Mid-IR and Far-IR. Sourced and modified after *https* : *//chem.libretexts.org/@go/page/*47515

atomic bond vibrations of different nature can be identified (Russell, Fraser, 1994; Nakamoto, 2006). These vibrations as in Figure 3.20, can be translational, when atoms move simultaneously in the same direction, in a Cartesian coordination system, rotational, which describe the principal axes of rotation of the molecule and vibrations of stretching and bending mode, which are related to changes of the bond length and angle, respectively, (Schrader, 2008; Balan, Kloprogge, 2017). The absorption of the infrared radiation is depended on the orientation of bond axis to the electric vector of the beam, with maximum absorption taking place when these axes are parallel. Additionally, absorption is sensitive to chemical composition and crystallinity, as well as isomorphous substitution when clay minerals are studied (Russell, Fraser, 1994).

When studying clay minerals with IR spectroscopy useful information can be extracted out of three main IR spectrum ranges, the Near-IR range, from 8000 cm^{-1} to 4000 cm^{-1}, where overtone of stretching and combination of stretching and bending mode vibrations take place. This range is usefull for studying, the presence of interlayer water in smectites, but also basic clay characterisation, crystal-chemical studies, structure modification etc. (Madejov, Plkov, 2017), The Mid-IR range extends from 4000 cm^{-1} to 400 cm^{-1}, where the main absorption of stretching and bending vibration of OH and Si-O functional groups takes place, and the main body of research has focused, for clay minerals and other materials functional group band allocation and clay mineral identification (Madejová et al., 2017). The Far-IR range extends from 400 cm^{-1} to 40 cm^{-1}, where low frequency lattice vibrations of stretching and bending mode are present,

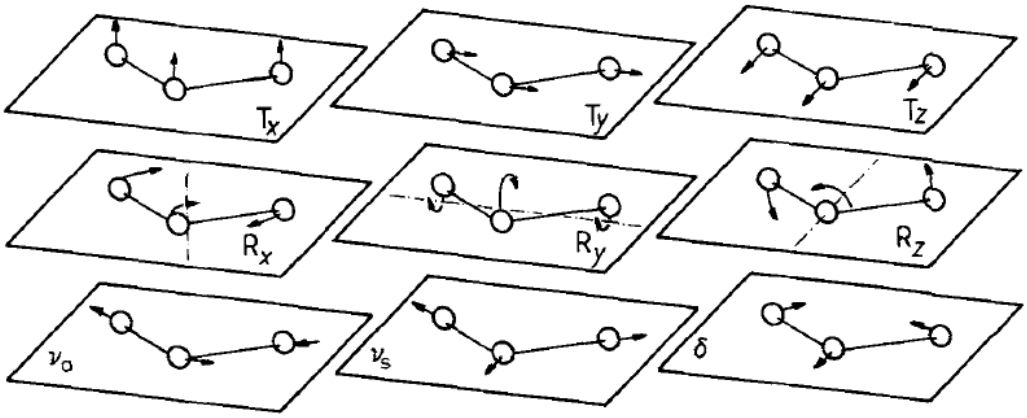

Figure 3.20: Molecular vibrations of a water molecule that can be identified with Infrared spectroscopy. T_x, T_y, T_y are of translation nature, R_x, R_y, R_y are of rotational nature, v_a of antisymmetric stretching nature, v_s of symmetric stretching nature and δ is the deformation or bending vibration. Taken from Schrader (2008).

(Angino, 1964)

In the studies of Chapter 5 and Chapter 6 a Nicolet 8700 infrared spectrometer was used, continuously purged with ultrapure N_2. The environmental chamber was appropriately adjusted to fit either sample holder suitable for clay mineral/KBr mixtures or pure clay mineral, as well as PE and/ or Si wafers.

3.5.2 ICP-AES

Inductively coupled plasma atomic emission spectroscopy (ICP-AES) or optical emission spectroscopy (OES), Figure 3.21, is a spectral method for determining elemental composition in an aqueous sample. The working principle of this method is based on the energy emitted by plasma excited electrons of solutions species, in the form of light, the intensity of which can be translated into concentration of the element in the solution.

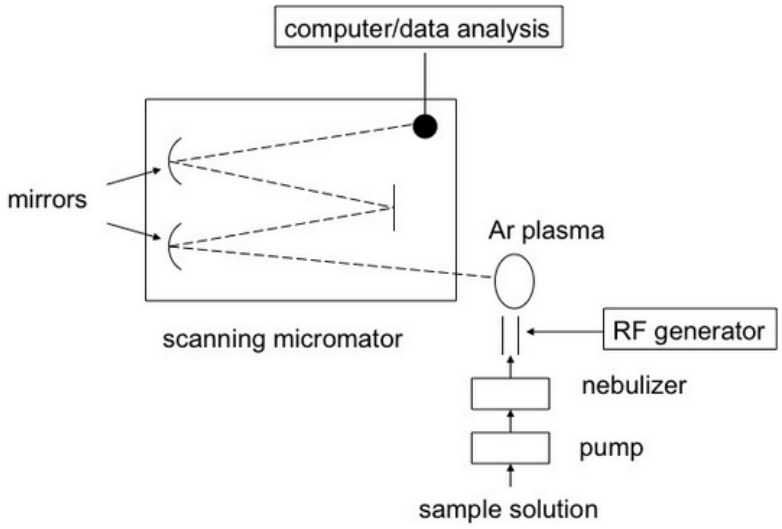

Figure 3.21: ICP-AES schematic representation. The sample is passed through a pump to the nebulizer where it becomes an aerosol. After that, through the Ar plasma where the atoms of the sample are excited. The radio-frequency (RF) generator provides energy that control the plasma torch output. In the end through series of mirror, and a detector, the light emission is converted into atom concentration. Adopted from *https* : *//chem.libretexts.org/@go/page/*55818

In more detail, electrons situated in different orbits of an element, will jump to various higher energetic states, after plasma-induced heat. Light of various wavelengths will be emitted as electrons return to their ground state, and these wavelengths are depended on the difference between the energy at the excited state and the ground state. The further the excited state of an electron is, the higher the emitted energy. Yet, electrons from the outer orbits of an element will require much less energy to be excited than electrons in orbits closer to the atom. That being the case, when an element is in high concentration in an aqueous solution, the outer-situated electrons will oversaturate the detector with high intensity. In that case, light emitted by inner-situated electron can give an accurate concentration of the element as proportionally will exhibit a lower count, and vice versa. When a solution of unknown concentration of an element is measured, standard solutions of known elemental concentration are pre-measured, in order to form a calibration line and match the unknown aqueous concentration, by relating the specific wavelengths of light emitted from the standard solutions and the light emitted of the element in the solution.

A Thermoscientific ICAP 6000 ICP-AES machine was used in order to measure the cation concentrations of salt solution used. Standard solutions for Na^+, Ca^{2+}, and K^+ were prepared

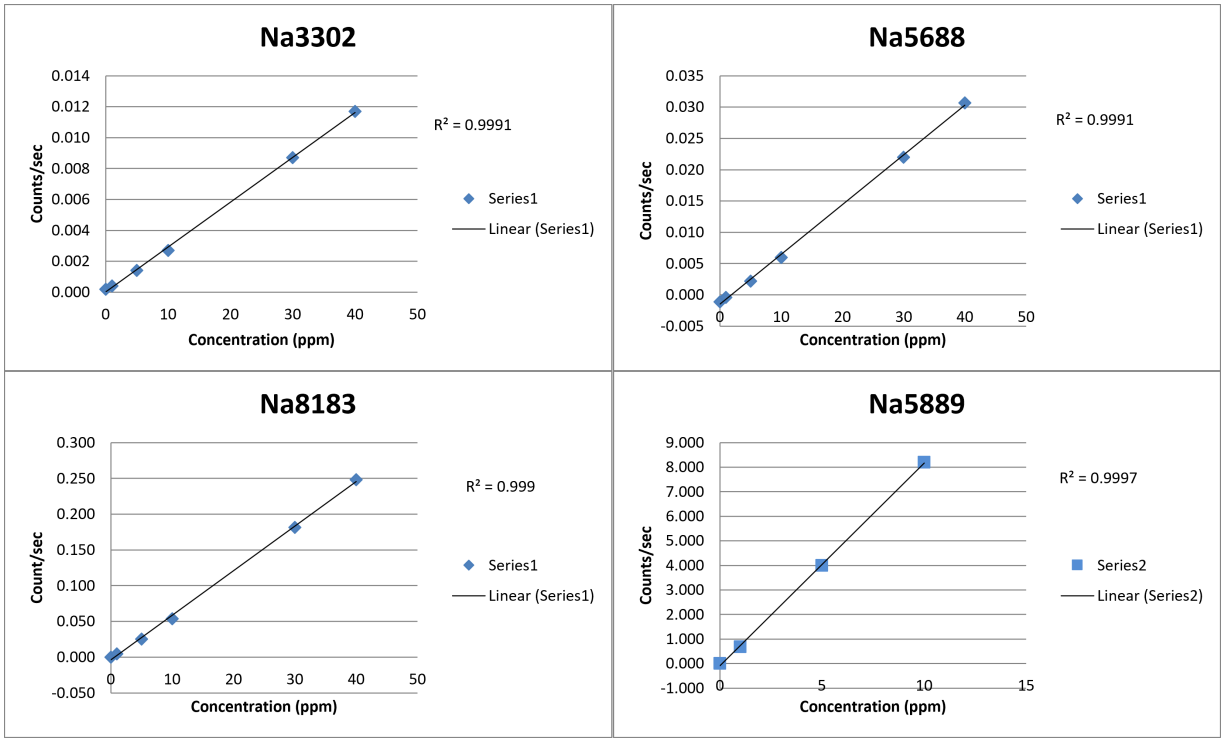

Figure 3.22: Calibration lines for the four Na different wavelengths measured by the ICP-AES, along the range of 0-40 concentration depending the saturation limit for each elemental wavelength.

at concentrations at the appropriate ppm concentration. In order to define the calibration curves and enable us to measure the unknown concentration of the experimental solutions.

In Figure 3.22 the calibration lines of the four different Na elemental wavelengths are shown. According to the counts/sec at the y axis, each wavelength has a different saturation limit for the various concentrations. In this case, the Na3302, Na5688 and Na8183 show low counts/sec values, meaning that these have less concentration sensibility and are able to match with high concentration of Na in a examined sample. On the other hand, Na5889 elemental wavelength, has high counts/sec values and does not give any reading above 10 ppm. That means that at high concentration it gets saturated and cannot account for Na content in a sample.

At Figure 3.23 measured concentrations of actual samples are given. For the Na:Ca 1/9 group of data, low Na concentration is expected, while the opposite for the Na:Ca 7.5/2.5. It can be seen that 3 repetitions are taken (Rep1, Rep2, Rep3) for each sample, as well as the average of the repetitions (AVG) along with the standard deviation (STD) and the error% are reported. For the Na:Ca 1/9, all elemental wavelengths give a similar Na concentration value, but with

	Na:Ca 1/9				Na:Ca 7.5/2.5			
	Na3302	Na5688	Na5889	Na8183	Na3302	Na5688	Na5889	Na8183
	ppm	ppm	ppm	ppm	ppm	ppm	ppm	ppm
AVG	4.432	4.205	5.385	4.381	23.49	24	^ *****	23.29
STD	0.067	0.033	0.07	0.039	0.34	0.17	-----	0.19
error %	1.516	0.7777	1.307	0.8849	1.45	0.7178	-----	0.8004
Rep1	4.5	4.231	5.378	4.393	23.18	23.81	^ -----	23.08
Rep2	4.366	4.169	5.458	4.412	23.45	24.04	^ -----	23.36
Rep3	4.43	4.216	5.318	4.337	23.86	24.14	^ -----	23.43

Figure 3.23: ICP-AES data measured from actual salt solutions, with ratio of Na:Ca at 1/9 and 7.5/2.5. The three repetitions (Rep1,Rep2, Rep3), the standard deviation (STD) and the error% are reported for each elemental wavelength, Na3302, Na5688, Na5889, Na8183 measured.

different STD and error. Although the Na5889 is better to estimate low Na concentration, it seems to overestimate Na content with a relatively high error%, while Na5688 and Na8183 being a better choice for Na determination in that case, with low STD and error%. For the Na:Ca 7.5/2.5, at which high Na concentrations are expected, we see that Na5889 is saturated, not able to measure the Na content, while the other three give again a similar value, with Na5688 and Na8183 being the most suitable. Similar judgement applied when all Na:Ca and Na:K ratios were acquired and chosen for the thermodynamic and adsorption isotherm analysis in the respective Chapter 7.

Chapter 4

Redox dependency of wettability of iron-bearing clay minerals: implications for enhanced oil recovery

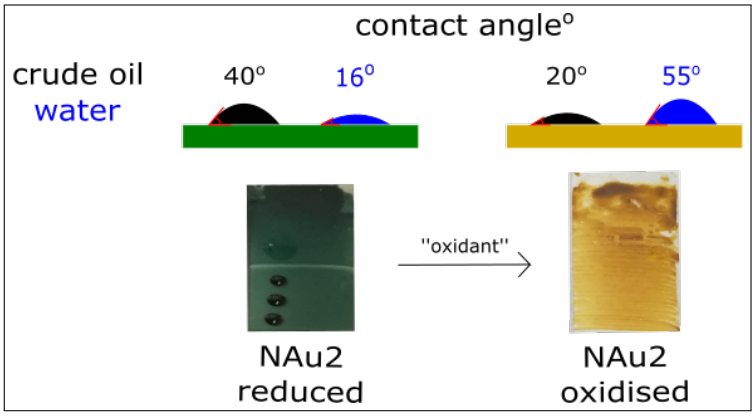

Note: This chapter's work was submitted (September 2021) as an article in Energy and Fuels, ACS Journal, and presented here with the same order and configuration.

Pre-introduction

In the previous chapters the theoretical background was covered regarding the structure, specific characteristics of clay minerals, reservoir rock wettability, oil adsorption mechanisms and implications induced after reduction of the Fe_{str}.

In this chapter contact angle measurements will be presented on Fe-bearing clay minerals. Contact angle measurements is a direct method to examine the wettability of a surface with relation to a fluid, yet with some drawbacks, such as roughness interferences, (see more in Section 3.4.1). In any case, numerous studies have been published based on such studies for clay minerals, reporting interesting results.

4.1 Introduction

The change in wettability state of a reservoir rock surface governs hydrocarbon production from oil reservoirs, though other factors, such as formation pressure or capillary pressure, also play a role. There are three different states of wettability: water-wet and oil-wet, when each denoted liquid is the wetting phase, and neutral-wet when there is no preference as to the wetting phase. Wettability is largely controlled by the minerals present at the rock-fluid interface, such as quartz, feldspars, clay minerals, oxides, along with other factors such as capillary pressure, pH, and mineral surface composition and roughness. Given the extended time-scales involved, the wetting state of an oil reservoir rock interface becomes thermodynamically equilibrated through geological time prior to production (Drummond, Israelachvili, 2002). Because different mineral surfaces have water or oil phase preference, a geologically equilibrated reservoir rock will be oil-wet to mixed-wet, as experimentally confirmed (Jackson et al., 2016), and move to fully water wetting during water flooding, used to produce the oil. Generally, this situation can be found in sandstone reservoirs (Jackson et al., 2016) but in the case of carbonate rocks the wettability is invariably strongly oil-wet (Deng et al., 2020)

Sandstone oil reservoirs, the focus of this study, are produced in three stages (Donaldson et al., 1989). Primary production takes place, due to the initial pressure of the reservoir environment, manifestedby gas cap drive, gas exsolution, natural aquifer inflow or compaction drive. As this variable primary drive / pressure is gradually decreasing, water or gas cap is re-injected into the reservoir in order to maintain a high pressure, above bubble point, to sustain secondary

production. The third stage of production is where enhanced oil recovery (EOR) techniques target the remaining oil. Residual oil strongly adheres to the mineral surfaces or is trapped in space not swept by the injection water and is practically immobile to pressure and conventional production techniques. There are many EOR methods with the most common being alkaline, surfactant, polymer, CO_2 flooding, steam injection and low-salinity water-flooding. The latter method has only recently been implemented at reservoir scale. All these methods aim to release the oil by reducing the oil viscosity, or by altering physicochemical characteristics of the mineral surfaces where the residual oil adheres. Minerals involved in oil adhesion often include clay minerals, such as kaolinite, chlorite, illite and smectites, as well as iron sulphides/oxides. In this study, we focus on clay mineral surfaces and their role in low-salinity water-flooding.

Low-salinity water-flooding (LSWF) is an experimentally established EOR method involving injection of water with lower salinity (up to 5000 ppm total dissolved solids) and higher sodium/calcium content compared to the initial reservoir brine (e.g., as high as 200,000 ppm). For LSWF to be effective, clay minerals, polar oil compounds and a formation brine rich in divalent cations need to all be present (Lager et al., 2008). Underpinning mechanisms described in the literature include wettability alteration from mixed-wet to water-wet due to multi-component ion exchange (Lager et al., 2008), pH increase and reduced interfacial tension (McGuire et al., 2005), and double layer expansion at the clay mineral surfaces, (Nasralla, Nasr-El-Din, 2014) and also fines migration (Tang, Morrow, 1999). These mechanisms and processes may act synergistically, or some may dominate for specific reservoir conditions (Jackson et al., 2016). To date, the effect of oxidation state changes of the reservoir minerals and how this can affect the LSWF processes has received little attention (Wang, Guidry, 1994; Fjelde et al., 2017), and only very recently, initial results on changes in wettability and relative permeability in iron-rich clay mineral-bearing sandstone have been published (Yesufu-Rufai et al., 2020; Unsal et al., 2020). This is surprising because redox-active minerals, including iron-bearing clay minerals (illite, chlorite, montmorillonite) and iron sulphides/oxides, are likely to be prevalent in oil reservoirs. Given the formation conditions of hydrocarbon reservoirs, (Ma et al., 2016) a highly reduced state prior to production is inevitable, yet there is evidence that after LSWF, particles containing oxidized iron (Fe^{3+}) are released into the produced water (Lager et al., 2011; Seccombe et al., 2010). These observations suggest a change in reservoir oxidation state from reduced to (partially) oxidized, during LSWF. Although the exact mechanism of reservoir oxidation is not fully understood, in particular the

impact of oxidants other than oxygen (e.g. sulphate or iodine in sea water, as injection water tends to be deoxygenated), the consequences for clay mineral wettability and, in turn, EOR need to be explored.

In sandstone reservoirs, clay minerals are prevalent as pore lining and pore filling minerals (Kareem et al., 2017). and determine how mixed-wet a reservoir rock surface will be. As shown in Figure 4.1, the negatively charged clay mineral surfaces exposed to the reservoir liquid(s) have a high affinity for many of the various oil compounds found in petroleum and bind them via different mechanisms. Most of the mechanisms, except van der Waals interactions, rely on the presence of negative excess charge of clay minerals that is caused by isomorphic substitution of Si and Al ions in the tetrahedral and octahedral sheets of the alumosilicate structure, as well as deprotonated hydroxyl groups in edge sites (Brigatti et al., 2006).

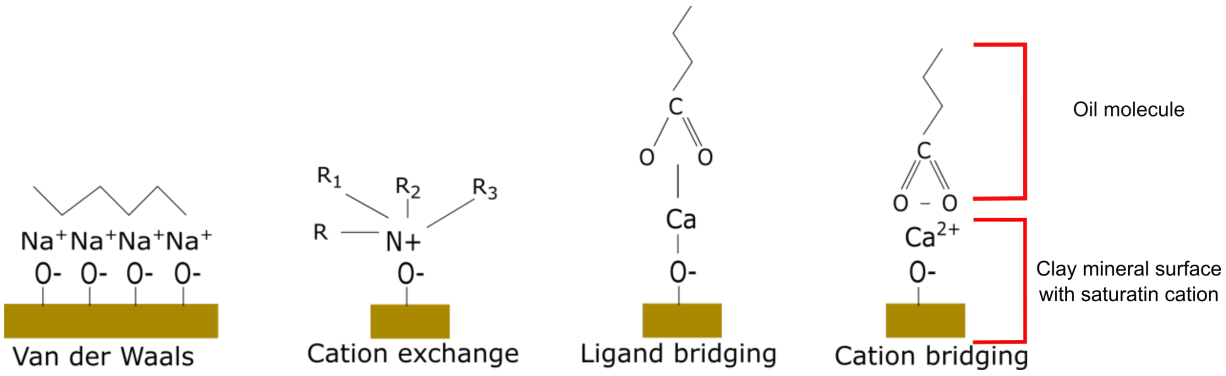

Figure 4.1: Different oil compound adsorption mechanism with clay surface, modified after (Lager et al., 2008)

Clay minerals can contain Fe in their octahedral (O) sheet, or in both O and tetrahedral (T) sheets. Reduction of this structural Fe^{3+} to Fe^{2+} induces several changes in the mineral structure and properties. Due to the increased electron density in the reduced state, the surface of the clay mineral is more negatively charged. For clay minerals with low Fe content and where there is low Fe reduction extent (less than 30% Fe(II)/Fe(total)) in Fe-rich clay minerals, this increasing surface charge is compensated by the adsorption of cations and consequently leads to an increase of the cation exchange capacity (CEC) of the clay mineral (Stucki, Roth, 1977). As reduction continues in clay minerals with high Fe content, uptake of protons becomes the main mechanisms for balancing the increasing negative excess charge (Lear, Stucki, 1985) , subsequently resulting in de-hydroxylation (Lear, Stucki, 1985; Stucki et al., 1984b) stabilizing the clay mineral structure (Drits, Manceau, 2000). Consequently, clay mineral surface charge increases with increasing Fe

reduction extent, reaches a peak, which will depend on the mineral (Stucki et al., 1984b) and decreases again at higher reduction extents (Drits, Manceau, 2000; Stucki et al., 1996). One of the mechanisms proposed to drive LSWF EOR is multi-ion exchange, and we hypothesize changes in CEC resulting from clay mineral Fe redox change affect this underpinning mechanism, which therefore need examining for effects in LSWF EOR.

In this paper, we hypothesize that clay minerals in the undisturbed reservoir are in a nearly fully reduced state (Ma et al., 2016) and that oxidation occurs during water flooding. If low salinity water is used in this secondary stage of production, combined effects of low salinity and clay mineral Fe redox changes will influence the macroscopic wettability of the clay minerals. To investigate this, we created clay mineral films at different initial pH values and under oxidized and reduced conditions, accounting for the change from initial reservoir conditions through to those encountered during the LSWF EOR implementation.

4.2 Experimental method

4.2.1 Materials Used

Iron-bearing clay minerals nontronite NAu2 ((M^+ 0.99)[Si 7.55 Al 0.16 Fe 0.29][Al 0.34 Fe 3.54 Mg 0.04]$O_{20}OH_4$, 37.42 wt% Fe_2O_3, M^+ = Ca 2.67, Na 0.11, K 0.02)((Gates et al., 2002; Keeling et al., 2000), clays.org) and illite IMt2 (Mg 0.09 Ca 0.06 K 1.37) [Al 2.69 Fe(III) 0.76 Fe(II) 0.06 Mn (tr) Mg 0.43 Ti 0.06][Si 6.77 Al 1.23]$O_{20}OH_4$, 7.32 wt% Fe_2O_3) (clays.org) were obtained from the Clay Minerals Societys Source Clays Repository (http://www.clays.org/). All clay minerals were used as received; no size-fractionation or purification was performed and the samples were hetero-cationic, with exchangeable Ca^{2+}, Na^+, and K^+, *inter alia*, as shown above (Keeling et al., 2000). Combined with the use of a crude oil with many polar oil compounds present, using natural minerals allowed a more realistic model of wettability change in oil reservoirs.

Table 4.1: a) Clay mineral chemical composition after (Keeling et al., 2000) and clays.org, b) Composition of crude oil used for performing the oil contact angle measurements, provided by BP, c) Polar compounds concentration and d) Physical properties of crude.

a) Clay Minerals Chemical Composition			**b) Hydrocarbon type (C<36)**	
Oxides	**NAu2**	**IMt2**	Normal paraffines	12.27
SiO_2	56.99	49.3	Isoparaffines	12.72
Al_2O_3	3.4	24.25	Aromatics	1.784
TiO_2	0	0.55	Napthenes (17<C<25)	7.535
Fe_2O_3	37.42	7.32	Aromatics (17<C<25)	10.22
FeO	0	0.55	Unknowns (C<25)	14.36
MnO	0	0.03	C36	36.77
CaO	2.67	0.43		
MgO	0.34	2.56	**c) Polar Components (mg KOH /gr)**	
Na_2O	0.11	0	Total Acidic Number (TAN)	1.2
K_2O	0.02	7.83	Total Basic Number (TBN)	0.52
P_2O_5	0	0.08		
F	0	0	**d) Physical Properties of C<36**	
S	0	0	Density (25°C)	0.8793
LOI	0	8.02	Viscosity (40°C)	41.71

The fluids tested were crude oil, provided by BP (Table 4.1), and deionized (DI) water. In the crude oil, the polar compounds of most interest are presented as the total acidic number (TAN = 1.2 mg KOH/g) and the total basic number (TBN = 0.52 mg KOH/g), as these compounds tend to constitute the residual (strongly bound) oil components adsorbed on the clay mineral. The crude oil had a density of 0.8793 g/cm^3 (T = 25 °C) and viscosity of 41.71 cSt (T = 40 °C).

4.2.2 Sample Preparation

Preparation of Clay Mineral Suspensions

Clay mineral suspensions were made by adding 0.3 g of clay mineral to 30 mL DI water, following two methods, which differed by the order pH adjustment was undertaken.

Method (i) (**'pre-pH adj'**): An initial pH adjustment was made, using NaOH or HCl solu-

tions of 0.1 M or 0.01 M, to achieve a pH range from pH 4 to pH 10, to test the effect of different pH on the clay mineral particle surfaces.

Method (ii) (**'post-pH adj'**): Clay mineral suspensions at pH 5, 7 and 9 were subjected to pH adjustment post mixing to counter any pH buffering from the clay mineral.

All suspensions were sonicated using a Fisher Scientific FB-120, for 16 min at an amplitude of 39% of 20kHz. After sonication, the suspensions were centrifuged (LMC-3000) for 2 min at 3000 rpm (1700 * g) keeping the supernatant and discarding any larger particles.

Preparation of Oxidised Clay Mineral Thin Films

Clay mineral films were prepared from the suspensions using glass slides (academy microscope slides, 76 * 26 mm, 1-1.2mm thickness, ground edge 45°, clear glass) that had been pre-washed with acetone and DI water. The glass slides were immersed in the prepared clay suspension and aged in an oven at 70°C for about 48 hours. During this time, water was evaporated from the suspension leaving the clay mineral on the glass slide in the form of a film.

It was noted that during the clay film preparation using clay suspension method (i) above, the pH eventually reached 8.5 and 9 for NAu2 and IMt2, respectively, regardless of the initially adjusted pH in the clay mineral suspension. In contrast, the pH remained constant when checked after sonication, for method (ii) that used post suspension pH adjustment.

Preparation of Reduced Clay Mineral Thin Films

All manipulations of reduced clay minerals were conducted inside an anoxic chamber (GS Glovebox Systemtechnik GmbH; N_2: 100%, $O_2 < 1$ ppm) and using solutions that were deoxygenated for 2h by bubbling with N_2 gas prior to transfer to the anoxic chamber. The reduced clay mineral films were formed by in situ reduction of the oxidized clay mineral films, following a modified citrate-bicarbonate-dithionite method (Stucki et al., 1984c; Neumann et al., 2011). In short, a buffer solution containing 9 mM sodium citrate and 0.22 M sodium bicarbonate was prepared in de-oxygenated DI water and heated to 70 °C. To ensure a complete clay mineral Fe reduction, excess sodium dithionite (0.9 g), corresponding to three times the clay mineral weight, was added to the buffer solution and stirred until fully dissolved. Then, the clay mineral films were immersed in the reducing solution for 3-4 hours, removed, rinsed and left to dry in the gloveboxs inert atmosphere. For contact angle measurements, the clay mineral films were transferred into

a glove bubble (CTS Europe Ltd.) containing an inert atmosphere of N_2. Film roughness may change due to the reduction and the time left in the reducing solution. However, the surfaces appeared continuous and considered suitable to proceed with contact angle studies.

4.2.3 Analytical techniques

In this present study, sessile drop contact angle measurements probed the wettability of iron-bearing clay minerals in oxidized and reduced states. Several contact angle studies with various methods and experimental set-ups exist determining wettability on clay mineral surfaces (Chau, 2009; Dimitrov et al., 1991; Lebedeva, Fogden, 2011; Shang et al., 2008, 2010). One of these methods is the sessile drop (static or dynamic) contact angle method which involves a liquid droplet dispensed on the surface of the material tested (Yuan, Lee, 2013). The contact angle is defined as the angle formed by material surface and the tangent on the liquid drop (Figure 4.2). When the contact angle of the droplet-material assembly is measured in air, the angle value describes the wettability of the surface: angles below/above 90° indicate that the surface is/is not wetted by the tested liquid and an angle of 90° indicates a neutral-wet state (Figure 4.2). Contact angles observed for different liquids can be compared and small differences suggest more/less wetting phases. However, contact angles measured can be greatly affected by the surface roughness (Drelich et al., 1996; Ballah et al., 2016), by amplifying the natural surface chemistry of philic or phobic behaviour (De Gennes et al., 2013), or by droplet contact angle irregularities between the right and left side (Yuan, Lee, 2013), giving unreliable surface wettability results. Surface anomalies also result in hysteresis (a difference between advancing and receding contact angle) in the contact angle measurement (Yuan, Lee, 2013). In order to evaluate hysteresis, we complemented the static contact angle measurements with advancing and receding contact angle measurement (dynamic contact angle measurements (Yuan, Lee, 2013)).

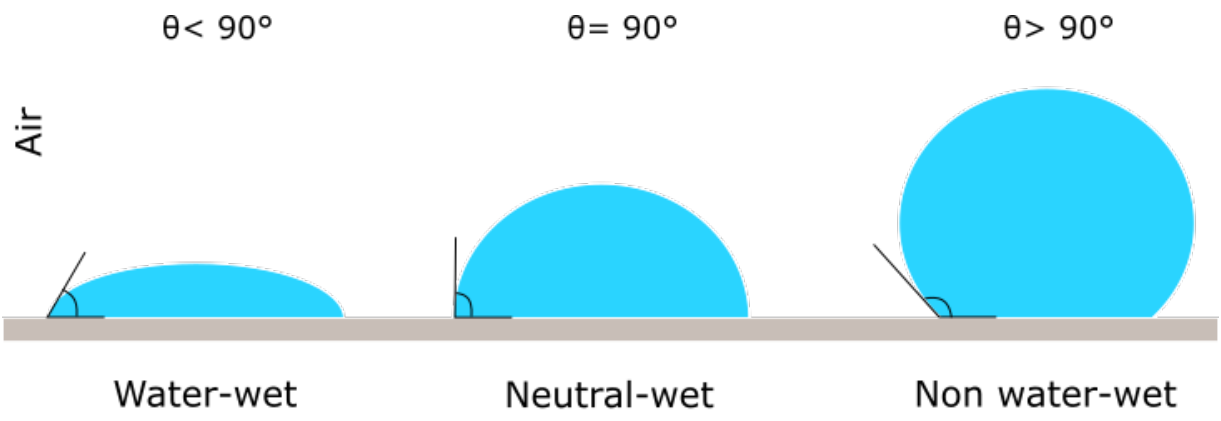

Figure 4.2: Contact angle value indexes for a water droplet showing: wetting (left), neutral (middle) and non-wetting (right) phase cases, modified after (Yuan, Lee, 2013).

In order to check the consistency of the surface, high magnification pictures were taken using a Hitachi SU-70 SEM instrument, utilizing carbon coating (by thermal evaporation - 20 nm) on the clay films. Particle size and other surface anomalies were identified in order to evaluate the clay film suitability for contact angle measurements.

The contact angle measurements were taken using a Ram-Hart standard goniometer (260-U1), coupled with a droplet auto-dispenser. The clay mineral film was mounted on the sample holder. A light source was projected on the sample and as the oil droplet was dispensed, a camera mounted on the opposite side recorded images. After droplet shape (sphere) and base line calibration, this live feed was constantly monitored, measuring the contact angle of the droplet on the clay film surface, as shown in Figure 4.3. It should be mentioned that contact angle values less than 15° exhibited by a liquid mean that the surface is strongly wetted by that liquid. Also, in cases of very low contact angles, the droplet height cannot be distinguished properly from the material surface, leading to erroneous contact angle values.

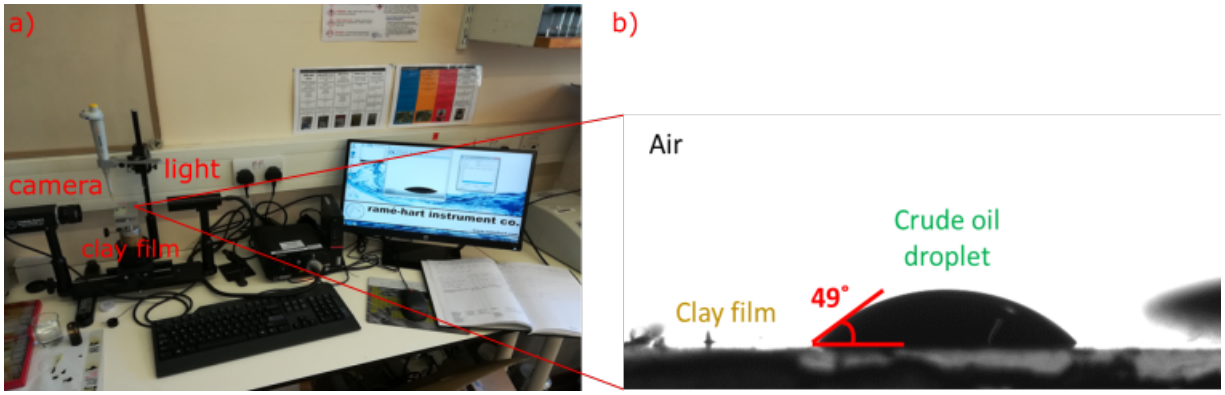

Figure 4.3: Contact angle measurement set up, showing a) Goniometer apparatus used for contact angle measurements, b) Picture taken from the software while measuring a static crude oil droplet of 49 degrees of angle, as indicated on the graph.

4.2.4 Contact angle experimental configuration

Static and dynamic contact angle (CA) measurements were taken with different configurations of drop size, number of measurements and time. For the first batch of clay mineral films resulting from preparation method (i), the static sessile drop (**SSD**) method was used, with various drop volumes of the liquids tested. For the second preparation method (ii) of clay mineral films, (semi-)static and dynamic sessile drop (**DSD**)methods were used, with fixed drop volume and time for each repetition for the crude oil and clay mineral films used. The DSD methods were used with oxidized clay mineral films only. Table 4.2 contains all the details on the experiments conducted.

For each droplet of liquid, the right and left contact angle was measured for the respective time, acquiring consecutive values for each side of the droplet, the number of which depended on the configuration used each time, as given in Table 4.2. For the full static experiment (**SSD**), a first average was determined, Ave_1, of the right and left angle, for each time interval, then a second average, Ave_2, on the total number of values on each droplet- repetition, for the total elapsed time, and then a third average, Ave_3, among the different oil (or water) droplets utilized per sample/ pH value (see explanatory Figure B.1 and Table B.1, in Appendix B). The error bars on the result graphs, shown below in Figure 4.5, Figure 4.6 , represent the angle variation of the third average, Ave_3, i.e., the values of the different droplets. For Figure B.2 - Figure B.15 graphs, presented values are of Ave_1.

For the dynamic experiments (**DSD**), similar calculations were carried out, showing Ave_1

Table 4.2: Static and dynamic sessile drop method contact angle (CA) experiment configuration.

Clay film measurements		
Static CA	Pre-dispersion adjusted pH values	4 - 9
	Repetition	4 - 5
	Droplet volume size (μL)	various
	Number of measurements/ droplet	50 - 100
	Time interval (sec)	0.01
	Oxidised/ Reduced	✓
Dynamic CA	Post-dispersion adjusted pH values	5, 7, 9
	Repetition	4 - 5
	Droplet volume size (μL)	20 μL
	Number of measurement - (semi-)static	300
	Time interval (sec)	0.1
	Droplet volume size - dynamic (μL)	10μL / step
	Number of steps	3
	Number of measurements - dynamic	10 / step
	Time interval (sec)	0.1
	Oxidised	✓

values in Figure 4.7 and Figure 4.8, because the evolution of contact angle over time was of interest. Although, error bars of Ave_1 are not presented on the graphs for graphical purposes, these are given for quoted values.

The DSD measurements were carried out in four different configurations. (1) For a semi-static 20 μl droplet, 300 measurements of 0.1 s intervals were taken, with the aim to determine the equilibration contact angle of a crude oil volume over a relatively long time frame, for comparison to the SSD measurements. (2) In a second measurement, the oil droplet volume was increased in three increments of 10 μl (final drop volume of 30 μl) and 30 measurements of 0.1 s intervals were taken for each volume increment. (3) Using the same increments, but taking only one measurement for each volume increment, the advancing contact angle was quantified over a shorter time frame. (4) Using the same approach as in (3), advancing and receding values were obtained, increasing and decreasing the droplet volume. For each type of measurement an identifier is given as in Table 4.3. The results are grouped for the three pH values (5, 7, 9).

All contact angles were evaluated during and after they were taken, in terms of right and left angles, consistency, drop shape, spreading consistency and error of each measurement to check the accuracy. Data for any identified highly unstable droplets for the specific time frame observed were removed by post measurement editing. Unstable values were still presented for the

Table 4.3: Dynamic contact angle measurements configuration and identifiers.

Dynamic contact angle					
Configuration method	Code name	Total Volume (μL)	Steps	No. of measurements	Interval time/ measurement (sec)
(1)	"Equil"	20	1	300	0.1
(2)	Advancing	10+10+10	3	30 / step	0.1
(3)	Advancing+	10+10+10	3	1 / step	0.1
(4)	Adv-Rec	10+10+10 -10-10	5	30 / step	0.1

dynamic experiments, however, to demonstrate the potential of the experiments for evaluating interactions between clay mineral films and crude oil.

4.3 Results

Here, the results are presented starting with the SEM clay film quality evaluation. First, the static CA measurements are presented for each mineral separately, NAu2 and IMt2, with reduced experiments proceeding the oxidized ones. Second, the dynamic CA measurements are shown again in the same manner, with only oxidized measurements. On the figures that clay suspension pH is plotted, each pH value corresponds to one sample or one clay film, terms used interchangeably. On the figures that time is plotted, corresponds to total time, for all repetitions/ droplets measured. Angles are in degrees, droplet height and width in mm.

4.3.1 Scanning Electron Micrographs

Figure 4.4, shows photographs (Figure 4.4i) and scanning electron micrographs (Figure 4.4 a-h) of thin films prepared from the two clay minerals. Both clay minerals changed colour upon reduction of their structural Fe with NAu2 showing a striking colour change from brown to blue, as reported previously (Schaefer et al., 2011), while IMt2 became colourless from its original beige colour (Figure 4.4i). Scanning electron microscopy (SEM) of the clay films show a consistent surface with no significant topography across the whole section, for both oxidized and reduced conditions and both clay minerals (Figure 4.4a, c; e, g). Higher magnification (Figure 4.4b, d; f, h) further corroborates the observation of continuous clay films for all conditions, with no observable differences for oxidized and reduced clay minerals. Distinct particles observed in the oxidized clay mineral films were absent after clay mineral Fe reduction, suggesting that the reduction procedure removed some of the surface roughness.

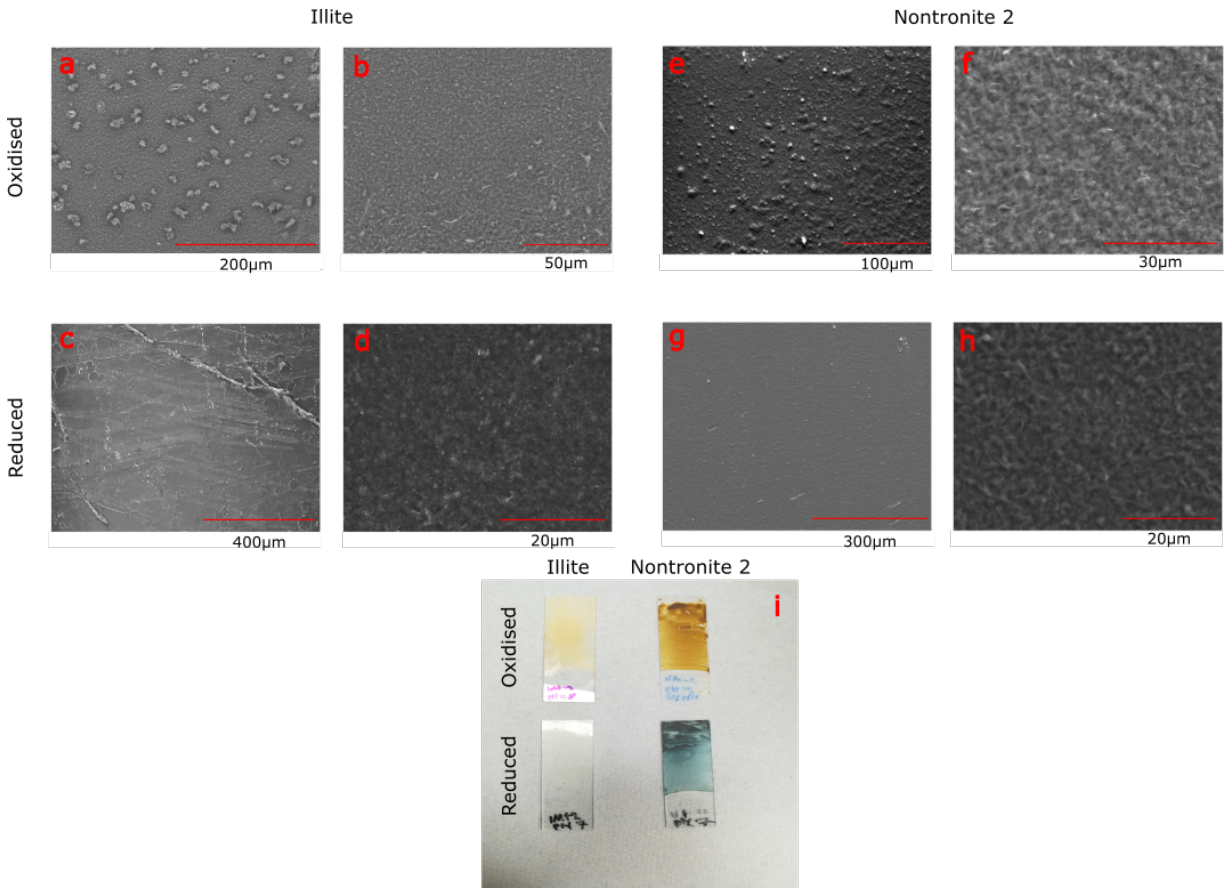

Figure 4.4: SEM pictures of IMt2 (oxidised: a, b; reduced: c, d) and NAu2 (oxidised: e, f; reduced: g, h) clay films. On the bottom picture (i) the clay films are shown as oxidised and reduced, prior to SEM imaging, with distinct colour changes.

4.3.2 Static Contact Angle Measurements

Nontronite 2 - NAu2

Static contact angles for the reduced NAu2 clay mineral films are shown in Figure 4.5a, in green for the crude oil and in red for oxygen-free DI water. We observed consistently higher contact angles for crude oil (around 40°, Table 4.4) compared to water (15°-20°), indicating a more water-wet than oil-wet surface under reducing conditions. Measurements with both crude oil and water showed very low standard deviations of less than ± 5° (Table 4.4 for oil values), indicative of stable droplets. The small variations observed across the range of pH values 5-10 (Figure 4.5a) suggests that pH value did not significantly affect the surface properties of reduced NAu2.

Static contact angles measured for oxidized NAu-2 clay films (Figure 4.5b) are consistently

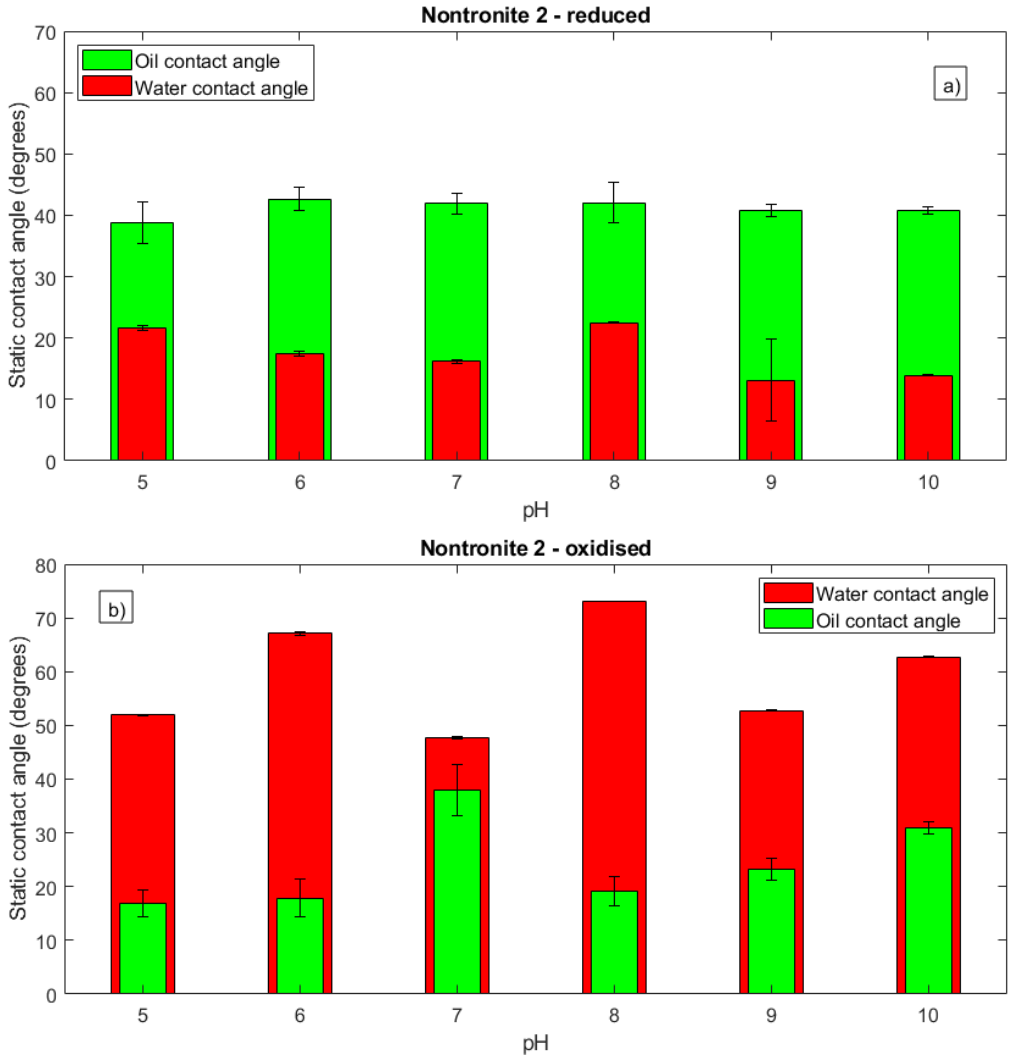

Figure 4.5: Static contact angle measurements for NAu2 clay mineral films mounted on glass slides, for reduced (a) and oxidized (b) clay minerals. Measurements were conducted with water (red) and crude oil (green). The pH value was pre-adjusted before clay film preparation (method (i)). Error bars show the standard deviation of final averages (Table 4.4).

higher for DI water (red) compared to crude oil (green), indicating a more oil-wet than water-wet surface. On average, the water-wet angle is 55° and the oil-wet angle 20°, resulting in a difference of 35° (Table 4.4). However, we observed much higher variations in contact angles measured across the range of pH values compared to our results for reduced NAu2 (Figure 4.5a), yet with no apparent trend relative to pH value. For the oil droplets, the contact angle varied between 17° and 37° with standard deviations $< \pm 5°$ (Table 4.4), apart from the clay film measured at pH 7 which exhibited higher values and higher standard deviations, while water-wet angles showed even higher variations with pH value (47°-73°) but lower standard deviations $< \pm 1°$. Our results suggest that the water droplets were more stable than the oil droplets on each clay film, and that contact angles were affected by clay film surface variations. This variability/ surface variations, however, cannot be attributed to different pH clay suspension values, owing to the clay mineral buffering effects observed in preparation method (i).

Illite - IMt2

Similar to reduced NAu2, reduced IMt2 also showed consistently higher contact angle values for crude oil (green bars: 23°-31°, Figure 4.6a, Table 4.4) than for DI water (red bars: <15°, Figure 4.6a), with small standard deviations ($< \pm 5°$). The difference in contact angle between water-wet and oil-wet is also very similar for both reduced clay minerals (IMt2: 15°-20°; NAu2: 20°-25°). Although these water values are at the limit of proper quantification for the static sessile drop (SSD) method used here, our observation of these very low contact angles strongly suggest more water-wet surfaces in reduced IMt2 compared to reduced NAu2.

In contrast to our observations for oxidized NAu2, average contact angle values measured for oxidized IMt2 clay mineral films are higher for oil droplets (20°-32°, Table 4.4) compared with DI water (13°-22°, Figure 4.6b), and are more similar to the observations for reduced IMt2 (Figure 4.6a). However, the difference in wetting cannot be determined as unambiguously as for the reduced IMt2 samples, because the oil and water wetting measurement error bars overlap for several pH values measured (Figure 4.6a). Moreover, water droplets seemed to be more stable (standard deviations $< \pm 3°$ for 4 out of 6 pH values) than oil droplets (standard deviations $> \pm 3.5°$ for most samples) on the oxidized IMt2 clay mineral films. These observations suggest that oxidized IMt2 is more water-wet than oil-wet, although less pronounced than in the case of reduced IMt2.

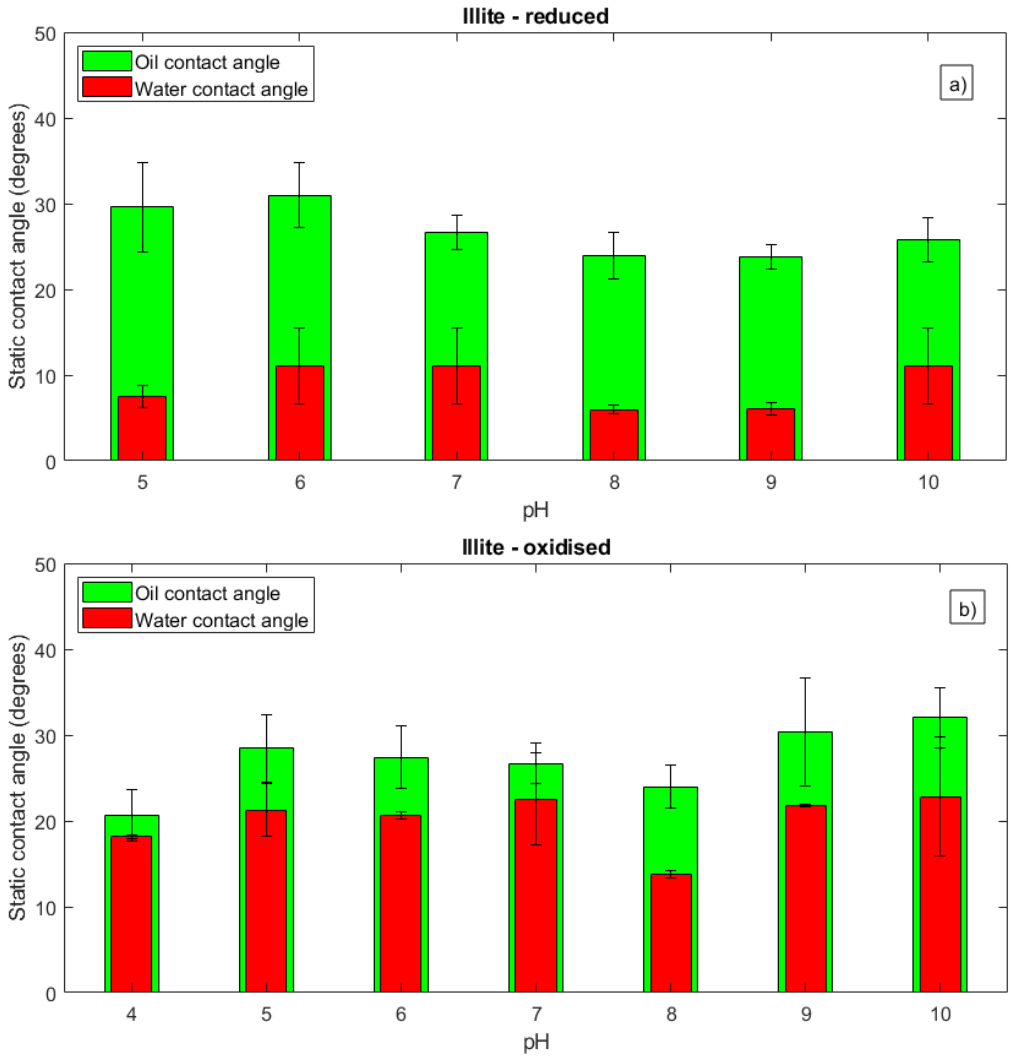

Figure 4.6: Static contact angle measurements for IMt2 clay mineral films mounted on glass slides, for reduced (a) and oxidized (b) clay minerals. Measurements were conducted with water (red) and crude oil (green). The pH value was pre-adjusted before clay film preparation (method (i)). Error bars show the standard deviation of final averages, Ave_3, (Table 4.4).

Figure B.2 from Appendix B, displays the contact angle values as well as the height and width of each droplet dispensed on the reduced NAu2 clay mineral film surface at pH 5. On the X axis, denotated as 'Elapsed time' in seconds, every 5-second interval represents one droplet. Values presented in these graphs represent the Ave_1 (as per Table B.1). So, for this example, 6 different droplets - repetitions (denoted *Rep 1, 2, 3, 4, 5, 6*) were measured for contact angle (scaled by 2 orders of magnitude in the figure), as well as the evolution of the height and width of each droplet was taken, all on different areas of the same clay film. As, each Rep represents a different droplet, it can be observed that the height is almost the same amongst the different droplets with width varying more in values, while at the same time the contact angle remained mostly stable for *Rep1 - Rep4*, increasing in value for *Rep5* and *Rep6*, following the same trend as for the width. Similarly trends were observed in Figure B.6 for reduced samples, and Figures B.3 & B.7 for oxidised samples of NAu2.

Data shown here suggest that the reduced sample at pH 5 (Figure B.2) show a more stable contact angle, droplet height and width profile, within the time of 5 seconds for each Rep comparing to that of pH 5 under oxidized (Figure B.3) conditions, where slight changes occurred during the experiments on the same attributes of the droplets, implying a surface with less roughness.

Similar observations about the contact angle variation exhibited can be made from Figures B.4, B.8 for reduced IMt2, and Figures B.5, B.9 for oxidised IMt2. The example of pH 5 (Figure B.4) under reduced conditions show that the droplet width values varied the least, while height and contact angle values seem to follow the same trend from droplet to droplet. Looking at the oxidized counterpart of pH 5 (Figure B.5) clay film, *Rep 3 - 5* show a positive trend amongst droplet contact angle, height, and width, while *Rep 1* and *Rep 2* show the opposite.

The pH adjustment of the DI water prior to clay suspension formation seemed not to affect the oil contact angle. Both, crude oil, and DI water, exhibited different contact angle values, without showing any trend as DI water pH was increasing, as per method (i). The pH buffering effects at pH 8.5-9, upon clay dispersion, suggest that the contact angle variability can be solely attributed to clay film surface variations and not surface charges differentiations due to pH.

Table 4.4: Crude oil static contact angle measurements for nontronite-2 and illite, under reduced and oxidised conditions.

Oxidised				
			Contact angle Values	
Method	pH	Time (s)	NAu-2	IMt-2
Static sessile drop	4	< 1	27.31 ± 2.41	20.6 ± 2.97
	5	< 1	16.85 ± 2.52	28.45 ± 3.93
	6	< 1	17.9 ± 3.47	27.42 ± 3.69
	7	< 1	37.95 ± 4.83	26.68 ± 2.39
	8	< 1	19.18 ± 2.67	23.97 ± 2.53
	9	< 1	23.21 ± 2.04	30.41 ± 6.27
	10	< 1	30.87 ± 1.14	32 ± 3.45
Reduced				
			Contact angle Values	
Method	pH	Time (s)	NAu-2	IMt-2
Static sessile drop	5	< 1	38.84 ± 3.38	29.57 ± 5.25
	6	< 1	42.65 ± 1.93	30.99 ± 3.78
	7	< 1	41.94 ± 1.72	26.64 ± 2.02
	8	< 1	42.07 ± 3.31	23.96 ± 2.71
	9	< 1	40.81 ± 0.97	23.79 ± 1.40
	10	< 1	40.75 ± 0.53	25.75 ± 2.58

4.3.3 Dynamic Contact Angle Measurements

During measurements in the static mode, changes in crude oil contact angle values over time were noted (Figures B.6 - B.9), which were most pronounced for the oxidized clay mineral films (Figures B.7, B.9). To examine the contact angle equilibration time, static crude oil contact angle measurements were complimented with dynamic contact angle measurement in the 'Equil' method (Table 4.3). For dynamic contact angle measurements, only oxidized clay films were used, which were prepared using method (ii), at pH values of 5, 7, and 9 (Table 4.2). Furthermore, the testing fluid was only the crude oil, as it exhibited higher value error in the static mode.

Nontronite 2 - NAu2

For oxidized NAu2 films at all pH values, high contact angles between 40°-60° were observed immediately after deposition of a crude oil droplet on the surface (Figure 4.7). The contact angle measured decreased over time to values <15°, with a more rapid decrease observed at pH 5 and less data spikes observed at pH 9 (Figure 4.7). Similar observations were made for all repetitions (additions of new crude oil droplets).

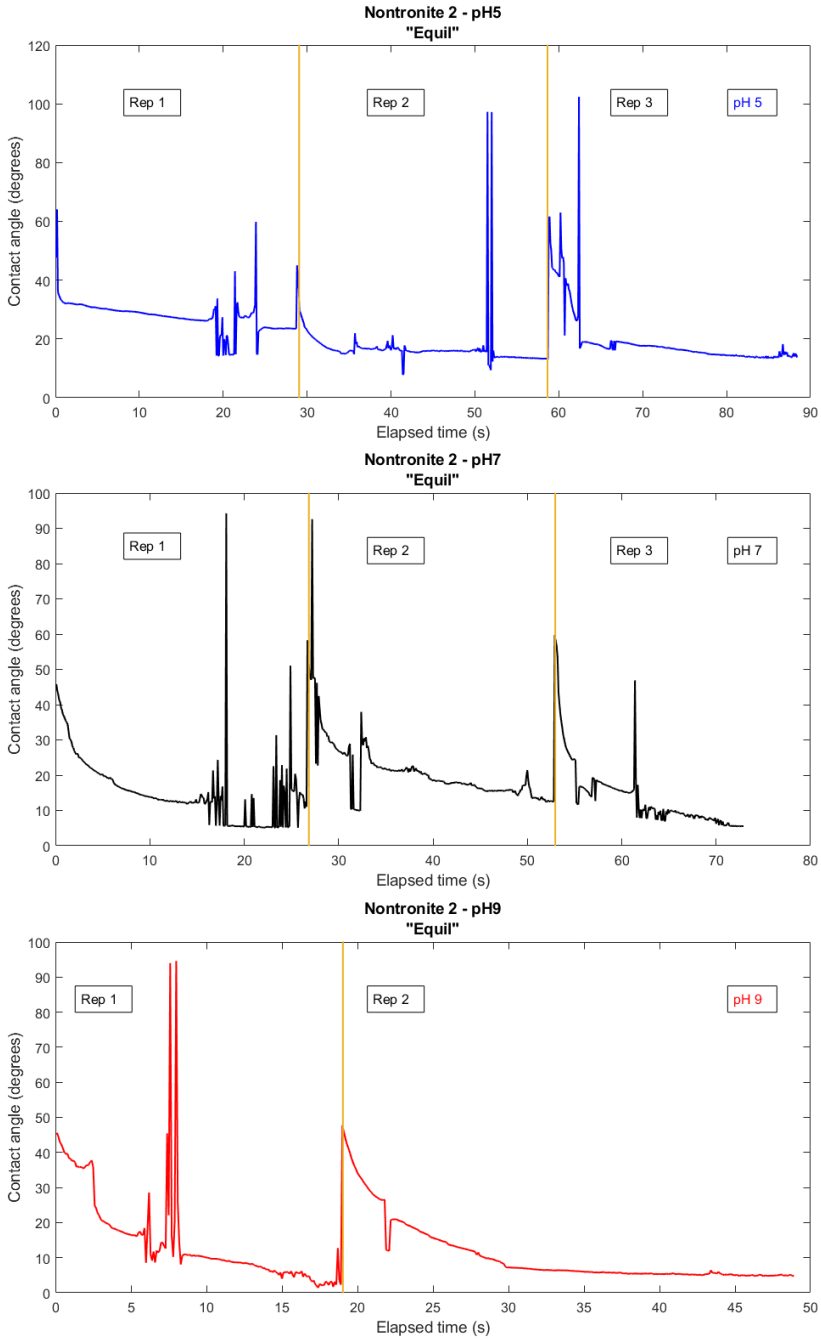

Figure 4.7: Crude oil contact angle profile against time for NAu2 films prepared at **(a)** pH 5, **(b)** pH 7, and **(c)** pH 9. Each repetition (*Rep*) corresponds to a new crude oil droplet observed at the surface of the sample, with the yellow vertical line indicating the beginning of the repetition. Spiking within each observation window (30 s) is due to droplet instability and/or software visual reading lagging.

Illite - IMt2

Dynamic contact angle measurements of oxidized IMt2 clay mineral films showed highly variable values (spiking) immediately after deposition of a crude oil droplet on the surface (Figure 4.8), impairing the determination of initial oil contact values. Similar to our observations for oxidized NAu2, these values decreased quickly and stabilized over time, yet for oxidized IMt2 reached values around 20°. A representative example of a stable oil droplet can be observed in Figure 4.8c, for repetition 2, with an initial contact angle value of 40.9±2.75° and a final contact angle value of 25.7±1.62°.

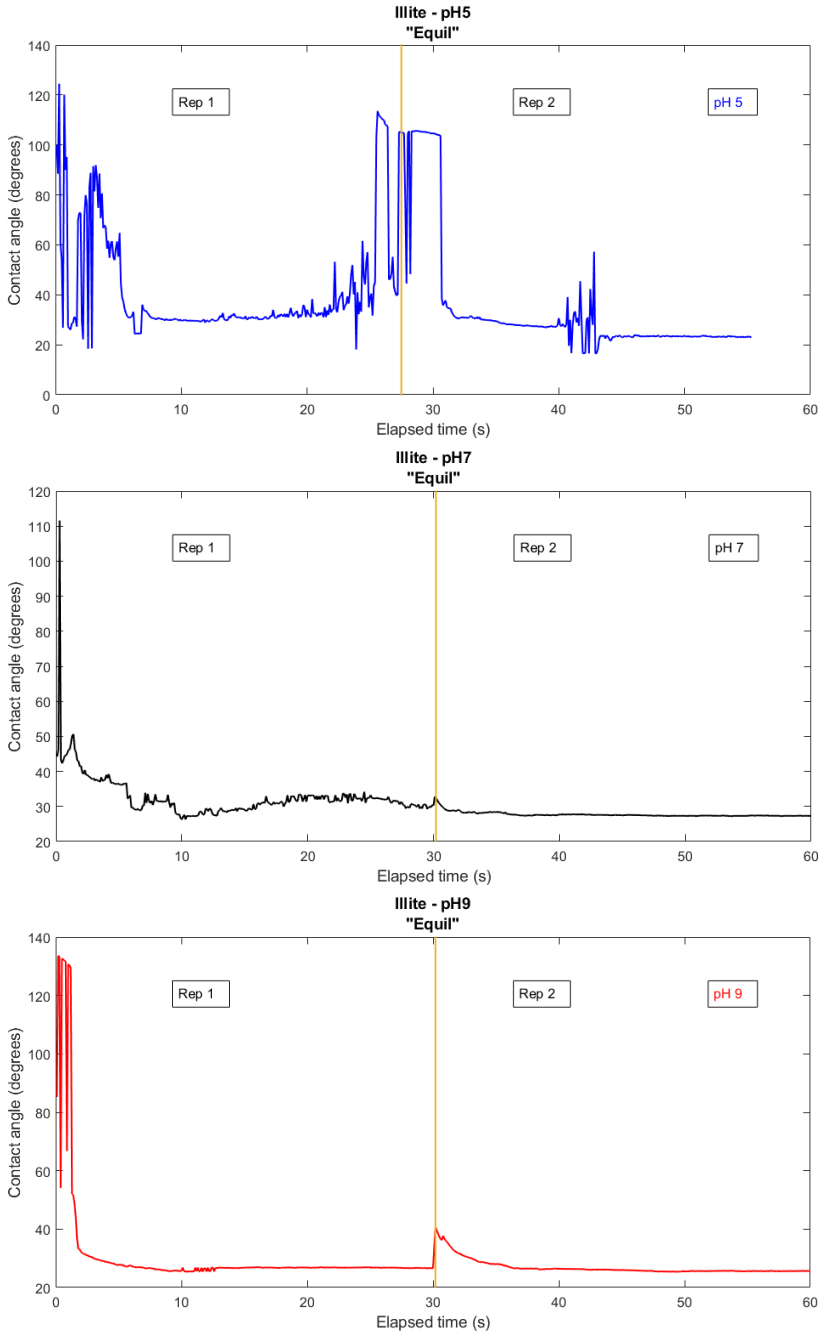

Figure 4.8: Crude oil contact angle profile against time for IMt-2 at **(a)** pH 5, **(b)** pH 7, and **(c)** pH 9. Each repetition (Rep) corresponds to a new crude oil droplet observed at the surface of the sample, with the yellow vertical line indicating the beginning of the repetition. Spiking within each observation window (30 s) is due to droplet instability or software visual reading lagging.

In Figure B.10 for NAu2 and pH 5, the 'Equil' method depicts the evolution of the contact angle along the height and the width of the oil droplet. It can be seen that in time, the contact

angle and height of the droplet decrease, while the width increases. Similar repetitive patterns can be observed for the Advancing method in the same figure, but in a shorter time span. As each repetition is divided into three steps (see Table 4.2), the contact angle seems to acquire the same initial and final value for every step, within this one repetition. This shows a good repeatability of measurements but also a consistent roughness across the clay film. The Advancing+ method, at which one contact angle value is taken for each 10 μl of crude oil added, shows a quite stable value at 60° for the first repetition and 50° for the second. Similar observations can be made for the pH 7 and pH 9 in Figures B.11 and B.12.

For the oxidised IMt2 case only 'Equil' and Advancing data were able to be acquired due to instability of the dispensed oil droplets and the difficulty of the software to establish solid tangents for measuring the right and left angle of the droplets. This instability can be seen across the data in Figures B.13, B.14, B.15. In this case it was more difficult to extract exact numbers of initial contact angles, as significant spiking was taking place, especially at the beginning of each repetition. Repeatability of measurements slightly improves as pH increases from pH 5 to pH 9. For all, pH 5, pH7 and pH 9 and 'Equil', as the oil contact angle decreases, the height decreases while the width of the droplet increases, with these changes taking place within few seconds after droplet dispensing.

Table 4.5 shows contact angle values for each kind of measurement, using representative values for each clay mineral, as presented in the Supplementary Material. Data were used from measurements based on the different modes used on this DSD setup. With the Equil method, the final contact angle tended to be better estimated, while with the Advancing+ method, the initial contact angle was better estimated. In addition, the Advancing+ method gave a repeatable pattern, for each 30 μl drop added in the 10 μl steps (e.g. see Figures SM9, SM10). When this pattern is identifiable, within a samples measurement, more representative contact angle values could be extracted. Differences between initial and final values were observed for all the different measurement methods and even for repeated measurements on the same clay film. The greatest difference, at around 35°, was noticed for the Equil approach, during which the oil droplet had the longest relaxation time (Table 4.3), whereas the Advancing+ method displayed the smallest differences between initial and final values ($< 23°$, Table 4.5). Moreover, the Advancing+ method initial and final values had a difference at, or below 20°. Taking one example for NAu2 and pH 5, the decrease in the contact angle was more than 20°, for the Equil method. The initial values

Table 4.5: Dynamic contact angle values of crude oil droplets on oxidized NAu2 and IMt2. Initial and final values are separated with / for each repetition presented on the table. The most representative repetitions are selected for each method and clay mineral.

Oxidised Dynamic Sessile drop method				
			Contact angle values	
			NAu-2	
pH	Method	Time (s)	Initial (*Rep*/*Rep*)	Final
5	Advancing+	0	58.7 ±0.75 / 51.5 ±0.55/ 44.2 ±1.5	50.2 ±5.45 /-/-
	Advancing	9	39.8 ±0.7 / 45.8 ±0.15	20.7 ±12.9 / 26.4 ±0.35
	"Equil"	30	47.7 ±0.28 / 45 ±1.34	23.5 ±7.77 / 13.1 ±0.14
7	Advancing+	0	43.4 ±2.2	42.4 ±2.55
	Advancing	9	38.7 ±0.2 / 41.2 ±0.65	20.8 ±0.8 / 17.7 ±5.2
	"Equil"	30	45.8 ±0.7 / 47.8 ±1.95	11.1 ±1 / 12.5 ±1.1
9	Advancing+	0	38.7 ±3	29.5 ±1.05
	Advancing	9	27.5 ±2.35 / 51.1 ±3.55	24 ±6.2 / 29.6 ±1.35
	"Equil"	30	45.6 ±0.4 / 47.7 ±0.55	5.6 ±2.3 / 10.7 ±4.85
			IMt-2	
pH	Method	Time (s)	Initial (*Rep*/*Rep*)	Final
5	Advancing+	0	N/A	N/A
	Advancing	9	40.2 ±2.4 / 40.9 ±0.35	25.1 ±0.75 / 38.4 ±7.15
	"Equil"	30	37.3 ±6.6 / 47.2	33.2 ±1.31 / 23.1 ±8.35
7	Advancing+	0	N/A	N/A
	Advancing	9	47.5 ±1.55 / 38.4 ±1.4	33.1 ±0.48 / 28.3 ±0.4
	"Equil"	30	44.2 ±0.7 / 32.8 ±0.85	30.3 ±6.1 / 27.3 ±0
9	Advancing+	0	N/A	N/A
	Advancing	9	27.4 ±1	29.9 ±1.45
	"Equil"	30	52.1 ±3.8 / 40.9 ±1.95	26.6 ±1.4 / 25.7 ±1.15

were comparable with the Advancing+ method, with the latter exhibiting higher initial values for some cases. For the IMt2 case, again at pH 5, the contact angle decrease was from 4° to 25°, looking at the Equil method, while for the Advancing+ method it was from 2° up to 15°.

4.4 Discussion

The main aim of this study was to gain understanding how oxidation of reservoir rocks, as has been observed after implementing low-salinity water-flooding (LSWF) in field scale trials, (Lager et al., 2011) affects the surface wettability of clay minerals, a key mineral component of reservoir rocks. Previous work mainly used core-flooding (Tang, Morrow, 1999) and/or field scale (Seccombe et al., 2010) trials and found that the wettability changed from mixed- or oil-wet to water-wet after LSWF (Jackson et al., 2016). Here, contact angle wettability studies on

chemically reduced clay mineral films, emulating the initial reservoir conditions of a sandstone reservoir, and oxidised clay mineral films, to represent the produced LSWF treated reservoir are presented. The effect of the change in oxidation state of clay mineral structural Fe from reduced, or ferrous, iron (Fe^{2+}) to oxidized, or ferric, iron (Fe^{3+}) on wettability changes is studied, and its potential implications for the interpretation of field data and oil production are considered (Lager et al., 2011).

Assessment of Clay Films for Contact Angle Measurements

Contact angle measurements on clay films were undertaken, and SEM used to evaluate the suitability of the formed films for measurement (Figure 4.4). Surface perturbations of similarly low degrees were noted in all clay mineral films and were considered suitably consistent between reduced and oxidised states to allow for comparative measurements between the two states. To better understand the observed surface perturbations, drop size and time retention sensitivity analysis in the form of DSD measurements were carried out. To fully quantify the clay mineral film roughness is particularly challenging, as for any substrate, (Tonietto et al., 2019) owing to variations in roughness measurement technique and length-scales considered. Contact angle measurements allow evaluating of roughness through hysteresis quantification (Drelich et al., 1996; Wang et al., 2020). Clay film precipitation process during clay film preparation, induced macro-scale surface roughness, observed visually, which can affect the contact angle value, *vide infra*.

As seen from Figures B.2 - B.9, no clear or unique trend could be identified across all the data, in terms of correlation between drop size and contact angle. Different size droplets exhibited different heights, widths and especially contact angles, even on the same clay film samples. Such variations would not exist on an ideal surface (Wang et al., 2020). From SEM (Figure 4.4) the surface appeared continuous on the micro-scale; variations in drop size and contact angle can be attributed to the mm-scale roughness within the single clay film and, potentially, some heterogeneity in the illite films. Variation in the plotted contact angle values (Figure 4.5, Figure 4.6), for oil and water droplets, is exhibited across all the clay films, with oxidized clay mineral films showing more variation than reduced films. Clay films prepared by Method (i), from solutions pH adjusted before clay mineral addition, were found to be buffered by the clay mineral at pH 8.5- 9. These films show differences between oxidised and reduced observed contact angles and

some variation between different pH values which may lie within the small chemical changes or through heterogeneity and variations in film roughness between samples; to observe the effect of pH, Method (ii) treats the clay minerals post suspension. Measurements taken on the reduced clay films (as per Method (i)) show lower variability between pH, suggesting the reduction process results in structural rearrangements. Owing to the oxidized clay mineral film variability in contact angle for oil droplets, dynamic contact angle measurements, on films as per Method (ii), were performed to complement the static measurements. Irrespective of the dynamic measurement approach (Table 4.3), clay mineral films of both NAu2 and IMt2 showed contact angle strongly depended on the time of observation, exhibiting hysteresis (Table 4.5). Interestingly, the difference between initial and final contact angle values determined with the Advancing+ and Equil methods was very similar, especially for NAu2 (20° and 20-30°, respectively; IMt2: 2-15° for each method), although the duration for each repetition was longer for the latter method. Two trends were identified for the whole NAu2 dynamic set of measurements: (i) Advancing+ initial contact angle value decreases as pH increases; (ii) The final contact angle value in the 'Equil' method decreases as the pH increases These both indicate increased oil wettability of the clay mineral film surfaces at higher pH values.

Most previous studies observed an increase of effluent pH value after LSWF, along with increased oil recovery, which suggests a decrease in oil-wettability of the reservoir minerals, Austad et al. (2010); RezaeiDoust et al. (2011, 2009); Piñerez Torrijos et al., (2016)[1]. These observations were attributed to either localized uptake of protons (H^+), leading to Ca^{2+}/H^+ exchange on clay mineral surfaces and concomitant acidic-basic (Figure 4.1, basic: cation exchange, acidic: ligand or cation bridging) oil compound desorption (Austad et al., 2010), or the formation of a surfactant, which will reduce the interfacial tension of the water-oil interface and lead to an alkaline-like flooding effect (McGuire et al., 2005), which strongly depends on crude oil composition (RezaeiDoust et al., 2009). It should be noted, however, that these prior experiments involved alteration of the water flood pH, whereas in the study here the effect of pH on the clay mineral surface prior to contact with oil/water phases was explored. Other studies suggest that a pH value increase may not always correlate positively with more oil recovery from LSWF (Jackson et al., 2016). Indeed, after the initial pH value increase and once a new equilibrium had

[1]Piñerez T,I,D., Austad, T.,Strand, S., Puntervold, T., Wrobel, S., Hamon, G. 2016, April. *Linking low salinity EOR effects in sandstone to pH, mineral properties ans water composition.* In SPE Improved Oil recovery Conference. OnePetro. https://doi.org/10.2118/179625-MS

been established during LSWF, a subsequent pH decrease was observed in some cases, (Piñerez Torrijos et al., 2016)[1].

The contact angle values obtained from the Equil and Advancing+ methods are very similar, indicating that even the short measurement time of the Advancing+ method (30 s) captured the characteristic temporal changes. However, reproducibility of the initial and final contact angle values is poorer for the Advancing method than the 'Equil' method, due to frequent spikes and lack of clear, repeatable patterns (e.g., Figure B.14). Representative contact angle values are presented in Table 4.5.

So far, for the clay film surfaces discussed, NAu2 was more suitable for measuring contact angles, than IMt2. It should be noted that, even though the clay film were created using the same method for both clay minerals, the surfaces acquired are different, with IMt2 having a more perturbed surface than NAu2. This is shown by the higher error that IMt2 static values exhibited than NAu2, in both reduced and oxidised state, (Figure 4.5, Figure 4.6). The reason for the difference in roughness is ascribed to the mineralogy, with nontronite being determined to be $> 99\%$ pure phase, whereas the illite contains minor impurity phases, mainly feldspar (ca 5%) and quartz (ca 17%).

By comparing the static and dynamic crude oil contact angle measurements, we can see that the former captures sufficiently the wettability of the clay films, within the evaluated variability given by the latter, for NAu2 (Figures 4.5b and B.12) and IMt2 (Figures 4.6b and B.15), with the static approximately correlating with the final dynamic contact angle values. The iron reduction within the clay minerals affected the clay film surfaces, and its mechanical properties, since the error exhibited by the static oxidised contact angle values decreased in the reduced counterparts. This alone could be a strong indicator that the surface roughness is decreased for both clay mineral surfaces and especially for the NAu2. Although this approach for studying wettability through clay mineral films might be considered idealistic, since the real mineral surface conditions in the rock are much more variable, this data strongly suggests there is an effect of iron reduction on wettability, as discussed below.

Effects of redox state on clay mineral wettability

During the reduction of the clay films, Na^+ is present in excess owing to the reductant. As such, Na^+ is expected to both cation exchange existing ions, and act to counterbalance ad-

ditional charge developed during reduction. The presence of excess Na^+ creates a LSWF-like environment.

For the NAu2 case, going from reduced to oxidized state, the wettability changed from water-wet to oil-wet (Figure 4.5 a, b). It is worth mentioning that the error exhibited on the oil contact angles for each sample at the reduced state is much less than that of the oxidized, while water contact angle error remained low across the samples. For the case of the IMt2, transitioning from reduced to oxidized state, in Figure 4.6 a, b, the wettability difference was diminished. As the reduced IMt2 was more water-wet, with water contact values below 15°, and oil contact values above 23°, the oxidised counterpart show no clear contact angle distinction between the two fluids tested, with oil and water wettability overlapped for most samples. The oil wettability varied from 36° down to 22°. This difference can be considered significant for precisely quantifying the oil wettability of an IMt2 clay mineral surface for the specific experimental set up. The contact angle of a liquid on a surface can be affected by many factors, such as air relative humidity (Shang et al., 2010), atmospheric pressure, temperature, liquid viscosity, liquid chemical composition liquid/surface tension, surface chemical composition, surface roughness, and the combination of these chemical and mechanical properties. In this study, most properties were essentially constant for the system tested. For the clay mineral and consequently the clay film surface, it is important to consider the chemical composition of the minerals, here there is a higher iron content in NAu2, than the IMt2, and also the different exchangeable cations for each mineral, with NAu2 being natively more Ca^{2+}-saturated, while IMt2 being natively K^+ saturated. This variation in cations will naturally induce hydration differentiation to these clay minerals. Other properties that affect the clay mineral surface complexation is the cation exchange capacity (CEC) of the minerals with NAu2 having 72 meq/100g (Gates, 2005) and IMt2 15 meq/100g (Hower, Mowatt, 1966), under oxidized conditions, as well as the specific surface area (N^2 - BET) 10.6 m^2/g and 17.5 m^2/g, respectively (Dogan et al., 2007).

Upon chemical reduction, several changes take place in the mineral structure, as briefly described in the introduction. Under strongly reducing conditions, increased layer net negative charge occurs when Fe^{3+} becomes Fe^{2+}, (Stucki et al., 1984b) which will increase the cation uptake, here for Na^+ present from the reduction process. As reduction progresses the additional negative charge is also balanced by dehydroxylation and formation of tri-octahedral sites. In the reduced state, the higher number of Na^+ cations, with a high hydration enthalpy, increases water

affinity and the hydrophilic, water wetting nature of the surface. This will be further increased by exchange of Ca^{2+} by Na^{+} (Vasilopanagos et al, 2021, in submission) [2]. There are also different oil molecule adsorption mechanisms, as shown in Figure 4.1, with divalent cation bridging being responsible for tethering of oil droplets containing carboxylate groups to the mineral surface. Reduced clay minerals with higher layer charge and more cations present would lead to higher oil wettability. In this study, though, the opposite is shown for both minerals, with increased oil wetting for the oxidised clay minerals. This supports the hypothesis that replacement of divalent cations with Na^{+} occurs during reduction, and the increased surface negative charge becomes compensated by Na^{+} upon reduction, both leading to increased water wetting. During reduction, in the case of nontronite NAu2, Ca^{2+} is mainly lost and replaced by Na^{+}, and, for illite IMt2, a further investigation with XPS (as presented in Chapter 3) has shown that the K^{+} is retained while trace amounts of Ca^{2+} is lost and replaced by Na^{+}, in addition to the increased negative charge on the layers being balanced by Na^{+}. As such, oil wetting through cation bridging will be significantly diminished in the reduced samples, reinforced by the formation of hydrated Na^{+} domains. In the case of oil reservoirs, the cations present during oil formation and onset of reducing conditions are likely to be important in establishing the wettability of the mineral surfaces.

For the oxidized case of NAu2 and IMt2 a different preferred wettability state may readily be observed. Both clay minerals favoured being oil-wet, with an average contact angle of 26° for oil droplets in both cases. There is a difference in relative water affinity, with NAu2 less water-wet than the IMt2, with contact angles showing an average of 55° against 8°. In similar studies, non-treated Arizona smectite and illite exhibited water contact angle values of 23.8° ± 1.7° and 34.2° ± 0.9°, respectively (Shang et al., 2010). Also, Arizona smectite (SAz1) and illite (API no.36) clay films were used for wettability measurements after Ca^{2+} clay saturation, where static (oxidized) water contact angle values were 44.5° ± 0.9° and 31.9° ± 1.1°, respectively (Shang et al., 2008). In the same study, dynamic contact angles were reported with advancing angles (sessile drop method) being 41.9° ± 2.5° and 30° ±0.4°, receding angles (Wilhelmy plate method) 9.9° ±2.3° and 0°, for SAz1 and illite no.36, respectively. Taking into consideration the different materials, settings and purposes of these studies, a similar high water contact angle for smectite, and low contact angle for illite, was observed only with the Ca-saturated measurements

[2] Vasilopanagos, C; Carteret,C; Neumann, A; Greenwell, H. C., Effect of Redox State on Water Sorption by Swelling and Non-Swelling Clay Minerals. MDPI Minerals 2021

and this study. For example, the non-treated Arizona smectite exhibits a cationic exchangeable composition of 2.82% Ca^{2+}, 0.063% Na^{+}, and 0.19% K^{+}, while NAu2 2.34% Ca^{2+}, 0.14% Na^{+}, and 0.01% K^{+}, (cation oxides %). Contact angle studies on nontronite-1 (NAu1), fractionated and saturated with different cations, showed that the surface can be significantly modified by the saturating cation, in terms of roughness and hydration, leading to different water affinity, with Ca^{2+} leading to a rougher surface and the most hydrophilic (Ballah et al., 2016). Water contact angle values were 21° for Ca^{2+}, 30° for Na^{+}, 40° and 50° for Li^{+} and K^{+}-saturated NAu1, respectively (Ballah et al., 2016). In comparison to the present study, the NAu2 (mainly Ca^{2+} rich) water wetting gave a contact angle of 50°-75° (Figure 4.5b), while for IMt2 (K^{+} rich) a contact angle around 20° was noted (Figure 4.6b). These observations underscore that the choice of saturating cation during clay treatment could play a significant role on the clay mineral hydration, such as altering illite wettability to more hydrophilic (Shang et al., 2010). As such, the combination of iron reduction increasing clay net negative charge, along with the presence of Na^{+} in the reduction chemistry, leads to significant changes in the clay mineral surface chemistry. Reduction leads to a higher water affinity in this present study, giving another perspective on multi-ion exchange effects and further explanation on changes occurring during LSWF methods in EOR.

4.5 Conclusions

This study provides the first direct evidence for how clay mineral wettability alters by changes in redox conditions, such as those that may occur in EOR during LSWF. The selected reservoir-proxies, iron-containing clay mineral films of NAu2 and IMt2 both exhibited increased water affinity under reduced conditions, such as may reflect reservoir conditions prior to production. The increased wettability by water in the reduced clay minerals occurs owing to two factors: (i) the increased net negative surface charge of the clay mineral increasing hydratable cation content at the surface; (ii) the identity of those cations being Na^{+} owing to the specific experiments undertaken here, and thus unable to provide cation bridging to polar oil molecules. As such, the pore fluid ionic composition during oil formation and onset of reducing conditions is likely to be critical in understanding initial reservoir rock wetting state.

The oxidised clay minerals, prior to reduction, showed different wetting, with NAu2 oil-wet and IMt-2 mixed-wet, indicating increased interactions of oil with the clay mineral surface.

During oxidation, such as might arise during a LSWF, the cation exchange capacity of the clay minerals will decrease. Though this may lead to increased oil wetting of the clay mineral, this may still lead to EOR through either selective loss of cation bridge forming divalent cations, or fines migration where the clay particles more easily detach from underlying sandstone quartz surface to migrate with the oil phase. Ongoing research is examining the changes in hydration of homo-ionic reduced and oxidised ferruginous clay minerals. Residual oil is known to be produced when de-oxygenated [3] sea water LSWF is used as an EOR method (Seccombe et al., 2010) and evidence supportive of reservoir rock oxidation is observed (Lager et al., 2011), with oxidants in sea water possibly playing a role in such processes (Jackson, Williams, 1988). Previous studies investigating whole reservoir cores with atomic force microscopy adhesion mapping or relative permeability curve analysis (Unsal et al., 2020; Yesufu-Rufai et al., 2020) showed a significant shift to water-wet conditions upon changing the redox conditions from oxidised to reduced, consistent with higher oil release upon LSWF. The authors suggest that clay minerals, and in particular those with high structural Fe content, were mainly impacted by changes in redox conditions and consequently responsible for the changes observed in wettability. However, reservoir cores contain several minerals that may be affected by the reduction procedure, for example carbonates which partially dissolved during exposure to dithionite-containing brine (Yesufu-Rufai et al., 2020), and none of the studies confirmed the extent of Fe reduction in the clay minerals or bulk mineral core (Unsal et al., 2020; Yesufu-Rufai et al., 2020). It is therefore conceivable that oxidation occurring during LSWF induces processes in addition to clay mineral Fe oxidation that could cause further oil release observed in complete reservoir cores.

[3]Robbana, Enis , Buikema, Todd , Mair, Chris , Williams, Dale , Mercer, Dave , Webb, Kevin , Hewson, Aubrey , and Chris Reddick. "Low Salinity Enhanced Oil Recovery - Laboratory to Day One Field Implementation - LoSal EOR into the Clair Ridge Project." Paper presented at the Abu Dhabi International Petroleum Conference and Exhibition, Abu Dhabi, UAE, November 2012. doi: https://doi.org/10.2118/161750-MS

Chapter 5

Hydration of Nontronite-1 (NAu1): Near-, Mid-Infrared and Water Vapour Adsorption

5.1 Introduction

Clay mineral hydration is a subject well studied by numerous researchers, with the water wetting of clay mineral surfaces playing a significant role in modifying clay mineral interactions with other fluids, as well as the transport of dissolved ions. Infrared (IR) spectroscopy can discern clay mineral structural vibrations and clay mineral/ water interaction vibrations, as water is adsorbed on the basal surfaces, edges, or within the interlayer of the mineral phase. Reduction-oxidation processes can have a profound effect on surface charge and the structure of iron-bearing clay minerals, and these changes can impact on clay mineral interactions.

Among the first to describe infrared spectra of phyllosilicate minerals were Farmer, Russell (1964), and since then many researcher have contributed to examining the IR spectra of smectites and, more specifically, nontronites as a mineral of interest, coupled with reduction-oxidation effects on clay mineral structure and clay mineral-water interactions in the M-IR and N-IR range Madejová et al. (2017); Frost, Kloprogge (2000); Gates (2005); Claire et al. (2002); Fialips et al. (2002); Bishop et al. (2002); Frost et al. (2002); Baron et al. (2016); Stucki (2011); Johnston (2017). While structural changes observed with IR spectroscopy, upon iron reduction, have been focused on O-H stretching vibrations, metal (M)-OH bending vibrations and Si-O stretching

vibrations Stucki (2011), cation-induced clay mineral hydration can affect the IR spectrum of nontronites in both M-IR and N-IR (Johnston, 2017). Different cations induce different degrees of hydration in the clay mineral structure, with weakly hydrating cations, such as Cs^+ and K^+, causing interlayer collapse, while other monovalent cations such as Li^+ and Na^+ induce more interlayer water, causing clay mineral swelling. Although divalent cations such as Ca^{2+} and Mg^{2+} can have higher hydration enthalpies, yet do not induce interlayer expansion, (Johnston, 2017). This cause (cation) and effect (hydration) phenomenon has been described for oxidised clay minerals mostly and are more variable for reduced clay minerals. This differentiation arises due to the fact that, upon iron reduction, the interlayer collapses, creating a different overall smectite structure which can be approximated by an illite-smectite mixture (Stucki, 2011). Khaled, Stucki (1991) investigated cation fixation in two iron-bearing smectites showing that upon iron reduction the amount of fixed or non-exchangeable cations increased, with an order of $Cu^{2+} < Zn^{2+} < Ca^{2+} < K^+$, which is the inverse of the hydration enthalpy of those cations. The same observation had been made for Na^+ cations by Lear, Stucki (1989) and Stucki et al. (1984a). The interlayer collapse causes this cation fixation, which leads to a dehydrated interlayer space, which in turn can affect the overall clay mineral hydration and potential to exchange cations.

With most clay mineral infra-red studies focusing on the structural characteristics and/or structural changes of the mineral lattice, a more integrated approach was taken for this present study, exploring nontronite NAu1 hydration in the near- (N) and middle- (M) infra-red (IR) range, as well as water vapour adsorption isotherms, in order to evaluate qualitatively and measure volumetrically the amount of water held, by the clay mineral, both in reduced and oxidised conditions. Different saturating cations were used, Na^+, Ca^{2+} and K^+, to isolate and investigate the different hydration effects induced by these specific cations. Using NAu1 as a proxy for iron-bearing clay minerals in a sandstone reservoir rock, where clay mineral interfaces form the oil-brine-rock interactions holding hydrocarbons, this experimental work aims to shed light on the clay mineral/fluid interactions that take place in such environment. The initial redox state of the reservoir rock would be a reduced state, where iron in minerals or oxides would occur as Fe^{2+}. In this reduced environment, the clay mineral hydration should be examined as it will govern the clay/ brine/oil interactions, such as wettability of clay minerals, cation exchange capacity and cation exchange reactions, all of which fundamentally govern oil recovery (Chapter 4, Chapter 7).

5.2 Materials and Methods

5.2.1 Materials Used

The nontronite NAu1 (hereafter referred to as NAu1 for the as received form) was purchased from the Clay Mineral Society (CMS) mineral repository (clays.org) in rock chip form. The described bulk mineralogical composition was Nontronite 90%, Kaolin 4%, Quartz 2%, Biotite <1%, Goethite 3% (Keeling et al., 2000). The elemental analysis provided with the sample was SiO2: 51.36 Al2O3: 8.150, Fe2O3: 35.94 MnO:0.013 MgO: 0.19, CaO: 3.56, Na2O: 0.03, K2O: 0.006 giving a formula for the nontronite of $(M^{+}1.05)[Si_{6.98}\ Al_{0.96}][Al_{0.35}\ Fe_{3.68}\ Mg_{0.04}]O_{20}(OH)_4$ (Gates, 2005).

For the clay mineral treatment procedure, described below, NaCl, $CaCl_2$, and KCl salt solution were used (Merck, analytical grade), as well as purified deionised water. For all experimental set-up under anoxic conditions, de-oxygenated DI water and salt solutions were also used.

5.2.2 Preparation of oxidised and reduced homoionic NAu1

After grinding with a Retsch RM100 equipped with stainless steel mortar and pestle for 10 min, the final NAu1 powder was treated in order to acquire particle size <2 μm. The as received NAu1 was made homo-ionic with the three different cations Na^{+}, Ca^{2+}, and K^{+},with these materials given the name NAu1-Na, NAu1-Ca and NAu1-K, respectively. The procedure followed is an adapted method after, Jackson (1958), and described further in Section 3.3.2. Once prepared, homionic NAu1 samples were freezed-dried and stored in plastic vials.

After clay mineral pre-treatment was complete, 50% and 100% chemical reduction were performed in order to examine the hydration under these different controlled conditions. The chemical reduction was carried out following a method adapted from (Stucki et al., 1984a; Neumann et al., 2011). Clay mineral reduction was performed inside an anoxic chamber (GS Glovebox Systemtechnik GmbH; N_2: 100%, O_2 < 1 ppm) and using solutions that were deoxygenated for 2 h by bubbling with N_2 gas prior to transfer to the anoxic chamber. The chemical reduction involved a buffer solution containing 9 mM sodium citrate and 0.22 M sodium bicarbonate and was prepared in de-oxygenated DI water and heated to 70 °C. By adding excess sodium dithionite (1.5 g), corresponding to three times the clay mineral weight (0.5 g), close to 100% iron reduction was achieved, while for 50% iron reduction, the dithionite added corresponded to

the stoichiometry of the clay mineral iron content dithionite reaction. Clay mineral reduction extent was evaluated with Mössbauer Spectroscopy (See Section 3.3.3). After re-saturating the reduced clay solution with the respective cation with 1 M concentration solutions, (especially for the Ca^{2+} and K^{+} cases), dried reduced NAu1 samples were acquired by leaving the suspensions of NAu1-Na, NAu1-Ca and NAu1-K in the antechamber of the glovebox used, under vacuum, for sufficient time. (See Chapter 3 for reduction extent Mössbauer spectroscopy). The total number of samples is shown in Table 5.1. For M-IR, all redox states and cations were analysed, while for N-IR and water adsorption isotherms, only oxidised and 100% reduced samples were analysed.

5.2.3 Samples Nomenclature

The samples were named using the following system. The nontronite, NAu1, was Na+ exchanged (NAu1-Na); K^{+} exchanged (NAu1-K); Ca^{2+} exchanged (NAu1-Ca). For each of these clays, the state of reduction was either oxidised (e.g. Na-OX); part reduced (e.g. Na-50RED) or fully reduced (e.g. Na-100RED). The humidity state was given the labels: vacuum (vac); or RH%. For example: Ca-Vac-OX or K-RH30-100RED.

5.2.4 Infrared Spectroscopy Measurements

A Nicolet 8700 Infrared Spectrometer was used to acquire spectra in middle- and near-infrared wavenumber, in (pseudo) absorption Log(1/R) mode. The main purpose of these experiments was to research the different hydration induced by the presence of the three different cations, Na^{+}, Ca^{2+} and K^{+} on the surface and the interlayer of the NAu1 while under different conditions of reduction.

For the M-IR spectra, 10 mg of NAu1-Na, NAu1-Ca, NAu1-K was mixed with 190 mg of KBr, forming a diluted mixture of clay mineral with 5% w/w concentration, for oxidised, partially and fully reduced cases. For the N-IR spectra, the NAu1-Na, NAu1-Ca, NAu1-K samples filled the sample holder. Three different relative humidity (RH) levels were considered, RH = 10%, RH = 30% and RH = 70%, along with Vac = vacuum (of air / N_2). The relative humidity (RH) was controlled by a humidity control stage mounted on the spectrometer. The sample names were updated to reflect the RH, e.g. NAu1-Na-RH30-50RED was the sodium saturated nontronite, measured at 30% relative humidity and reduced to 50% of the Fe(III) being converted to Fe(II). The sequence of measured spectra consisted of:

$$Air \rightarrow N_2 \rightarrow RH70\% \rightarrow Vaccum \rightarrow RH10\% \rightarrow RH30\% \rightarrow RH70\%$$

which allowed the hydration-dehydration response of the clay mineral to be studied too. This sequence was followed for all measurements, apart from the reduced samples, with these starting from the 'N_2' step. For each step in the above process, 30 min equilibrium time was allowed in order to get a representative spectrum for each relative humidity % (RH%) condition applied.

Normalisation was performed, for the M-IR data, when spectra of different saturating cation are plotted together with the peak intensity at 1020 cm^{-1}, representing the Si-O stretching and the amount of clay mineral used, is used as equal to the maximum value and the absorption values at 4000 cm^{-1} as equal to the minimum value.

Additionally, background subtractions were utilised for the N-IR data, when comparing reduced *vs* oxidised data. This baseline subtraction is made for both, oxidised and reduced spectra using the OriginLab© Software (version 2019). A 'user defined' baseline determination was selected, for which 'anchor point' were found, 15 in number, with a 'second derivative (zeros)' method. Adjacent-Averaging smoothing is used with smoothing window size and threshold being kept at values of 3 and 0.5, respectively, auto-selection software values . Anchor point position was modified in order to achieve the best baseline possible, after a 'BSpline' interpolation method.

Water vapour adsorption isotherms

Water adsorption isotherms were taken in order to quantitatively examine the hydration of NAu1, with different cationic saturation and redox conditions. For these experiments accurately measured amount of the samples, varying from 40 mg to 70 mg were used. All isotherms were taken using a MicrotracBEL Belsorp-Max volumetric adsorption analyser equipped with three pressure sensors (133 kPa, 1.33 kPa and 13.3 Pa). In the case of the water vapour isotherm, a long acquisition time (7 days per isotherm) was required because of the slow equilibrium kinetics. Isotherms were acquired for the NAu1-Na,Ca,K oxidised & reduced. Samples were initially outgassed at 100 °C under vacuum (3.10 -6 Pa) during 20 hours.

The specific surface area was calculated from the water adsorption isotherm at 298 K by the Brunauer, Emmett and Teller (BET) method through multipoint calculation by choosing the result given by the best linear fit in the 0.1 to 0.3 P/P_0 range. The calculated BET specific surface areas (S_{BET}) for the adsorption branch are based on a classical adsorbate cross-sectional

Table 5.1: Nontronite-1 (NAu1) mineral cationic saturations and extent of reduction used in the infrared and water vapour isotherm measurements.

Samples	Clay mineral	Cation		
	NAu1	Na	Ca	K
	Redox State	Oxidised	50% reduced	100% reduced
Methods for all samples	MIR	✓	✓	✓
	NIR	✓		✓
	Water isothem	✓		✓

area (σ) for which a water molecule area of 14.8 Å^2 was used.

5.3 Results

5.3.1 NAu1 spectrum in IR

MIR Spectra of NAu1-Na-OX-Vac and NAu1-OX-Air

In Figure 5.1 the spectrum of NAu1-Na-OX acquired under vacuum is shown, for M-IR, from 550 cm^{-1} up to 4000cm^{-1}. For the wavenumber region of 550 cm^{-1} to 1200 cm^{-1}, main bands observed were the Fe-O out-of-plane vibration at 678 cm^{-1}, which is considered dignostic band for nontronites, but also may indicate tetahedral substitution, (Bishop et al. (2002) and references therein), with no tetrahedral Fe^{3+} measured in the NAu1 by Gates et al. (2002). The other key peaks were assigned as the $[Fe^{3+}]_2OH$ bending vibration at 821 cm^{-1} and then the Si-O vibrational envelope up to 1200 cm^{-1}, with the central peak at 1020 cm^{-1}. The peak at 843 cm^{-1} was attributed to $AlFe^{3+}OH$ (Frost, Kloprogge (2000) and references therein). Baron et al. (2016) associates peak 840 cm^{-1} to low content of tetrahedral Fe^{3+}, which shifts to higher wavenumbers with increasing content of tetrahedral iron. Nonetheless, the intensities of $[Fe^{3+}]_2OH$ and $AlFe^{3+}OH$ are determined from the Fe/Al ratio in the octahedral layer, or the Al substitution by Fe. In the NAu1 case, the substitution is almost complete, with a final Fe/Al ratio at 3.62/0.35 (per $O_{20}(OH)_4$), thus the former peak intensity is higher than the latter, (Gates, 2005).

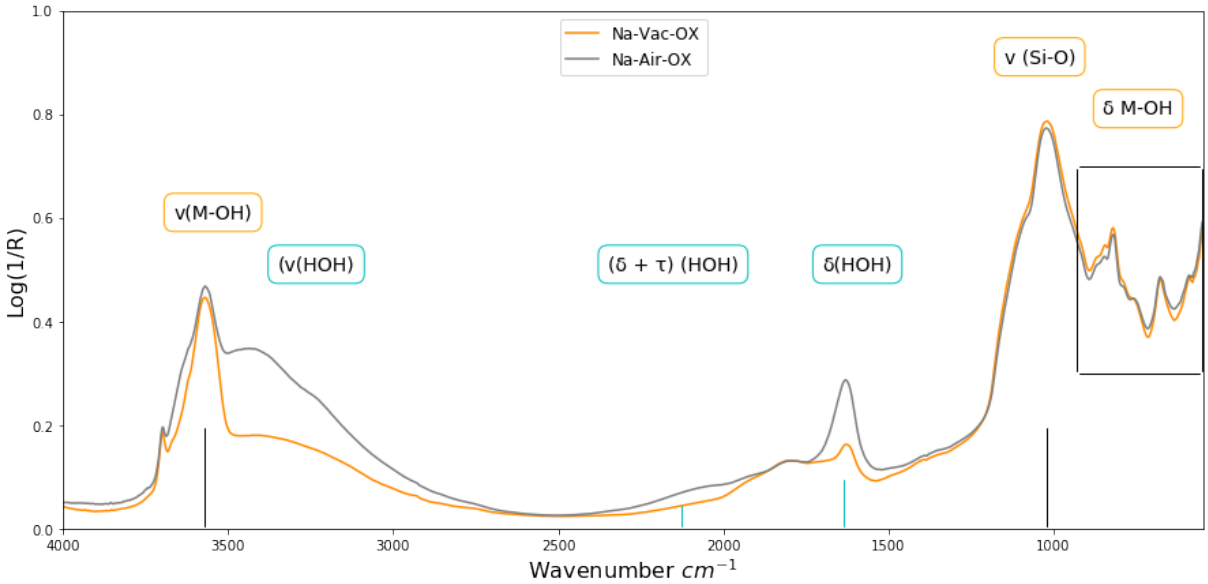

Figure 5.1: NAu1-Na vacuum (Vac) and air conditions spectra. Major annotations are plotted on the spectrum for identifying main NAu1 characteristics in M-IR.

The OH bending band was located at 1635 cm^{-1} representing water adsorption on the clay mineral. This region can stretch from below 1628 cm^{-1} up to 1680 cm^{-1}. The high-end wavenumber values correspond to cation-coordinated interlayer adsorbed water. Further deconvolution of the envelope reveals several components, with the wavenumbers at 1650 cm^{-1} corresponding to water in the cation hydration sphere and at 1635 cm^{-1} adsorbed water. Below this value, weakly hydrogen bonded water is allocated at 1613 cm^{-1}, (Frost et al., 2000; Frost, Kloprogge, 2000). At the 2127 cm^{-1} the lattice (τ) and bending vibration of water is located, but not very well identifiable at the vacuum spectrum, but in the 'Air' spectrum can be distinguished, Figure 5.1.

From 3000 to 3800 cm^{-1}, the main M-OH stretching band of nontronite overlapped with the adsorbed water stretching band. While the FeFeOH vibrated at 3570 cm^{-1}, the water stretching mode vibrated at lower frequencies of arounf 3490 cm^{-1} and 3285 cm^{-1} (Garfield nontronite in Fialips et al. (2002)). In the same region, other structural groupings can also vibrate for different Fe, Al, Mg configurations, (Fialips et al., 2002), which, however, may not be tha case for NAu1, as the Al^{3+} and Mg^{2+} content was very low in this case. Frost, Kloprogge (2000) recognised water stretching vibration at similar frequencies when they studied a ferruginous smectite and a nontronite. These vibrations were associated, by both studies, to water located in the interlayer and coordinated to cations present.

Despite NAu1 being grouped as a dioctahedral smectite, trioctahedral structures are present in the mineral, either as admixtures or possible structural differentiations of NAu1. For example, the position at 3700 cm^{-1} is associated with the tri-octahedral structure (v)M_3OH grouping, such as (v)$Mg_2Fe^{2+}OH$ or (v)Mg_2AlOH in biotites (micas) (Madejová et al., 2017).

NIR Spectra of NAu1-Na-Vac-OX and NAu1-Na-RH10-OX

In Figure 5.2 below, the N-IR spectrum range can be observed. At the low wavenumber region from 4000 cm^{-1} to 4500 cm^{-1} three main combinational vibration $(\delta + v)$ of OH are in the bands positioned at 4010 cm^{-1}, 4156 cm^{-1}, 4377 cm^{-1}. The first two are related to the band of 678 cm^{-1} Fe out-of-plane vibration (Bishop et al., 2002), the 4377 cm^{-1} is attributed to $(\delta + v)$ $[Fe]_2^{3+}OH$. A more subtle band exists at 4470 cm^{-1} and it was attributed to $(\delta + v)$ $AlFe^{3+}OH$ according to (Bishop et al., 2002) for Fe smectites, while (Frost et al., 2002) attributes this peak to $(\delta + v)$ $Fe^{3+}Fe^{3+}OH$, which varied from 4472 up to 5073 (for NAu1 in their study) for different Fe smectites. At band position of 5263 cm^{-1} was assigned as the combined vibration of water molecules ($(\delta + v)HOH$), with strong hydrogen bonding, (Johnston, 2017). Finally, at 6974 cm^{-1}, the hydroxyl stretching overtone (2v(OH)) was found, which was attributed to $[Fe^{3+}]_2OH$ grouping and reflecting the high Fe/Al ratio in this NAu1, (Madejová et al., 2017)

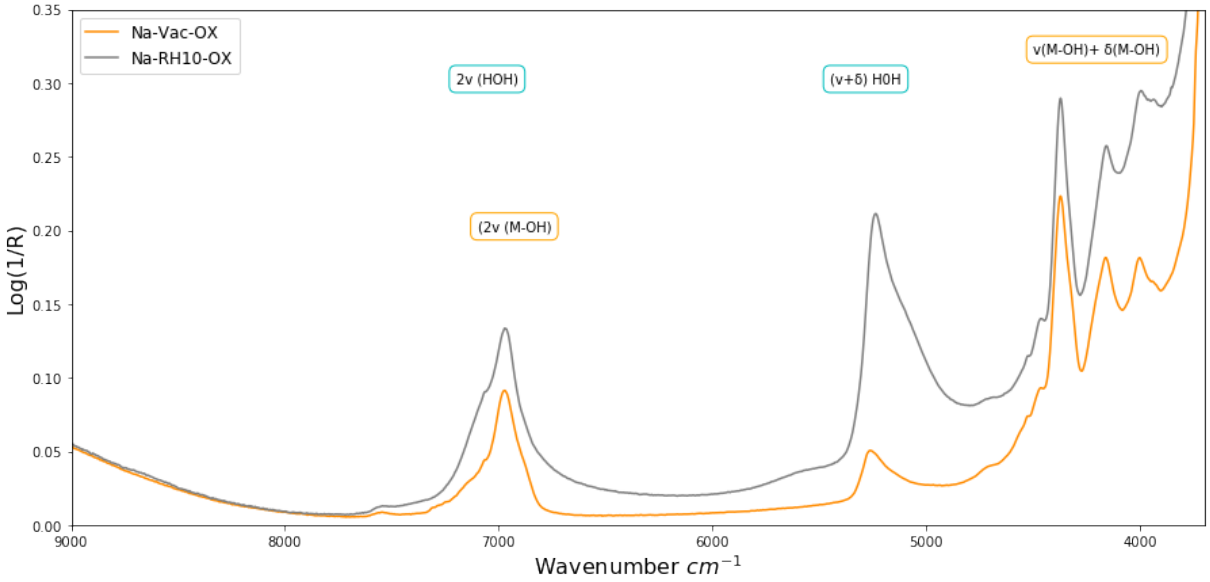

Figure 5.2: N-IR spectrum of NAu1-Na, under vacuum and oxidised conditions. Annotation of the major bands are plotted along the spectrum.

5.3.2 Water absorption induced changes in the M-IR spectrum of NAu1 with different cations and different redox states

MIR Spectra of NAu1-OX with Na^+, K^+ and Ca^{2+}, under different relative humidity conditions

In Figure 5.3 the infrared spectra of NAu1-Na-OX are plotted to give a first comparison of the effects of different relative humidity, vacuum (Vac), RH10% and RH70% induced in the clay mineral. More specifically, the water adsorption affected the 1635 cm^{-1} region the 2127 cm^{-1} and the 3000-3570 cm^{-1} region, with increasing intensities induced RH% increased. A similar trend would be expected when NAu1-Ca and NAu1-K are plotted (Appendix C, Figure C.2 and Figure C.3).

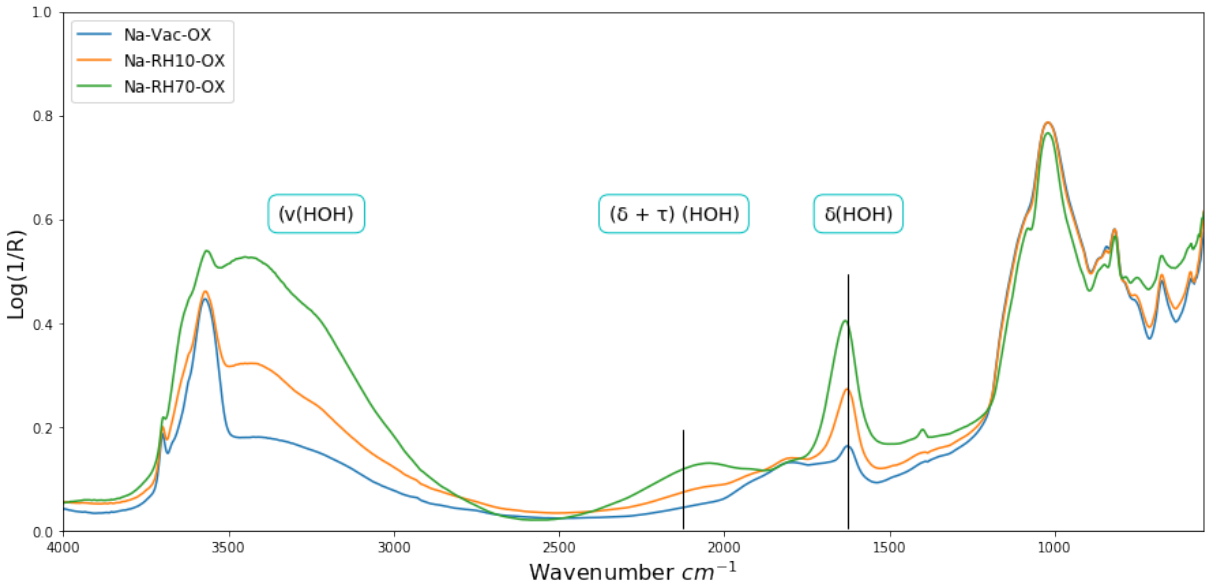

Figure 5.3: NAu1-Na spectra comparison under different relative humidity degrees,Vac RH10% and RH70%

In Figure 5.4, the NAu1-Na,Ca,K oxidised spectra are plotted for comparison, with the Vac spectra grouped at the bottom of the graph, while the RH70% spectra grouped higher with an offset. After normalisation, the hydration induced relative to the saturating cation can be examined. It can be seen that for the 3000-3700 cm^{-1} region, more water is adsorbed, when Ca^{2+} is present, at RH70%, followed by Na^+ and K^+. For the Vac spectra, the least water is remained in the clay structure, when potassium is present, increasing for Na^+ and Ca^{2+}. The same trend is viewed at the other two water-related band regions, where the bending (and lattice) of water

is located at 1635 cm^{-1} and 2127 cm^{-1}, respectively.

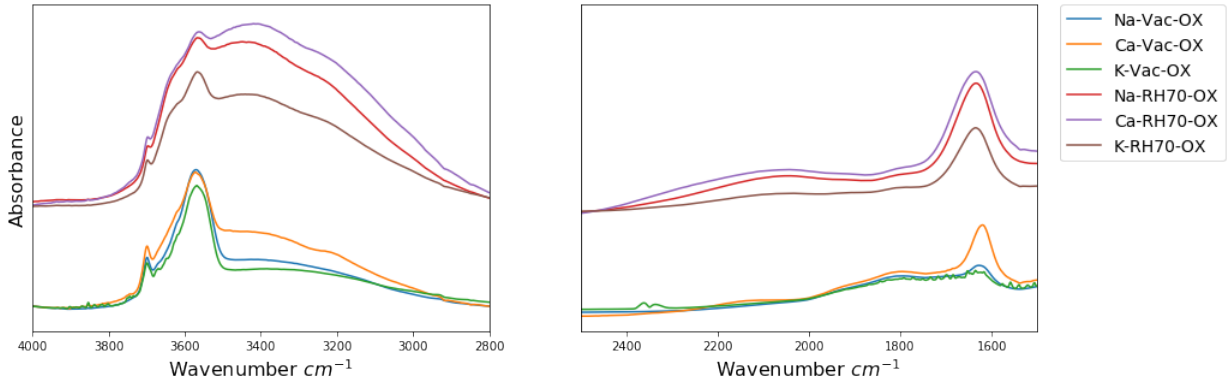

Figure 5.4: Cation and RH comparison at the water bending δ (H_2O) region. RH70% spectra are amplified artificially for depiction purposes

Investigating the δ (H_2O) region, a band shifting is observed on the centred 1635 cm^{-1} peak, which is different for each saturating cation examined. At Table 5.2 it is clear that the remaining water adsorbed under vacuum is bonded differently to water present under 70% relative humidity. As mentioned before, peak intensity below 1628 cm^{-1}, represents weakly hydrogen bonded adsorbed water, (Frost et al., 2000). That being the case, Ca^{2+} bound water under vacuum at 1619 cm^{-1} may be assigned to weakly bonded interlayer water. On the other hand, Na^+ and K^+, the case is the opposite, water is still hydrogen bonded under vacuum. However, when looking at the wavenumber values for the RH70% spectra, hydration behaves at a similar way, in terms of bonding, irrespective of cation identity. All fall in the category of adsorbed water. Regarding the absorption values, Ca^{2+} induces more water than Na^+ and K^+, with K^+ adsorbing the least.

The combination band of $(\delta + \tau)$ H_2O shows an increased intensity at the area of 2127 cm^{-1}, comparing the vacuum and the RH70% spectra. Even though exhibiting rather wide envelope, same hydration trend for each of the cations was indicated.

Table 5.2: δ (H_2O) peak intensities, relative-to-Na intensities and wavenumber values for vacuum and RH70% spectra.

Spectrum	Wavenumber cm^{-1}	Absorption (Log(1/R))	Relative-to-Na absorption
Na-Vac	1628	0.1631	1
Ca-Vac	1619	0.3237	1.984
K-Vac	1635	0.1431	0.877
Na- RH70	1634	0.4872	1
Ca- RH70	1634	0.5333	1.094
K- RH70	1634	0.3099	0.636

MIR Spectra of NAu1 with Na^+, K^+ and Ca^{2+}, under different relative humidity conditions: effect of reduction

Samples of 50% and 100% reduction degree were also tested, examining the cationic hydration effects on the NAu1. Super-imposing the spectra of the three redox state and three cations in various combinations interesting observation can be made.

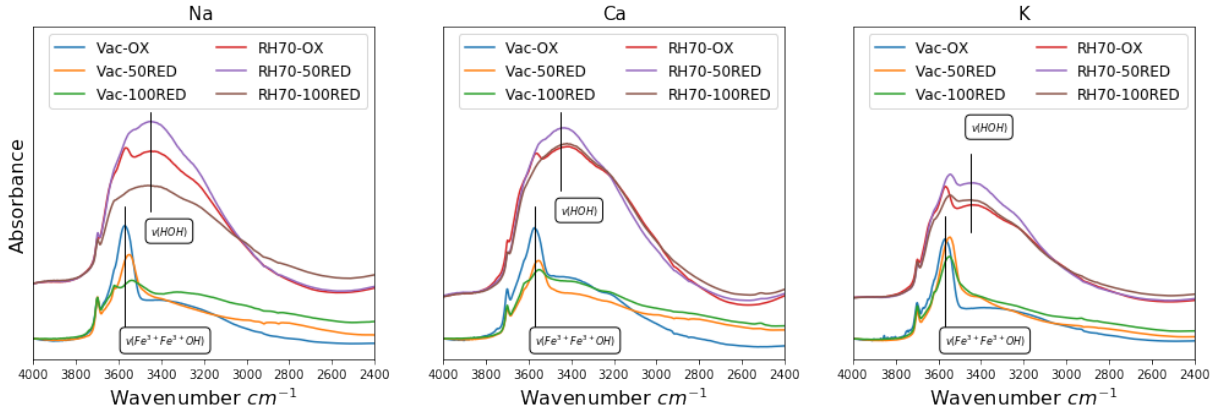

Figure 5.5: NAu1 spectra in oxidised, 50% reduced and 100% reduced state, categorised after cation saturation.Annotated are the stretching $Fe^{3+}Fe^{3+}OH$ band at 3570 cm^{-1} and the stretching HOH adsorbed water band at 3450 cm^{-1}

In Figure 5.5 each of the graphs showing NAu-1 with Na^+, Ca^{2+} and K^+ shows the water intake, for each of the three redox states, depending on the cation present in the clay mineral for the 3000-3800 cm^{-1}. For the Na^+ case and under vacuum (Vac) conditions, the FeFe-OH peak at 3570 cm^{-1} vibrates in gradually lower wavenumbers, upon reduction, and the absorption intensity decreases, as the Fe^{3+} becomes Fe^{2+} in the mineral structure. Under RH70% it can be

observed that the hydration, acts differently for the three different degrees of reduction. When compared to NAu1-Na-RH70-OX, the NAu1-Na-RH70-50RED shows higher hydration, while NAu1-Na-RH70-RED100 shows the least hydration. A similar pattern can be seen for the Ca^{2+} and K^{+} exchanged NAu1, at which the 50% reduced NAu1 water intake was greater than the oxidized, and the 100% reduced NAu1 equivalent dropped back to equal or lower water quantity as in the corresponding oxidised homo-ionic NAu1. Mössbauer data for these partially and fully reduced samples show reduction degrees of, 35% and 85%, respectively. However, re-oxidation may have occurred during sample mounting on the IR, which is more apparent for the NAu1-Ca-100RED and NAu1-K-100RED samples, judging from the shifting of the 3570 cm^{-1} peak.

Focusing more on the Na^{+} and Ca^{2+} cases in Figure 5.6, the hydration extent difference is exaggerated when the NAu1 is fully reduced. For the oxidised (OX) and 50% reduction (50RED) samples, the hydration induced can be considered quite similar when at RH70%. Under vacuum, Ca^{2+} retains more water in the mineral structures for all three redox conditions. (See Appendix C for Na^{+}, Ca^{2+} and K^{+} comparison, Figure C.4).

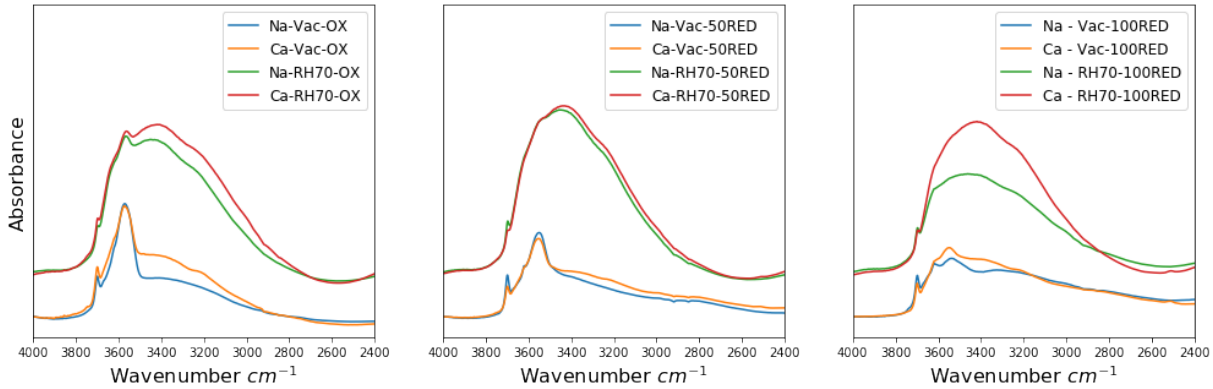

Figure 5.6: NAu1-Na (Na) vs NAu1-Ca (Ca) induced hydration under oxidised, 50% reduced and 100% reduced state. Higher hydration difference is observed under fully reduced conditions.

In Table 5.3, the (δ) OH wavenumber shifting is gathered for the cation cases of sodium and calcium. H_2O-bending is not greatly affected by the clay mineral reduction. The associated band positions shift the same for all redox states, for each cation individually.

Table 5.3: Wavenumber band shifting for (δ) OH, regarding Na and Ca cation clay saturation under vacuum and RH70%, for all redox states considered.

		Wavenumber(cm^{-1}) shifting		
Redox state	RH	NAu1-Na	NAu1-Ca	NAu1-K
		(δ) OH	(δ) OH	(δ) OH
Oxidised	Vacuum	1628	1619	1635
	RH70%	1634	1634	1634
Reduced	Vacuum	1627	1622	1628
50%	RH70%	1634	1634	1634
Reduced	Vacuum	1629	1620	1630
100%	RH70%	1634	1634	1634

5.3.3 Water absorption in N-IR spectrum

NIR Spectra of NAu1-OX with Na^+, K^+ and Ca^{2+}, under different relative humidity conditions

The near infrared spectral region is useful for studying the effects of induced hydration in clay minerals, as the water content can be compared without overlapping interferences from structural features, at the combination region at around 5000 to 5200 cm^{-1}. variable degrees of relative humidity were induced in NAu1-Na-OX, with notable water changes in the spectra(Appendix, Figures C.6 & C.7 for NAu1-Ca-OX and NAu1-K-OX). At the water vibrational region, the peak intensity increases, as expected, while its position was shifted from 5263 cm^{-1}, under vacuum, to 5240 cm^{-1} under RH70%. At the same time, in the overtone region, a second, more subtle peak appears at 7070 cm^{-1}, which is amplified in relation to the vacuum spectrum and is attributed to (2v)AlFe^{3+}OH (Frost et al., 2002; Madejová et al., 2017)

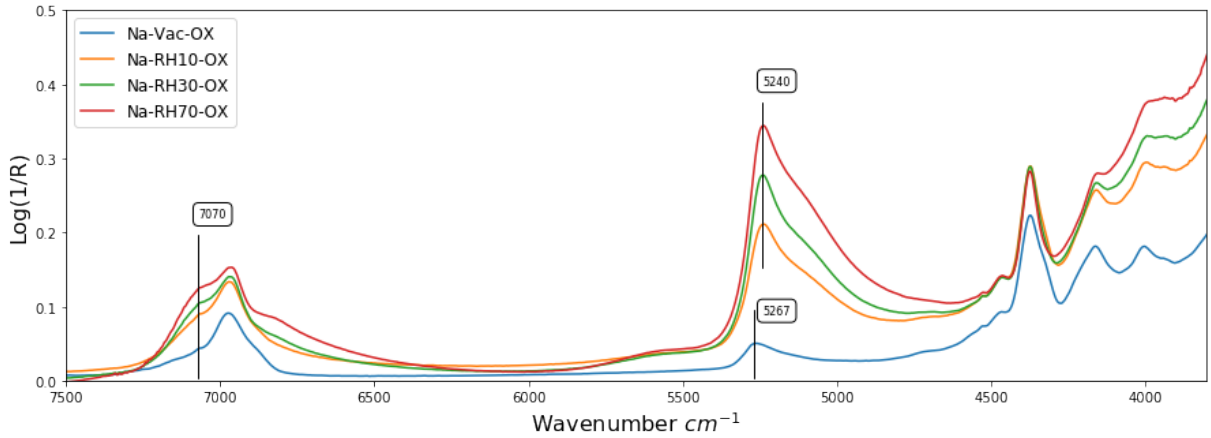

Figure 5.7: Relative humidity spectra of NAu1-Na. Relative humidity degrees at vacuum, 10%, 30% and 70%. Annotated are the key affected bands: the 5267 cm^{-1} adsorbed water overtone band (blue spectrum), which evolves to the 5240 cm^{-1} upon hydration (orange, green, red spectra), as well as the 7070 cm^{-1} overtone band, which increases in relative intensity upon hydration.

NIR Spectra of NAu1 with Na^+, K^+ and Ca^{2+}, under different relative humidity conditions: effect of reduction

In order to put cation hydration into perspective, a comparison was made, across the different cations, under oxidised and 100% reduced conditions. In Figure 5.8, all the different cationic hydration was plotted for vacuum and RH70% conditions. Under vacuum, relatively more water is retained, rather weakly bonded, when Ca^{2+} was present (Ca-Vac-OX), while the least water was retained, when K^+ was saturating the clay mineral. The same trend was shown for the second case with higher intensities for all three cations. The slight band shifting positions at the 5200 cm^{-1} region identified in Figure 5.7, for Na^+, was the same for Ca^{2+} and K^+, shown in the Appendix C, Figure C.6 and Figure C.5, of this chapter.

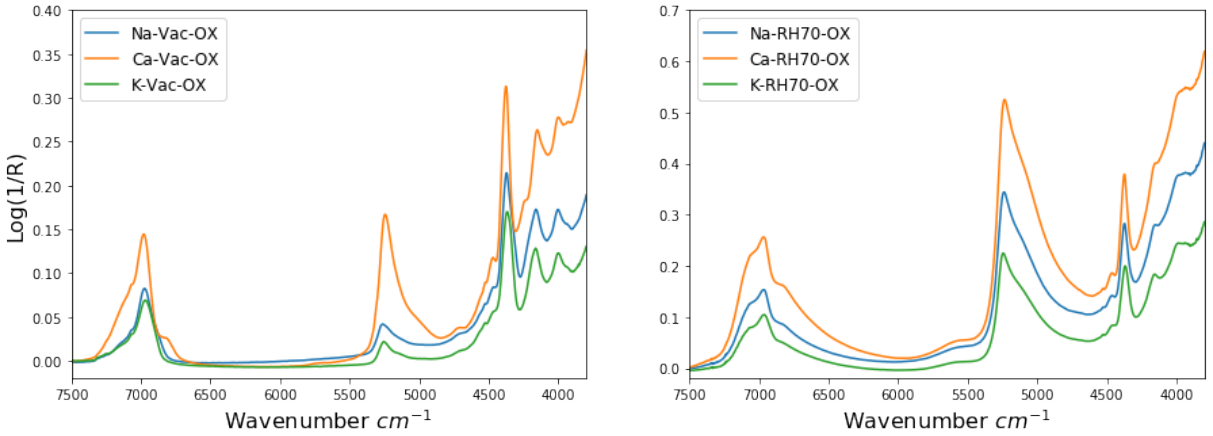

Figure 5.8: Spectra showing the cross-cation (Na, Ca, K) relative humidity comparison of NAu1. On the left-hand side the vacuum spectra and on the right-hand side the RH70% spectra are shown

Measuring NIR spectra on reduced nontronites can be challenging, due to their dark colours (dark green) upon reduction. Because of that, absorption occurred from higher wavenumbers, and created a high background on the spectra (Appendix C, Figures C.5 & C.6 & C.7). In order to compare oxidised and reduced spectra, this background was subtracted to qualitatively observe the hydration differences. In Figure 5.9 the relative hydration, Vac and RH70% samples are shown for each of the saturating cations, under reduced conditiotns, and in in Figure 5.10, the NAu1-Na,under oxidised *vs* reduced conditions is compared, too. At the first comparative graph, some retained hydration was observed, when Ca^{2+} (Ca-Vac-OX) was present in the clay mineral, under vacuum, while for RH70% the 5220 cm^{-1} band appeared to be sharp, exhibiting a down-shift of 20 cm^{-1} with respect to the oxidised cases (Figure. 5.8). This observation is more clear at Figure 5.10, looking at the Na-RH70-OX and Na-RH70-100RED, in the same wavenumber region, (red and green line). Regarding the hydration extent, in Figure 5.10, at the region of 5220 cm^{-1}, no hydration retention was observed, for the reduced NAu1-Na, when comparing the Na-Vac-OX versus Na-Vac-100RED, while at RH70% the reduced spectrum Na-RH70-100RED showed lower hydration extent than the oxidised Na-RH70-OX. While the 7000 cm^{-1} OH-stretching overtone region, showed a hydration dependence on Figure 5.7, for the oxidised NAu1-Na, under the 100% reduced conditions, no vibration occurred, (See Appendix, Figure C.8 for Ca^{2+} and K^{+}, OX *vs* 100RED comparison).

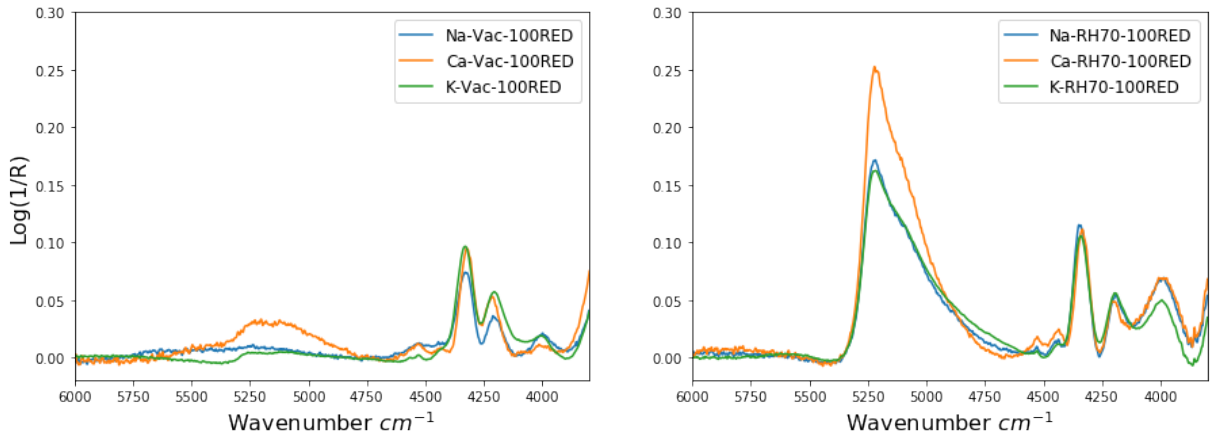

Figure 5.9: Cation comparison vacuum (left) and relative humidity of 70% (right), under reduced conditions.

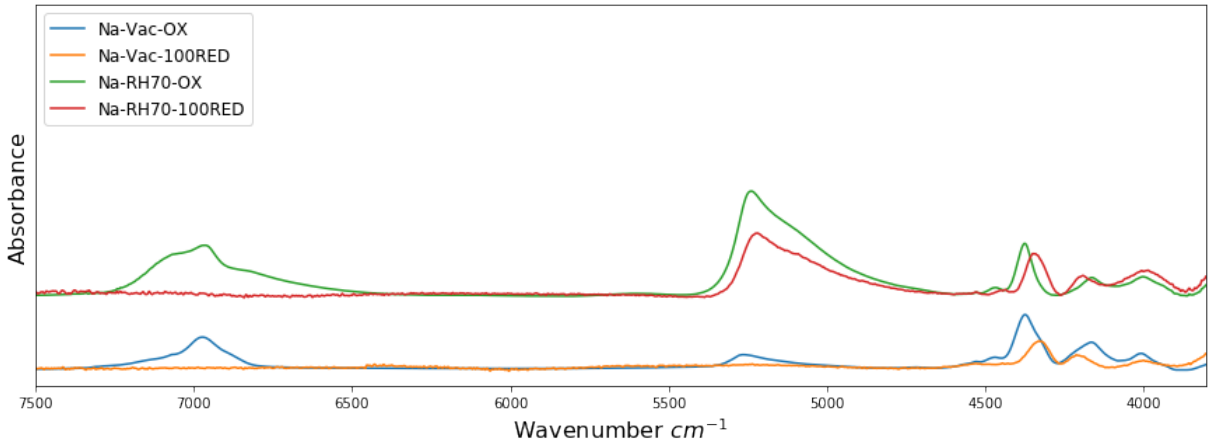

Figure 5.10: NAu1-Na comparison under oxidised and 100% reduced conditions, for vacuum and 70% induced humidity. Same trends are observed for Ca and K cases.

Furthermore, at the low end of the NIR spectrum, the structural grouping band shifting also occured. The band of 4010 cm^{-1} downshifted to 3999 cm^{-1} , while the 4156 cm^{-1} was up-shifted to 4210 cm^{-1}. The 4377 cm^{-1} is down-shifted to 4320 cm^{-1} (for vacuum spectra) or 4343 cm^{-1} (for RH70% spectra) and the 4470 cm^{-1} seemed to be extremely low to non-existent under these reduced conditions. However, absolute values of shifting observations should be approached with caution, as they may be affected by the baseline readjustment. Nonetheless, it is clear reduction caused shifting on these overtone (v+δ) M-OH vibrating bands, (Neumann et al., 2011).

5.3.4 Water vapour adsorption isotherms

Although, infrared spectroscopy is a very useful and widely used technique for identifying molecular interactions within the clay mineral structure and specific clay mineral-water interactions, it cannot give quantitative results regarding the absolute amounts of water cumulatively held by the clay mineral in its different sites, basal plane, edge site and interlayer. For that reason, water vapour adsorption - desorption isotherms were utilised to directly address that matter.

In Figure 5.11 the water adsorption/desorption isotherms of NAu1 are presented, for each cation-saturation case, Na^+, Ca^{2+}, K^+, under oxidised and reduced conditions, obtained by water vapour volumetry.

Table 5.4: BET Surface Area and energetic constant from water isotherms at 298 K, for the homoionic NAu1, reduced and oxidised

	BET		
Samples	V_m (cm^3/g STP)	S_{BET} (m^2/g)	C_{BET}
NAu1-Na	93	370	6.4
NAu1-Ca	157	624	13.2
NAu1-K	67	267	6.6
NAu1-Na (100% RED)	87	347	6.6
NAu1-Ca (100% RED)	140	558	20.2
NAu1-K (100% RED)	58	233	8.4

V_m= volume of vapour adsorbed at standard temperature pressure (STP) per gram of dry sample
S_{BET}= specific surface area
C_{BET}=dimensionless constant related to the enthalpy of adsorption of the adsorbate vapour on the powder sample

For the oxidised NAu1-Na, the adsorption path was close to a Type III (after the IUPAC classification, (Thommes et al., 2015)). The desorption path exhibited hysteresis especially at the mid-to-lower pressures accounting for a H3 hysteresis loop type (after IUPAC classification). Same observations was made for the oxidised NAu1-K. Regarding the NAu1-Ca oxidised case, the water vapour adsorption had a Type II shape, with no knee point at low pressures. Although the monovalent Na^+, K^+ and the divalent Ca^{2+} have different adsorption/desorption shapes in the isotherms, all three cases did not have a distinctive monolayer-to-multilayer hydration profile. In addition, the adsorbed multilayer thickness of NAu1-Na and NAu1-K cases seem to increase indefinitely after P/P_0 =1.

In terms of absolute water volume (V_m) NAu1-Ca was hydrated more than NAu1-Na and NAu1-K, with values up to 157 cm^3/g (Table 5.4), with NAu1-Na having the highest hydration

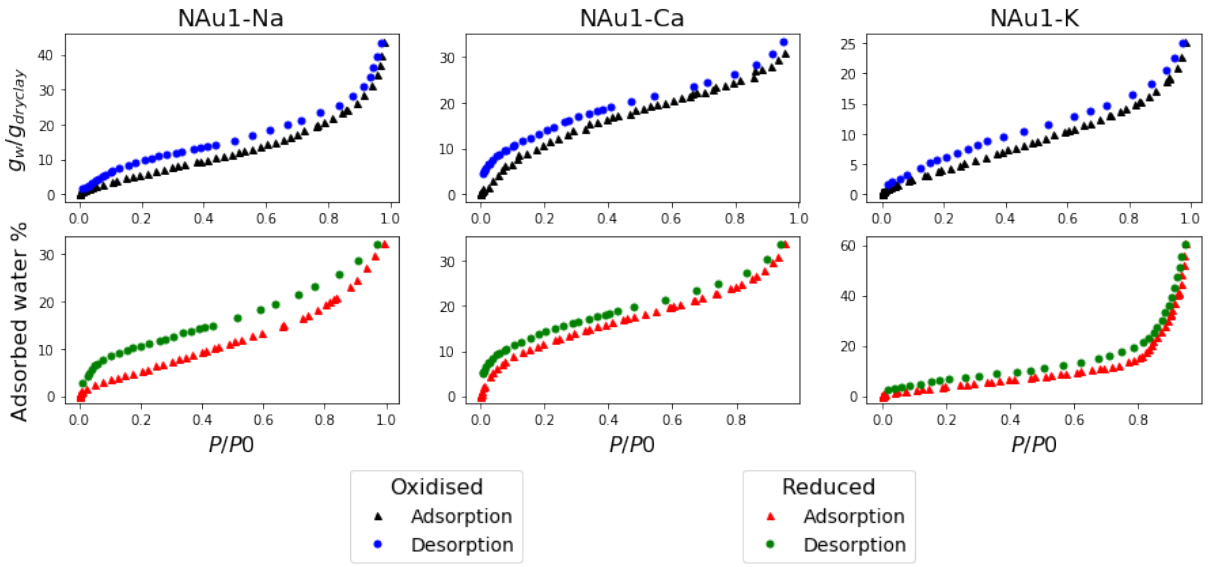

Figure 5.11: Water vapour isotherms of NAu1-Na, NAu1-Ca and NAu1-K, under oxidised and 100% reduced conditions. For oxidised conditions black triangles denote water adsorption and blue dots water desorption and for reduced conditions, red triangles denote water adsorption and green dots water desorption.

extent, above 40%, at P/P_0 =1, Figure 5.11. The specific surface area (S_{BET}) of NAu1-Ca was the highest, followed by the NAu1-Na and NAu1-K. A high (C_{BET}) energy constant means a stronger water affinity, with Nau1-Ca having the highest, Table 5.4.

Looking at the graphs for the different NAu1-RED samples, given in the second row of Figure 5.11, the NAu1-Na adsorption/desorption paths had the same shape, with more hysteresis induced at the lower pressures P/P_0. The NAu1-Ca exhibited a slight more distinctive knee point at around P/P_0 =0.1, indicating a monolayer coverage first, before multilayer water adsorption, accompanied with little changes at the hysteresis loop. NAu1-K had a low hydration/dehydration rate, with a kick point at P/P_0 =0.8 where the hydration/dehydration rate increases dramatically. All three cases show no limits on the adsorbed multilayer thickness at P/P_0 =1

The calculated specific surface area (S_{BET}) of all reduced samples showed lower values than the oxidised counterparts, as well as the overall adsorbed water vapour volumes V_m. However the water affinity, indicated by the C_{BET} energy constant values, increased for all three cases.

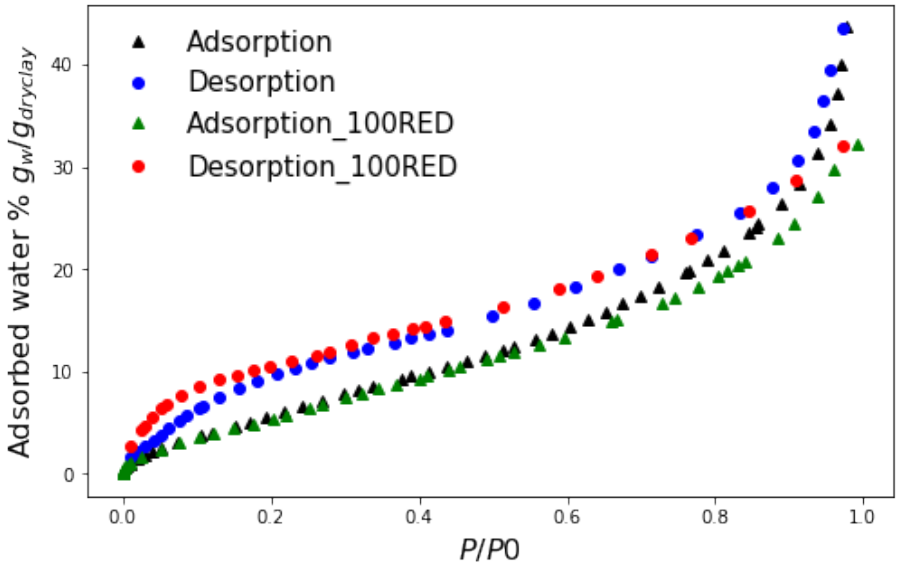

Figure 5.12: Water vapour isotherms for Na-NAu1 samples under oxidised (black and blue), and reduced (green and red) conditions.

In Figure 5.12 an oxidised *vs* reduced NAu1-Na comparison was made. Reduced adsorption-desorption paths had a higher hysteresis than the oxidised ones. For the adsorption paths of the oxidised *vs* reduced sample, there was a good matching up to 0.6 P/P_0 value, where they diverged, with reduced sample adsorbing 10% less water, (end of green line).The desorption paths were matching from 0.8 to 0.2 P/P_0 values, where the water intake hysteresis was amplified below 0.2 P/P_0, comparing the blue (oxidised) and red (reduced) lines on the graph.

5.4 Discussion

5.4.1 Preparation of cation exchanged and reduced samples

In this study, cation exchanged, homoionic (Na^+, Ca^{2+}, K^+) NAu1 was used in order to study the effects that cation-induced hydration would have on the clay mineral. Using XPS analysis, as described in Chapter 3, the homo-ionisation extent was determined, revealing that the oxidised samples of NAu1-Na, NAu1-Ca, and in extension the NAu1-K, were saturated only by the cation indicated. Regarding the reduced samples, it was expected that some Na^+ would be adsorbed/ exchanged during the reduction process, as Na-salts were used, affecting the homo-ionic nature of NAu1-Ca and NAu1-K. For that reason, a Ca^{2+} and K^+ re-saturation step was performed to minimise this effect. Nonetheless, in Khaled, Stucki (1991), the homo-ionisation process was

performed after the reduction process, even if it was established that iron reduction in iron-rich clay minerals will cause interlayer collapse, potentially hindering cation exchange processes.

Reduction extent was verified with Mössbauer spectroscopy, a method detailed in Chapter 3. Partially reduced samples showed a 30-35% iron reduction extent, (noted as 50RED in this study for convenience), while fully reduced samples showed a 90% iron reduction extent, (noted as 100RED). Respective Mössbauer data can be viewed at Chapter 3, Section 3.3.5.

Reduction extent can also be appreciated in a more qualitative way by looking at the IR spectrum for NAu1-Na, NAu1-Ca, and NAu1-K, in the region 3500-3600 cm^{-1}, as shown in Figure 5.5. The peak of 3570 cm^{-1}, associated to $Fe^{3+}Fe^{3+}OH$ vibration grouping, changed in position and relative intensity, upon reduction, in iron-rich minerals, by shifting to lower wavenumber and decreasing its intensity. These changes have been described extensively in Fialips et al. (2002); Claire et al. (2002), among others. In the same manner, the shifting of the 3570 cm^{-1} band in iron-rich clay minerals can be used to identify reduction-reoxidation, when reduction process reversibility was studied (Claire et al., 2002). In Figure 5.5, it was observed that the NAu1-Na spectra showed a gradual downshifting of the 3570 cm^{-1} band, (blue to orange to green spectra), while the NAu1-K spectra of partially and fully reduced cases (orange and green respectively) vibrate almost at the same wavenumber, indicating the reduced samples were partially re-oxidised. This re-oxidation can barely be distinguished for NAu1-Ca, at the same figure (Fig. 5.5). This re-oxidation however, should not be connected to the nature of saturating cation, but rather an unwanted experimental artefact.

5.4.2 Effect of cation and effect of oxidation on water isotherms

Interpreting the water vapour adsorption data, it was observed that the oxidised NAu1-Ca had a higher overall hydration than NAu1-Na and NAu1-K. These two samples exhibited similar adsorption-desorption patterns, with NAu1-Na sample having a higher hydration extent at P/P_0=1, Figure 5.11. These observations can be fundamentally connected to the interlayer expansion or not, that different cations induce in the clay mineral as well as the hydration enthalpy. Ca^{2+} has the highest hydration enthalpy, K^+ the lowest enthalpy, causing stronger interaction between clay mineral platelets, and Na^+ induces clay mineral swelling.

Water vapour adsorption isotherms exhibited dehydration effects upon reduction of the NAu1, as shown in Figure 5.12, where NAu1-Na oxidised and reduced isotherms are plotted together

for comparison. At P/P_0=1 values, the reduced sample NAu1-Na had less water intake than the oxidised counterpart, while the NAu1-Ca had almost the same, with the reduced NAu1-K exhibiting a opposite trend than the other two, having held higher amount of water vapour. At the same time, less amount of water (Vm) was adsorbed, as shown at Table 5.4. Despite that, the C_{BET} parameter, increases upon reduction, indicating a stronger clay mineral water interaction. One indication of this clay mineral- water interaction can be seen at Figure 12 where at 0 - 0.1 P/P_0, more water was held in the reduced than the oxidised sample, on the desorption path (red dots). This may be attributed to the higher negative charges that govern the clay mineral resulting to it maintaining a water film around it, or that due to interlayer collapse (Stucki (2006) and references therein), cations are inaccessible and water is trapped in that space, causing hysteresis in the hydration-dehydration process, (Verburg, Baveye, 1994; Stucki, 2011). Other studies suggest this hysteresis may be due to charged Al complexes, related to the reduction process, that may block access to the interlayer space, (Heller-Kallai, 1997). This subtle increased hydration can also be identified from the vacuum IR data, Figure 5.6, as already pointed out by Stucki (2011), and references therein, and is discussed further below.

At Table 5.4, changes of the specific surface area (SSA) were also reported, based on the adsorption of the water vapour molecules on the clay mineral surface. The SSA was decreased upon reduction, indicating less available space for adsorbing water molecules. This change of SSA upon reduction was also observed by Lear, Stucki (1989), when tested with treated and homoinised -Na clay mineral. In conclusion, NAu1 has less available space for adsorbing water, regardless of saturating cation identity; water which is more attracted on the clay mineral.

5.4.3 Infrared spectroscopy analysis of structural changes in NAu1 layers upon reduction

Summarising the IR data regarding, the structural changes NAu1 undergone upon reduction, two main observation can be made. The 843 cm^{-1} band could be attributed to AlFe-OH grouping as its absorption intensity is readily decreased even at 50% reduction, Figure C.1 (Appendix C). Similarly, at the N-IR range, the absorption bands at 7000 cm^{-1} are aso disappeared upon reduction, at 100% degree, (with no 50% reduction data acquired). Hence, these bands should be associated to (2v)$Fe^{3+}Fe^{3+}$OH grouping, for the particular NAu1 used.

5.4.4 Cation exchange effects on M-IR samples under vacuum: cation related bonds

Examining the Figure 5.4, Table 5.2 and Table 5.3, it can be seen that there is a cation dependence on the vibration of the 1627 cm^{-1}, under vacuum conditions, across the three redox states. For the oxidised samples (Table 5.2), the sequence of increasing wavenumber vibration was $Ca^{2+} < Na^{+} < K^{+}$. This can be indicative of the bond strength between the clay mineral (di-trigonal cavity or surface charged sites) and the saturating cation. It has been modelled that the position of each of those cations, above the trigonal cavity differs, with K+ situated inside the cavity, Na^{+} placed above the cavity, and Ca^{2+} occupying a position on the side of the cavity, in between charged sites (Underwood et al., 2016). This variation is depicted on the MIR spectrum, where higher wavenumber oscillation, as in this case, can be related to interaction strength. Knowing that K^{+} has a very small hydration shell, in respect to Ca^{2+} and Na^{+}, and its relative position within the interlayer causing closer interaction between clay platelet, it is logical to see increased wavenumber of vibration.

At Table 5.3, the wavenumber of vibration for each cation varied across the redox states, with NAu1-Na oscillating almost constantly at 1628 cm^{-1}, NAu1-Ca increasing from 1619 (oxidised) to 1622 (partially reduced) to 1620 cm^{-1} (fully reduced), and NAu1-K vibrating from 1635 to 1628 to 1630 cm^{-1}, all under vacuum conditions. When, for example, partial reduction state is examined, it can be seen that NAu1-Ca vibrates at lower wavenumber than NAu1-Na and NAu1-K, an observation that takes place for the fully reduced state, too. It is interesting though that while NAu1-Ca slightly increased its vibration across redox states, NAu1-K slightly decreased its vibration.

Nonetheless, vacuum conditions do not always mean totally dry conditions, unless heated, which means cation hydration shell water can interfere at this particular band, as it is discussed next.

5.4.5 Understanding the effect of cation exchange on hydration in reduced and oxidised NAu1

The IR data showed changes due to hydration in three spectral areas; the δ(HOH)region at 1630 cm^{-1}, the (δ + τ) (HOH) region and the the v(OH) + the v(H0H) region at 3000 cm^{-1} - 3800 cm^{-1}. (Figure 5.3 and Figure 5.4) While the two first are related only by the water

adsorbed, the third arises as due to the overlap of structural OH and adsorbed water. This has implications for quantitatively, analysing the hydration data, however a clear trend can be derived as for the cation-induced hydration. In terms of the amount of water present, the trend for the cations studies was $K^+ < Na^+ < Ca^{2+}$, which is a familiar trend in clay mineralogy with respect to hydration and cation selectivity. For the water bending (δ) region, shift of the band to higher wavenumbers (up-shift) was observed, when humidity was introduced from 1619 cm^{-1} (Ca^{2+}),1628 cm^{-1} (Na^+), 1635 cm^{-1} (K^+) to 1634 cm^{-1} for all cases, Table 5.2. The actual cm^{-1} of the prior and post hydration is associated with adsorbed water or water bonded with the cations present, (Frost, Kloprogge, 2000; Frost et al., 2002). This band shifting is not observed on the stretching region, being a quite wide envelope, with two different stretching structures being read from the spectrometer, (Figure 5.4).

Similar observations, in terms of cation hydration extent with RH% incremental increase, is observed for the 50% and 100% reduced samples (See Appendix, Figures C.1, C.2, C.3), when compared exclusively; cation-induced hydration extent has the same increasing sequence. When the different redox states are compared all together, (Figure 5.5 and Figure 5.6), it was found that hydration extent increased for the 50% reduced samples, for all cation cases, and then decreased again for the 100% reduced samples, below the oxidised hydration samples. Looking at the v(OH) band for the NAu1-Na, under vacuum, at Figure 5.5, we can see that the 3570 cm^{-1} intensity decreases as well as the wavenumber position down-shifts, gradually for higher reduction degrees, both a spectral fingerprint of the changes taking place during the reduction. In particular, effects due to the de-hydroxylation of the clay mineral for negative charge compensation the *cis*-to-*trans* site Fe^{2+} migration (Manceau et al., 2000a).

When the samples are at a relative humidity of RH70%, the hydration extent increased for the 50% samples, seen at Figure 5.5, which is probably observed for the first time. During the first stages of reduction, the clay mineral compensated the increase of negative charges, (created through $Fe^{3+} \rightarrow Fe^{2+}$ change), by adsorbing more cations on its sites, eventually increasing its cation exchange capacity (CEC), (Stucki, Roth, 1977; Stucki et al., 1984a). As such, there is a reduction degree boundary, where the clay mineral is at its highest hydration state. Eventually, when 100% reduction takes place, the clay mineral is dehydrated and the interlayer collapsed (Stucki, 2006). This hydration behaviour is most clear, when the clay mineral is sodium saturated, with NAu1-Ca and NAu1-K displaying less of this effect, either due to different hydration

enthalpy of these cations or due to the re-oxidisation, noted earlier. In Figure 5.6, the hydration extent of Na^+, Ca^{2+} are very similar, for the oxidised and 50% reduced sample, while the dehydration is more amplified when Na is present at 100% reduced sample.

In an attempt to better explain the NAu1-Na hydration behaviour, the reduction model of Manceau et al. (2000b,a); Drits, Manceau (2000) was considered. Initially, the clay mineral will adsorb Na^+ from the reducing solution for charge compensation. When the tri-octahedral structure start to form, the negative charges will increase even more, de-hydroxylation takes places to compensate the charges. However, this is not continued indefinitely, as the Fe^{2+} should keep its six-fold coordination, eventually, achieved by new hydroxyls being created. In order for this to be achieved the mineral adsorbs protons (H^+), by the dissociated water in the tri-octahedral spaces created, bonded with the under-saturated O_{ext} groups forming new hydroxyl
.

The oxidised NAu1 has a structural formula of (Keeling et al., 2000)

$$Na_{1.05}(Si_{6.98}Al_{1.02})(Fe^{3+}_{3.68}Al_{0.29}Mg_{0.04})O_{20}(OH)_4$$

According to the above-described proposed model, the total sorbed cations during reduction can be calculated with the equation

$$m = p + n$$

where p, n are Na^+ and H^+, respectively, (Drits, Manceau, 2000). The reduced structural formula can be derived by

$$Na_{1.05+p}(Si_{6.98}Al_{1.02})(Fe^{3+}_{3.68-m}Fe^{2+}_{m}Al_{0.29}Mg_{0.04})O_{20}(OH)_{4-n}$$

Because parameters m, p, and n are denoting negative (m) and positive (p, n) charges in the mineral structure, the amount of m charges created corresponds to the Fe^{2+} and the same amount should be subtracted from the Fe^{3+}, as well as p is added to the total Na^+ amount. The total amount of n is considered, at this point, being consumed for the dehydroxylation of the mineral, at high reduction degrees.

Additionally, p and n are depended by the reduction level which leads to the following equa-

tions for calculating their value.

$$p = m_{rel} m_{tot} / (1 + K_0 m_{rel})$$

and

$$n = K_0 m_{rel}^2 m_{tot} / (1 + K_0 m_{rel})$$

with $m_{rel} \leq 1$ denoting the reduction degree, the m_{tot} the total iron content and the K_0 a positive sample-depended constant, the value of which depends on the m_{tot} and the oxidised cation exchange capacity (CEC) of the clay mineral. The relations governing the K, m_{tot} and CEC in smectites (with the exception of montmorillonite) are given by (Drits, Manceau, 2000)

$$K_r = 9.32 - 1.06 m_{tot} + 0.02 m_{tot}^2$$

and

$$K_r = K_0 / CEC$$

Taking into consideration the above formulae the sorbed Na^+ and H^+ can be calculated for any reduction degree, with this case being at 50% and close to 100%. At table 5.5 the resulted values can be evaluated.

Table 5.5: NAu1 calculations for Na^+ - p and H^+ - n sorption after partial and full reduction

NAu1			
Total Fe content	m_{tot}	3.68	
Cation exchange capacity	CEC	1.05	
	K_r	5.69	
	K_0	5.97	
Reduction degree	m_{rel}	0.5	0.9
Sorbed Na	p	0.46	0.52
Sorbed H	n	1.37	2.79

So far, it is considered that all sorbed H^+ (n) amount is accounted for dehydroxlation by the clay mineral. If that was the case, then the OH left in the structure per unti cell ($O_{20}(OH)_{4-n}$) would be 2.65 and 1.25, for partial and full reduction, respectively. However, it is inferred by Manceau et al. (2000a); Drits, Manceau (2000) that, at least, 2.93 OH are needed so that the iron can be in six-fold coordination in the mineral lattice. That being said, the actual dehydroxylation,

for partial and full reduction will be $4-2.93=1.07$. For the partially reduced NAu1, 1.37 H^+ are sorbed, with 1.07 being expensed for OH loss and the rest 0.3 H^+ balancing the charge, leading to a structural formula of

$$H_{0.3}Na_{1.51}(Si_{6.98}Al_{1.02})(Fe^{3+}_{1.84}Fe^{2+}_{1.84}Al_{0.35}Mg_{0.04})O_{20}(OH)_{2.93}$$

With the same manner, for the fully reduced NAu1, the total H^+ amount sorbed is 2.79, with 1.72 of them re-saturating O_{ext}, forming new hydroxyls and balancing the structure of the mineral, leading to a structural formula of

$$H_{1.72}Na_{1.56}(Si_{6.98}Al_{1.02})(Fe^{2+}_{3.68}Al_{0.35}Mg_{0.04})O_{20}(OH)_{2.93}$$

The above calculations show practically, how the structural formula of NAu1 changed upon various reduction degrees. Any clay mineral hydration will be associated with the extra Na^+ adsorbed, up to a certain Fe^{2+}/Fe^{3+} ratio. Further reduction extent will not cause Na^+ adsorption, but is compensated by H^+, not involved in the actual hydration extent of the minerals. It is interesting that the interlayer dehydration effects via interlayer collapse, at high reductions degrees, cause such difference in hydration extent. However, the difficulty of actually measuring the OH content (Manceau et al., 2000a; Drits, Manceau, 2000) after various degrees of reduction, and validating these calculations, makes any attempt of calculating structural formulae not entirely accurate. In Figure 5.6, the (down-shifting) 3570 cm^{-1} band has a different intensity for the oxidised, partial and fully reduced state, yet on the above structural formulae the OH content is considered the same (2.93) for partially and fully reduced cases, taking the 'worst' case scenario into consideration.

In addition, Claire et al. (2002) suggested that this water formed from the initial dehydroxylation may stay in the mineral structure, but the above model and the calculations show that this protons don't actually have such an effect, as, if that was the case, the fully reduced sample would be more hydrated. This is also supported by the overall de-hydration observed in NIR and water adsorption data, which are discussed next. The interesting fact is that hydrogen is supposed to be strongly selected and hydrate clay minerals, (Jenny, 1932), but in the confinement of the tri-octahedral channels, hydrogen protons are absorbed rather than adsorbed. Hendricks et al. (1940) report at their work on montmorillonites that hydrogen has a very little effect on clay hydration since hydrogen cation is very small and 'is embedded in the silicate sheet near

the site of effective negative charges'.

Figure 5.8 shows the N-IR spectra of the oxidised samples, under vacuum and RH70%. Hydration increases at the same manner as mentioned already. Just comparing the three samples under reduced conditions in Figure 5.9, at RH70%, 100RED, we can see the same hydration trend of $K^+ < Na^+ < Ca^{2+}$ hydration series, (Jenny, 1932). In addition, the same dehydration effect is also distinct when looking at the N-IR spectra at fig.5.10. Under both, vacuum and 70% relative humidity, the hydration energy of Na^+ is less under reduced conditions. Here (Fig. 5.9 & 5.10) we must consider some distortion of the data, due to baseline readjustment, but the point is that clay mineral indeed is dehydrated under high reduction degrees, as described before, by Stucki (2006) and references therein.

5.4.6 Implications for enhanced oil recovery

This study was conducted in order to understand in more detail the wettability changes recognised in the literature of low-salinity waterflooding (LSWF) enhanced oil recovery (Chapter 2), as well as the wettability changes observed at the previous chapter (Chapter 4), where contact angle measurements were presented.

Briefly, wettability changes are result of several parameters, upon LSWF, such as multi-ion exchange, among others. The basis of the current study is how different clay mineral saturating cations affect clay mineral interactions, in terms induced hydration, governing the wettability of these minerals, and also the structural changes, upon iron reduction, manifested by structural changes, with increased negative charges, increased cation exchange capacity, collapsed interlayer among others. Both clay mineral hydration and iron reduction effects was approached with the experimental work above.

First, the water vapour adsorption isotherms showed that at fully reduced state, NAu1-Na is less hydrated than when oxidised (Figure 5.12), but had a stronger interaction with water, (Table 5.4, C_{BET}). Same hydration response was acquired, when looking at Figure 5.5, at the MIR and at Figure 5.10 at the NIR spectra, at the regions of 3500 and 5200 cm^{-1}, respectively. Interestingly, when NAu1-Na was partially reduced it held more water than oxidised or reduced state (Fig. 5.5). It is known that during LSWF there is cation exchange from Ca^{2+} to Na^+, and a more water-wet condition on the surface of minerals. At the same time, oxidation indicators (Fe^{3+}) were also found in field scale trials. If indeed LSWF induces re-oxidation effects, in

the initially reduced reservoir prior any production, then the water-wet state of the reservoir, after EOR, could be an intermediate state, as the partially reduced condition presented here. Similar hydration responses were acquired by NAu1-Ca and NAu1-K, which showed slightly less hydrated (Figure 5.12, Table 5.4), at the water vapour adsorption test, when fully reduced, and slightly more hydrated, at the MIR spectra when partially reduced (Figure 5.5).

At the previous chapter it was shown that clay minerals were more water-wet when fully reduced. By this observation it can be inferred that amount of water is not the only parameter that will govern the wettability of these minerals, but the bond strength of clay mineral and cations, and in extension the hydration induced due to their presence. The vibration frequencies NAu1-Na, NAu1-Ca, and NAu1-K differ in the region of 1627 cm^{-1}. As discussed already, it can be suggested that Ca^{2+} is less tightly held than Na^{+} and K^{+}, across redox states, under vacuum conditions. If that is the case, then the multi-ion exchange (or Ca^{2+}-to-Na^{+}), proposed as a LSWF drive mechanism, can be supported by this observation. Of course, any reaction takes place in a fully hydrated environment, where as shown, at Table 5.3, vibration frequencies were identical, yet these little variations can affect the micro-dynamics of the system observed.

5.4.7 Conclusions

Fe-bearing clay minerals have been studied extensively with IR techniques, regarding hydration processes and structural modifications after Fe reduction. The spectra presented in this work, are quite in accordance with the existing literature, regarding the structural changes and the hydration of the clay minerals mainly under oxidised conditions. However, here, NAu1 hydration is examined in a higher resolution, isolating the effects of the different saturating cations, such as Na^{+}, Ca^{2+}, K^{+}, first, and second examining the NAu1 hydration, under partially and fully reduced conditions, at which higher degrees of hydration are observed for the partially reduced sample and the lowest degrees for the fully reduced one. That could be further evidence to account for clay re-protonation, without positive effects on the hydration, and interlayer collapse, blocking access to the adsorbed cations and limiting their contribution towards the mineral hydration, when high levels of reduction are achieved. Water vapour adsorption isotherms also showed a reduction extent dependence, with less water vapour adsorbed under reduced conditions, yet, the water adsorbed is more strongly held onto the clay mineral surface.

This work is done in order to decipher the processes that take place during enhanced oil

recovery (EOR) methods in the oil industry. As already discussed on the literature review and the previous chapter, low salinity water flooding deploys mainly sodium cations in order to achieve a more water-wet clay mineral wettability. When iron-bearing clay minerals are under reduced state, these IR and water vapour data show that the less water is adsorbed, but a more clear monolayer water adsorption takes place, which can possibly promote surface water wettability, especially for the NAu1-Na, which is the saturating cation of interest. Eventually, the injected water high in sodium, low salinity water, will exchange cations with the established clay/ reservoir brine/oil system in the reservoir rock leading to a more water-wet system and more oil production. The cation exchange reaction process under reduced conditions will be explored at the next chapter.

The presence of Fe^{3+} in Endicott field (Lager et al., 2011), after low-salinity water flooding, show an oxidising effect of the method for that specific reservoir. If that's the case, the initial reduced state of the reservoir should be known prior to any enhanced production method, secondary or tertiary and subsequently this redox state should be taken into account when EOR methods are designed and implemented.

Nonetheless, these findings can give new insights on how the wettability changes, how oil adsorption/desorption is affected eventually from the hydration state of the clay mineral, under variable redox state, from the hydrocarbon source rock to oil migration and wettability establishing in the reservoir rock or even how other EOR methods can changes the redox state and eventually all the other factors mentioned, favouring the production of the residual oil, leading to a more sustainable oil field life.

Chapter 6

Mid-infrared and far-infrared examination of nontronite-1 clay mineral - redox and cation saturation effects

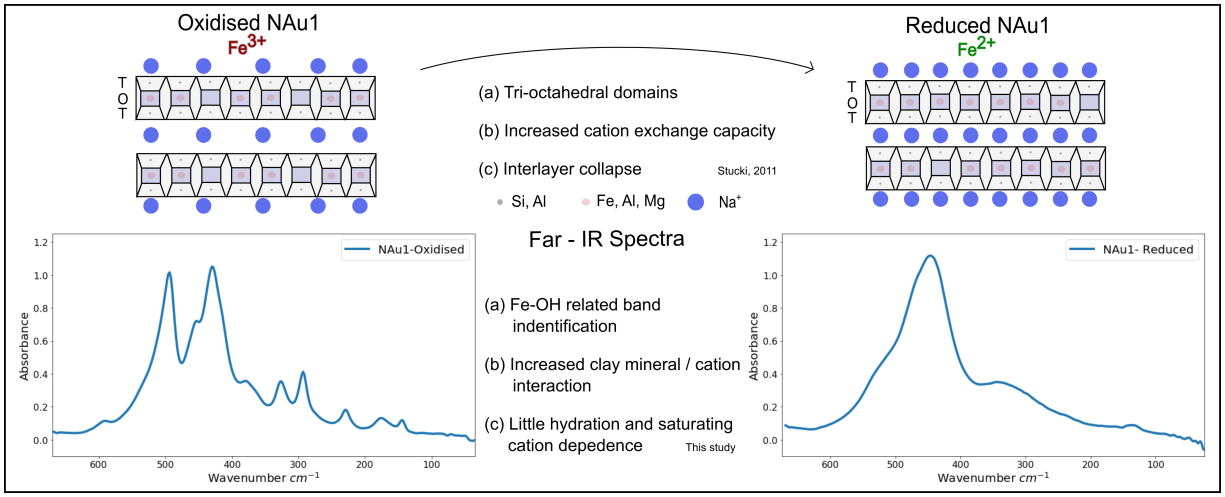

Note: This chapter's work was submitted (September 2021) as an article in Spectrochimica Acta Part A: Molecular and Biomolecular Spectroscopy, Elsevier and presented here with the same order and configuration.

6.1 Introduction

Clay mineral hydration, fluid flow properties and interactions with dissolved species are all heavily dependent on the charge present on the clay mineral and the nature of the exchangeable cations at the clay mineral surfaces. During changes in oxidation state of redox active clay minerals (e.g. those with high iron content), the surface charge and the amount and type of the exchangeable cations alter, with subsequent impacts on the transport of fluids passing through the clay minerals, or mobilisation of the clay mineral particles. In the study presented here, the mid (4000 cm^{-1} - 400 cm^{-1}) and far (400 cm^{-1} - 40 cm^{-1}) infrared spectra of the ferruginous clay mineral nontronite-1 (NAu1), under oxidized, partially and fully reduced conditions, were investigated. The purpose of these experiments was to identify changes in the lattice of the NAu1 clay mineral, when Fe^{3+} was reduced to Fe^{2+} and the interactions with the cations present and the impact this had on clay mineral hydration. Though the mid-infrared (MIR) spectrum has previously been studied in relation to these changes with sodium (Na) saturated NAu1 only, hitherto the far-infrared range vibrations have not been very well determined, even for the more readily measured oxidised clay minerals. There are several studies addressing this matter, but without assignment of definitive vibrational modes, on the peaks appearing in phyllosilicates and micas, the mineral classes mainly studied so far. In addition to examining the lattice vibrations under various degrees of reduction, individual effects induced by saturating the clays with specific cations are considered for the far-infrared (FIR) range, when NAu1 is saturated by Na^{+}, Ca^{2+} or K^{+}, under different degrees of chemical reduction. This work establishes a better understanding of NAu1, and related iron-bearing clay minerals, when reactions and interactions are considered at their surface in various environments and applications such as the energy industry, agriculture or waste management and disposal.

6.2 Literature Review on Clay Mineral FIR Studies

6.2.1 Infrared spectroscopy of nontronite

Among the earliest to publish infrared spectra of clay minerals was Farmer, Russell (1964), who described and allocated vibrational bands to the stretching modes of OH groups, mainly in the 3600 cm^{-1} region as well as lattice vibrations at the 1300 to 400 cm^{-1} region, using a series of different trioctahedral and dioctahedral clay minerals. In the same study a nontronite was

examined, revealing the absorption bands shown in 6.1.

Table 6.1: Main infrared bands of nontronite, modified after (Farmer and Russell, 1964).

Nontronite	
Vibration mode	Wavenumber (cm^{-1})
OH stretching *	3570 *
Si-O stretching	1091 1034 (p) 1017
R-O-H bending	848 818
Si-O-R^{3+} and R^{3+} -OH	786 753 680 (p) 587 (p) 493 450 430

*(Madejov et al., 2017), p= perpendicular polarisation

Since this initial study, all of these IR bands have subsequently been well characterised and allocated to different, or more specific, groups of atoms, including: 1030 cm^{-1} to the Si-O stretching mode, 848 cm^{-1} to AlFeOH bending (or 870 cm^{-1}, depending on the Al content of the mineral), 818 cm^{-1} to FeFeOH bending, 786 cm^{-1} to MgFeOH bending, 680 cm^{-1} to out-of-plane Fe-O or to AlFeOH, 493 cm^{-1} to Si-O-Fe bending, 450 cm^{-1} to Si-O-Si bending and 430 cm^{-1} to Si-O-Fe bending, (Farmer, Russell, 1964; Goodman, 1976; Baron et al., 2016; Frost, Kloprogge, 2000). Extensive IR band assignments have been made for the OH stretching region at 3000 - 3700 cm^{-1}. For nontronites the main peak is at 3570 cm^{-1}, where the FeFeOH group (OH stretch) is identified, with other M-OH stretches being overlapped by the adsorbed water O-H stretching mode shoulder at lower frequencies down to 3000 cm^{-1} (Madejová et al., 2017)).

6.2.2 Far-infrared spectrum of clay minerals

Although the mid- and near- infrared spectra of clay minerals under oxidised and reduced conditions have been studied in detail, far-infrared band allocations (from <400 to 40 cm^{-1}), especially when associated with reduction changes have not been explored to the same extent. There are reports containing far infrared spectra in the literature for micas, smectites, and other phyllosilicates, as detailed below, but no definitive structure assignments have been made thus far at

these low frequencies.

Among the first to report far-infrared data for clay minerals was Angino (1964), presenting spectra of montmorillonite, bentonite, illite and kaolinite, within this frequency range. The study recognised that complex molecular libration and low frequency stretching and bending modes were present in the far-infrared range, and that it offered a good technique for distinguishing the four minerals, since they all showed similarities in the mid-infrared frequencies. However, while strong intensities were concentrated at around 200 cm^{-1}, 264-280 cm^{-1} as well as at 350 cm^{-1}, at this point bands below 100 cm^{-1} were considered too weak to be interpreted sufficiently.

Ishii et al. (1967) subsequently attempted to calculate bond energies of the crystal lattice of the mineral based on Si_2O_5 and octahedral coordinated cation vibrations. Based on these energy modes and the observed adsorptions on the spectra of several minerals, the study allocated the following assignments shown in Table 6.2, (from Ishii et al., (1967) and modified after Zwinkels, Michaelian (1985)).

Table 6.2: Ishii et al. (1967) work on band allocation. Δ, v and v_T stand for bending, stretching, and translation-stretching vibrations, respectively.

Wavenumber (cm^{-1})	Band assignment
603	δ OSiO
543	v, δ SiOAl
476	δ OSiO
475-286	δ OSi $---$ v_T OH
258	O^O - O
209	δ OSiO
208-114	Interlayer vibrations
113	δ OSiO

In more detail, Si_2O_5 and $AlSi_3O_{10}$ monolayer lattice absorption (see Figure 5 in Ishii et al. (1967)) was calculated (based on the GF matrix method) for various infrared active modes of micas at three main wavenumbers, 1015, 543 and 285 cm^{-1}. The 1015 cm^{-1} peak correspond to the Si-O-Si anti-symmetric stretching mode, the 543 cm^{-1} a coupling between symmetric stretching and bending vibrations, and the 285 cm^{-1} was assigned to vibration of mixed Si-O vibrations and octahedral vibration or non-bridged oxygen against bridged ones (Michaelian, 1986; Ishii et al., 1967). Other bands of interest were described at 476, 113 and 209 cm^{-1}, being of different vibration energy modes allocated to Si-O bending. In addition, Ishii et al. pointed out that between 700 and 250 cm^{-1} OSiO bending and OH libration vibrations should be expected. In-phase vibration of octahedral Al^{3+} and the adjacent oxygen sheet could be located at 200

cm^{-1}, as observed in micas and phlogopite (Ishii et al., 1967; Farmer, 1974). Below 250 cm^{-1}, interlayer cation vibrations (discussed further below) were assigned in the spectra, and for di-octahedral clay minerals, the main calculated peaks associated with the cations were 211 cm^{-1} and 190 cm^{-1}, while for tri-octahedral 178 cm^{-1} and 159 cm^{-1}. The observed wavenumber for these vibrations in the physical minerals were 90 cm^{-1} and 108 cm^{-1}, respectively. Nonetheless, it is apparent that the calculated and observed absorption peaks diverge, quite significantly in some cases.

Larson et al. (1972) reported far-infrared spectra of a nontronite, among other minerals, showing main absorption peaks at around 320 cm^{-1}, 280 cm^{-1}, 220 cm^{-1} and 160 cm^{-1}, all in approximation from the plots provided in that study. Yet, the interpretation provided was largely based on previous works. Goodman (1976) conducted a comparative spectroscopy study of several nontronites, in the mid- and far-infrared, without giving significant interpretation on the far-infrared range, yet nontronite-1 (NAu1) has a very similar spectrum with that of the Garfield nontronite.

Farmer (1974) gave some more fundamental insight into the far-infrared frequencies of clay minerals, supplementing the studies by Ishii and co-workers Farmer (1974). More specifically, the K^+ intensity bands were distinguished as being located at 108 cm^{-1} for muscovite, for in-plane vibrations, with out-of-plane vibration at 144 cm^{-1} for muscovite and 154 cm^{-1} for phlogopite. In addition, if Na+ was present in the interlayer in-plane vibrating at higher frequencies was observed, owing to Na^+ being lighter in mass, in the range of 100-120 cm^{-1}, and with Ca^{2+} at 135 cm^{-1}.

Velde, Couty (1985), in their work, did not observe significant vibrational interferences from the interlayer, after isotope substitution, such as OH/OD, and cation exchange in chlorite, kaolinite, pyrophillite, micas and smectite, noting that the main absorptions were due to OH-related and Si-O structures, especially at the low frequency end of the spectrum. However, the study did not exclude the possibility of interlayer vibrations altogether. OH-related vibrations were determined by the apparent shift when deuterium was substituted for hydrogen in the structure. Shifting in the minerals studied showed variability from 10% when looking at octahedral cation substitution related to hydroxyl changes, up to 30% in chlorites for the OH/OD pair. Overall, band displacement was less than 10 cm^{-1}, meaning little vibrational effect of OH in that infrared region. With the series of ion exchange reactions, either in the interlayer, or in the lattice, of the

Table 6.3: Tabulation of the interpretation of the vibrations present in the FIR spectrum range.

	Vibration Region cm^{-1}					
	I	II	III	IV	V	VI
	50-112	118-145	150-180	192-218	225-250	262-283
Ishii	Interlayer ion-oxygen mode or interlayer translasion					
Farmer 1974	–//–					
Farmer 1974					Si-O lattice vibrations combined with OH	
Ishii, Farmer			Overlap lattice vibration and interlayer ion vibration			
Velde Couty	Interlayer cation (K^+)- O stretching (dioct. micas) Or Si-O network (trioct. mics)	Si, Al-O lattice vibration	Hydroxyl - related vibrations	Al octahedral ions and Si, Al - O tetrahedral units	Tetrahedral oxygen vibration - effects from interlayer cation	Intermittently present
Scroeder	Interlayer torsional mode	Interlayer translation mode				

minerals, the authors concluded that:

- *Region I* (Table 3), little shift in absorption was observed due to the presence of different cations, owing to changes in mass, but rather more complex changes, such as interlayer and structural ion substitution, leading to overall ionic charge changes, gave rise to more significant shifts. For trioctahedral clay minerals, the band shift was related to Si-O network changes.

- *Region II*, arguing Ishiis et al. (1967) assignment of interlayer ion-oxygen stretching, by the little variation observed in band position, concluded that these variations are small for accommodating changes due to cation masses, attributing this region solely to Si, Al-O lattice vibrations.

- *Region III* is related to OH vibrations for tri-octahedral minerals, but not so, for di-octahedral, even if they show absorption in that region.

- Absorption in *Region IV* was correlated to combined Al octahedral ions and Si, Al-O tetrahedral unit vibrations, while in Region V, absorption is better expressed in di-octahedral clay minerals, attributing vibrations to Si-O bonds that create the tetrahedral sheet. This bond may be affected by the interlayer cation present.

Other far-infrared related studies have focussed on the presence of different cations in the interlayer, all noting changes at or below 100 cm^{-1}, which will be discussed in the context of findings of this study later (Badreddine et al., 2002; Diaz et al., 2002; Prost, Laperche, 1990; Schroeder, 1992).

6.2.3 Aims and objectives

Both MIR and FIR data were acquired and are presented in this study, but the main emphasis is given to the FIR spectral range. As such, the purpose of this study is first to identify and attempt to assign the vibrational bands of NAu1 in the low IR wavenumber range, both under oxidised and reduced conditions (partially or fully), improving understanding of the changes that the mineral undergoes upon iron reduction. Second, we seek to explore how the presence of different exchangeable cations, with different hydration shell structure, can affect the MIR and FIR patterns, which, in turn, can impact clay mineral surface reactions.

6.3 Materials and methods

6.3.1 Materials

The clay mineral nontronite NAu1 was supplied from the Clay Mineral Repository (www.clay.org). Upon receiving the NAu1 mineral, the sample was ground to a fine powder, using a Retsch RM100, equipped with stainless steel mortar and pestle, for 10 min. No sieving was performed at this stage as various clay mineral treatments were utilised, such as fractionation, and homoionisation. Bulk mineralogical composition of NAu1 is of 90% nontronite, 4% kaolin, 2% quartz, <1% Biotite and 3% goethite (<2m particle size, (Keeling et al., 2000)). Also, NAu1 is an iron(III) rich member of the smectite group of clay minerals. The dioctahedral sheet of nontronite is composed mainly of trivalent iron (Fe^{3+}) cations, although some substitution by trivalent aluminium (Al^{3+}) and divalent magnesium (Mg^{2+}) does occur. The tetrahedral sheet is composed mainly of silicon (Si^{4+}). Thus, nontronite is characterised by having most of the layer charge located in the octahedral sheet. The layer charge is mainly balanced by divalent calcium (Ca^{2+}) and smaller amount of Na^+ and K^+. These cations are exchangeable, so pure Na^+ or K^+ nontronite can be obtained. NAu1 is a typical nontronite with a chemical composition consisting of 35.94% Fe_2O_3 and 8.15% Al_2O_3 (ignited basis). Its typical structural formula is $M^+_{1.05}(Si_{7.00}Al_{1.00})(Fe^{3+}_{3.62}Al_{0.35}Mg_{0.04})O_{20}(OH)_4$, (clays.org, (Gates, 2005)).

6.3.2 Cation exchange of clay minerals

NAu1 was fractionated with centrifugation using conical tubes and a Thermoscientific 75003180 swing bucket rotor, at 500 rpm, 16 °C for 7.45 min, to acquire a particle size fraction of < 2 m and separate out larger iron oxides and other mineral phases. For the purpose of this study, NAu1 clay mineral was first saturated with NaCl 1M, with 3 consecutive washes in 3 days, and then samples of the Na^+ exchanged NAu1 was further saturated with $CaCl_2$ or KCl of 1M concentration for the same time; eventually acquiring NAu1-Na, NAu1-Ca and NAu1-K homoionic cation saturated samples. All samples were then purified, with consecutive DI water washes and centrifugation, until any mineral phase impurities, such as Fe oxides, carbonates or kaolin, are cleaned out.

6.3.3 X-ray photoelectron spectroscopy (XPS) analysis

X-ray Photoelectron Spectroscopy (XPS) analysis of the NAu1-Na and NAu1-Ca was conducted to assess exchanged-cation homogeneity onto clay mineral. The characterizations were performed using a KRATOS Axis Ultra X-ray spectrometer (Kratos Analytical, Manchester, UK) equipped with a monochromated AlK X-ray source (h = 1486.6 eV) operated at 150 W. Samples were mounted on Cu tapes, passed into the spectrometer, through the oxygen-free preparation chamber.

6.3.4 Reduction of cation-exchanged clay minerals - Infrared sample preparation

The homo-ionic clay mineral samples were reduced such that 50% and 100% of the structural Fe(III) was converted to Fe(II), following a method adapted from Neumann et al. (2011); Stucki et al. (1984a). Clay mineral reduction was performed inside an anoxic chamber (GS Glovebox Systemtechnik GmbH; N2: 100%, O2 $<$ 1 ppm) and using solutions that were deoxygenated for 2 h by bubbling with N_2 gas prior to transfer to the anoxic chamber. The chemical reduction involves a buffer solution containing 9 mM sodium citrate and 0.22 M sodium bicarbonate was prepared in de-oxygenated deionised (DI) water and heated to 70 °C. Adding excess sodium dithionite, corresponding to three times the clay mineral weight, close to 100% iron reduction is achieved, while for 50% iron reduction, the dithionite added corresponds to the stoichiometry of the clay mineral (iron content) dithionite reaction. After re-saturating the reduced clay solution with the respective cation, (for the Ca^{2+} and K^+ cases, as the counter ion for dithionite was Na^+) using the method described above, dried reduced homo-ionic NAu1 samples were acquired by leaving the suspensions in the antechamber of the glovebox used, under vacuum, for sufficient time. (See Section 3.3.5, Figure 3.10 and Figure 3.9, for reduction extent determination by Mössbauer spectroscopy). All clay mineral treatment protocol and clay mineral iron reduction preparation was performed at Dr Anke Neumann's laboratory facilities at Newcastle University, UK.

Dry samples were re-suspended in deoxygenated water to acquire clay suspensions of 5 g/L concentration, from which 200 μl were dispensed on a 13 mm polyethylene (PE) pellet diameter for FIR analysis and Si pellet for MIR analysis. After drying in a desiccator with flowing N_2, clay films of NAu1-Na, NAu1-Ca and NAu1-K were precipitated on the PE / Si wafers. The

weight of the precipitated clay mineral was at 1.0 mg for every case, determined by measuring the wafer before and after the film precipitation.

6.3.5 Far-infrared (FIR) Measurements

Far-infrared measurements, recorded in the range 670-40 cm^{-1} on a Nicolet 8700 apparatus continuously purged with ultrapure N_2, were carried out with a DTGS-PE detector and a silicon substrate beam splitter. Middle-infrared measurements, recorded in the range 4000-400 cm^{-1} on a Nicolet 8700 apparatus continuously purged with ultrapure N_2, were carried out with a DTGS-KBr detector and a KBr beam splitter. Samples were prepared as described in the Sample Preparation section (Section 3.4). A pure PE pellet or a pure Si pellet was used as background. For background and samples, two spectra were averaged to minimize random noise. The spectral resolution was 4 cm^{-1} and 100 scans were co-added for each spectrum. The apparatus used a humidity control stage to examine spectral differences when water vapour is adsorbed by the mineral, as well as under vacuum conditions (10^{-5} mbar).

6.3.6 Sample Nomenclature

The samples were named as per the following. The nontronite, NAu1, was Na^+ exchanged (NAu1-Na); K^+ exchanged (NAu1-K); Ca^{2+} exchanged (NAu1-Ca). For each of these clays, the state of reduction was either oxidised (e.g. Na-OX); part reduced (e.g. Na-50RED) or fully reduced (e.g. Na-100RED). The humidity state was given the labels: vacuum (vac); or RH%, for example: NAu1-Ca-Vac-OX is the oxidised NAu1-Ca under vacuum, while NAu1-K-RH30-100RED is the fully reduced NAu1-K sample with 30% relative humidity.

6.4 Results

6.4.1 X-ray Photoelectron (XPS) analysis

XPS data were obtained, given in Table 4, in order to check the cation composition on the clay mineral surface upon clay treatment as described in Section 3.2. For consistency purposes the calculated Fe/Si ratio was 0.63 and 0.62 for NAu1-Na and NAu1-Ca, respectively, while the cation/Si ratios of interest are Na/Si: 0.13 and Ca/Si:0.09. These data show that the samples used were homo-ionic and any shifts in lattice vibration or cation hydration vibrations, and the

Table 6.4: XPS mass concentration % data of NAu1-Na and NAu1-Ca oxidised samples.

NAu1-Na		NAu1-Ca	
Peak	Mass Conc. %	Peak	Mass Conc. %
Si (2p)	22.5	Si(2p)	20.7
Al (2p)	4.5	Al(2p)	4.1
Fe (2p)	14.3	Fe(2p)	12.8
O (1s)	47.2	O (1s)	47.4
Na (2p)	3.0	Ca (2p)	2.0
C(1s)	8.5	C(1s)	13.0

combinations of the two, were solely due to the change of cation. The same behaviour should have occurred for the NAu1-K, and all reduced counterparts, as a re-saturating step was added upon reduction.

6.4.2 Effects of reduction on MIR spectra of NAu1

Changes in the IR spectra arising due to the reduction of Fe in nontronite have been studied extensively. Changes in the structure of the clay mineral take place in order to balance the excess negative charges created by the addition of electrons. Namely these are, cation adsorption leading to increase of cation exchange capacity (CEC) of the mineral, dehydroxylation, Fe migration from *cis-* to *trans-* site and re-protonation of the lattice so that Fe^{2+} keeps its six-fold octahedral coordination (Drits, Manceau, 2000; Manceau et al., 2000a; Stucki, Roth, 1977). In addition, as a result of the increased negative charge during the reduction process, interlayer collapse, interlayer dehydration, as well as decrease of the specific surface area of the mineral all result from reduction of the Fe^{3+} to Fe^{2+} (Stucki, 2006). Most of these mineral structural changes can be observed with IR techniques, which are sensitive to the local environment for -OH stretching and bending vibrational modes, and the Si-O stretching and bending vibration modes, leading to band oscillation in lower wavenumber (down-shift, eg. Figure 6.1a, peak [1]) (Fialips et al., 2002), or peaks disappearing, since the di-octahedral structure changes and new tri-octahedral domains are present after reduction, (Manceau et al., 2000a). On the following spectra (Figure6.1), these changes are denoted for the NAu1 used in our study, for all the key wavenumber regions.

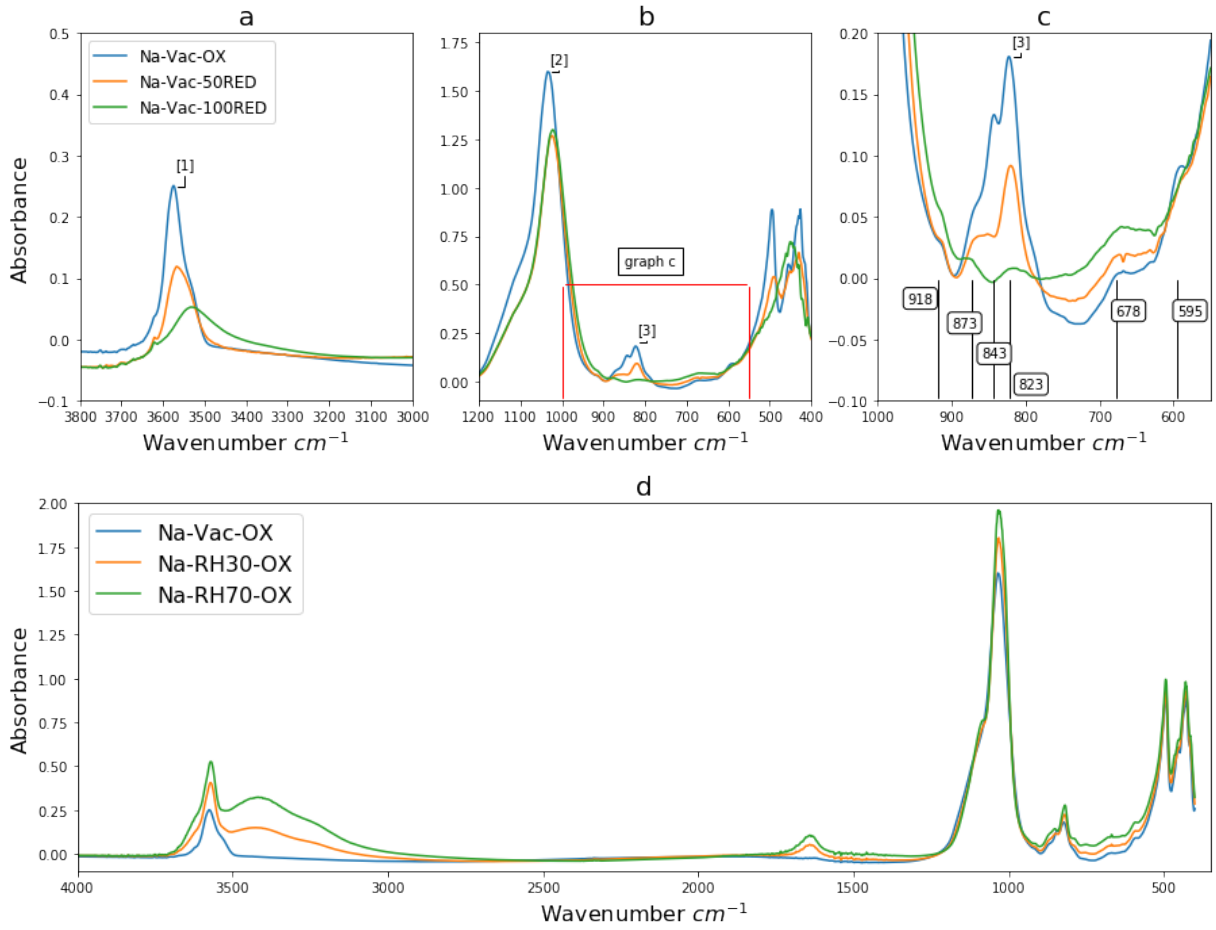

Figure 6.1: NAu1 vacuum (Vac) MIR spectra, under oxidized (OX), partially reduced (50RED) and fully reduced (100RED) conditions. (a) The [1] peak denotes the FeFeOH (3570 cm^{-1}) stretching vibration (OX) and its evolution upon reduction (50RED & 100RED). (b) The Si-O stretching (1000 cm-1), at peak [2] and bending (>600 cm^{-1}) and the OH bending region (900 - 600 cm^{-1}) with denoted peak [3] of FeFeOH bending vibration. (c) Closer view of the same region with bands allocation e.g., 823 cm^{-1}, on the various groupings present (see text for all bands denoted). The reduction effects can be appreciated in (c) as OX spectrum (blue) changes to 50RED (orange) and 100RED (green). (d) NAu1-Na spectral patterns upon relative humidity of 30% and 70% induced. Main affected areas are the 1628 cm^{-1} corresponding to adsorbed water bending vibrations and the region of 3000-3500 cm^{-1} corresponding to adsorbed water stretching vibrations, overlapping structural M-OH vibrations.

In Figure 6.1a, the blue line corresponds to the oxidised (OX), the orange line to partially reduced sample (50RED) spectrum and the green line to the fully reduced sample (100RED). The peak denoted as (1) is attributed to the $Fe^{3+}Fe^{3+}$O-H stretching grouping and, after reduction, the intensity decreased as well as the band position shifting to lower frequencies due to changes in that grouping configuration, (Fialips et al., 2002), with concomitant formation of iron tri-

octahedral structures in the crystal lattice appearing at around 3650 cm^{-1} (Fialips et al., 2002; Manceau et al., 2000a). In Figure 6.1b the main peak denoted as (2) corresponds to the Si-O stretching vibration, which under reduction also decreased in intensity and wavenumber. The down-shifting has been associated to the increase of electron density and/or the *cis* to *trans* iron migration (Fialips et al., 2002). At peak (3) there are two frequency bands of interest. First, the 843 cm^{-1}, $Fe^{3+}Fe^{3+}$O-H bending (Keeling et al., 2000), which is readily diminished, even when partially reduced (orange spectra), and flattens out, while the 823 cm^{-1}, $Fe^{3+}Fe^{3+}$O-H bending mode decreases gradually and flattens out when full reduction is attained (green spectra). With an expanded view of the region 1000-550 cm^{-1} , shown in Figure 6.1c, the bands unaltered upon reduction may be discerned as 918 cm^{-1} $Al^{3+}Al^{3+}$O-H bending (Farmer, 1974), the 873 cm^{-1}, $Al^{3+}Mg^{2+}$O-H bending (Bishop et al., 2002), with the 678 cm^{-1}, Fe-O out-of-plane vibration (Farmer, 1974), down-shifting upon reduction (6.1c, green line) (Fialips et al., 2002), while the 595 cm^{-1}, Fe^{3+}-O_{apical}-Si bending structure, with rather small intensity for the (OX) spectrum, seems to disappear after both degrees of reduction (Baron et al., 2016). Minor shoulders could possibly exist at 750-800 cm^{-1} attributed to $Fe^{3+}Mg^{2+}$O-H, (OX spectrum) (Baron et al., 2016). More changes were present in the lower wavenumber end of these spectra, namely below 550 cm^{-1}, and will be explored further in the Far-IR spectrum range section of this present study. Figure6.1d shows the adsorbed water, when relative humidity of 30% and 70% was induced, affected the band of 1628 cm^{-1} and the region of 3000-3500 cm^{-1} corresponding to water bending and stretching vibrations, respectively. The same effect was observed in the MIR spectra of partially and fully reduced NAu1-Na, as well as when NAu1-Ca and NAu1-K were analysed at the same hydration and reduction degrees, (Appendix D, Figures D.1, D.2, D.3). The specific effects of the different saturating cations on the MIR range are discussed later.

6.4.3 Far-infrared spectra of NAu1 at oxidised, partially and fully reduced redox states

FIR spectrum range was from 670 cm^{-1} to 40 cm^{-1}. As such, there is a small overlap with the mid infrared range, as can be seen from Figure 6.2.

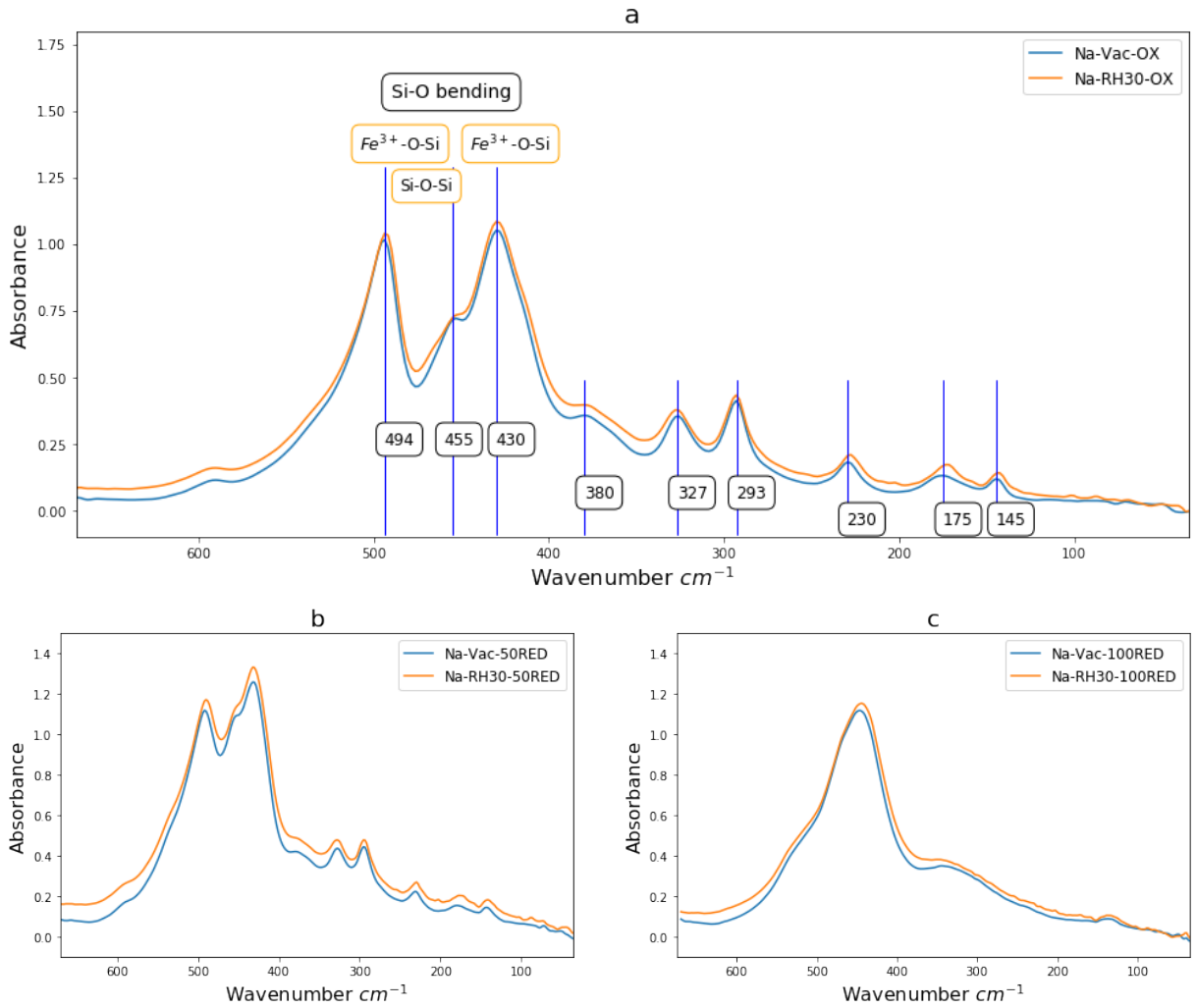

Figure 6.2: Far-infrared spectrum of sodium (Na) saturated nontronite, NAu1-Na. (a) oxidised conditions, with absorption peaks annotated, with respective band allocation where known. (b) partially reduced conditions. This spectrum still resembles well the oxidised spectrum. (c) fully reduced conditions. This spectrum has almost a totally different pattern when compared to the other two.

The Si-O bending region was observed in the region of 400 - 550 cm^{-1}, with Fe^{3+}-O-Si and Si-O-Si groupings vibrating at 494 cm^{-1}, 430 cm^{-1} for the former, and at 455 cm^{-1} for the latter (Frost, Kloprogge, 2000). These absorption maxima are annotated for the vacuum spectrum (Vac in Figure 6.2 a. See Figure 6.5 for schematic representation). Other major transmission peaks occurred at 380 cm^{-1}, 327 cm^{-1}, 293 cm^{-1}, 230 cm^{-1}, 175 cm^{-1}, 145 cm^{-1}. Below 100 cm^{-1} the vacuum spectrum was virtually flattened with no significant absorption peaks, unless the spectrum was focused, which is discussed later.

When 30% relative humidity (RH) was induced, some of these bands down shifted, especially

the ones below 230 cm^{-1}. The relative shifting was not extensive, but it can be inferred that these band vibrations were affected by the cation present in the interlayer and, consequently, by its state of hydration. In addition, two minor transmission peaks appeared just above 200 cm^{-1}, and one between 145-175 cm^{-1}, in the 30% RH spectrum, compared to the vacuum spectra. The region of the vacuum spectrum from 400 to $>$ 230 cm^{-1} appeared unaffected upon mineral hydration (Figure 6.2a).

Similarly, the NAu1 spectra, under 50% reduced conditions at Figure 6.2b, showed the same band positioning and the same band shifting at the frequencies described before. When the fully reduced spectrum was considered, a totally different transmission pattern was observed, Figure 6.2c. There was only one absorption peak observed between 400 and 500 cm^{-1}, while another two were distinguished, just above 300 cm^{-1} and just above 100 cm^{-1}, with both being very broad.

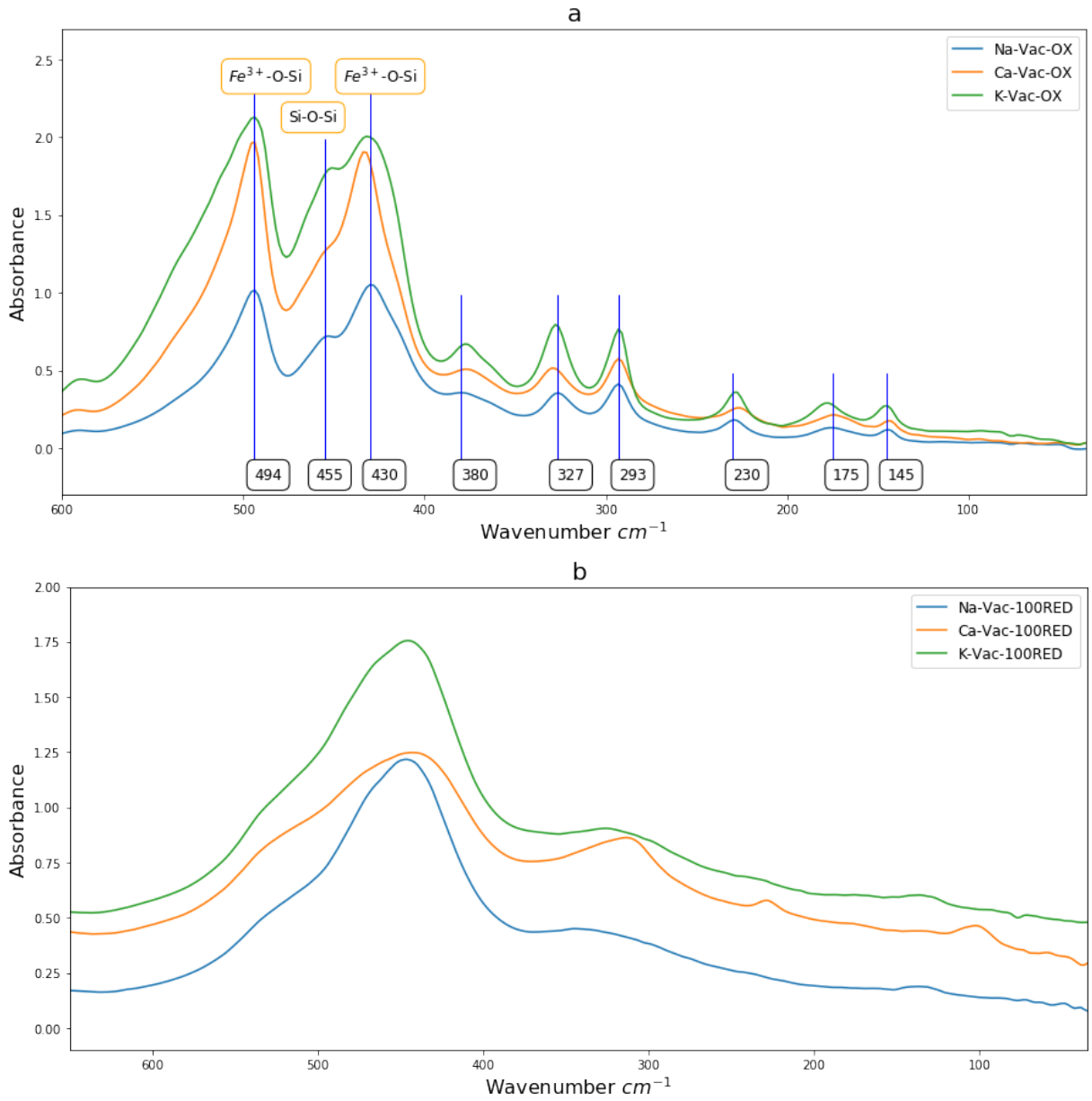

Figure 6.3: NAu1-Na, Ca and K spectra, under vacuum (Vac). (a) NAu1 spectrum under oxidised conditions. The annotated bands correspond to the NAu1-Na spectrum and are used as a baseline for comparing the NAu1-Ca and NAu1-K spectra. (b) NAu1 spectrum under fully reduced conditions. All three spectra have similar patterns. NAu1-Ca spectrum shows an additional vibration at 100 cm^1, which is irrelevant to the NAu1 mineral phase (see text).

On Figure 6.3(a) and Figure 6.3(b) an overall comparison is made of the spectra of nontronite exchanged with Na^+, Ca^{2+}, and K^+, under oxidised and fully reduced conditions, respectively, and under vacuum. Both Ca^{2+}, and K^+ had a variable effect upon the spectrum, when compared to Na^+, shown in Figure 6.3a. While wavenumbers of 494, 455, 380, 293 cm^{-1} were unaffected

or close to unaffected, by the presence of the different cations, the bands at wavenumbers of 430, 327, 230, 175, 145 cm^{-1} exhibited more prominent changes. The more prominent changes of these groups of bands indicates a close relation to the identity of cation in the nontronite interlayer. Translational interlayer modes have previously been attributed to the 120-180 cm^{-1} bands, (Schroeder, 1992), and torsional interlayer vibration in the range of 50-115 cm^{-1} (Ishii et al., 1967; Schroeder, 1992). In nontronite NAu1 there were no significant bands below 145 cm^{-1}, which could be assigned to a torsional mode. This lack of clear torsional bands was recognised (Schroeder, 1992), when examinined two montmorillonites, and attributed this phenomenon to the low octahedral layer negative charge, unable to strongly interact with the hydrated interlayer cations. On the other hand, when the negative charges originated in the tetrahedral sheet, it was more likely that torsional modes would be observed in the FIR spectra. The NAu1-Ca case, Figure 6.3b, shows an additional peak in the region of 100 cm^{-1}, due to sodium bicarbonate residues from the reduction process, as well an increased transmission at the 230 cm^{-1} region, which may be affected by the same residues.

6.5 Discussion

6.5.1 Effect of iron reduction on the mid-and far-infrared spectra of nontronite

Iterating the results shown at Figure 6.1, spectral changes were identified across the MIR range. Iron reduction caused down shifting and/or lower relative intensity of several bands, such as the 3570 cm^{-1} associated to $Fe^{3+}Fe^{3+}$O-H stretching mode or the Si-O stretching band at the region of 1000 cm^{-1}. Other significant changes were identified at the bands of 821 and 843 cm^{-1}, associated with $Fe^{3+}Fe^{3+}$O-H bending modes, which, upon reduction, were greatly diminished. These aforementioned Fe-related bands were affected after the iron reduction, as evidenced by the new configuration of the Fe^{2+} present, into trioctahedral domains, emerging at the 3650 cm^{-1} band.

A more comprehensive approach to the structural changes occurring upon reduction can be gained after looking at the FIR range of the same samples. Putting all three vacuum spectra in a graph, the differences can better be appreciated, and further conclusions be drawn. Looking at Figure 6.4, it is clear that all the main absorptions were related to lattice domains of Si-O, Fe-O

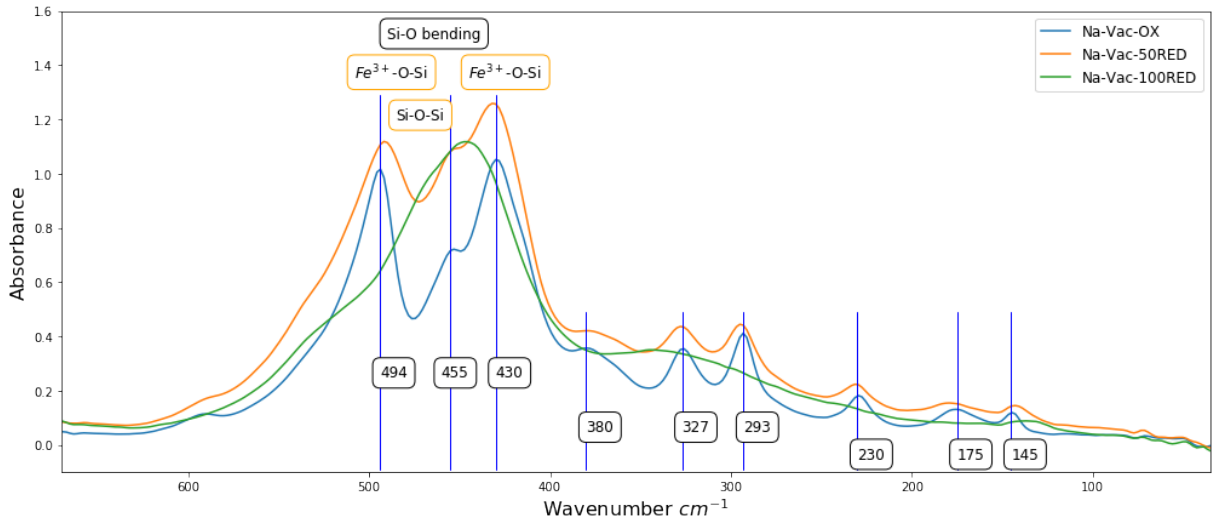

Figure 6.4: Far-infrared spectra of NAu1-Na (vacuum- Vac conditions), under oxidised (OX), 50% reduced (50RED) and 100% reduced (100RED) conditions. Annotated absorption peak frequencies correspond to the oxidised (OX) sample.

or a combination of the two. First, the 494 cm^{-1} peak nearly disappeared when the sample was fully reduced, (100 RED spectra). The 455 and 430 cm^{-1} showed a decreased transmission under 50% reduced conditions, (comparing the relative vertical distance between the two maxima, in the oxidised and 50% reduced spectra), while for the 100% reduced spectra, there are two possibilities. It was observed that the 430 cm^{-1} peak decreased for the 50% reduced in intensity but was not shifted. Following that trend, it would disappear after full reduction. If that was the case for the fully reduced sample, then at the 455 cm^{-1}, region the main transmission peak down-shifts, and a shoulder appears towards higher frequencies, which may be trioctahedral characteristics of the Fe^{2+}-O-Si - like structure. The second possibility was that, under fully reduction, the 430 cm^{-1} peak was up- shifting, having a trioctahedral domain structure, and the 455 cm^{-1} up-shifted as well. However, this interpretation is speculative. Since the Si-O stretching, 1030 cm^{-1} band, also down-shifted after reduction (Fialips et al., 2002; Neumann et al., 2011), the most probable explanation is the former.

For the 290-380 cm^{-1} group of transmission peaks observed in the oxidised spectra, a wide, low-intensity envelope appears in the fully reduced (100RED) spectra. For the partially reduced case, a small up-shift was observed for the 293 and 327 cm^{-1}, but not for the 380 cm^{-1} absorbance. For the fully reduced case, the 380 cm^{1} absorbance seems to flatten out, while the other two became coalesced into the single one at 350 cm^{-1}. This frequency can also be related

to the trioctahedral domains created at high degrees of reduction. For the 230 cm^{-1} and 175 cm^{-1} transmission peaks (OX spectra), up-shifting was observed under partial reduction, while they flattened out under full reduction. On the other hand, the 145 cm^{-1} peak was shifted gradually to lower wavenumbers at partial reduction and full reduction conditions, eventually occurring at around 130 cm^{-1} (green spectra, Figure 6.4), which again was associated to Fe^{2+} trioctahedral domains or Fe^{3+} altered domains with longer bond lengths, similar to the changes of the 3570 cm^{-1} peak (Figure 6.1a) which decreased in absorption intensity and wavenumber.

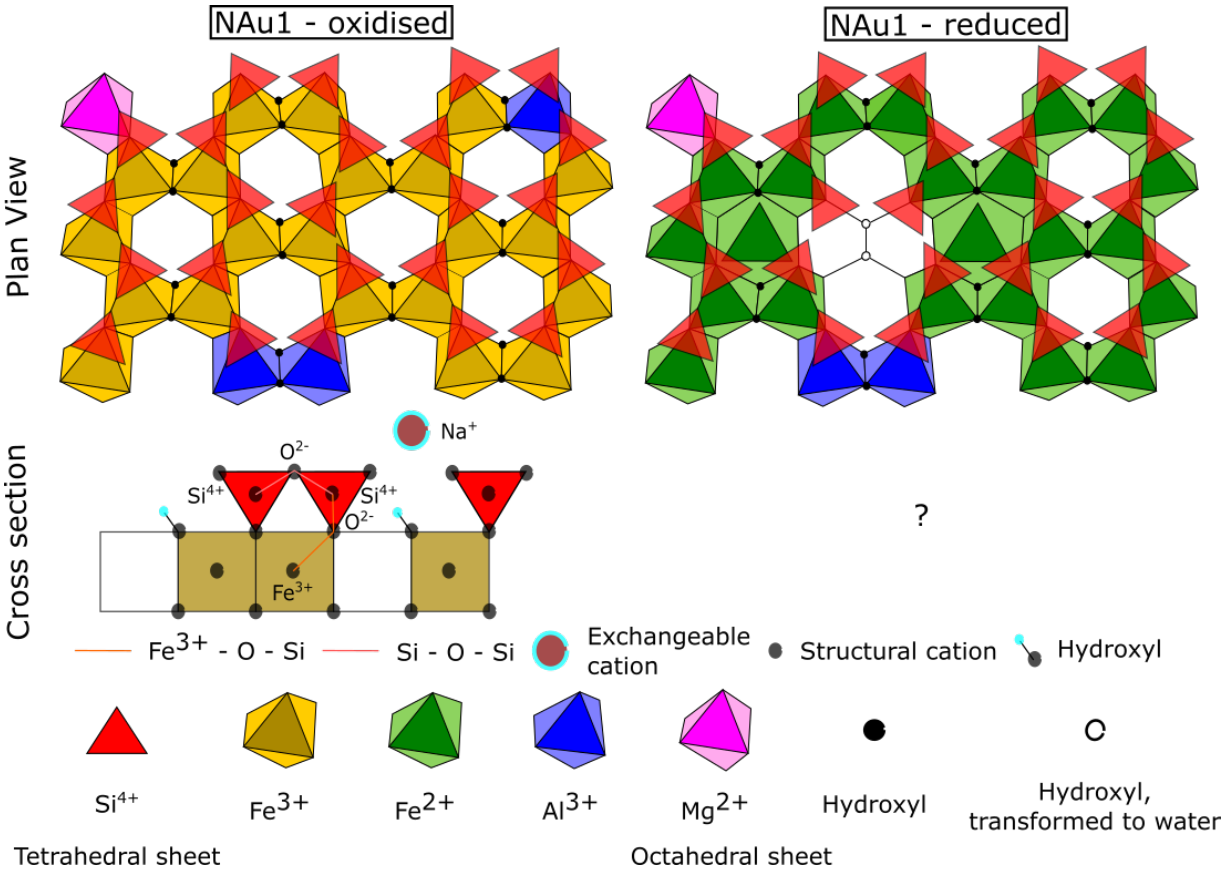

Figure 6.5: Schematic representation of the NAu1 dioctahedral structure (oxidised conditions) and tri- di-octahedral (reduced conditions) in plan view and cross section view. Oxidised conditions of iron are denoted by the orange colour of the octahedral iron, and the reduced conditions by the green colour of the octahedral iron, as this change occurs physically when NAu1 is reduced. Octahedral aluminium and magnesium are present is small concentration in NAu1, (Keeling et al., 2000), with their distribution and content ratio in the graph not representing the true occurrence. The plan views are adopted and modified from (Brigatti et al., 2006) for depicting the dioctahedral and tetrahedral structure of a smectite and (Neumann et al., 2011) for depicting the structural changes and the trioctahedral domains created upon iron reduction.

In pyrophyllite (structural formula: $Al_2Si_4O_{10}(OH)_2$), using data presented by Velde, Couty (1985), as there are no interlayer cations or hydration, the structural vibrations can be examined for comparison and to aid unambiguous assignment of the clay mineral sheet lattice vibrations within the NAu-1 . The peaks of 328 cm^{-1} coincides well with the 327 cm^{-1} of NAu1, showing a Si-O dependence. The peak of 160 cm^{-1} in pyrophyllite showed an OH dependence, which could be correlated to the 175 cm^{-1} band of nontronite, since this band is diminished upon reduction (Figure 6.4). Other areas of pyrophyllite could relate to that of NAu1, such as 200 cm^{-1} and 252 cm^{-1} to the 230 cm^{-1}, but probably the presence of different octahedral central cations (Al^{3+} vs Fe^{3+}, respectively), give rise to different vibration wavenumbers.

Band assignment for the NAu1 (Uley green) of these low-frequency vibrations has been attempted using FT-Raman spectroscopy, (Frost et al., 2000; Kloprogge, 2017). Prominent peaks are at 364 cm^{-1} for SiO_4 units, 287 cm^{-1} and 239 cm^{-1} for $OH---O$ triangle vibrations of symmetrical and anti-symmetrical stretching mode. This triangle OHO structure arises only in di-octahedral smectites, with the non-bridged oxygen of the SiO4 interacting with the hydrogen of the octahedral OH tilted towards the octahedral cavity (Frost et al., 2000). Also, the bands of 187 cm^{-1} and 166 cm^{-1} are for Fe-O anti-symmetric stretching vibration and 87 cm^{-1} for FeO stretching vibration of Fe in the octahedral position (Frost et al., 2000). Similarly, FT-Raman on montmorillonites (Kloprogge, 2017), showed prominent peaks at 287 cm^{-1}, corresponding to $OH---O$ triangle, 200 cm^{-1} assigned to vibrational mode of AlO6 , which depended on the central cation occupying the octahedra. Another band that also was dependent on the central octahedral cation was that of 175 cm^{-1} of O-Al-O nature, which downshifted to 165-150 cm^{-1} when iron was present in that central position. Also, this band could be associated with cation and/or water vibrations, causing variability of the position of this band. The 145 cm^{-1} band was described as an Si_2O_5 vibrating structure (Kloprogge, 2017) but also it could be associated to the 175 cm^{-1} downshifted to 145 cm^{-1} due to presence of Fe (Frost et al., 2000), and one at 96 cm^{-1} assigned to cation vibrations (Kloprogge, 2017).

At this point, the interpretation provided has been correlated with the current literature (see Table 6.5). For the oxidised and partially reduced spectra, assignments have been made according to a number of previous studies (Farmer, Russell, 1964; Frost et al., 2000; Ishii et al., 1967; Kloprogge, 2017; Velde, Couty, 1985). For the fully reduced sample, which should have trioctahedral spectral characteristics, reported frequencies of such clay minerals in (Velde, Couty,

1985), support these suggested assignments in Table 6.5. However, as discussed above in conjunction with FIR and Raman the interpretation of some bands, e.g., 145 cm^{-1}, varies amongst the current literature. Summarising, for the fully reduced NAu1 spectrum (Figure 6.4, green line), the main transmission peaks were at 455 cm^{-1} most likely related to Si-O-Si bending vibrations, a broad peak at the region of 340-350 cm^{-1} of Si-O structure, possibly incorporating trioctahedral structures and a band peak at 137 cm^{-1} of Si-O nature. All the other peaks present at the oxidised and the partially reduced spectra should be related to di-octahedral domains of octahedral or octahedral-tetrahedral iron groupings. In Figure 6.1(b) and Figure 6.1(c), non-iron dioctahedral groupings were observed and remained upon reduction. However, those would not be significant in the FIR range due to their small intensity.

6.5.2 The effect of hydration on the mid- and far-infrared spectra

MIR Hydration Effects in NAu1

Hydration-triggered spectral changes were observed as shown in Figure 6.1d, Figures 6.2, D.1, D.2, D.3. Hydration effects on clay minerals, at the MIR spectrum range, were displayed by Johnston (2017). At the region bands of 1628 cm^{-1} and 3000-3500 cm^{-1}, the spectra of all samples, NAu1-Na, NAu1-Ca and NAu1-K, consecutively increased in relative intensity values, upon relative humidity induction in the system.

FIR Hydration Effects in NAu1

Some authors attributed major absorption peaks as arising due to the interlayer cation vibrational modes (e.g., Ishii et al. (1967)), while others did not, assuming some minimal effects on the spectrum from cation presence impacted the clay mineral lattice vibrational modes (e.g., Velde, Couty (1985)). From the present work, two changes were noted when comparing hydrated nontronite and the nontronite under vacuum. First, the positions of almost all main bands were down-shifted. Second, low-intensity transmission peaks appeared. Both these observations occurred during hydration. The hydration-induced downshift affected the 494 cm^{-1}, 455 cm^{-1}, 230 cm^{-1}, 175 cm^{-1}, and 145 cm^{-1} bands, while a small up-shift was seen for the 327 cm-1 band (Figure 6.2a). These changes were only 3 cm^{-1}, yet consistent for the oxidised and partially reduced spectra, as detailed in Table 6.5.

Usually, band down-shifting appears when the bond or interaction length increases, or the

Table 6.5: Main absorption peaks of NAu1 under different redox state examined. Band position maxima are shown, comparing the vacuum and the RH30% spectrum, across the redox states. Main difference observed is band shifting, from relative humidity comparison and band appearing/disappearing form redox state comparison.

Oxidised		Assignement [1]	50% reduced (50RED)		100% reduced (100RED)		Assignement [2]
Vacuum	RH30%		Vacuum	RH30%	Vacuum	RH30%	
494	494	SiOFe [a]	494	494	470 (sh)	470 (sh)	trioc. domain
455	455	SiOSi [a]	455	455	447	443	SiOSi
430	430	SIOFe [a]	430	430			
380	390	δ OSi ν_T OH [b]	380	380	345	350	SiO related + trioc. domain
327	327		327	327			
293	293	OH—O [d]	231	229			
230	228	Si-O[c] OH—O [d]	231	229			
175	173	$Al(Fe)_{oct}$ [c] O-$Al(Fe)_{oct}$ -O [d]	179	177			Si-O related

[1] a= Frost & Klopprogge(2000, 2000b), b= Ishii 1967, c= Velde&Couty 1985, d=Frost &Kloprogge 2000a,
[2] this study
δ = bending, (sh) =shoulder, trioct. domain = trioctahedral domain

bonding strength decreases and changes in ion mass, so the vibrational energy decreases. As these vibrational bands represent mainly interactions of the octahedral layer atoms with interlayer cations, as the interlayer cations hydrate, these interactions will take place across longer distances, resulting in a shift to lower energies. Similar shifts were attained at partial reduction, too. It might be assumed the increased negative charge density during reduction would increase the cation affinity to the clay mineral layer, hence decreasing the bonding distance with the octahedral layer and causing an upshift. However, as reduction initially proceeds, the negative charges are compensated by Na^+ uptake from the reducing agent, increasing water content present and the interaction distance. The fully reduced spectrum, presented in Figure 6.2c, showed a down-shifting only for the major peak at 447 cm^{-1}. As there was no other discernible transmission peak, it would be difficult to attribute hydration effects on the lattice vibrations, as opposed to the oxidised and partially reduced nontronite spectra above.

The emerging bands at the low-frequency end of the spectra upon hydration, indicate cation positional vibrations in the interlayer and labelled [1]-[10] in Figure 6.6. These cation-vibration-related transmissions occur below 250 cm^{-1}. In Figure 6.6, the NAu1-Na spectral patterns are depicted, at vacuum (OX-Vac), as baseline, and 30% relative humidity (RH), across the three different redox states. By comparing the blue spectrum with the rest of the spectra, the labelled peaks appeared at RH30% and remained for all three redox states. As Na^+ was the only cation present along with its hydration sphere, across the hydrated clay mineral under different redox states, these bands indicate a hydration dependence, where vibrations are of a cation/water coupling effect. When, full reduction has taken place (Figure 6.6, red spectra), all the major bands below 250 cm^{-1} disappeared, while the annotated [1]-[10] peaks remain, supporting the above argument. At the same time, these emerging bands, as annotated at the Figure 6.6, could be due to water vapour rotation (Randall et al., 1937) , not necessarily linked to the cations present, (see Figure 6.7, too); so the interpretation of these bands should be approached with caution.

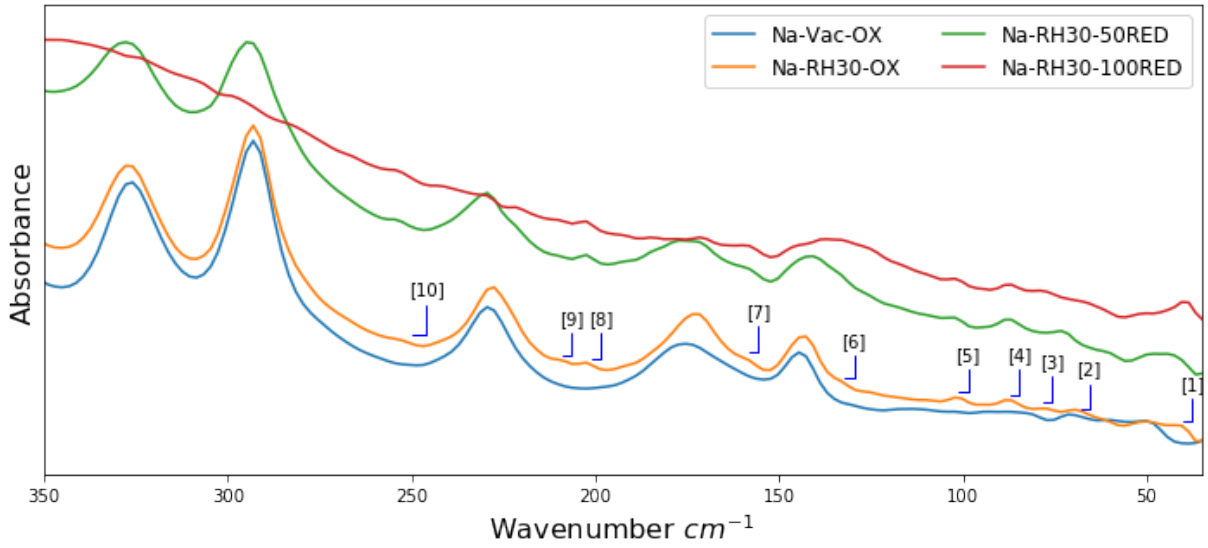

Figure 6.6: Far-infrared spectra of NAu1-Na at RH30%, under oxidised (OX), 50% reduced (50RED), and 100% reduced (100RED) conditions, at the range of 350-35 cm^{-1} frequencies. Hydration-triggered (RH30%) transmission of low intensity is observed on several wavenumber annotated with no. index, [1]-[10]. These transmission bands stay consistent across the different redox condition spectra.

6.5.3 Cation exchange effects on the NAu1 mid- and far-infrared spectrum

So far, the case of NAu1-Na, under oxidized, partially, and fully reduced conditions has been discussed. The changes that take place during the reduction can be observed on the respective spectra when compared in Figure 6.1 and Figure 6.4. In addition, an interpretation attempt of the possible hydration transmission peaks was made in Figure 6.6, where minor, but specific, spectral differences were noted when moving from the nontronite when oxidised and reduced transitioning from vacuum to 30% relative humidity. Here, two more cations are now considered, examining the spectral effects on the nontronite NAu1, under oxidized and fully reduced conditions.

As vacuum conditions were considered in that case (Figure 6.3 and Figures D.2, D.1, D.3 for MIR), the mass, charge, and ionic radius of each cation (Schroeder, 1992; Velde, Couty, 1985) as well as the proximity of the cation to the charge site determined the interaction of the band and the cation, rather than hydration extent. Na^+ and K^+ are of the same charge, but K^+ and Ca^{2+} have a similar mass. On the other hand, Na^+ and Ca^{2+} have similar dehydrated ionic radius, of 0.99 Å, with K^+ having a dehydrated ionic radius of 1.33 Å (Israelachvili, 2011). At the same time, the position of each cation on the mineral surface differs as has been shown by computer simulation using replica exchange sampling (Underwood et al., 2015). For the case of Na^+, when

in a metastable state of weak hydration, it was located above a single clay oxygen (O) of the siloxane cavity, at a distance of 2.3 Å. On the other hand, K^+ formed an energetically stable complex above the siloxane cavity at 1.3 Å distance, but also a metastable one, similar to Na^+, situated above an O of the siloxane structure at a distance of 2.6 Å. Ca^{2+}, being a divalent cation, had a stable distance that was situated at 3.8 Å above the siloxane cavity. Although these distances of Ca^{2+} and K^+, from the plane of the siloxane cavity, are considered for hydrated cations Underwood et al. (2016), it can be speculated that when cations are partially hydrated, or dehydrated, as in the case of this present study for the samples analysed under vacuum, they retain the same distance and localisation variations.

As far as MIR spectra were concerned, the band that showed cation dependence across the redox states was the one at 1620-1650 cm^{-1}, which corresponded to adsorbed water bending vibrations. When the vacuum and RH70% spectra for all cations, across redox states, were examined, changes were noticed in terms of wavenumber of oscillation, as shown at Table 6.6.

Table 6.6: Tabulation of the changes observed on the adsorbed water bending vibration band, at 1628 cm^{-1}, upon relative humidity of 70% and reduced conditions (partial and full).

	Wavenumber cm^{-1}								
NAu1	Na			Ca			K		
	OX	50RED	100RED	OX	50RED	100RED	OX	50RED	100RED
Vacuum	1628	1634	1635	1623	1623	1623	1630	1650	1637
RH70&	1639	1641	1635	1632	1635	1632	1632	1650	1637

For the NAu1-Na sample, it can be seen that the 1628 cm^{-1} band, under vacuum and oxidised conditions, up-shifted when the relative humidity increased to 70%. This upshift was associated to hydrogen bonded adsorbed water Frost, Kloprogge (2000); Frost et al. (2000). The same upshifting took place for the partially reduced sample (50RED), while for the fully reduced sample the band was not affected by the changing humidity. A similar trend of upshifting upon relative hydration was observed for the NAu1-Ca and NAu1-K samples, except for the NAu1-K at partial and full reduction. When the wavenumber of oscillation was examined across the redox states, an upshifting was apparent for the partial reduced samples, with a consecutive downshifting for the fully reduced samples, regardless of the relative humidity. For the NAu1-Na and NAu1-K (RH70) the fully reduced samples vibrated at higher (1635 cm^{-1} and 1637 cm^{-1}) wavenumber than the oxidised (1639 cm^{-1} and 1632 cm^{-1}), with the partially reduced samples

having the highest value (1641 cm^{-1} and 1650 cm^{-1}), while the oxidised and fully reduced NAu1-Ca (RH70), vibrated at 1632 cm^{-1} with partially reduced at 1635 cm^{-1}.

Overall, a non-linear relationship can be observed between band shifting and reduction extent, which can be linked with the curvy-linear relationship of increased negative charges and reduction extent identified by (Stucki et al., 1984c). Negative charges will increase upon early reduction, in a linear way, but at high reduction extents, negative charges will eventually decrease as structural transformation becomes favourable rather than increased net layer charge. This change in negative charges is manifested by the shifting of the band at 1628 cm^{-1}, which will vibrate at higher wavenumber, denoting the strongest clay mineral/cation interaction at partial reduction, with a small downshifting and slightly weaker interaction when at the fully reduced state. Furthermore, it is notable that the NAu1-Na at fully reduced state did not change wavenumber of vibration (1635 cm^{-1}) for vacuum and RH70%, a phenomenon which appeared for the NAu1-K for the partially and fully reduced cases, too. This can be taken as further evidence of interlayer collapse and interlayer dehydration upon reduction, as described by (Stucki, 2011). As these two structural changes take place upon reduction, the saturating cations are tightly held within the collapsed interlayer, with no ability to interact with the additional hydration induced in the system. NAu1-Ca, on the other hand, showed a hydration dependence at the fully reduced state. Eventually, the positioning of the saturating cations, within the interlayer, as described above, was also manifested in the MIR spectrum range, facilitating or not, interlayer hydration at high iron reduction extent.

Studies using two different vermiculites (a high negative charge smectite), with negative charges originating from mainly tetrahedral substitutions (Al^{3+} or Fe^{3+} for Si^{4+}), examined a series of cation exchange reaction with concomitant far-infrared spectra analysis, in order to establish the exchange and selectivity sites of the mineral. Vermiculite exhibits a cation selectivity $Na^+ < Ca^{2+}(<K^+)$, which is attributed to the stronger polarisation effect of the Ca^{2+} water molecules and the tetrahedral oxygen (Badreddine et al., 2002). At the same time, the selectivity for Cs^+ and Rb^+ is higher than for K^+, ($K^+ < Cs^+ = Rb^+$) as the former larger radii cations were better trapped in the di-trigonal cavity of the silicate sheet than the latter. This selectivity was evidenced in the far-infrared range with absorption bands at 57, 63, 76 cm^{-1} (Badreddine et al., 2002), meaning that the most selected cation vibrated at lower frequencies. That, however, could be a result of the mixed structure the mineral acquired (smectite-like,

phlogopite-like intercalations) described in that study. Diaz et al. (2002) on undertaking similar exchange reaction studies, using a different vermiculite, also identified the same cation selectivity trend and FIR patterns, attributing the downshifting of the more selected Cs^+ and Rb^+ to their larger radii, increasing the distance of the interlayer planes, and the cation O (ditrigonal cavity) distance interaction.

Providing a first interpretation on the changes observed in Figure 6.3a, at the wavenumbers 430 and 327 cm^{-1}, the Ca^{2+} and K^+ spectra showed a slight up-shifting, attributing this to the higher charge of Ca^{2+} and/or the preferential K^+ positioning within the hexagonal cavity, or the similar mass that Ca^{2+} and K^+ have, leading to stronger layer-cation interactions. On the other hand, for the 175 and 145 cm^{-1} bands, Ca^{2+} showed a down-shifting and K^+ an up-shifting in relation to the Na^+ spectra. The 230 cm^{-1} band showed no difference for Na^+ and K^+, while it was down-shifted for Ca^{2+}, indicating a cation charge dependence interaction. It can be seen that specific structures within the nontronite clay mineral lattice may interact differently with the dehydrated cation present in the interlayer.

In muscovite (di-octahedral) the K^+ band downshifted upon heating (110 to 97 cm^{-1}), due to de-hydroxylation and iron oxidation in the structure (Prost, Laperche, 1990). As interlayer K^+ interacted with the structural hydroxyl group of the octahedral layer, when iron migrated to the vacant position upon de-hydroxylation, the K^+-O interaction distance increased, lowering the frequency of vibration. The opposite was observed, with band upshifting (78 to 91 cm^{-1}) in biotite (tri-octahedral), which upon deprotonation and iron oxidation, exhibited a K^+-O distance decrease, increasing the vibration frequency (Prost, Laperche, 1990). Nontronite (NAu1) is a di-octahedral smectite and, upon iron reduction, de-hydroxylation took place, leading to *cis-* to *trans-* iron migration and creation of tri-octahedral domains (Figure 5). It has been discussed, *vide supra*, that the 145 cm^{-1} band (Figure 6.4, blue line), of the oxidised NAu1 spectra, may be related to the interlayer cation identity, which also shows a downshift upon reduction to 137 cm^{-1} (green line) regardless of the cation exchanged here (Figure 6.3(b)). Other changes due to the different cations, in Figure 6.3(b), were minimal. The main band, in the region of 447 cm^{-1} was close to unaffected, as well as the region at 137 cm^{-1}. The region at 345 cm^{-1} showed a differentiation, with Ca^{2+} and K^+ shifting to lower wavenumbers than the Na^+ spectrum. Some minor changes also occurred below 90 cm^{-1} (Figure 6.3(a) and Figure 6.3(b)), which potentially could be due to cation torsional vibration modes, under reduced conditions, with the NAu1-K

spectrum showing less changes than the NAu1-Na and NAu1-Ca spectra.

Figure 6.7 shows the vacuum and the 30% relative humidity spectra for each cation, pairwise, under oxidized conditions. That way, the effects of hydration for each of NAu1-Na, NAu1-Ca, NAu1-K can be examined individually, when looking at the vacuum and the 30% relative humidity spectra, as well as across the 3 different redox states. The NAu1-Na spectra (grey and blue) along with the peak annotations, are considered for a baseline. Figure 6.7 looks more closely at the low end of the FIR range, and it is worth noting that at higher wavenumbers the only band affected by the induced hydration is the one at 430 cm^{-1} for the NAu1-Ca sample, which undergoes downshifting (see Appendix D, Figure D.4), blue and orange spectra). In the frequency range depicted in Figure 6.7, two types of hydration effect could be distinguished, one affected the major transmission bands and, two, new peaks appeared with rather low transmission energy, but consistent across the three samples. The peaks for the NAu1-Na are annotated as (1), (2), etc as a comparison baseline.

The first hydration effect can be distinguished for the 293 cm^{-1} band, which show an upshifting for the NAu1-Ca (Ca-RH30%, orange line) and the NAu1-K (K-RH30%, green line) when compared to their vacuum counterparts (Ca-Vac, black line, and K-Vac, red line, respectively). The 175 cm^{-1} band also exhibits hydration effects for all three samples, showing a downshifting when the hydrated spectra were compared with the vacuum spectra.

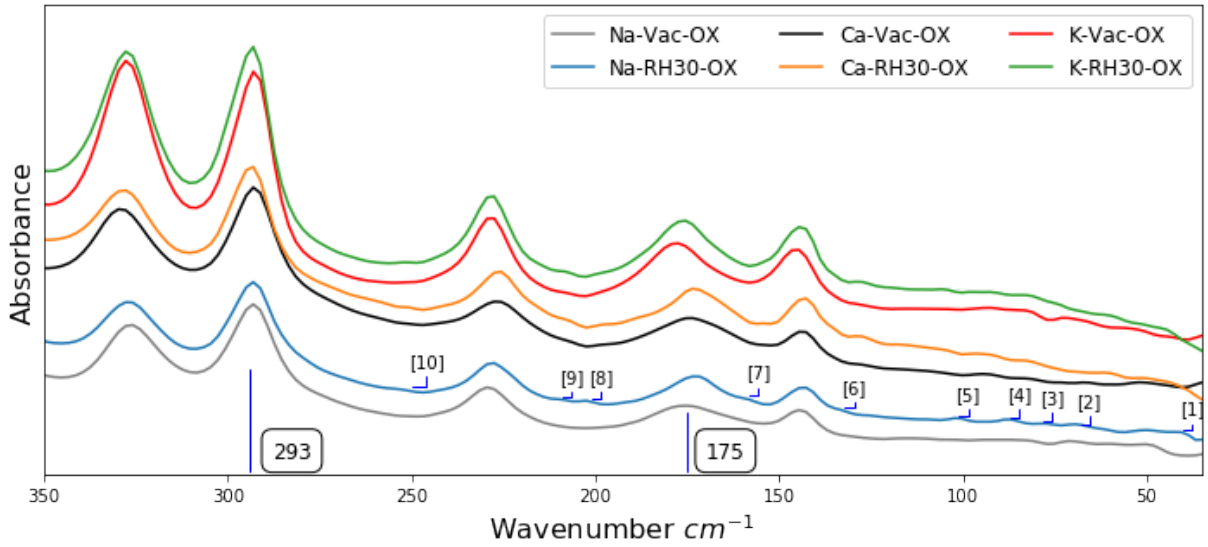

Figure 6.7: Hydration effects for each saturating cation Na (grey and blue), Ca (black and orange), and K (red and green), under vacuum (Vac) and RH30% (30), for each pair of spectra of oxidised nontronite respectively.

The second hydration effect was identified in Figure 6.6, for NAu1-Na (blue line, annotated peaks) and reproduced at Figure 6.7 along with the spectra of NAu1-Ca and NAu1-K. Annotated peaks [6]-[10] are present in the three different spectra (blue, orange, green), regardless of the cation present, indicating interlayer water vibrations. The group of [1]-[5] peaks are not the same for all hydrated spectra. Na^+ and K^+ have similar patterns for these bands, whereas Ca^{2+} does not show much hydration interference in this 100-40 cm^{-1} wavenumber range.

In Table 6.7, all the changes observed in the FIR patterns, for oxidised conditions, at vacuum, RH30% and different saturating cation are reported. For the changes observed under vacuum conditions, the NAu1-Na spectrum was considered the baseline for comparison for the NAu1-Ca and NAu1-K spectra (Table 6.7(a)), while for the changes under 30% relative humidity, the comparison was made for each saturating cation individually, between the vacuum and the 30% relative humidity counterparts.

6.6 Conclusions

The present study examined the nontronite, NAu1, at the mid- and far-infrared spectrum range, at three different redox states, oxidised, partially reduced and fully reduced, identifying several changes on these spectral patterns. The MIR spectra exhibited gradual hydration at relative humidity of 30% and 70%, at spectral region of 1620-1650 cm^{-1} and 3000-3800 cm^{-1}, assigned to H_2O bending and OH stretching, respectively. At the same time, structural changes were observed for bands of $Fe^{3+}Fe^{3+}OH$ nature of stretching and bending mode, at 3570 cm^{-1} and the area of 816-843 cm^{-1} , as has been described in the literature. Regarding the FIR data, oxidised and partially reduced spectra showed high similarity, with bands decreasing in relative intensity for the latter redox state. Fully reduced spectrum showed the most changes across the FIR range examined here, from 600 cm^{-1} to 40 cm^{-1}, pointing to a complete different clay mineral structure, as expected due to structural changes upon iron reduction (Drits, Manceau, 2000). Most of the major bands identified were affected dramatically by iron reduction, by diminishing in relative intensity or shifting to lower wavenumber of vibration. Notably, bands below 400 cm^{-1}, for the fully reduced case, showed low spectral definition, probably incorporating Si-O structures as well as iron trioctahedral structures. Nonetheless, iron reduction can be an effective way of distinguishing iron bands, vibrating at these low-frequency wavenumbers, in ferruginous clay minerals.

Table 6.7: a) Wavenumber spectral differences of NAu1-Na, NAu1-Ca, NAu1-K under vacuum and oxidised conditions. Changes of NAu1-Ca and NAu1-K are recorded in respect to the NAu1-Na spectrum (baseline spectrum). See Figure 3a for graphical representation. b) Wavenumber spectral differences of NAu1-Na, NAu1-Ca, NAu1-K upon RH30% and oxidised conditions. Changes recorded at each RH30% column are based on their Vacuum equivalent for each sample. See Figure 6.7 for graphical representation.

a) Wavenumber changes under vacuum					b) Wavenumber changes upon RH30%					
Allocated band	Wavenumber (cm^{-1})	NAu1-Na	NAu1-Ca	NAu1-K	NAu1-Na		NAu1-Ca		NAu1-K	
					Vacuum	RH30%	Vacuum	RH30%	Vacuum	RH30%
Fe^{3+}-O-Si	494	Baseline Spectrum	0	0	494	0		0		0
Si-O-Si	455		0	-2	455	0		0		0
Fe^{3+}-O-Si	430		+3	+2	430	0		-1		0
	380		-2	-2	380	0		0		0
	327		+3	+1	327	0		0		0
	293		0	0	293	0		+1		+1
	230		-3	-1	230	-2		0		0
	175		-2	+3	175	-2		-1		-1
	142		-1	+1	145	-1		-1		-1

Parallel to the structural examination of the NAu1, the effects of different saturating cations (Na^+, K^+, and Ca^{2+}), on the NAu1 MIR and FIR spectrum, was investigated. The only MIR band affected by the cation present was the H_2O bending, which shifted to higher wavenumber upon hydration, for all sample cases. This band exhibited a dependence on the reduction state of the NAu1, showing an increasing clay mineral/cation interaction strength order of oxidised< fully reduced< partially reduced, matching well with observations laid in the literature and discussed above. On the other hand, major bands, in the FIR spectrum, exhibited minimum effects by the cation exchange, with shifted vibrations to higher or lower wavenumber while other minor bands were observed, at the <250 cm^{-1} region only upon hydration at a relative humidity (RH) of 30%. No major bands were observed to be directly attributed to cation vibration, although those would be located at the region at or below 100 cm^{-1}, where minor effects of the different cations possibly exist (Figure 6.7, Vacuum spectra). Further examination of FIR data for the specific mineral, could focus on simulating and calculating the vibrating components at this low frequency infrared range, as well as examining under altered redox conditions, other iron-bearing clay minerals, which can be proved useful when cation adsorption phenomena are of interest.

Chapter 7

Cation exchange processes of reduced iron-bearing clay minerals

7.1 Introduction

Cation exchange is one of the most fundamental characteristics of clay minerals, soils and, more generally, ion exchange is prevalent across many other materials, such as alginate and related biopolymers (Pandey et al., 2007), zeolites (Inglezakis, 2005), layered double hydroxides and related minerals (Aisawa et al., 2005), as well as in activated carbon (Dai et al., 2010), biochar and numerous engineered polymer systems, *inter alia*. The first cumulative study on ion exchange processes was conducted by Jenny (1932), citing prior research spanning from 1855 to 1930, and also conducting exchange experiments with different clay materials, addressing among others, the ions release and the lyotropic series (later formalised as the Hoffmeister series). Since these early works, a vast amount of research has been carried out on the ion exchange process, with a number of different models proposed.

Yet, despite this body of literature, ion exchange processes of minerals under reduced conditions are not well studied, to the best of our knowledge, despite these reduced conditions being prevalent and important in many natural systems including the anoxic zones within soils and sediments where transport properties are important to many biogeochemical cycles. A reason for this 'gap' may be the fact that after knowing the ion exchange process and the changes occurring after iron reduction in ferruginous clay minerals, patterns can be predicted in a deductive way of thinking, however, given the structural changes that may occur, such as dehydroxyla-

tion (Stucki et al., 1996) and framework coordination changes, which result in collapse of the interlayer (Stucki, 2011, 2006), it is far from clear that the cation exchange properties will be controlled by surface charge differences in a predictable way. In this chapter, the cation exchange processes of clay minerals will be briefly reviewed, and experimental data of carefully controlled cation exchange reactions will be presented. As has been already discussed, clay minerals are able to exchange cations on their basal plane, at external surfaces and within the interlayer regions, as well as at layer edge sites, and this chapter will focus on the cation exchange mechanisms between reduced and oxidized clay minerals, and the thermodynamics of this exchange process that takes place, recognised since 1819 (Jenny, 1932). Since then, numerous studies have been published, proposing mechanisms and models, describing this process which has application, such as in environmental remediation (Vijayalakshmi et al., 2017), product manufacturing, and in the oil industry (Farajzadeh et al., 2017), with the latter the main focus of this study. Overall, the purpose of the first part of this chapter is to describe and give the theoretical background in order to be able to examine and interpret the following experimental data. The specificity of these experiments of being under reduced conditions, make it important to explore the different proposed models as well as to take into account hysteresis phenomena, which are expected, in order to best approach the results.

Ion selectivity on charged surfaces has originally been established by the works of Hofmeister, (Hofmeister, 1888), according to the ability of ions stabilising protein solutions with a decreasing order of:

$$Citrate^{3-} > SO_4^+ > PO_4H^{2-} > F^- > CH_3COO^- > Cl^- > Br^- > NO_3^- > ClO_4^- > SCN^-$$

$$N(CH_3)_4^+ > NH_4^+ > Cs^+ > Rb^+ > K^+ > Na^+ > H^+ > Ca^{2+} > Mg^{2+}$$

when anions or cations are the counterions of positively or negatively charged surfaces, respectively. These ions have been divided in two groups, the kosmotropic (right-hand side of cation series) and chaotropic (left-hand side of cation series) cations, noting the ability to contribute or not into the creation of water structures when interacting with water, in the immediate ion proximity (first water sphere). In the work of López-León et al. (2008) and references therein, it was shown that the presence of a surface and the charge properties can affect this lyotropic

series, which in many cases has shown an inversion, mainly at the anionic series, not explained by the original work (Hofmeister, 1888; Kunz et al., 2004). When clay minerals are under consideration, the negative charges governing their surface will exhibit a cation selectivity sequence, similar to the one showed above. The two main factors that also affect the selectivity order, are the charge sign of the surface, as well as the hydrophobicity/ hydrophilicity of the surface and the possible combinations of the two. Furthermore, when colloidal stability is of interest, the well-known double layer expansion theory (or DLVO theory by (Derjaguin, Landau, 1993; Overbeek, Verwey, 1948), the ionic strength of the bulk water will affect the stabilisation/destabilisation of solid particles, e.g., higher ionic strength will cause particle aggregation due to the reduced interparticle electrostatic potential, as the counterions will balance the surface charges. However, hydrophilicity of colloidal particles can introduce repulsive forces, stabilising the colloidal solution, even at high ionic strengths (López-León et al., 2008).

As clay mineral particles are of interest, authors (López-León et al., 2008), examined negatively charged particle of hydrophobic and hydrophilic characteristics concluding that in the first case, Na^+ counterions introduced higher solution stability than $NH_4{}^+$, following the original Hofmeister rule, as Na^+ a more kosmotropic ion will not be selected by the hydrophobic surface, diminishing less the negative potential of the particles, and sustaining colloidal suspension. Ca^{2+} ions, on the other hand, will induce colloidal destabilisation regardless of the charge sign or water affinity of the surface, (López-León et al., 2008). In the second case of negatively charged and hydrophilic surface, Na^+ will be more selected on the particle surface, in conjunction with lyotropic inversion anionic effects explored in the same study, resulting in colloidal destabilisation. In general, hydrophobic and hydrophilic surfaces can be described of chaotropic and kosmotropic behaviour, too, favouring adsorption of ions of similar nature (entropic rule) (López-León et al., 2008). This approach is similar to that of Teppen, Miller (2006), which describes cation selectivity at clay mineral surfaces as a cation partitioning process. Less hydrated cations in the bulk solutions will be partitioned on the surface or interlayer of clay minerals, where this cation hydration state is more favoured.

Direct atomic force microscopy interaction forces measurements of the Hofmeister effects on clay mineral particles showed that mica (substrate) and montmorillonite (probe) a repulsive forces sequence of $Li^+ > Na^+ > K^+ > Cs^+$, meaning that clay mineral colloids would remain in suspension following the same order, (Feng et al., 2020). Furthermore, at high salt concentration,

the difference of repulsive forces induced by these cations would be minimised, as can be predicted by the classical DLVO theory. Conversely, it was established in the same study that Cs^+ would screen the electric potential more effectively than Li^+, affecting the clay particle surface reactions, (Feng et al., 2020). The thermodynamic quantification of Hofmeister effects on cation exchange equilibrium was demonstrated by Liu et al. (2013) calculating the relative adsorption ratio of divalent and monovalent cations with the order of $Ca^{2+} > Mg^{2+}$ (Ca/Mg = 1.407) > K^+ (Mg/K= 1.467) > Na^+ (K / Na = 1.646) > Li^+ (Na/Li =1.11). These results were consistent for different clay minerals of soils, with different charge density, leading to the conclusion that the force of adsorption is a result of electrostatic and polarisation of cations in the proximity of the mineral surface electric field, (Liu et al., 2013).

As it is apparent thus far, Hofmeister phenomena can greatly affect cation exchange reactions on clay mineral surfaces (and within the interlayer), since the adsorption energy of these cations is affected by surface nature, electrolyte concentration and other effects on the mineral surfaces. Direct imaging of the replacement of potassium for sodium in the montmorillonite interlayer showed that cation exchange is a chemical-mechanical process, at which interlayer collapse due to potassium presence take place seconds after the cation exchange, (Whittaker et al., 2019). The result of this process is two distinct montmorillonite phases of fully sodium or potassium saturated, in equilibrium, without intercalations of these two montomorillonite, sodium-rich, potassium-rich, phases, which is determined by the cation ratio in solution and water activity, (Whittaker et al., 2019). Water activity is considered an important factor by the authors, as more interlayer collapsing should be expected in dry bulk density compacted clays. The water phase contribution into ion exchange reactions was also demonstrated by Rotenberg et al. (2009), in a study measuring the hydration enthalpy of cations and of ion exchange overall. In an exchange system of Na^+-to-Cs^+ in montmorillonites, it was determined that even if the exchange of sodium by caesium in the minerals interlayer is endothermic, the opposite exchange in the aqueous phase (Cs^+-to-Na^+) is an exothermic reaction, dominating the enthalpy changes in the whole exchange system. This further supports the work of Teppen, Miller (2006), which also demonstrated that the ionic exchange free energy was unfavourably affected by the clay phase ($\Delta G >> 0$) and that the hydrophobicity of Cs^+ is favoured in the interlayer space, and Na^+ in the aqueous phase, driving the exchange reaction, (Rotenberg et al., 2009).

7.2 Ion exchange theory

7.2.1 Thermodynamics

All proposed ion exchange models can be classified in three groups; nonmechanisitc models using thermodynamic principles, mechanistic models utilising the difuse double layer theory and mechanistic models based on the ion hydrations energetics and electrostatic interactions (Kumar, Jain, 2013).

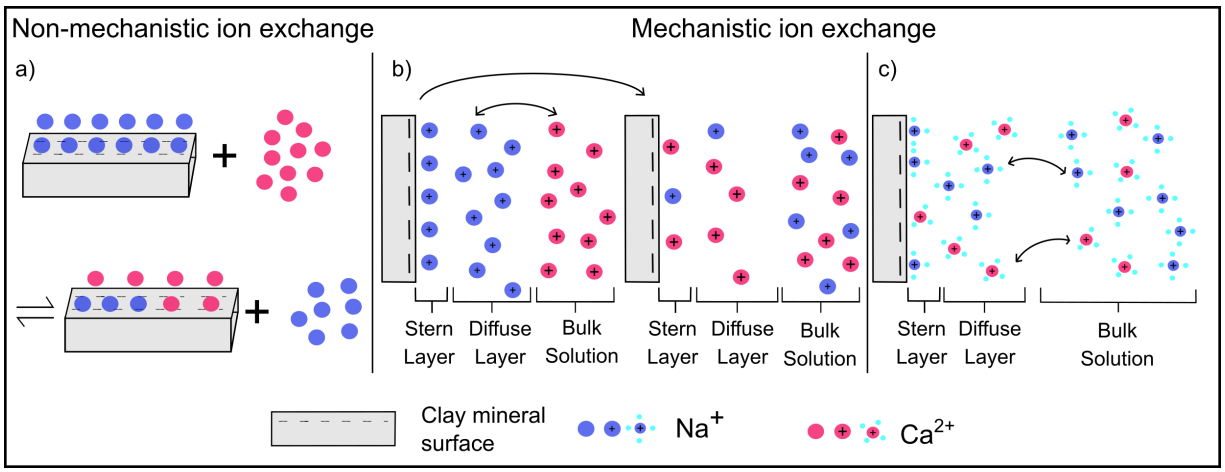

Figure 7.1: Schematic representation of non-mechanistic (a) and mechanistic ion exchange (b, c) models, as described mainly by Gaines, Thomas (1955), Eriksson (1952), Eisenman (1962); Teppen, Miller (2006), respectively.

Looking at the thermodynamic principles and considering a cation exchange of a Na-saturated clay mineral (X), in a $CaCl_2$ solution the reaction will be

$$2NaX + CaCl_2 = CaX_2 + 2NaCl \tag{7.1}$$

the equilibrium constant for this reaction would be

$$K_{ex} = \frac{[CaX_2][NaCl]^2}{[NaX]^2[CaCl_2]} \tag{7.2}$$

where [ ] denotes activity.

The activities of solution components can be re-written as the product of the actual concen-

tration in the solution and the activity coefficient of the ion in the solution,

$$K_{ex} = \frac{[CaX_2](Na^+)^2\gamma^2_{Na^+}}{[NaX]^2(Ca^{2+})\gamma_{Ca^{2+}}} \tag{7.3}$$

the activities of the cations on the clay surface should be defined in a similar way.

Vanselow (1932) discussed two approaches, first, considering the clay mineral as fine solids (monobasic hypothesis) which would lead to use the actual cation concentration in the K_{ex}, or second, considering the clay mineral forms mixed crystals or solid solution of the adsorbing cations, which lead to introducing molecular fraction of the NaX and CaX_2 into the K_{ex}. Eventually, substituting solid activities with mole fraction, the K_{ex} becomes

$$K_{ex} = \frac{N_{Ca}f_{Ca}(Na^+)^2\gamma^2_{Na^+}}{N^2_{Na}f^2_{Na}(Ca^{2+})\gamma_{Ca^{2+}}} \tag{7.4}$$

where $N_{Ca} = \frac{Ca^{2+}}{Na^+ + Ca^{2+}}$ the concentration mole fraction of CaX_2 and $N_{Na} = \frac{Na^+}{Na^+ + Ca^{2+}}$ of NaX, f_{Ca} and f_{Na} are the activity coefficients of the cations related to the solid phase, which when considered as an ideal surface with little cation interaction on the charge site equal to unity. (Vanselow, 1932; Gast, 1972). Eventually, Vanselow presented the following equilibrium constant

$$K_V = \frac{N_{Ca}(Na^+)^2\gamma^2_{Na^+}}{N^2_{Na}(Ca^{2+})\gamma_{Ca^{2+}}} \tag{7.5}$$

Gaines, Thomas (1953) approached the solid phase activity coefficient differently, introducing the equivalent mole fractions regarding the solid-phase cation cation composition, in contrast to the work of (Vanselow, 1932; Argersinger et al., 1950), and derived expression for the cation solid-phase activity coefficients, Gaines, Thomas (1955),Sposito (1981), where the equivalent mole fraction for Na^+ and Ca^{2+} in the solid phase (E) or in the solution (Y) are given in Eq. 7.6. Equivalents differ from the traditional mole fraction of Vanselow and Argersinger, as the valence of non-monovalent cations is considered,too. m stands for the mole fraction or each cation, while subscripts gt and GT stand for the Gaines-Thomas approach.

$$\begin{aligned} Y_{Na}, E_{Na} &= \frac{m_{Na}}{m_{Na} + 2m_{Ca}} \\ Y_{Na}, E_{Ca} &= \frac{2m_{Ca}}{m_{Na} + 2m_{Ca}} \end{aligned} \tag{7.6}$$

with the proposed reaction selectivity coefficient, K_{gt}, being

$$K_{gt} = \frac{E_{Ca}(Na^+)^2\gamma^2_{Na^+}}{E^2_{Na}(Ca^{2+})\gamma_{Ca^{2+}}} \tag{7.7}$$

whereas the equilibrium constant, K_{GT}, is defined as

$$K_{GT} = \frac{E_{Ca}(Na^+)^2\gamma^2_{Na^+}}{E^2_{Na}(Ca^{2+})\gamma_{Ca^{2+}}} * \frac{f_{Ca}}{f^2_{Na}} = K_{gt} * \frac{f_{Ca}}{f^2_{Na}} \tag{7.8}$$

The thermodynamic equilibrium expression of the above equilibrium constant and the solid phase activity coefficients f_{Ca} and f^2_{Na} (Gaines, Thomas, 1953; Escudey et al., 2001) is

$$\begin{aligned} \text{(i)} \quad & lnK_{GT} = lnK_{gt} + lnf_{Ca} - lnf^2_{Na} \\ \text{(ii)} \quad & lnf_{Ca} = -E_{Na}(1 + lnK_{gt}) + \int_0^{E_{Na}} lnK_{gt}\, dE_{Na} \\ \text{(iii)} \quad & lnf^2_{Na} = (1 - E_{Na})(1 + lnK_{gt}) - \int_{E_{Na}}^1 lnK_{gt}\, dE_{Na} \end{aligned} \tag{7.9}$$

where, E_{Na} is the equivalent mole fraction of Na^+ in the equilibrated solid phase, lnK_{gt} the natural logarithm of Eq. 7.7. Eventually, Equation 7.9(i) reduces to equation 7.10, which determines the natural logarithm of the thermodynamic equilibrium constant for a bi-valent (M^+, M^{2+}) cation exchange reaction, with exclusion of the water activity as it was considered negligible (Gaines, Thomas, 1955).

$$lnK_{GT} = \int_0^1 lnK_{gt}\, dE_{Na} - 1 \tag{7.10}$$

For a homo-valent (e.g. Na/K) exchange reaction the solid-phase cation activity logarithms as well the true equilibrium constant take the following form to account for the stoichiometric symmetry.

$$\begin{aligned} \text{(i)} \quad & lnf_K = -E_{Na} lnK_{gt} + \int_0^{E_{Na}} lnK_{gt}\, dE_{Na} \\ \text{(ii)} \quad & lnf_{Na} = (1 - E_{Na}) lnK_{gt} - \int_{E_{Na}}^1 lnK_{gt}\, dE_{Na} \\ \text{(iii)} \quad & lnK_{GT} = \int_0^1 lnK_{gt}\, dE_{Na} \end{aligned} \tag{7.11}$$

Sposito (1981) used a more holistic approach on the thermodynamics of ion exchange, giving the possibility of calculating the solid-phase activities, f_{Na}, f_{Ca}, for each proposed equilibrium

constant (e.g. K_{GT}) and feeding them into the equation

$$K_{ex} = \frac{f_{Ca} N_{Ca} (NaCl)^2}{f_{Na}^2 N_{Na}^2 (CaCl_2^2)} \tag{7.12}$$

where, ( ) are aqueous-phase ion activity and N is mole fraction of solid-phase adsorbed cations. The f_{Na} and f_{Ca} can be calculated as in Eq. 7.13 , with full final expression of activity coefficients and equilibrium constants in Tables 7.1, and Table 7.2.

$$\begin{aligned} f_{Na} &= \frac{(NaX)}{N_{Na}} \\ f_{Ca} &= \frac{(CaX_2)}{N_{Ca}} \end{aligned} \tag{7.13}$$

Gapon (1933) wrote the initial cation exchange reaction different to what it is considered so far (7.1),

$$2NaX + CaCl_2 = 2Ca_{1/2}X + 2NaCl \tag{7.14}$$

The solid-phase activities in that case can be derived from (Sposito, 1981)

$$\begin{aligned} f_{Na} &= \frac{E_{Na}}{N_{Na}} \\ f_{Ca} &= \frac{E_{Ca}^2}{N_{Ca}} \end{aligned} \tag{7.15}$$

Yet, no matter how the reaction is considered stoichiometrically, the Gapon convention can be used as easily as the other two.

Table 7.1: Solid-phase activity coefficients for the three selectivity equilibrium constants. Modified after Sposito (1981)

Authors	Activity relation assumed	Activity coefficient
Vanselow	$(NaX) = N_{Na}$	$f_{Na} = 1$
	$(CaX_2) = N_{NCa}$	$f_{Ca} = 1$
Gaines and Thomas	$(NaX) = E_{Na}$	$f_{Na} = (2 - N_{Na})^{-1}$
	$(CaX_2) = E_{NCa}$	$f_{Ca} = 2(1 + N_{Ca})^{-1}$
Gapon	$(NaX) = E_{Na}$	$f_{Na} = (2 - N_{Na})^{-1}$
	$(CaX_2) = E_{NCa}$	$f_{Ca} = 4N_{Ca}(1 + N_{Ca})^{-2}$

Table 7.2: Model expressions for K_{ex} that govern the homo-heterovalent cation exchange reaction

Authors	Selectivity coefficient
Vanselow	$K_V = \frac{N_{Ca}(NaCl)^2}{N_{Na}^2(CaCl_2)}$
Gaines Thomas	$K_{GT} = \frac{2(1+N_{Ca})^{-1}N_{Ca}(NaCl)^2}{(2-N_{Na})^{-2}N_{Na}^2(CaCl_2)}$
Gapon	$K_{GT}^2 = \left(\frac{2(1+N_{Ca})^{-1}N_{Ca}}{(2-N_{Na})^{-1}N_{Na}}\right)^2 \frac{(NaCl)^2}{(CaCl_2)}$

Electric double layer theory in clay mineral ion exchange

Keeping the above thermodynamic outlook brief, a mechanistic approach was developed by Eriksson (1952) and based on the diffuse double layer (See Chapter 3, Section 2.5.3) of individual clay particles. In Eriksson's system, only the cations and the negative charges of the clay minerals (exchanger) were taken into account, along with the diffuse double layer that form in a very dilute clay mineral / salt solution system. Within this constraint of the system, an exchange constant was then derived, considering that the diffuse layer acts as a membrane to the whole exchange process, Figure 7.1. The exchange constant, K, for a heterovalent exchange reaction then, according to Eriksson, takes the form of:

$$K = \frac{[Na]^2(Ca)X}{(Na)^2[Ca][Na + 2Ca]}$$

where brackets [] denote concentrations present, parenthesis () as ion activities in the solution, X the charge concentration of the clay mineral. This equation takes a longer form when analytically presented. However, the fact that it is describing a very specific system, which is very dilute (activity of cations equal to their concentration) in order for the clay particles to form a diffuse double layer, and the exchange is about heterovalent cations, it is limited in its application to many natural systems. Modifications by Neal, Cooper (1983) and Nir (1986) tried to account for the lack of the model to describe homovalent cation exchange, yet, overall, it cannot demonstrate selectivity of e.g. K^+ over Ca^{2+}, even if Ca^{2+} has higher charges and should have been selected more, as the negative charges of the exchanger increases (Kumar, Jain, 2013). Trying to decipher the above considerations, Erikson tried to describe a small-scale process that most likely does take place in such exchange reactions. However, it was not enough to describe accurately the whole process for all various conditions.

Coulombic and hydration energy in clay mineral ion exchange

Eisenman (1962) on developing and explaining the ion selectivity electrodes, argued the free energy of exchange is governed by the net change in Coulombic and hydration energies for the exchanging ions, (Kumar, Jain, 2013). Eberl (1980) applied this theory and based on the Gaines-Thomas convention, which initially includes the moles of water in the interlayer, suggested that the equilibrium constant and the free energy were dependent on the clay's electric field expressed as equivalent anionic radius and the interlayer water content, which is determined by the saturating cation. Eisenman calculated the free energy exchange of Cs^+ with other alkali cations, when Cs^+ is dehydrated and partially hydrated in the interlayer, (using certain assumptions for the latter case). Eventually, it was established that there was preference for the lesser hydrated cation in the interlayer, when interlayer water decreases and layer charge density increases (Kumar, Jain, 2013). A different perspective on the cation hydration energy was given by Teppen, Miller (2006), as the authors considered the exchange reactions as a cation partitioning process. When two cation with the same valance in aqueous phase, the weakly hydrated one will adsorb onto the clay mineral due to its less water content, while the strongly hydrated will remain in the aqueous solution. That concept can explain cation selectivity series, organic cation adsorption as well as organic/inorganic adsorption reactions.

It is important to stress here that all ion exchange processes are affected by hysteresis phenomena, regardless as to whether a non-mechanistic or a mechanistic model is considered from the above. Verburg, Baveye (1994) reviewed experimental data of cation exchange in 2:1 clay minerals. Many authors have reported irreversibility of cation exchange in clay minerals, but with a closer look a rule was observed as to when this irreversibility took place. In Table 7.3 below, (after Verburg, Baveye (1994)), cations are divided in to three groups. When exchange takes place with cations of the same group, hysteresis was not observed, while it was when cations of different groups were involved.

According to the kinetics of such exchange reactions, the cation exchange takes place within the first few seconds (3 s to 30 s) and, in some cases, up to some minutes. This fast stage of reaction can be considered as a first relaxation time. After that, the system enters a second, thermodynamically much slower period, during a second relaxation time, which leads to equilibrium. This second stage can last from months to years, (Verburg, Baveye, 1994). Essentially, the observation scale determines whether a process is governed by thermodynamic controls or

Table 7.3: Cation classification in groups at which hysteresis is not observed according to the literature. Modified after Verburg, Baveye (1994)

Group 1	Group 2	Group 3
Na^+	K^+	Ca^{2+}
Li^+	Rb^+	Ba^{2+}
	Cs^+	Sr^{2+}
	NH_4^+	Mg^{2+}
		Mn^{2+}
		Cu^{2+}
		Ni^{2+}

not.

In more mechanistic considerations, other factors can interfere with cation exchange reactions/ reversibility. These can be the charge heterogeneity, the charge density (Maes, Cremers, 1977; Shainberg et al., 1987), sorption sites of clay minerals (Sawhney, 1972), clay mineral swelling (Laird, Shang, 1997) as well as the quasi-crystal configuration of clay particles in aqueous solutions, (Teppen, Miller, 2006; Kumar, Jain, 2013).

7.2.2 Ion adsorption isotherm models

Adsorption isotherm equations were initially formulated to describe gas adsorption on a solid surface. An example is the Langmuir equation (Langmuir, 1918), which, with substitution of pressure parameter with the solution concentration of a cation, can describe the adsorption of this cation on a solid phase. The non-linear form of the equation (7.16) is

$$C = \frac{K_l * b * C_{eq}}{1 + b * C_{eq}} \tag{7.16}$$

where C is the equilibrium solid-phase concentration of the cation (mg/L), C_{eq} is the equilibrium solution-phase concentration of the cation (mg/L), K_l is the monolayer adsorption capacity and b is the adsorption maximum (mg/kg). The basic requirement for implementing this equation is that the adsorbed cation forms only a sigle adsorption layer, with Sposito (1979) adding two more assumption for implementing this equation in a ion exchange reactions: (i) the adsorption sites must be uniform and localised, as well as the exchanging ions should not interact and, (ii) that the exchange is one-to-one ion process. With these considerations/assumptions a

Competitive Langmuir (CL) isotherm was thermodynamically derived, for ion exchange reactions

$$\begin{aligned} \text{(i)} \quad M_A &= \frac{K_A/K_B * a_A/a_B}{1 + K_A/K_B * a_A/a_B} \\ \text{(ii)} \quad n_1 &= \frac{b * K_1/K_2 * C_1/C_2}{1 + K_1/K_2 * C_1/C_2} \end{aligned} \tag{7.17}$$

where M_A the mole fraction of A cation adsorbed on the solid phase with a_A, a_B the activities of the cations in the equilibrium solution. K_A, K_B is the affinity parameters for each cation which can be thermodynamically calculated too, (Sposito, 1979). n_1 is the amount of adsorbed cation (mmol/gram), C_1 and C_2 the equilibrium solution concentrations of the competing cations (mmol/gram), b is the maximum adsorption and K_1, K_2 the adsortion cpacity for each cation involved as presented in (Altın et al. (1998) and references therein.)

As opposed to the specific or necessary assumption that Langmuir model requires (or the specific adsorption process it can describe), the Freundlich equation, although initially empirical derived, with Sposito (1980) thermodynamically deriving the same equation, better describes adsorption (or ion exchange) processes on a heterogeneous solid phase. The mathematical general expression of the Freundlich isotherm model is

$$C = K_f * C_{eq}^{1/n} \tag{7.18}$$

where C is the equilibrium solid-phase concentration of the cation, C_{eq} is the equilibrium solution-phase concentration of the cation, K_f indicating the adsorption capacity, while 1/n the adsoption intensity or surface heterogeneity, indicating the energy relative distribution and solid surface heterogeneity. When $0<1/n<1$, the adsorption is favourable with $1/n>1$ unfavourable, while when $1/n=1$ the adsorption is irriversible, (Hatch et al. (2012),Al-Ghouti, Da'ana (2020) and references therein).

Concluding these introductory concepts of Hofmeister theory, ion exchange mechanisms, proposed thermodynamic or mechanistic models and adsorption isotherm models, the basic background is given to address the following cation exchange results. For the analysis of these results, a more traditional approach was adopted, despite the changes of paradigm concerning the ion exchange processes that was underlined by Rotenberg et al. (2009). The thermodynamic parameters were calculated according to the conventions of Gaines, Thomas (1953, 1955) as well as the use of the Langmuir (Eq. 7.16) and Freundlich (Eq. 7.18) adsorption site models for fitting the

measured adsorption data. However, the findings of this experimental work are further discussed against the more recent theories displayed so far.

7.3 Experimental procedure

Materials

As already mentioned at the introduction, the purpose of the following experiments is to determine the equilibrium constant(s) of cation exchange reactions which involved three smectites, the nontronite-1 (NAu1), nontronite-2 (NAu2), montmorillonite (SWy3), under fully reduced conditions. All three minerals are supplied by the CMS Repository [1] in the US, (See Chapter 3, for chemical formulae of the minerals).

NAu1 and NAu2 account for the high iron content (20% w/w - 22 % w/w) model mineral, while the SWy3 accounts for the low iron content (3% w/w) mineral. The purpose of using both nontronites is to possibly observe differences in the exchange reactions, due to the structural difference they have as such, the additional NAu2 tetrahedral substitution Al^{3+} by Fe^{3+}, and the lower cation exchange capacity of NAu2, (Keeling et al., 2000). That would lead to differences in the charge distribution of the clay mineral, potentially affecting the exchange reaction. SWy3, on the other hand has some Fe^{2+} in its structure in addition to Fe^{3+} [2].

The salt solutions used are of mixed composition Na/Ca and Na/K in five different ratios 1/9, 5/5, 7.5/2.5, 9/1, with constant concentration of 0.5 M for initial saturation and 0.01 M for subsequent equilibration. salts were supllied from Sigma Aldrich (Merck) - ACS reagent grade. The actual experimental procedure is an adaptation after Shainberg et al. (1987) and Wada, Weerasooriya (1990).

Method

0.5g of Na-saturated clay mineral with < 2 μm particle size was fully reduced in a citrate/ bicarbonate/ sodium dithionite solution for a minimum of 4 hours in a glovebox (GS Glovebox Systemtechnik GmbH; N_2: 100%, O2 $<$ 1 ppm). After washing with deoxygenated-DI water and getting rid of reduction by products, the clay mineral was suspended in $30mL$ of the $0.5M$ salt solution for 60 hours. Then, after centrifugation and decanting, solids were suspended in $30mL$

[1] $(https://www.clays.org)$
[2] $(https://www.clays.org/sourceclaysdata/)$

of the $0.01M$ solution (***mixing solution***) of the same cationic ratio, three times over the course of 3 days, with supernatant, after centrifugation, of each batch retained, resulting in a $90ml$ solution denoted as ***equilibrium solution***. Solids were suspended in $30ml$ of 60-70% ethanol, centrifuged and decanted, to discard any trapped water from the previous step.

Finally, solids were suspended consecutively in $30mL$ of ammonium acetate solution with $1M$ concentration, again over 3 day, resulting in a $90mL$ ammonium acetate solution which contains the amount of the adsorbed cations during the exchange reaction, and denoted as ***extracted solution***. With this second extraction reaction, (Figure 7.2 , and Figure 7.3 reaction (2)), the concentration of the saturating cation(s) was acquired, so that the equivalent mole fraction E (Equation 7.6) can be calculated, as well as the solid phase activity coefficient lnf (Equation 7.11). All cation exchange reaction experiments were conducted in a glovebox.

Nomenclature

In the following sections clay minerals will be referred to as follows, NAu1 for nontronite-1, NAu2 for nontronite-2, SWy3, for montmorillonite. Thermodynamic parameters are the selectivity coefficient K_{gt}, the equilibrium constant K_{GT}, and the thermodynamic equilibrium constant lnK_{GT}, with gt or GT, standing for the Gaines-Thomas approach. Where values of these parameters are cited from the literature, they read as K or lnK without any subscript. Cations as Na^+, Ca^{2+}, K^+, while exchange reaction appears as (NAu1-) Na→ Ca, or Na→ K, etc. Equivalent mole fraction E and Y are noted as E_K or Y_{Ca}.

7.4 Analytical measurement and thermodynamic calculations

A Thermoscientific ICAP 6000 ICP-AES machine was used in order to measure the cation concentrations in the mixing, equilibrium and extracted solution. Standard solutions for Na^+, Ca^{2+}, and K^+ were prepared at concentrations of 0 ppm, 1 ppm, 5 ppm, 10 ppm, 20 ppm and 40 ppm. All experimental solutions were diluted 10x times to be within the linear calibration lines, for each elemental wavelength of Na^+, Ca^{2+} and K^+.

After ICP-AES data acquisition in ppm units, all concentrations are converted to molar concentrations. These will be used for ionic strength, activity coefficients and molar fractions determination. All these calculations and plotting were undertaken using Python.

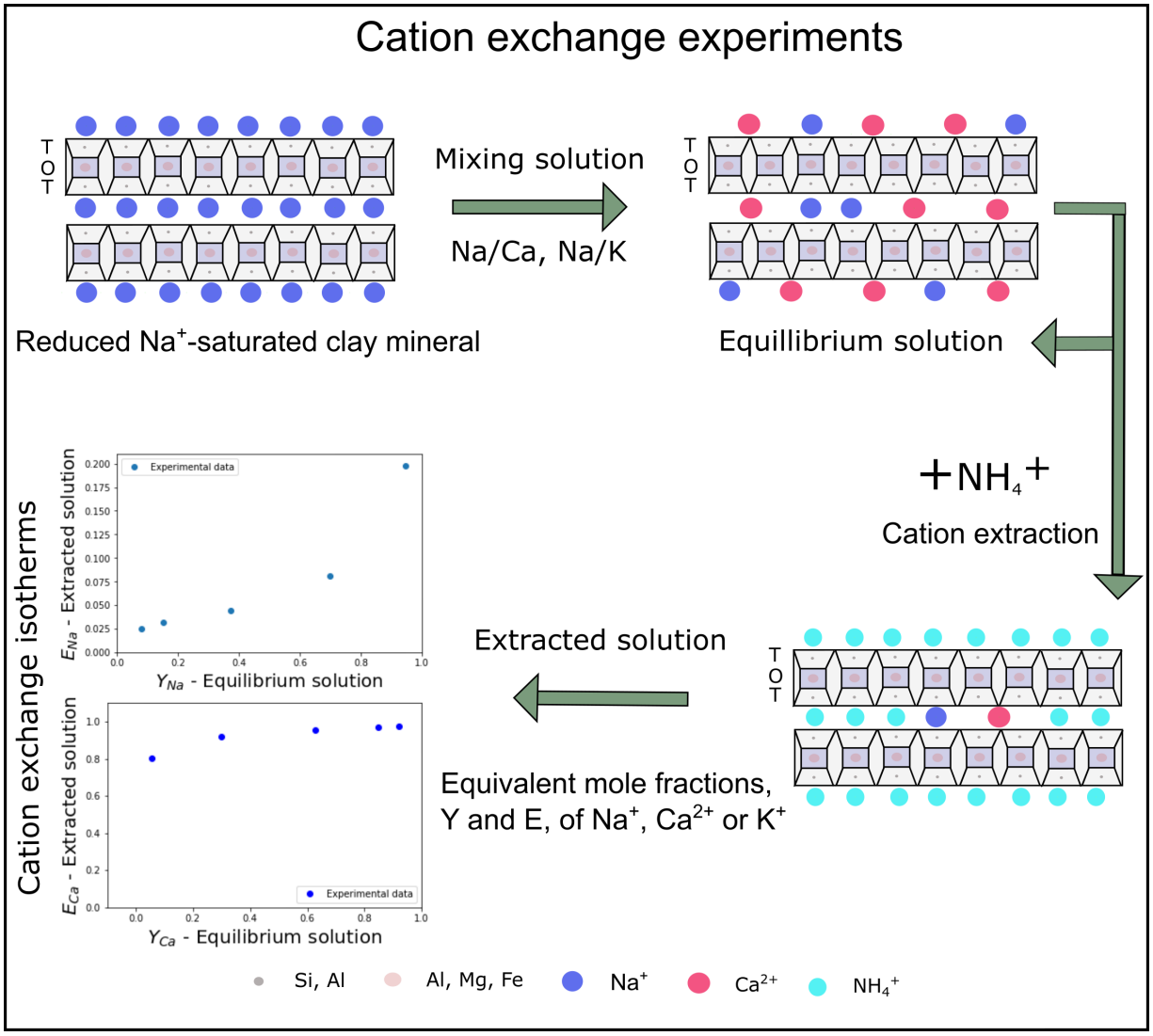

Figure 7.2: Cation exchange reaction experiment flow chart. The flow starts from the Na^+-saturated clay mineral, which is mixed first with a 0.5 M solution of Na/Ca or Na/K ratios, with subsequent equilibration of 0.01 M solution of the same ionic ratio. This 0.01 M solution is the mixing solutions noted in the graph, and equilibrium solution is the product of the clay mineral / mixing solution reaction. Afterwards, the solids were mixed with 1 M ammonium acetate (NH_4^+) for adsorbed cations extraction, which used with the equilibrium solution data, calculating the equivalent mole fraction E and Y respectively, for generating the final cation exchange isotherm graphs.

The calculation of the ionic strength of the mixing and equilibrium solution used Equation 7.19

$$I = \frac{1}{2}\sum_i z_i^2 c_i \tag{7.19}$$

where c_i and z_i are the molar concentration and the charge of ion i respectively.

For the aqueous phase ion activity coefficients, the extended version of the Debye-Huckel equation (eq.7.20) was used, in order to account for the cation size, during the reaction,

$$log\gamma_i = -Az_i^2\left(\frac{\sqrt{I}}{1+Ba_i\sqrt{I}}\right) \tag{7.20}$$

Table 7.4: Effective size of cations

Cation	a_i (nm)
Na^+	0.4
Ca^{2+}	0.6
K^+	0.3

where $A = 0.5085M^{-1/2}$ and $B = 3.281M^{-1/2}nm^{-1}$, for standard conditions of water (25°C), while a_i (Table 7.4) is the effective ion size, which includes the hydration shell, (Kielland (1937); Sposito (1981); Bethke (2007)).

For the cation exchange data shown here, the Gaines-Thomas approach was adopted using the appropriate Equations 7.6 - 7.10, although the Sposito approach, as shown in table 7.2, would give fairly similar results. Looking at the K_{gt} Equation 7.7 for the selectivity coefficient, some clarifications should be made, as to the values used for each component. For the E_{Ca} the equivalent molar fraction was calculated from the ***extracted solution***, while the Na^+ activity was calculated from the ***equilibrium solution***. Similarly, the E_{Na} was calculated from the ***extracted solution*** and Ca^{2+} was calculated from the ***equilibrium solution*** composition.

Apart from the Na-Ca exchange, which is explained so far, Na-K exchange reaction data was also obtained. In that case, appropriate modifications (Equation 7.11) are made (after (Gaines, Thomas, 1953, 1955), corresponding to the different stoichiometry of the reaction, while the calculation engagement rules, described above, remained the same. Regarding the Equation 7.10 (and Equation 7.11), the values of $lnfCa$ ($lnfK$), $lnfNa$, $lnKGT$ were explicitly calculated (See Appendix E.1). Also, the true equilibrium constant for the equivalent mole fraction range of a study, can be determined by calculating the area of a plot of lnKgt-ECa (or lnKgt-EK), *vida*

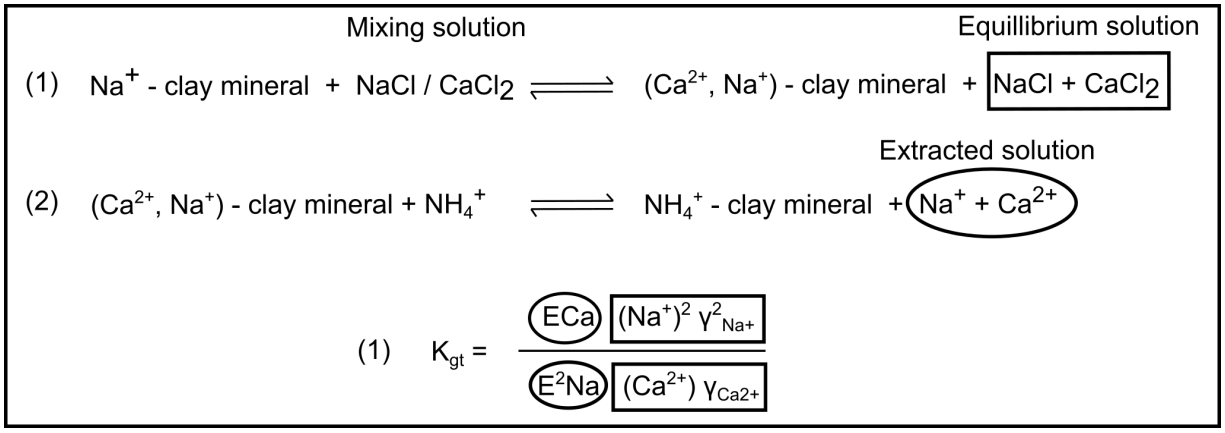

Figure 7.3: Schematic representation of the Na→Ca cation exchange reaction of a reduced clay mineral. The K_{gt} was calculated using the equivalent mole fraction E, of Ca and Na, from the extracted solution, as well as the concentration () and activity coefficient, γ, of Na^+ and Ca^{2+} in the equilibrium solution. Clay mineral solids of reaction (1) products should be considered with stoichiometric subscript of 2, due to Ca^{2+} saturation. Practically though, clay mineral will be saturated with both Na^+ and Ca^{2+} as shown.

infra.

For every clay mineral/cation exchange reaction considered here, the standard free energy ΔG_{ex} of exchange was calculated, according to the Equation 7.21, with lnK_{GT} explicitly calculated from Equation 7.10 (or Equation 7.11(iii)), R the gas constant in Joule / mole*K and T, the absolute temperature at standard conditions, in Kelvin

$$\Delta G_{ex} = -RTlnK_{GT} \tag{7.21}$$

Along with the thermodynamic evaluation presented, cation exchange isotherms were acquired by plotting the equivalent molar fraction of the cation i (Na^+, Ca^{2+}, K^+) in the equilibrium solution Y_i versus the equivalent molar fraction of the same cation (post-reaction solid phase) in the extracted solution E_i. Isotherm fitting was performed using the IsoFit® (developed by Matott, Rabideau (2008)), for all suitable isotherms that can describe such processes, with only the Langmuir and Freundlich models giving good fitting correlations. The input data used were the equivalent mole fractions of Ca^{2+} and K^+ in the equilibrium and extracted solutions, and not the equilibrium concentrations or the respective mole fractions. However, the equivalent mole fraction of K^+ in the Na→K reaction is the same with the mole fraction, since the cationic stoichiometry is 1:1.

7.5 Results

In this section the results are present per mineral used, covering NAu1, NAu2 and SWy3, under reduced conditions, only. For each mineral section, both Na→Ca and Na→K exchange reactions are considered with exchange isotherms and cation exchange equilibrium constant be given for each case.

As a reference, the two exchange reactions will have a chemical form of:

$$\begin{aligned} &\text{(i)} \quad 2NaX + CaCl_2 = CaX_2 + 2NaCl \\ &\text{(ii)} \quad NaX + KCl = KX + NaCl \end{aligned} \tag{7.22}$$

7.5.1 Nontronite-1 (NAu1)

Na → Ca exchange reactions

For the case of NAu1, the cation exchange (desorption (Na^+) and adsorption (Ca^{2+})) isotherms are presented in Figure 7.4.

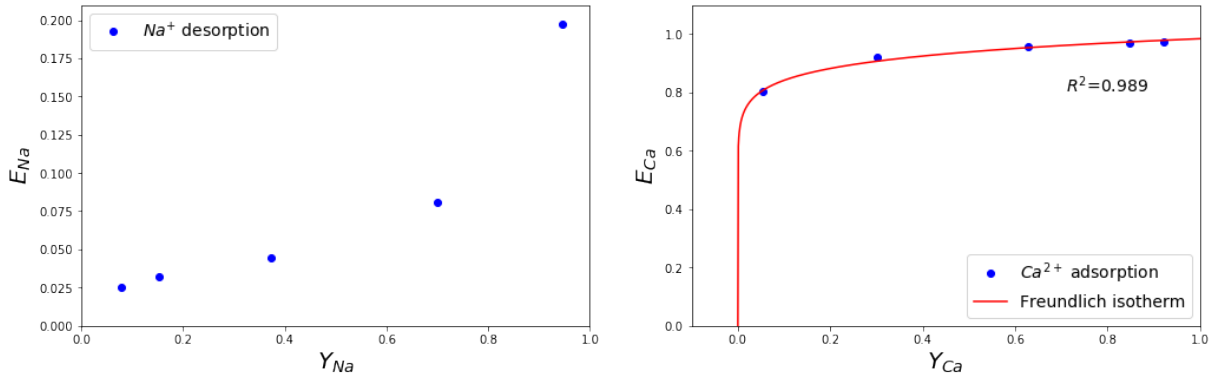

Figure 7.4: Cation exchange isotherms of sodium (left) and calcium (right) with NAu1 as exchanger phase. E_i, Y_i denote the equivalent mole fraction of the denoted cation in the adsorbed and aqueous phase upon equilibrium, respectively. Red line is the fitted Freundlinch isotherm to the experimental data.

Looking at the Ca^{2+} adsorption isotherms in Figure7.4, it is a H-curve isotherm type (Sposito, 1981, pg. 134), which corresponds to a high affinity of the cation examined, in that case Ca^{2+}. Using the IsoFit®, a Freundlich isotherm was fitted, with fitting parameters of $K_f = 0.984$, $1/n = 0.068$ indicating a strong Ca adsorptivity on the clay mineral surface, with $R^2 = 0.989$, as shown in the graph too. For the E_{Ca} values below 0.8, the Freundlich isotherm is extrapolated

to $(0, 0)$.

Although the adsorption isotherm can be a good indication of the result of a reaction, the reaction exchange equilibrium constant should be calculated too. In Table 7.5 the equilibrium K_{gt}, the natural logarithm of the equilibrium exchange constant lnK_{GT} (Eq. 7.10) along with the free energy of the exchange reactions ΔG are presented. The equilibrium constant has an average value of 7.97 kJ/mole. However, according to the K_{gt} values of each Na/Ca ratio, at low Ca^{2+} mixing-solution content, high Ca^{2+} selectivity is expressed by NAu1. Same interpretation was obtained from looking at the ΔG values, which only the Na/Ca =9/1 ratio takes negative values, indicating that the reaction was favoured towards the right, i.e. cation exchange. In overall, the average ΔG was positive, showing that the reaction did not take place spontaneously.

Table 7.5: NAu1 equilibrium constant and free energy of exchange for the reaction Na/Ca.

Na:Ca ratios	Kgt	lnKGT	ΔG (J/mole)
1/9	0.827	-6.543	16239.59
2.5/7.5	1.839	-5.291	13133.11
5/5	6.198	-3.408	8459.33
7.5/2.5	12.974	-1.462	3629.69
9/1	17.839	0.638	-1585.46
average	7.936	-3.213	7975.25

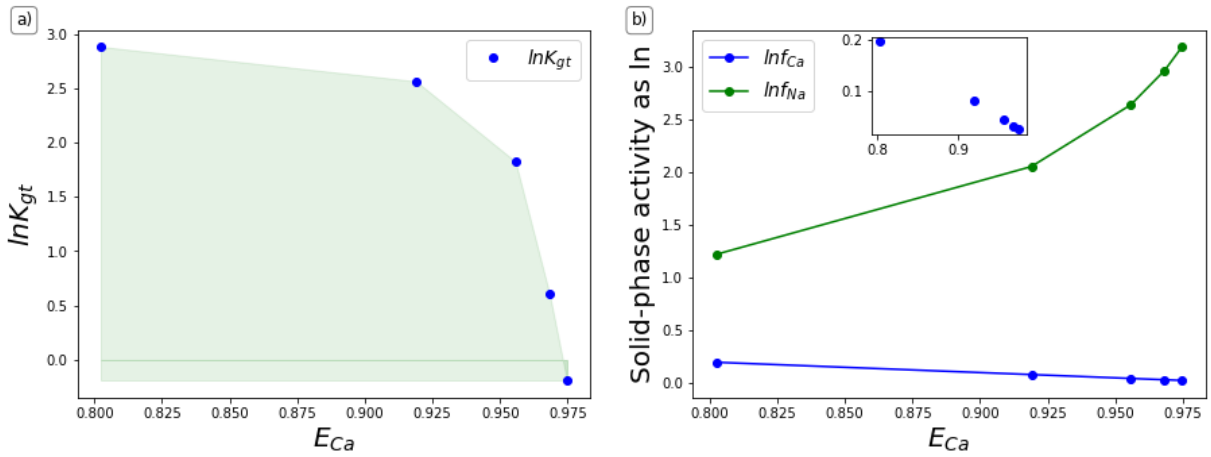

Figure 7.5: a) The equivalent mole fraction of Ca^{2+}, E_{Ca}, in the solid-phase after equilibration against the natural logarithm of the equilibrium coefficient lnK_{gt}. b) Natural logarithms of solid-phase activity coefficients lnf_{Ca} and lnf_{Na} interrelation when plotted with E_{Ca}, the equivalent mole fraction of Ca^{2+} after equilibration. Sub-figure shows the negative linear relation between the lnf_{Ca} and the E_{Ca} for the particular range of cation concentration.

In Figure 7.5a, the E_{Ca} against the lnK_{gt}, the equivalent mole fraction of Ca^{2+} in the

solid phase after equilibrium (extracted solution), and the natural logarithm of the selectivity constant, respectively, are plotted. From this graph the true equilibrium constant can be acquired by integrating the area below the curve, for the known values of lnK_{gt} and E_{Ca}, (Gast, 1969; Wada, Weerasooriya, 1990)

The evaluation of the solid-phase activity coefficient lnf_{Ca} and lnf_{Na}, after equilibrium can be appreciated in the Figure 7.5b, with lnf_{Na} taking increasingly higher values as E_{Ca} increases, while lnf_{Ca} decreases. The higher activity of Ca in the solid-phase at lower concentrations is in accordance with the lower free energy at the same range of concentration as in Table 7.5.

Na → K exchange reaction

Looking at the Na→K exchange case of NAu1, the K^+ exchange isotherm (Fig.7.6) has a shape of L-curve type (Sposito, 1981), indicating affinity toward the substituting cation K^+.

A Freundlich model isotherm was fitted, with parameters of $K_f = 1.081$, $1/n = 0.452$ and $R^2 = 0.965$.

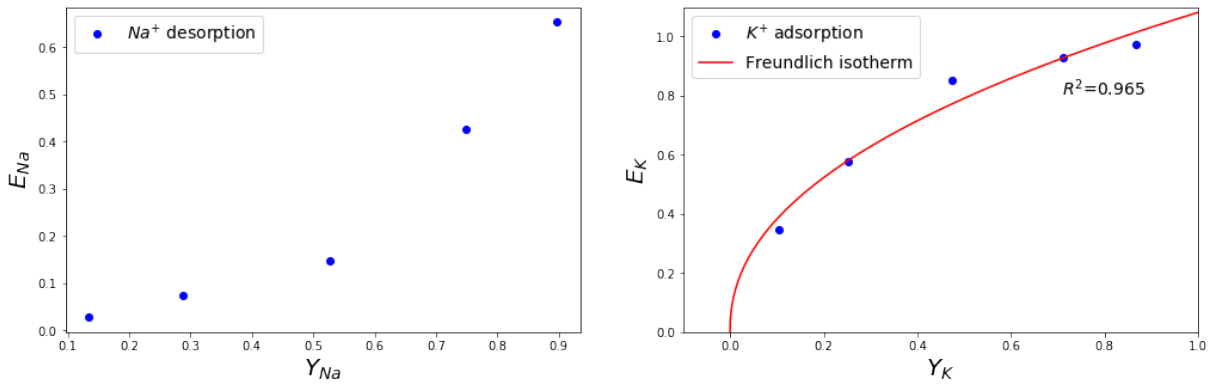

Figure 7.6: Cation exchange isotherms of sodium (left) and potassium (right) with NAu1 as exchanger phase. E_i, Y_i denote the equivalent mole fraction of the denoted cation in the adsorbed and aqueous phase upon equilibrium, respectively. Red line is the fitted Freundlinch isotherm to the experimental data.

Calculated thermodynamic parameters are presented at Table 7.6, with K_{gt} being positive for all Na:K ratios. The average negative free energy of the Na→ K reaction indicate that it takes place spontaneously, with NAu1 preferring K^+ over Na^+, in that case. In Figure 7.7a the E_K versus lnK_{gt} is plotted, showing that for NAu1 across the five Na/K rations tested, there was no big selectivity difference. Additionally, in Figure 7.7b the solid-phase activities coefficients of Na^+ and K^+, as logarithms, show that they are equivalent, potentially meaning small inter-

cation interaction or competitiveness. Since the logarithms have the value of zero the f_{Na} and f_{Ca} will be equal to 1, after equilibrium the system acts as ideal solid solution, similar to the hypothesis of Vanselow (1932) .

Table 7.6: NAu1 equilibrium constant and free energy of exchange for the reaction Na/K.

Na:K ratios	Kgt	lnKGT	ΔG (J/mole)
1/9	8.138	2.096	-5203
2.5/7.5	7.920	2.069	-5135
5/5	9.853	2.287	-5677
7.5/2.5	6.255	1.833	-4550
9/1	7.219	1.976	-4905
average	7.877	2.052	-5094

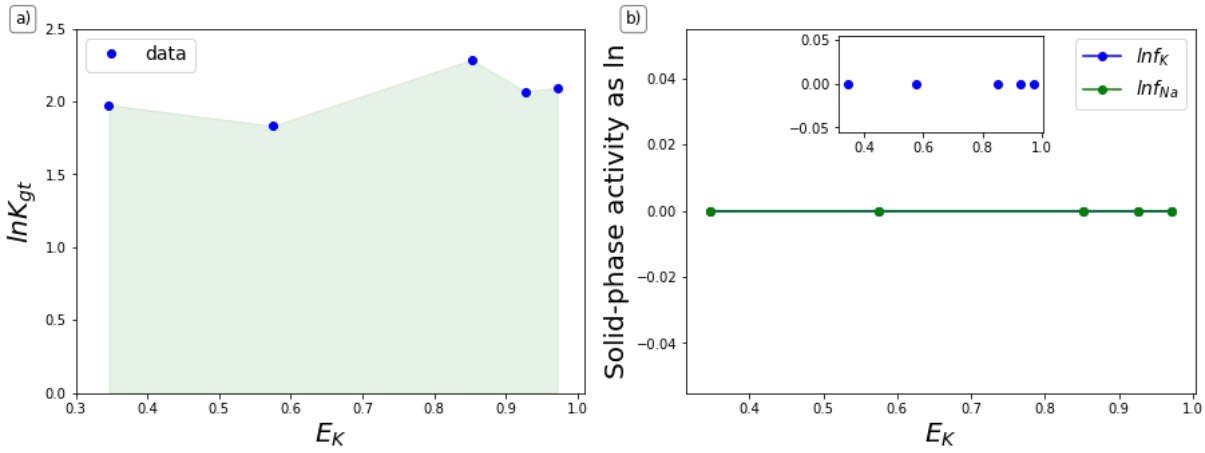

Figure 7.7: a) The equivalent mole fraction of K^+, E_K, in the solid-phase after equilibration against the natural logarithm of the equilibrium coefficient lnK_{gt}. b) Natural logarithms of solid-phase activity coefficients lnf_K and lnf_{Na} interrelation when plotted with E_K, the equivalent mole fraction of K^+ after equilibration. Sub-figure shows the relation between the lnf_K and the E_K for the particular range of cation concentration

7.5.2 Nontronite-2 (NAu2)

Na →Ca exchange reaction

The cation exchange isotherms for NAu2 are shown in Figure 7.8. Similarly, a Freundlich isotherm was fitted, for the Ca^{2+} adsorption isotherm, with extrapolation being applied for the lower values of E_{Ca}. Fitting parameters were $K_f = 0.961$, $1/n = 0.06$, indicating a high Ca^{2+} selectivity on the NAu2 surface, forming a H-curve adsorption isotherm type with $R^2 = 0.898$.

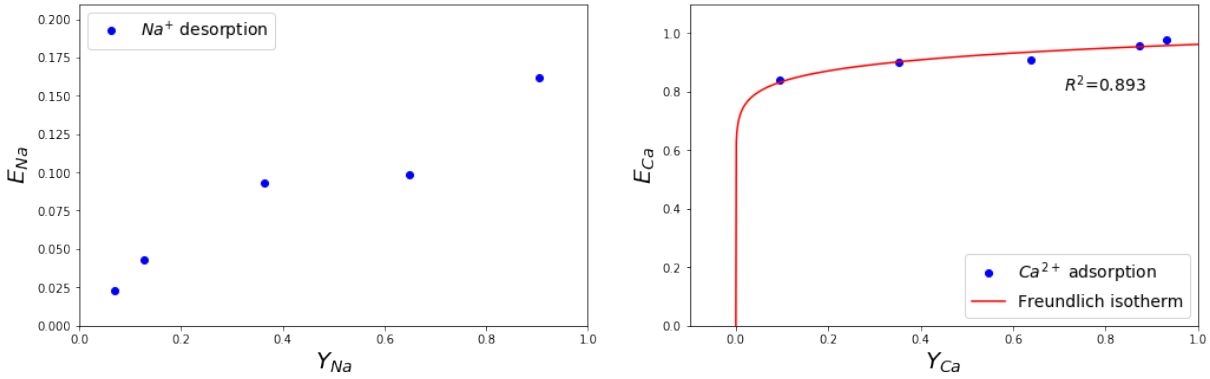

Figure 7.8: Cation exchange isothemrs of Na^+ (left) and Ca^{2+} (right) with NAu2 as exchanger phase. E_i, Y_i denote the equivalent mole fraction of the denoted cation in the adsorbed and aqueous phase upon equilibrium, respectively. Red line is the fitted Freundlinch isotherm to the experimental data.

At Table 7.7, the valuae of the exchange coefficients, the logarithm of the equilibrium constant and the free energy of the reaction NAu2 - Na→Ca can be found. The logarithm of the equilibrium constant took negative values for all Na/Ca ratios, while the free energy was positive respectively. As Ca^{2+} concentration got lower, the free energy got lower too, indicating a less energy-consuming reaction. Additionally, at Figure 7.9a the E_{Ca} versus the lnK_{gt} was plotted from which the true equilibrium constant can be found. At Figure 7.9b the relation between the solid-phase activity coefficient with the E_{Ca} was plotted, showing a a higher activity of Na^+ over Ca^{2+} at all tested concentrations.

Table 7.7: NAu2 equilibrium constant and free energy of exchange for the reaction Na/Ca.

Na:Ca ratios	Kgt	lnKGT	ΔG (J/mole)
1/9	1.235	-6.383	15842
2.5/7.5	1.497	-4.910	12185
5/5	1.914	-3.093	7677
7.5/2.5	5.232	-1.973	4897
9/1	12.722	-0.094	233
average	4.520	-3.290	8167

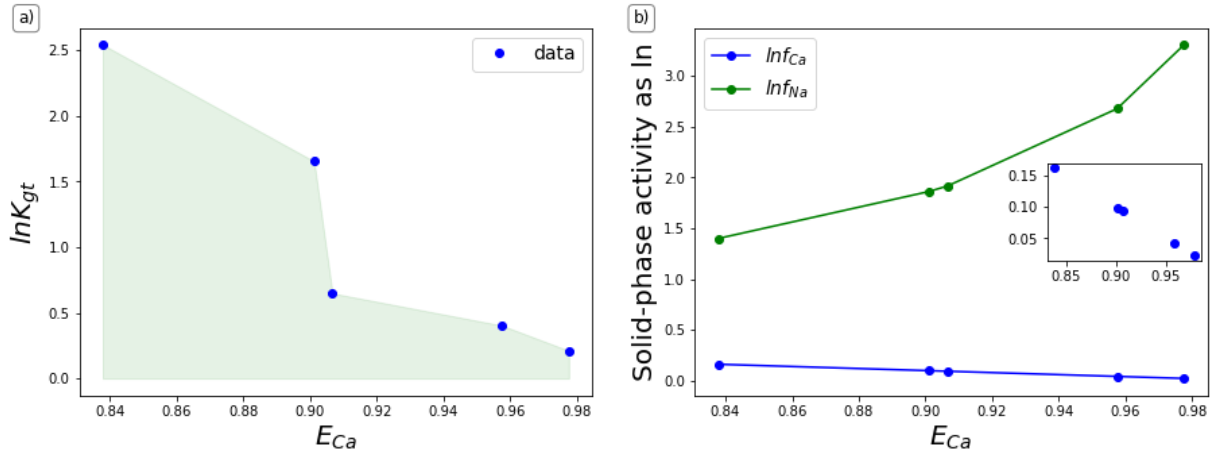

Figure 7.9: a) The equivalent mole fraction of Ca^{2+}, E_{Ca}, in the solid-phase after equilibration against the natural logarithm of the equilibrium coefficient lnK_{gt}. b) Natural logarithms of solid-phase activity coefficients lnf_{Ca} and lnf_{Na} interrelation when plotted with E_{Ca}, the equivalent mole fraction of Ca^{2+} after equilibration. Sub-figure shows the negative linear relation between the lnf_{Ca} and the E_{Ca} for the particular range of cation concentration.

Na → K exchange reaction

For the case of NAu2 reacting with a Na→K aqueous solutions, the exchange isotherms are given below at Fig. 7.10. Similarly to NAu1, the K^+ was a L-type of isotherm, indicating a preference of NAu2 towards the substituting cation. A Freundlich model isotherm was fitted with parameters $K_f = 1.022$, $1/n = 0.316$ and $R^2 = 0.981$.

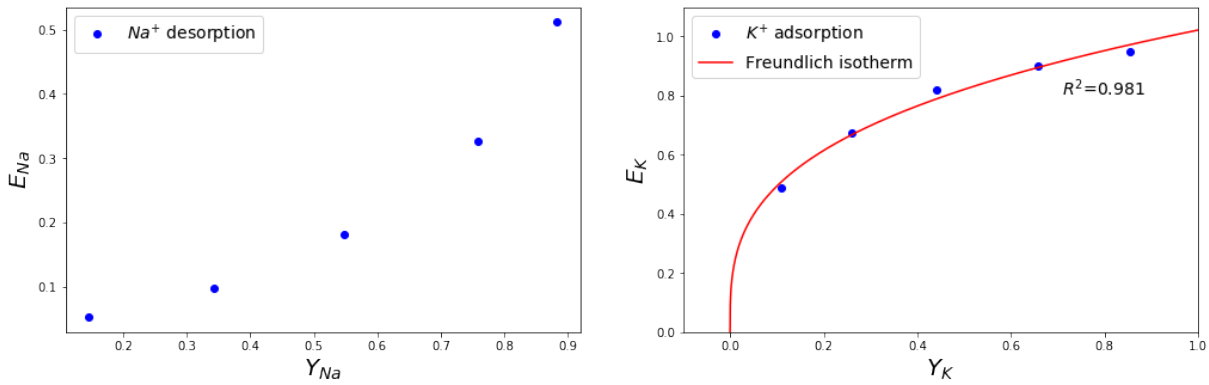

Figure 7.10: Cation exchange isotherms of Na^+ (left) and K^+ (right) with NAu2 as exchanger phase. E_i, Y_i denote the equivalent mole fraction of the denoted cation in the adsorbed and aqueous phase upon equilibrium, respectively. Red line is the fitted Freundlinch isotherm to the experimental data.

NAu2 under the Na→K reaction show a high average equilibrium selectivity coefficient K_{gt}

in Table 7.8. In Figure 7.11a the relation between the lnK_{gt} and the E_K is shown. At high K^+ concentrations (Na/K = 1/9, 2.5/7.5) the lnK_{gt} takes high values of around 13. At the mid-to-lower K concentrations (Na/K = 5/5, 7.5/0.5, 9/1) the lnK_{gt} is one order of magnitude lower, with slightly increasing values as Na^+ concentration increases. The negative free energy values shown in Table 7.8, correspond to this trend, showing however that the reaction at all tested Na/K ratios favoured Na-to-K exchange. Finally, in Figure 7.11b, the two solid-phase activity logarithms were equal to zero, indicating minimum cation interaction during the reaction.

Table 7.8: NAu2 equilibrium constant and free energy of reaction exchange Na/K.

Na:K ratios	Kgt	lnKGT	ΔG (J/mole)
1/9	3.909	1.363	-3383
2.5/7.5	6.770	1.912	-4746
5/5	9.574	2.259	-5606
7.5/2.5	11.809	2.468	-6127
9/1	13.943	2.635	-6539
average	228945	6.774	-16811

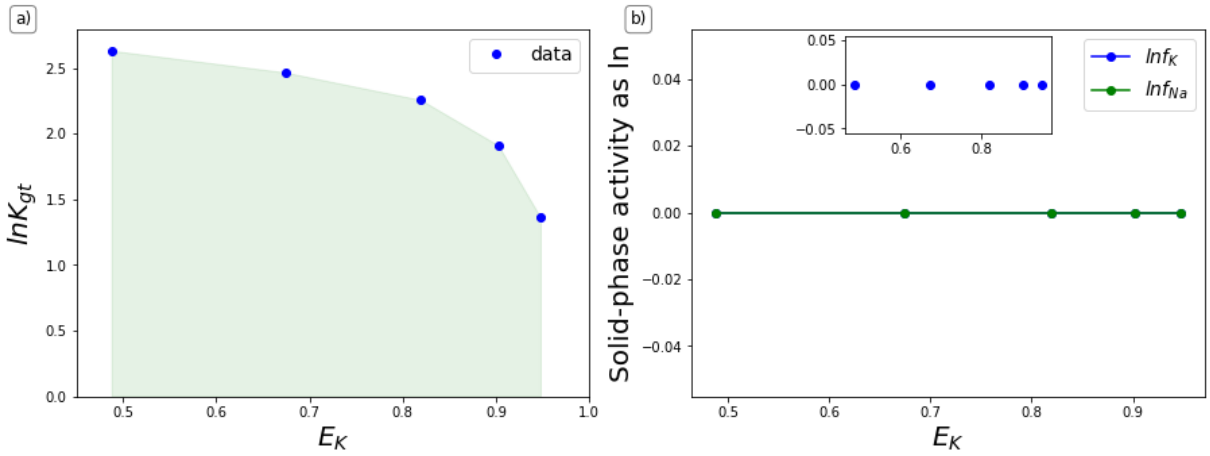

Figure 7.11: a) The equivalent mole fraction of K^+, E_K, in the solid-phase after equilibration against the natural logarithm of the equilibrium coefficient lnK_{gt}. b) Natural logarithms of solid-phase activity coefficients lnf_K and lnf_{Na} interrelation when plotted with E_K, the equivalent mole fraction of K^+ after equilibration. Sub-figure shows the relation between the lnf_K and the E_K for the particular range of cation concentration.

7.5.3 Montmorillonite (SWy3)

Na → Ca exchange reaction

The montmorillonite SWy3 was also used for this kind of experiments as a low iron-bearing clay mineral, which occur more frequently in sandstone reservoirs. This mineral has both Fe^{2+} and Fe^{3+}, in both tetrahedral and octahedral sheets, yet in small amounts. That would give a different behaviour in adsorption/desorption experiments, among many other, as shown in Figure 7.12.

Examining the Ca^{2+} adsorption isotherm, a Langmuir model isotherm was fitted and plotted along with the experimental data. The fitting parameters took values of $K_l = 1.074$, $b = 16.976$ and $R^2 = 0.917$.

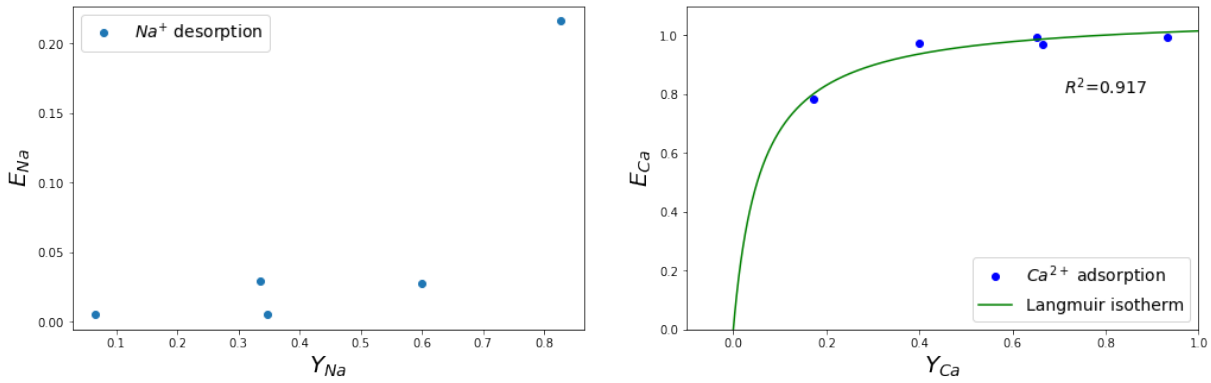

Figure 7.12: Cation exchange isotherms of Na^+ (left) and Ca^{2+} (right) with SWy3 as exchanger phase. E_i, Y_i denote the equivalent mole fraction of the denoted cation in the adsorbed and aqueous phase upon equilibrium, respectively. Green line is the fitted Langmuir isotherm to the experimental data.

SWy3 exhibited a fluctuating behaviour regarding the selectivity of Ca^{2+}, as reaction reached equilibrium. This can be observed in Table 7.9, with K_{gt} values not having a stable relation to the decreasing Ca^{2+} concentration for Na/Ca ratios tested. Consequently, the lnK_{gt} - E_{Ca} plot (Fig. 7.13a) showed no distinct data trend, with a convex shape being the most probable. In Figure 7.13b it is shown that the $lnfNa$ took higher values at high Ca^{2+} concentration, thus the two graphs do not coincide in their interpretation. However, the average free energy of the reaction has a positive value (Table 7.9), supporting the interpretation of figure 7.13b.

Table 7.9: SWy3 equilibrium constant and free energy of reaction exchange Na/Ca

Na:Ca ratios	Kgt	lnKGT	ΔG (J/mole)
1/9	12.852	-7.032	17452
2.5/7.5	340.974	-3.602	8941
5/5	9.274	-3.831	9508
7.5/2.5	45.323	-2.396	5948
9/1	2.114	-1.311	3254
average	82.107	-3.635	9021

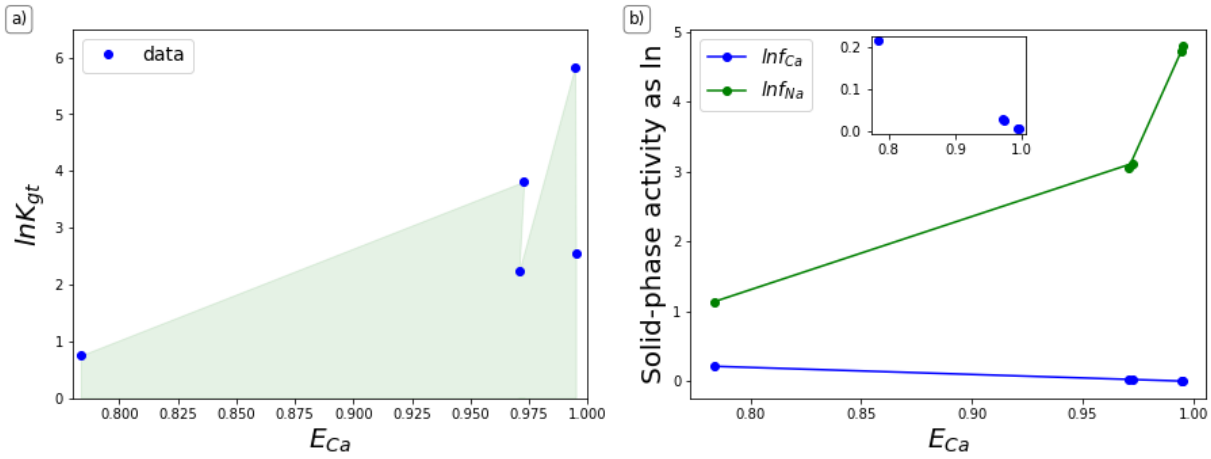

Figure 7.13: a) The equivalent mole fraction of Ca^{2+}, E_{Ca}, in the solid-phase after equilibration against the natural logarithm of the equilibrium coefficient lnK_{gt}. b) Natural logarithms of solid-phase activity coefficients lnf_{Ca} and lnf_{Na} interrelation when plotted with E_{Ca}, the equivalent mole fraction of Ca^{2+} after equilibration. Sub-figure shows the negative linear relation between the lnf_{Ca} and the E_{Ca} for the particular range of cation concentration.

Na → K exchange reaction

The last case of Na→K reaction with SWy3 is shown below. The exchange isotherms of sodium and potassium can be seen in Fig. 7.14. More specifically, the K^+ adsorption isotherm is of L-type curve, with Freundlinch and Langmuir model isotherms been fitted to the data. The fitting parameters took values of $K_l = 1.146$, $b = 4.73$ and $R^2 = 0.980$ for the Langmuir isotherm, while for the Freundlich these were $Kf = 0.996$, $1/n = 0.369$ and $R^2 = 0.925$ with Langmuir isotherm giving a slightly better fitting. The K_l and K_f values of the two models are very similar, corresponding to the adsorption capacity of the reduced SWy3. The main fitting difference was for Freundlich isotherm, which seems to overestimate the E_K values at low and high concentrations of K^+ in the clay mineral.

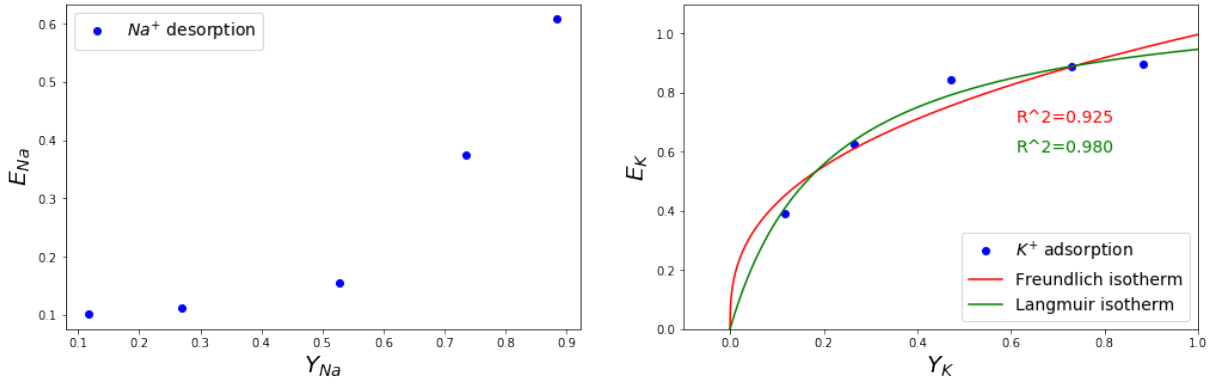

Figure 7.14: Cation exchange isotherms of Na^+ (left) and K^+ (right) with SWy3 as exchanger phase. E_i, Y_i denote the equivalent mole fraction of the denoted cation in the adsorbed and aqueous phase upon equilibrium, respectively. Green line is the Langmuir isotherm and red line the Freundlich isotherm fitted to the experimental data.

The Swy3- Na→K reaction exhibited positive K_{gt} values across the Na/K ratios tested, Table 7.10. The corresponding lnK_{gt} - E_K graph in Fig. 7.15a shows that at for the K concentration the reaction favoured the adsorption of K over Na, even when Na^+ and K^+ had equal concentrations in the solution. When Na^+ concentrations increased then the reduced SWy3 had a higher affinity towards Na^+. Looking at the free energy values in Table 7.10, the reaction took place more easily at high Na^+ concentrations, with the average free energy remaining negative,in overall. The values of lnf_{Na} and lnf_K against the E_K are shown in Figure 7.15b, being zero, hence the f_{Na} and f_K are equal to one, indicating little interaction between the two cations.

Table 7.10: SWy3 equilibrium constant and free energy of reaction exchange Na/K.

Na:K ratios	Kgt	lnKGT	ΔG (J/mole)
1/9	1.812	0.594	-1475
2.5/7.5	4.529	1.510	-3748
5/5	9.899	2.292	-5689
7.5/2.5	7.440	2.006	-4980
9/1	7.977	2.076	-5153
average	6.331	1.696	-4209

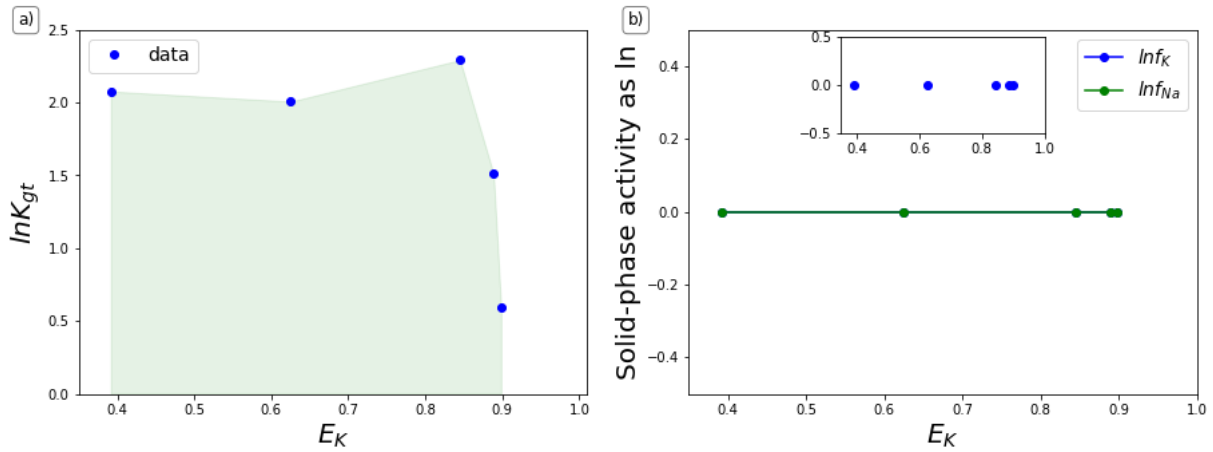

Figure 7.15: a) The equivalent mole fraction of K^+, E_K, in the solid-phase after equilibration against the natural logarithm of the equilibrium coefficient lnK_{gt}. b) Natural logarithms of solid-phase activity coefficients lnf_K and lnf_{Na} interrelation when plotted with E_K, the equivalent mole fraction of K^+ after equilibration. Sub-figure shows the relation between the lnf_K and the E_K for the particular range of cation concentration

7.6 Discussion

Cation adsorption on clay minerals involves mainly three adsorption sites, the basal plane, edge site and interlayer space. The edge site charges are traditionally considered to be depended on pH, which are positive in an acidic medium and progressively negative in increasing pH values, (Lagaly, 2006). Adsorption also, can be affected by temperature as well as reaction time, however in the above experiments, standard conditions were only considered, with pH being at the vicinity of 7-8. As such, variations that the above factors could introduce to the experiments were eliminated.

7.6.1 Experimental methodology approach

In Appendix E.2, a series of tables are presented, which demonstrate the salt solution composition, for the initial mixing solution, the equilibrium solution and extracted solution in ppm (unless stated otherwise). As described in the methods section (Section 7.3), there is a saturation step of Na/Ca or Na/K solution ratios of 0.5 M with the mixing solution given in Tables E.1 - E.6, having a total concentration of 0.01 M. It can be seen that the equilibrium solution is heavily affected by this first saturation step, as the equilibrium solution exhibited higher concentration of Na^+, Ca^{2+}, or K^+ than the mixing ones (in ppm). In fact, no such effects were explicitly

reported on the works that these set of experiments was based on (Wada, Weerasooriya, 1990; Shainberg et al., 1987). On the other hand, the extracted solution, which corresponds on the adsorbed cations by the clay minerals, exhibited a lower concentration than the mixing solution. At the last column of these tables, the total adsorbed ionic concentration is also given in milliequivalents (meq). It can be seen that, for each mineral and reaction, this total concentration stayed very similar across the different Na/Ca or Na/K salt ratios. This is an interesting observation which will be discussed later in conjunction with the reduction effects on cation exchange reactions.

7.6.2 Na → Ca exchange on Na^+- clay minerals

Thermodynamics

Evaluating the thermodynamics of each exchange reaction, several similarities and differences can be observed. For the Na→Ca reaction the three minerals exhibited positive average selectivity coefficient (K_{gt}) Tables 7.5, 7.7, 7.9, with the natural logarithm of each case being plotted against the equivalent Ca^{2+} mole fraction in the solid phase, E_{Ca}, as shown in Figures 7.5, 7.9, 7.13. The area below the experimental data is shaded, and accounts for the real equilibrium constant $lnKGT$ (Gast, 1969; Wada, Weerasooriya, 1990; Bleam, 2012). In a full Ca^{2+} (or Na^+) concentration range (or equally mole fraction range) from 0-1, the integral of the selectivity coefficient lnK_{gt} gives the true equilibrium constant lnK_{GT}. For this study, and the measured experimental data the corresponding areas, hence the equilibrium constants, are 0.414 for NAu1, 0.172 for NAu2, and 0.523 for SWy3, with E_{Ca} ranging from 0.8 to 1, showing that in a highly reduced environment, SWy3 will perform better in exchanging Na^+ for Ca^{2+}. Literature data for the same Na→Ca reaction, but with different clay minerals and under oxidised conditions, showed $lnKGT$ values of 0.717 in Wada, Weerasooriya (1990), 0.196 (per equivalent of exchange) in Maes, Cremers (1977) and Gapon's selectivity coefficient value of 0.455 in Shainberg et al. (1987).

It is important to note that diagrams of selectivity coefficient (lnK_{gt}) versus the equivalent mole fraction of adsorbed cation (E_i), exhibited different relationships in the literature. In some cases, this relation is linear e.g. (Wada, Weerasooriya, 1990) while in other it is of higher polynomial order, e.g. (Gast, 1969). Direct comparison of true equilibrium constant $lnKGT$ values in such different systems and relations could lead to incorrect conclusions. Benson (1982),

in an ion exchange tabulation work, noted the equilibrium constant variability of a reaction, of homo-valent or hetero-valent nature, between just two montmorillonites. Figure 1 in Maes, Cremers (1978) demonstrates how different solid phase, as the exchanger component of a Na→Ca reaction (See Appendix, Figure E.1) , along with other parameters such as cation exchange capacity, or e.g. the mixing solution ionic strength, can affect the reaction progression and the cation distribution in the aqueous and solid phase, upon equilibrium.

After Equation 7.10 was solved explicitly and values were fed in equation 7.21, as shown in tables 7.5, 7.7, 7.9 at third and fourth columns, respectively, the free energy of the three mineral system can be compared. All three minerals have a similar average free energy, ΔG, at 7.95 kJ/mole for NAu1, 8.16 kJ/mole for NAu2 and 9.02 kJ/mole for SWy3. Since $\Delta G > 0$ then the reaction does not take place spontaneously, but it requires energy. However, there is trend which indicate that, as the Ca^{2+} concentration dropped, the ΔG also dropped, indicating reaction favourability towards the right hand side of the Reaction 7.22(i). This is specially profound for the NAu1 case as in Table 7.5, where the final ratio of Na:Ca = 9/1, gives $\Delta G < 0$.

In Figures 7.5, 7.9 and 7.13 the equivalent mole fraction of Ca^{2+}, E_{Ca}, versus the logarithm of solid-phase activity are plotted, showing an increase of Na^{+} activity as the E_{Ca} increased, or in other words, at low Na^{+} concentrations, for all three mineral phases. In absolute values, Na^{+} seemed to exhibit higher activity coefficient on SWy3 surface, Figure 7.13, than the other two mineral, while Ca^{2+} activity coefficient is almost the same for three minerals. That coincides with the high adsorption of Ca^{2+}, as indicated by the adsorption isotherms.

Ca^{2+} adsorption in clay minerals

From an experimental point of view, the Ca^{2+} adsorption isotherms, showing a rapid Ca^{2+} saturation of the clay minerals sites, forms an adsorption plateau at higher E_{Ca} values. Knowing that the clay minerals are heterogeneous materials, and having fitted a Freundlich isotherm (for NAu1 and NAu2) supporting that, it can be assumed that there are sites with stronger affinity to Ca^{2+}. Those sites will adsorb Ca^{2+}, leading to an early saturation of the clay mineral with the said cation (Shainberg et al., 1980), as well as to a decrease of the surface potential of the clay mineral, consequently reducing the drive energy for further adsorption (Nir, 1986; Nir et al., 1986). In conjunction with the thermodynamic approach made, we see that at high Ca^{2+} concentration the K_{gt} is lower than in high Na^{+} concentration (Tables 7.5, 7.9 7.13). A

similar behaviour, however, was observed (Shainberg et al., 1980) when testing an illite which is a non-expandable clay mineral, while the tested montmorillonite increased Ca^{2+} selectivity with increasing Ca^{2+} concentration. It is postulated that expandable smectites, as those in our case, would form quasi-crystal on high E_{Ca} values (or high Ca^{2+} concentration) and that should affect cation selectivity. The external sites of the quasi-crystals should exhibit a preference on Na^{+} while the internal sites should exhibit a selectivity for Ca^{2+} (Shainberg et al., 1980). This can be explained applying the diffuse double layer theory, as high Ca^{2+} adsorption on the outer sites, would diminish the electric potential which in turn will decrease too, not being able to continue this process, hence Na^{+} will be preferred in that case. On the other hand, within the space of the internal site, the double layer of each clay platelet will be combined leading to an increased electric potential and a strong interaction with Ca^{2+} cations (Shainberg et al. (1980) and references therein, with similar observation been made by Endo et al. (2002); Kopittke et al. (2006)). All in all, this inverse behaviour of the smectites, under reduced conditions, could be an indication of clay platelet dispersion, during the experiments, with lack of quasi-crystal formation, due to the increased negative charges, as an effect of the reduction.

7.6.3 Na → K exchange on Na^{+} - clay minerals

Thermodynamics

For the Na→K reaction, the natural logarithm of the selectivity coefficient lnK_{gt} coincides to the logarithm of the thermodynamic equilibrium constant, as already indicated in Equation 7.11. In Tables 7.6, 7.8, 7.10 these values are presented along with the free energy ΔG, for each Na/K ratio. For all minerals, the $\Delta G < 0$, with NAu1 exhibiting a similar free energy for all the Na/K ratio concentrations, while NAu2 and SWy3 exhibited a higher (less negative) ΔG at the high K^{+} concentration end. Interestingly, for the Na/K ratios 9/1-5/5, the NAu1, and SWy3 the lnK_{gt} values are closer (Figures 7.7, 7.15), even though they have different CEC and iron content. One explanation for that could be the fact that, SWy3 compensates the increase in negative charges, upon reduction, by adsorbing cations (Drits, Manceau, 2000). On the other hand, NAu2 for the same Na/K ratios has higher lnK_{gt} than both other clay minerals (Figure 7.11), potentially affected by the charges originating from the tetrahedral Al-to-Fe substitutions. Integrating the area below the data one finds that the true thermodynamic equilibrium (for the tested concentration range) is 1.26 for NAu1, 1.06 for NAu2 and 1.04 for SWy3. Studies on the

same exchange reaction using different montmorillonites, under oxidised conditions, have shown equilibrium exchange constant lnK values spanning from 0.256 to 0.609 (Benson, 1982)

Regarding the logarithms of activity coefficient as shown in Figures 7.7b, 7.11b, 7.15b, they are equal to zero, (or alternatively $f_{Na}, f_{Ca} = 1$), meaning that cations act in the same manner on minerals surface. However, as we saw, relative concentration of Na/K does have an effect, with Na^+ being favoured at low concentrations, especially for the SWy3 case at Figure 7.15a.

K^+ adsorption in clay minerals

The K^+ adsorption isotherms, of L-type (Sposito, others, 1984), showed a lesser competition between the two homo-valent cation, when compared with the Ca^{2+} adsorption isotherms. Of course it is known that K^+ is preferred by clay minerals, over Na^+ (and Ca^{2+}). The thermodynamic evaluation showed a relative Na/K concentration dependence, which the higher the Na^+ concentration, the higher the K_{gt}, especially for NAu2 and SWy3, as NAu1 showed similar values across the Na/K ratios.

7.6.4 Effects of iron content distribution in clay minerals - Adsorption models comparison

In Table 7.11 the model isotherm fitting parameters can be compared for each reaction Na→Ca and Na→K in respect to each mineral used. Comparing the two high iron-content minerals of NAu1 and NAu2, with a Freundlich isotherm fitted, it can be seen that they have very similar adsorption capacity -K_f, 0.984 mg/g, 0.961 mg/g and adsorption intensity - 1/n, 0.068, 0.061 with NAu2 having lower values for both parameters. As already has been mentioned, the NAu2, in its oxidised state, has a lower cation exchange capacity (CEC) of 0.72 meq/g, as opposed to 1.02 meq/g for NAu1 (Gates, 2005), which is depicted in the adsorption capacity of the minerals. On the other hand, NAu2 has tetrahedral substitutions of Al^{3+} to Fe^{3+}, in its oxidised state, thus the charge distribution is different, which is depicted in the adsorption intensity or heterogeneity. This charge distribution difference will be amplified under reduced conditions where negative charges increase. Since the 1/n has an inverse relation with the adsorption intensity, the NAu2 exhibits a lower valuer than that of NAu1, depicting that charges difference on the NAu2 surface, contributed by both tetrahedral and octahedral sheets. For the case of SWy3 (CEC=0.75meq/g), a Langmuir isotherm was fitted, which implies a different adsorption process (or cation exchange

process) than the other two. It seems, though, that reduced SWy3 has a higher adsorption capacity K_l=1.074 than the other two, for the same reaction system. A poorer fitting ($R^2 = 0.8$) with Freundlich isotherm was calculated with K_f=1.035 and 1/n=0.132, isotherm, giving a similar adsorption capacity to the Langmuir one, and a lower adsorption intensity than the reduced NAu1 and NAu2. The uncertainty of the poor Freundlich isotherm fitted on SWy3 data, maybe originating from the lack of low Ca^{2+} experimental concentration values.

The Na→K and the reduced NAu1 and NAu2, exhibit similar behaviour, with NAu1 having slightly higher cation adsorption capacity, K_f= 1.081 mg/g than the NAu2, with lower adsorption intensity towards K^+, as a product of negative charge origin and distribution. For the reduced SWy3 data, both a Freundlich and a Langmuir isotherm were fitted. For the Freundlich isotherm, the mineral has lower cation adsorption capacity, K_f-=.996 mg/gram than NAu1, NAu2, but its adsorption intensity, 1/n=0.369, is very similar to NAu2, 0.316, but remains higher than that of NAu1. Additionally, the Langmuir model isotherm, estimates a higher adsorption capacity at K_l=1.146 mg/g.

Table 7.11: Freundlich and Langmuir isotherm fitting parameters for the reactions of Na→Ca and Na→K with reduced NAu1, NAu2 and SWy3 clay minerals.

	Isotherm fitting parameters								
	Na→Ca			Na→K					
	Freundlich isotherm								
	K	1/n	R^2	K	1/n	R^2			
NAu1	0.984	0.068	0.989	1.081	0.452	0.965			
NAu2	0.961	0.061	0.898	1.022	0.316	0.981			
	Langmuir isotherm			Freundlich isotherm			Langmuir isotherm		
	K	b	R^2	K	1/n	R^2	K	b	R^2
SWy3	1.074	16.976	0.917	0.996	0.369	0.925	1.146	4.73	0.980

Overall, for the exchange adsorption isotherms, we can see that the adsorption capacity is reaction dependent, hence cation dependent, along with the respective cation exchange capacity, CEC, with clay minerals having less capacity when tested at the Na→Ca. Adsorption intensity seems to be affected by the different negative charges distribution amongst the three minerals, originating from the tetrahedral and/or octahedral sheet substitutions. The specific behaviour of SWy3, in terms of adsorption intensity, compared to the other two, may comes from the fact that SWy3 has both ferric and ferrous iron in its structure, as well is a *cis*-vacant smectite (Neumann et al., 2011). In the context of iron reduction process and structural rearrangement in the mineral structure, SWy3 compensates excess negative charges during iron reduction, by

cation adsorption and not by dehydroxylation, as is the case for NAu1 and NAu2 being *trans*-vacant smecttes, (Drits, Manceau, 2000). On a additional note on the SWy3, it exhibits a dual adsorption behaviour, especially for the Na→K, with both models fitted, with good correlation factors. That may indicate that not all adsorption sites are saturated. Furthermore, for the same reaction system, it can be seen that Freundlich isotherm does not reach a plateau at high potassium mole fraction, E_K, indicating a infinite surface coverage by the adsorbed cation, from a mathematical standpoint, (Reed, Matsumoto, 1993).

7.6.5 Iron reduction effects on cation exchange processes

As inferred in the above paragraphs, increased negative charges, upon reduction, potentially play a significant role on the cation adsorption and/or exchange processes. The negative charges, w, can be calculated and expressed as a function of, m, the Fe^{2+} in mmoles/gram of clay as in Equation 7.23 (Drits, Manceau, 2000).

$$w = w_0 + p = w_0 + m/(1 + K_0 * m_{rel}) \tag{7.23}$$

with w_0 and p being the Na^+ and Fe^{2+} in mmoles/gram of clay, respectively, and K_0 being a positive sample-depended constant, which value depends on the total iron content and the cation exchange capacity of the mineral in its oxidised state. For correlation of the calculation of this parameter look at Chapter 5, Section 5.4.5).

The reduction degree of NAu1, NAu2 and SWy3 was around 90%, m_{rel} =0.9 [3], while the total charges, w_0, balanced by adsorbed cations, hence the cation exchange capacity in oxidised conditions, are 1.02, 0.72 and 0.75 in meq/gram and total iron content 3.68, 3.83, 0.42 per unit cell ($O_{20}(OH)_4$ after ((Gates, 2005)). The calculated negative charges upon 90% reduction will be 1.55, 1.47, 0.77 in meq/gram. However, this equation and the particular reduction model, should be used with caution especially for the montmorillonite, because they can exhibit a different reduction mechanism than nontronites. As SWy3 is a *cis*-vacant smectite, requires greater activation energy for iron migration to the vacant site of the lattice, in comparison to *trans*-vacant smectites, which eventually leads to almost exclusively excess negative charges compensation by cation adsorption (initially Na^+), and not by dehydroxylation, (Drits, Manceau, 2000). From that perspective, SWy3, as shown in Table 7.11, has a higher adsorption capacity in

[3] HF digestion measurements and calculations and Mössbauer data, see Chapter 3

the Na→Ca reaction system, while a lower for the Na→K reaction system, when comparing for the same model isotherm, or higher in both cases when comparing the K_f, K_l values. Since, the adsorption requires first an exchange of cation, and since SWy3 has more cation to exchange, it can speculated that this mineral may have the highest adsorption capacity of the three, for the specific reduction degree of around 90%.

On the other hand, the total ionic concentration measured, as adsorbed cations on the clay mineral surfaces (Tables E.1 - E.6, Appendix) showed that first, this concentration remains the same across the Na/Ca or Na/K salt ratios, for each mineral, and second that the highest concentration in meq was exhibited by NAu1 while the lowest by SWy3. The above theoretical CEC calculations showed an increase of that parameter upon reduction, but also we know that under these redox conditions, the interlayer collapses, not allowing cations to participate on exchange reactions or other processes. In the case that the actual numbers are considered in more detail, 0.5 g of each mineral was used, so the NAu1 exchange data correspond to 0.775 meq, the NAu2 to 0.735 meq and the SWy3 to 0.385 meq (half of the calculated values above). For the NAu1-Na→Ca reaction, an average of 0.51 meq of cations were extracted, while for the NAu1-Na→K reaction, an average of 1.3 meq. For the NAu2 an average of 0.3 meq or cations were extracted for both reactions while for SWy3, and average of 0.7 meq of cations were extracted. Apart from the NAu1-Na→K reaction, the rest averages correspond to the 65% of 0.755 meq/0.5 g for NAu1, 40% of the 0.735 meq/0.5 g for NAu2 and 19% of the 0.385 meq/0.5 g of SWy3. This can be considered a further indication of hysteresis in the examined exchange system, as has been suggested by Verburg, Baveye (1994). The NAu1 NaK reaction showed double the available meq concentration than the NAu1 Na→Ca reaction, which could attributed to experimental inherited error, however fairly consistent. This attempt to examine the solution mass balance in conjunction with the calculated CEC upon iron mineral reduction showed that NAu1 has the highest adsorption capacity, with SWy3 having the lowest.

Overall, the data above show an increased selectivity towards calcium (Ca^{2+}), as H-type adsorption isotherm indicated (Giles et al., 1960; Sposito, others, 1984), with a small variability amongst the minerals, with potassium (K^{+}) showing a high selectivity as well, under the same pH, temperature and redox state conditions. However, from the thermodynamic evaluation for both reactions, the Na-to-Ca exchange requires energy input, ($\Delta G > 0$), while the Na-to-K exchange takes place spontaneously, $\Delta G < 0$. So, the adsorption or exchange process of the

two cations, Ca^{2+}, K^{+}, when competing for Na^{+}, differs amongst on the tested substrates. It has been recognised that such exchange reactions can be affected by the clay clay nature and content, ionic strength, salt concentration, charge distribution and electric potential (Shainberg et al., 1980; Endo et al., 2002; Kopittke et al., 2006) with the actual ion exchange process being a chemical-mechanical process when observed in a time scale of seconds (Whittaker et al., 2019).

As there are not many cation exchange studies on NAu1 and NAu2 under oxidised or reduced conditions (Ilgen, Trainor, 2012; Ilgen et al., 2017; Ghorbanzadeh et al., 2015), and the montmorillonitic studies can vary largely (Benson, 1982), no direct connections can be made safely for the behaviour of these minerals under oxidised conditions for the reactions tested here. Nevertheless, the concentration range used for the exchange reactions, indicate that the inverse reaction Ca-to-Na is more favourable, and that K^{+} is preferred over Na^{+}, leading to increasing selectivity Hoffmeister-like series of $Ca^{2+} < Na^{+} < K^{+}$, as is reported by Hanshaw (1963) and calculated by (Underwood et al., 2016).

7.6.6 Implications for enhanced oil recovery

Putting these findings into a reservoir rock perspective, under the scope of low-salinity waterflooding, it can be argued that the redox state of the clay minerals do have a impact on the multi-ion exchange processes described in the literature. In this simple clay mineral/ brine system, the minerals will adsorb spontaneously Na^{+} instead of keeping Ca^{2+} or other divalent cations in their vicinity, hence verifying the many studies reporting decrease of Na^{+} concentration, and increase of Ca^{2+} concentration, after low-salinity water injection, in core-flooding experiments (e.g., Nasralla, Nasr-El-Din (2011)). In a much complex system, the competition will be greater, as big oil molecules, basic and/or acidic, will either directly attach the clay mineral surface or form bridges with divalent cations, on specific sites (edge sites) (Farajzadeh et al., 2017). Additionally, in the same study, it was recognised that oil-aging period, as well as temperature will affect parameters of clay minerals, such as the decrease cation exchange capacity of clay minerals due to cation/basic oil molecules competition for charge sites. Eventually, low salinity water injection will lead to divalent cation and oil molecules exchange to Na^{+} (Farajzadeh et al., 2017).

Interestingly, Nir (1986) described such a low-salinity process in soils, which by washing and removing the strongly-adsorbed divalent cations, screening the clay mineral surface, would

diminish the charge site competition and the monovalent cations can be readily (re)adsorbed onto the clay minerals, regardless of the concentration of adsorbing sites. All in all, the clay mineral surface negative charges can be increased under reduced conditions, however, that is not the only affecting factor for the adsorption/desorption and exchange processes, but evidently, factors such as cation hydration, charge site specific selectivity, water phase activity, temperature and oil composition play a significant role for the system in examination.

7.7 Conclusions

To iterate the findings of this study, increased specific adsorption of Ca^{2+} was recognised for NAu1 and NAu2, well described by a Freundlich isotherm, as well as a increased adsorption for SWy3, better described by a Langmuir isotherm. The thermodynamic evaluation showed a $\Delta G > 0$ for this Na-to-Ca exchange reaction. The K^+ adsorption selectivity was less than Ca^{2+}, according to the Freundlich parameters, with a $\Delta G < 0$ for all clay minerals. Selectivity coefficient and free energy values showed that both reaction are more favourable at low Ca^{2+} or K^+ concentrations relatively to Na^+, meeting the most basic low-salinity assumption that Na^+ will affect positively the multi-ion exchange process taking place during low-salinity waterflooding EOR method.

Chapter 8

Final Synthesis

8.1 Original objectives and key findings

The main goal of this PhD project was to capture a better understanding of the physico-chemical processes taking place during the low-salinity waterflooding (LSWF). The starting point was the examination of reduction-oxidation processes that was identified as part of this enhanced oil recovery (EOR) method, which eventually leads to further hydrocarbon recovery, decreasing the residual oil saturation in sandstone reservoirs. It has been recognised, in a limited number of studies Wang, Guidry (1994); Fjelde et al. (2017) and more recently Yesufu-Rufai et al. (2020); Unsal et al. (2020), that oxidation state of clastic rocks influences wettability, favouring a more water-wet state under reduced conditions and a more oil-wet state under oxidised conditions. However, these early findings do not necessarily explain in detail, why and how underlying processes cause this wettability changes depending on the oxidation state of the rock.

For this lack of fundamental understanding of the wettability alterations, this project approached the problem with several studies, in different scales of observation from cm-mm to nm. First, it was established with direct wettability measurements that indeed reduced clay mineral films are more water-wet under reduced conditions, than when under oxidised. Along with the static contact angle measurements, revealing these results, a further examination, of dynamic contact angle measurements, of these clay mineral film surfaces was conducted evaluating the suitability of measuring crude oil and water contact angles on these surfaces, as well as the credibility of the static measurements.

Second, the focus was shifted to a much smaller scale of observation (nm), divided in two

parts: (a) Infrared spectroscopy, studying the influence of redox state on the hydration of the clay minerals, coupled with water vapour adsorption studies. These hydration studies were further constrained by saturating the clay mineral used, with different cations (Na^+, Ca^{2+}, K^+). That gave us the ability to isolate the different hydration induced by these cations and study better the response of the overall hydration of the clay mineral. Furthermore, as the clay mineral was studied across the infrared (IR) spectrum, Near-, Mid-, and Far- range, different information was acquired within each IR range. The Near-IR and Mid-IR ranges were affected by the hydration extent, via the control of the relative humidity (RH), and the reduction degree of the sample, oxidised, partially reduced and fully reduced. The Far-IR range was affected mostly by the reduction degree, and in a lesser extent by the RH induced or the saturating cation.

Key findings:

- At the Mid-IR range, nontronite spectra (NAu1-Na) at RH70%, increased in relative intensity at the adsorbed-water regions of 1630 cm^{-1} and 3000-3800 cm^{-1}, with order of oxidation state as fully reduced < oxidised < intermediate reduced. Similar responses were observed for the NAu1-Ca, and NAu1-K.

- At the Near-IR and Mid-IR ranges, less hydration extent (at RH70%) was observed for the fully reduced samples, at the region of 5200 cm^{-1}.

- Water vapour adsorption isotherm measurements on the homoionic clay mineral, showed similar to MIR-NIR hydration responses under oxidised and fully reduced conditions, with samples (NAu1-Na, Ca, K) having adsorbed less water under reduced conditions, and exhibiting an increased interaction between the mineral phase and the water vapour.

- At the Far-IR range, major spectral pattern alterations were noted, identifying which bands were affected the most by the reduction degree, with nature of Fe^{3+} and/or -OH, with different grouping configuration.

- Cation effects on the NAu1 spectra were mostly recognised at Mid-IR and in a lesser extent at the Far-IR. Clay mineral / cation interactions increased in an order of oxidised < fully reduced < partially reduced, as a result of the curvilinear relation of iron reduction extent and negative charges on the mineral surface. For example, Na^+ and K^+ interacted more strongly with the clay mineral, at partially reduced state, than Ca^{2+}. That observation

can be a key unlocking the multi-ion exchange processes undergo during LSWF, and the Na^+ saturation that is preferred for the EOR method.

The other part, (b), cation exchange studies, evaluated the cation exchange processes through cation exchange adsorption isotherms, studying two cation exchange reaction, Na→Ca and Na→K, using three different clay minerals, covering high and low iron content, under reduced conditions. Ion exchange processes are a well-studied subject, with several theoretical models proposed, trying to describe how they take place on clay mineral cation exchange sites. In the case of our studies, extra complexity was expected due to interlayer collapse upon reduction, introducing hysteresis, which is also a described parameter in similar studies (Verburg, Baveye, 1994). Despite this fact, our studies approached the cation exchange reactions using thermodynamic calculations. The key findings are summarised below:

Na→Ca reaction

- Increased Ca^{2+} adsorption over Na^+, for all clay minerals, with $\Delta G > 0$.
- Freundlich model isotherm better fitting the NAu1, NAu2 exchange data, while Langmuir model isotherm the SWy3 exchange data.

Na→K reaction

- Increased K^+ adsorption over Na^+, with $\Delta G < 0$.
- Freundlich model isotherm better fitting the NAu1, NAu2 exchange data, while both, Freundlich and Langmuir model isotherms fit well the SWy3 exchange data.

It seemed counterintuitive that clay minerals, especially NAu1 and NAu2 exhibited such increased Ca^{2+} adsorption with a $\Delta G > 0$. As there is specific and non-specific cation adsorption onto clay mineral surfaces (Nir, 1986), it may be the case that these minerals have such specific charge sites that get saturated by Ca^{2+} or other divalent cations. Some of the latest research advances on cation exchange reactions showed that these processes are quite complex, with many parameters contributing differently during the reaction (Whittaker et al., 2019). The thermodynamic approach adopted here do not account for the water phase activity, which it has been shown that is the driving factor of cation exchange. On the other hand, more mechanistic approaches, as briefly displayed at the introduction of Chapter 7, consider different scales of

observation for these processes, again using thermodynamic equations. All in all, all approaches together can give a better understanding and describe different aspects of the process. As far as reduced clay minerals are concerned, the thermodynamic approach may not seem the best fit, as the interlayer collapses and increased hysteresis phenomena can be observed in such cases. However, cation adsorption isotherms gave good fitting with the model Freundlich and Langmuir adsorption isotherms, which in turn were postulated after certain assumptions. Nonetheless, this experimental work gives a first picture of how reduced clay minerals exchange cations on their surfaces. Given any drawbacks of this experimental set up, it is a starting point for improving the cation exchange examination by using more accurate and probably more mechanistic approaches for determining selectivity coefficients and reaction Gibbs free energy, further contributing to areas such as agriculture, waste management and disposal and the oil industry.

8.2 Concluding Thoughts

In an attempt to compile all experimental data shown in this thesis, the following model can be proposed. Prior any hydrocarbon production, the sandstone reservoir will be in a highly reduced state. This situation is established quickly after desposion of the sedimentary rock or a product of the reducing nature that hydrocarbons can have on the reservoir rock upon oil migration within geological time, (Ma et al., 2016). When crude oil production commences the primary production mode oil is extracted naturally due to the drive regime of a given petroleum system. As reservoir pressure drops waterflooding is implemented in order to sustain a viable pressure in the system for production continuation. At that point, the secondary production mode begins, with water injected usually being seawater (high salinity) or produced reservoir brine. When this production period ends, enhanced oil recovery (EOR) methods are deployed (tertiary recovery), targeting the residual oil, which is usually trapped into pores or strongly adsorbed onto clay minerals. The traditional EOR methods can be CO_2 injection, alkaline-surfactant-polymer (ASP), steam injection among others. Low salinity waterflooding (LSWF) has come into play as it is a cost effective EOR method. This method caused, on some occasions, the production of Fe^{3+} particles (Seccombe et al., 2010), indicating an oxidising effect on the rock, additionally to the mineral dissolution effects proposed, (Lager et al., 2011). Also, it has been experimentally observed that LSWF performs better when implemented during secondary recovery (instead of the reservoir brine / high salinity water), than when implemented during

tertiary recovery (e.g., Nasralla, Nasr-El-Din (2014)), without particular mention about redox phenomena. So, there is an underlying mechanism that controls the performance of that method, between the two modes. According to the results of Chapter 4, we established that reduced clay minerals are more water-wet than oil-wet. Then on Chapter 5 and 6, we observed that under partially reduced conditions clay minerals are more hydrated than oxidised and reduced (in that order), and at the same time, saturating cations which fundamentally create the hydration regime, are more strongly held under partially reduced conditions than fully reduced and oxidised.

So, we propose that during secondary LSWF, the fully reduced clay minerals, get partially re-oxidised (sea water oxidation potential), and at the same time, the double layer effect due to reduced ionic strength act upon clay mineral, releasing attached oil. This is facilitated, too, by the increased negative charges at partial reduction state (higher than fully reduced), as a repulsive force between clay platelets and/ or clay / oil particles. At fully reduced state, we observed on Chapter 7, that clay minerals will exchange more easily Ca^{2+} for Na^{+}, which is backed up by the results on Chapter 6, where (M-)IR bands associated with adsorbed water showed cation dependence and revealed clay mineral/ cation interaction intensity. On the other hand, at tertiary LSWF, the partial reoxidation may have occur during the secondary high salinity water injection, with the electrostatic forces of tertiary recovery LSWF having less of effect on clay mineral surface. Also, under oxidised conditions, clay swelling can significantly inhibit fluid flow, causing formation damage. This fines migration effect has been reported both beneficial and non-beneficial for additional oil recovery during LSWF, (Bartels et al., 2019).

Although the above model is being proposed on reproducible experimental results, there are some gaps which need to be addressed and suggested below as future work. Nonetheless it adds a perspective on the current literature, which for example, Nasralla, Nasr-El-Din (2014) attributed this differential phenomenon of secondary *vs* tertiary recovery efficiency to double layer expansion at the rock surface, during secondary recovery, leading to oil production, while the lack of oil production during tertiary recovery was due to fines migration and formation damage of the core plugs. However, such results and conclusions are depended heavily on the experimental set-ups and protocols for core flooding which are not universal across research laboratories, (Bartels et al., 2019). Other explanation for this phenomenon is the mixing of high salinity (secondary recovery)- low salinity (tertiary recovery) water mixing, or that mobile oil saturation is less at tertiary recovery, (all detailed in Bartels et al. (2019) and references there

in). Finally, at the same review, it is stressed out that current experimental procedure need to be better connected as we move from small length scale observations ((sub-) pore) to large scale observations (reservoir). It is not guaranteed that low salinity effects or low salinity recovery observed on either end of the length scale spectrum is automatically observed on the opposite side of the spectrum. That creates a problem for screening and evaluating potential reservoir for low salinity waterflooding implementation, (Bartels et al., 2019).

8.3 Recent advances in Low-salinity waterflooding research

Latest research shows a trend of trying to model low salinity waterflooding, to better approximate the laboratory or field scale results. Some models are more focused on the geochemical side of the process, where the multi component ion exchange mechanism is of main interest (Chen et al., 2019; Takahashi et al., 2019). Models also focus on the rock heterogeneities and how these can affect fluid flow, causing reservoir brine / low salinity water effects such as fingering, water mixing, resulting to lower performance of the EOR method (Al-Ibadi et al., 2020). Additionally, a body of research also is focused on visualising low salinity effects through microfluidics and/or micro-CT set-ups, capturing in real time any changes taking place upon LSWF. Those phenomena could either be for mineral- fluid or fluid-fluid interactions. For example, Saadat et al. (2020), developed a microfluidic method for visualising LSWF processes. Amirian et al. (2019) demonstrated the clay mineral nature dependence of low salinity effects, with kaolinite, an edge-charged dominant mineral, performing better than illite, a basal-charged dominant mineral, in their microfluidic set-up along with ζ-potential measurement. Another interesting study was conducted by Du et al. (2019), who showed additional oil recovery, on various length scale systems, without clay mineral presence. The results demonstrated the sweep efficiency of low salinity water, but also a time-dependence on the low salinity effects detected. Apart from the research on the rock-fluid interactions, fluid-fluid interactions are also of importance, related to interfacial tension between crude oil and reservoir brine. Tetteh et al. (2020) showed that when low salinity or sea-like water came into contact with crude oil, suppressed oil snap-off and created microdispersions and oil remobilisation, while Behera, Sangwai (2020) explored the effects of monovalent and divalent cations on interfacial tension between pure hydrocarbon, revealing variable results, depended on both salt combination and concentration as well as model oil type.

8.4 Future Work

Future work, in the context of the above experiments, can focus on measuring crude oil contact angles on clay minerals that occur more frequently in sandstone reservoirs, such as montmorillonite and chlorite. Also, contact angle measurement can be further extended in more sophisticated stages, which the relative humidity can be controlled, directly affecting the oil affinity on the clay mineral film. The oxidation state of clay minerals can be also manipulated, in conditions of partial reduction of e.g., 10%, 30%, 70% etc. In that way, when the initial oxidation state of a clastic reservoir is acquired, an additional wettability information for rock characterisation studies can be logged.

The clay mineral hydration studies (Chapter 5) demonstrated the significance of the hydration state/ extent of mineral phases, under reduced and oxidised conditions. Relative humidity X-ray diffraction (RH-XRD) studies on the homo-ionic NAu1 samples or any clay mineral examined here, can give valuable information about the clay mineral platelets stacking and water content under reduced and oxidised conditions. X-ray photoelectronic spectroscopy (XPS) can also be utilised for direct measurements of model oil (e.g., carboxylic acids) / clay surface interaction under reduced and oxidised conditions. Such experimental set-up could reveal how differently heavy oil compounds are adsorbed on the clay mineral surfaces, depending on the saturating cation, contributing to the residual oil, being the main target of the various enhanced oil recovery methods and the low salinity waterflooding.

Regarding the cation exchange reactions examined in Chapter 7, extended experiments can be done in variable reduced state e.g., 10%, 30%, 70% etc. and oxidised conditions, for the particular minerals used here, or other more frequent in sandstone rocks. This can give a better understanding on how clay minerals and other phases exchange cations and cationic species on their surface, under variable oxidation states. Also, iron species Fe^{2+} and Fe^{3+} can be used as saturating cations, under various clay mineral reduction states, in order to compliment experiments described in Fjelde et al. (2017). The information acquired can be used into geochemical modelling, when a more detailed approach is required.

When sea water is used for LSWF, specific deoxygenation protocols are followed to avoid pipe corrosion. However, sea water has an oxidation potential through different species, such as I^-, Br^-, SO_4^{2-} . These species in the time scale of a field scale LSWF operation can bring re-oxidation changes, which can affect clay mineral adsorption capacity and rock/hydrocarbon interaction in

overall. So, the study of sea water / rock interaction can prove a valuable information for LSWF or any EOR method designing. Yet, this requires that the initial oxidation state of the reservoir, prior to any production is measured, too. This kind of studies and the evaluation of the reoxidation effects can be done with Mössbauer spectroscopy, with the time scale/ duration of the experiment being an important factor, as Bartels et al. (2019) demonstrated.

Zeta potential measurements on fully and partially reduced clay minerals can also be further investigated, in order to establish the electrostatic regime of clay mineral regime which will govern interparticle interactions as well as clay / hydrocarbon interactions.

Concluding this final section, it can be supported that by studying individual reservoir minerals under dynamic and batch conditions, as well as systematically screening environmental variables, such as pH, Eh, salinity, etc., fundamental understading can be built up. This can, then, be fitted to CT scans of cores to predict responses to LSWF and EOR.

Appendices

Appendix A

Chapter 3

A.1 XRD data

Phase identification was carried out by means of the X'Pert accompanying software program PANalytical High Score Plus in conjunction with the ICDD Powder Diffraction File 4 - Minerals (2019), the ICDD Powder Diffraction File 2 Database (2004) and the Crystallography Open Database (July 2016; `http://www.crystallography.net`).

NAu1

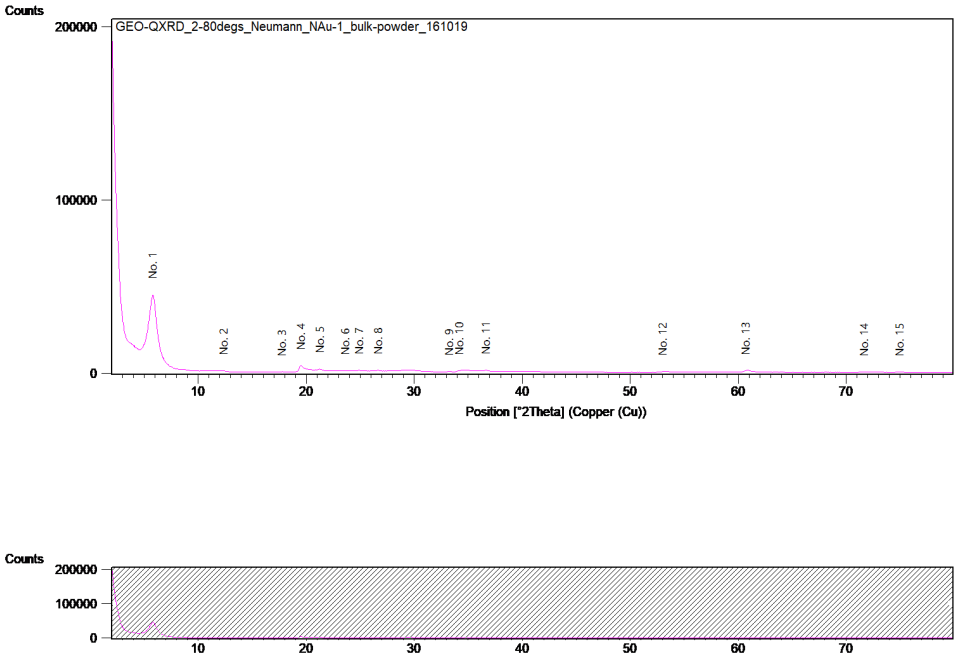

Figure A.1: Natural NAu1 XRD data.

NAu2

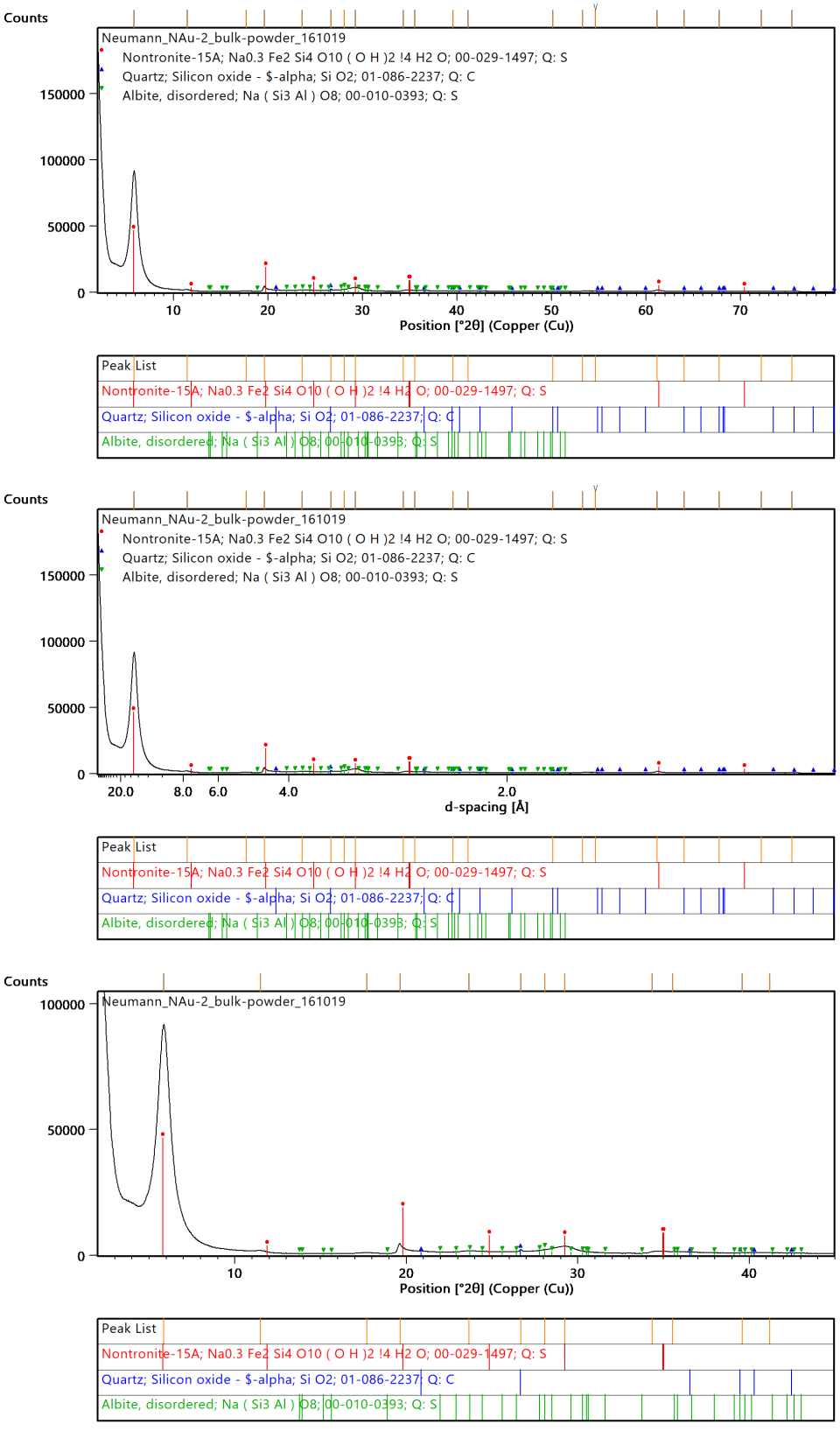

Figure A.2: Natural NAu2 XRD data

IMt2

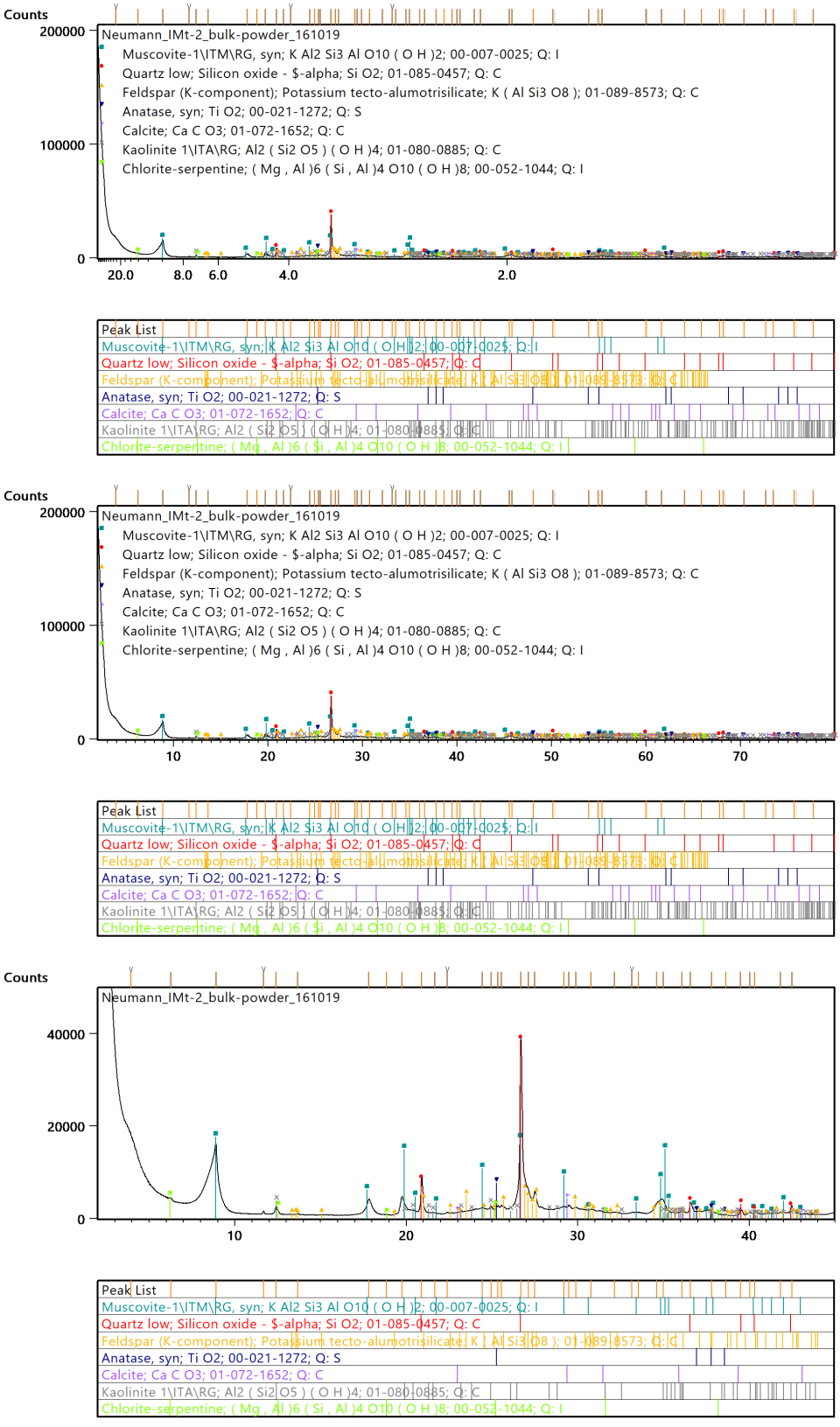

Figure A.3: Natural IMt2 XRD data

SWy3

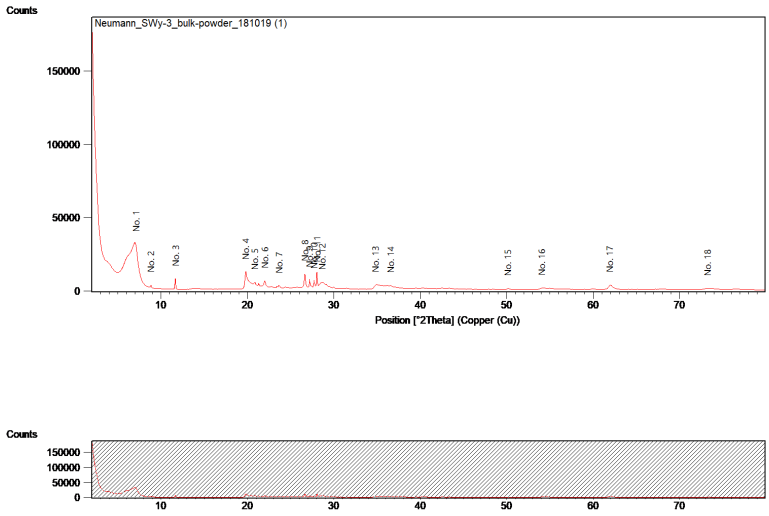

Figure A.4: Natural SWy3 XRD data

A.2 Mössbauer Spectroscopy

NAu2

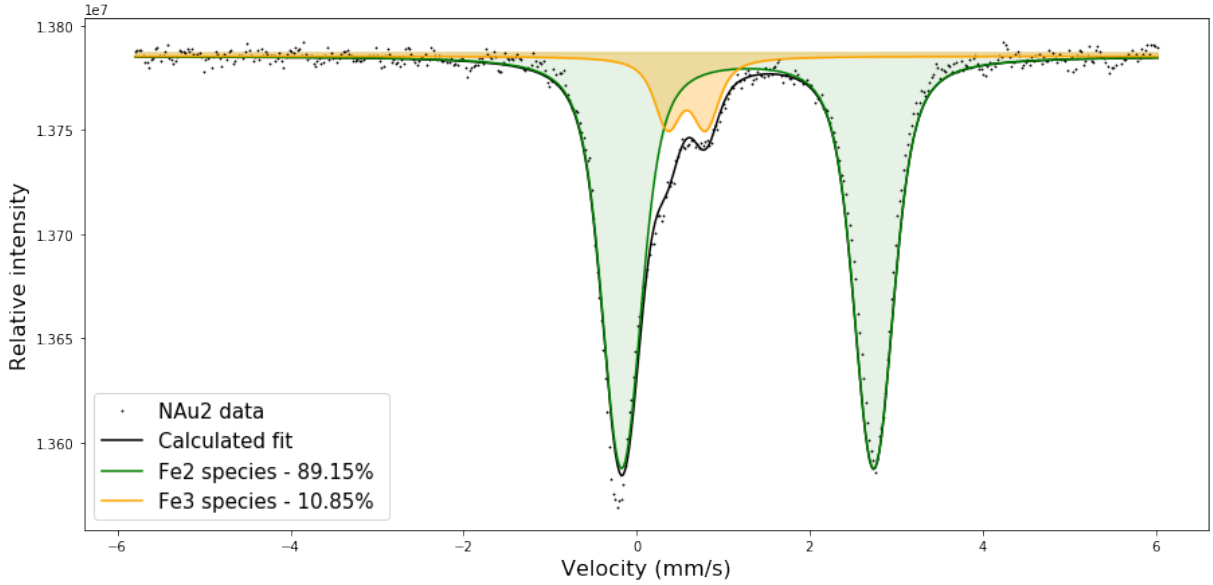

Figure A.5: Reduced NAu2 Mössbauer data fitted showing a reduction Fe(II)/Fe(III) degree of 89%

Table A.1: Fitting parameters of NAu2 and SWy Mössbauer data

	Fe species	IS (mm/s)	Area	QS (mm/s)	Sigma	Site population %
NAu2	Fe^{2+}	1.284	281087	2.91	0.317	89.15%
	Fe^{3+}	0.579	34200	0.43	0.151	10.85%
SWy3	Fe^{2+}	1.27	77298	3.031	0.209	91.3%
	Fe^{3+}	0.44	7400	0.995	0.752	8.7%

SWy3

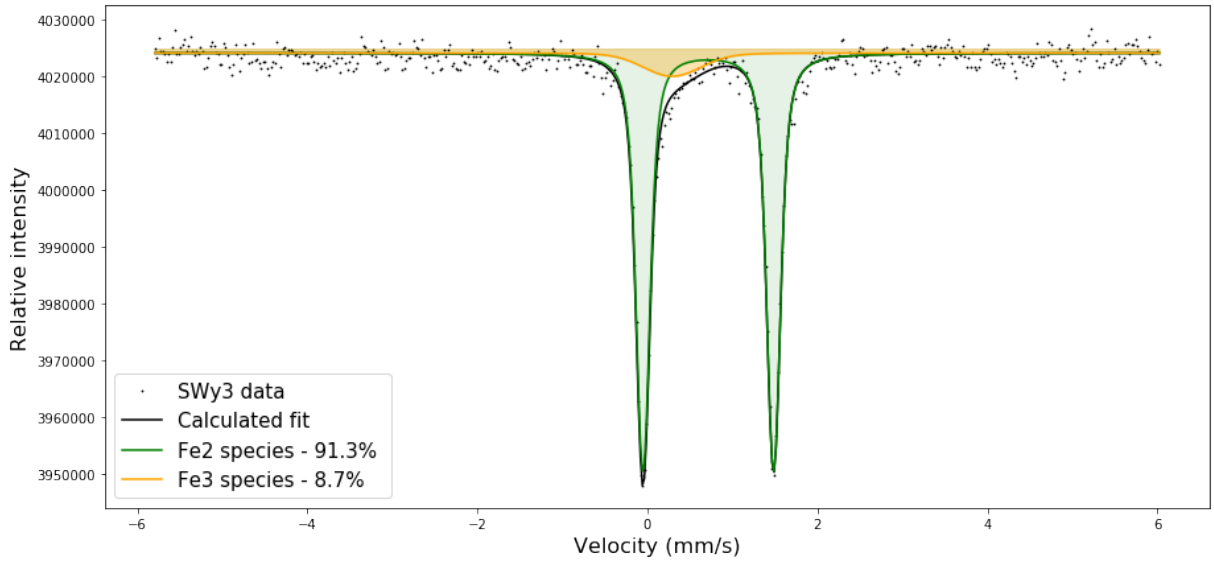

Figure A.6: Reduced SWy3 Mössbauer data fitted, showing a reduction Fe(II)/Fe(III) degree of 91%.

Appendix B

Chapter 4

B.1 Methodology

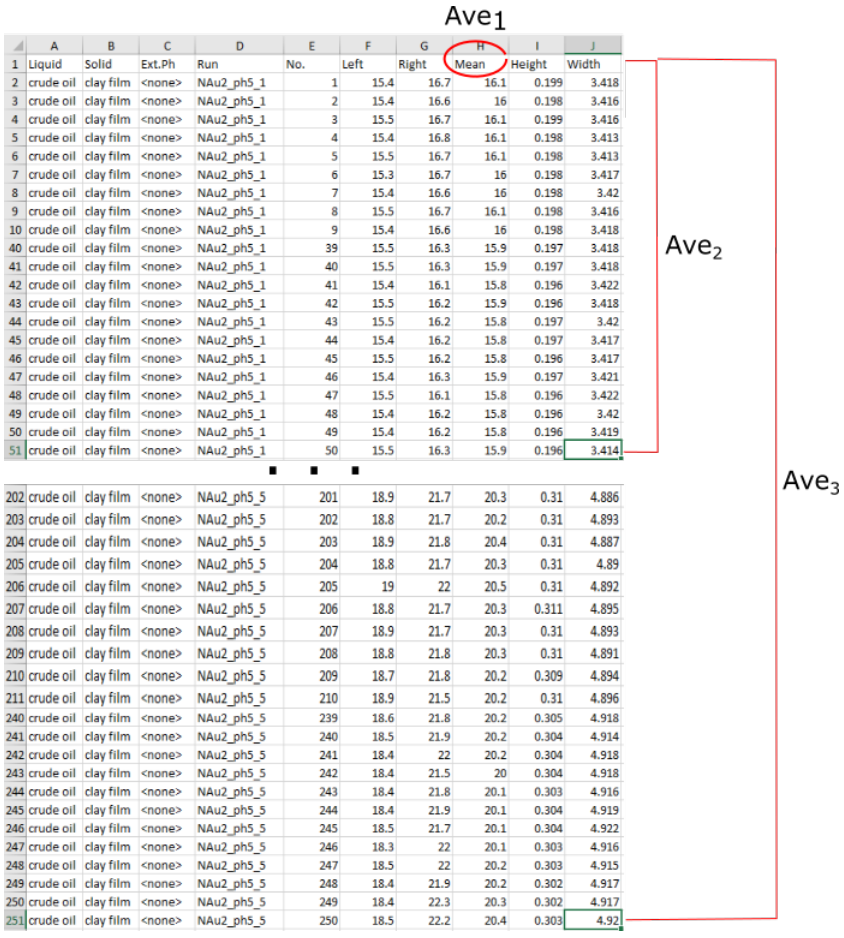

	A	B	C	D	E	F	G	H	I	J
1	Liquid	Solid	Ext.Ph	Run	No.	Left	Right	Mean	Height	Width
2	crude oil	clay film	<none>	NAu2_ph5_1	1	15.4	16.7	16.1	0.199	3.418
3	crude oil	clay film	<none>	NAu2_ph5_1	2	15.4	16.6	16	0.198	3.416
4	crude oil	clay film	<none>	NAu2_ph5_1	3	15.5	16.7	16.1	0.199	3.416
5	crude oil	clay film	<none>	NAu2_ph5_1	4	15.4	16.8	16.1	0.198	3.413
6	crude oil	clay film	<none>	NAu2_ph5_1	5	15.5	16.7	16.1	0.198	3.413
7	crude oil	clay film	<none>	NAu2_ph5_1	6	15.3	16.7	16	0.198	3.417
8	crude oil	clay film	<none>	NAu2_ph5_1	7	15.4	16.6	16	0.198	3.42
9	crude oil	clay film	<none>	NAu2_ph5_1	8	15.5	16.7	16.1	0.198	3.416
10	crude oil	clay film	<none>	NAu2_ph5_1	9	15.4	16.6	16	0.198	3.418
40	crude oil	clay film	<none>	NAu2_ph5_1	39	15.5	16.3	15.9	0.197	3.418
41	crude oil	clay film	<none>	NAu2_ph5_1	40	15.5	16.3	15.9	0.197	3.418
42	crude oil	clay film	<none>	NAu2_ph5_1	41	15.4	16.1	15.8	0.196	3.422
43	crude oil	clay film	<none>	NAu2_ph5_1	42	15.5	16.2	15.9	0.196	3.418
44	crude oil	clay film	<none>	NAu2_ph5_1	43	15.5	16.2	15.8	0.197	3.42
45	crude oil	clay film	<none>	NAu2_ph5_1	44	15.4	16.2	15.8	0.197	3.417
46	crude oil	clay film	<none>	NAu2_ph5_1	45	15.5	16.2	15.8	0.196	3.417
47	crude oil	clay film	<none>	NAu2_ph5_1	46	15.4	16.3	15.9	0.197	3.421
48	crude oil	clay film	<none>	NAu2_ph5_1	47	15.5	16.1	15.8	0.196	3.422
49	crude oil	clay film	<none>	NAu2_ph5_1	48	15.4	16.2	15.8	0.196	3.42
50	crude oil	clay film	<none>	NAu2_ph5_1	49	15.4	16.2	15.8	0.196	3.419
51	crude oil	clay film	<none>	NAu2_ph5_1	50	15.5	16.3	15.9	0.196	3.414
202	crude oil	clay film	<none>	NAu2_ph5_5	201	18.9	21.7	20.3	0.31	4.886
203	crude oil	clay film	<none>	NAu2_ph5_5	202	18.8	21.7	20.2	0.31	4.893
204	crude oil	clay film	<none>	NAu2_ph5_5	203	18.9	21.8	20.4	0.31	4.887
205	crude oil	clay film	<none>	NAu2_ph5_5	204	18.8	21.7	20.3	0.31	4.89
206	crude oil	clay film	<none>	NAu2_ph5_5	205	19	22	20.5	0.31	4.892
207	crude oil	clay film	<none>	NAu2_ph5_5	206	18.8	21.7	20.3	0.311	4.895
208	crude oil	clay film	<none>	NAu2_ph5_5	207	18.9	21.7	20.3	0.31	4.893
209	crude oil	clay film	<none>	NAu2_ph5_5	208	18.8	21.8	20.3	0.31	4.891
210	crude oil	clay film	<none>	NAu2_ph5_5	209	18.7	21.8	20.2	0.309	4.894
211	crude oil	clay film	<none>	NAu2_ph5_5	210	18.9	21.5	20.2	0.31	4.896
240	crude oil	clay film	<none>	NAu2_ph5_5	239	18.6	21.8	20.2	0.305	4.918
241	crude oil	clay film	<none>	NAu2_ph5_5	240	18.5	21.9	20.2	0.304	4.914
242	crude oil	clay film	<none>	NAu2_ph5_5	241	18.4	22	20.2	0.304	4.918
243	crude oil	clay film	<none>	NAu2_ph5_5	242	18.4	21.5	20	0.304	4.918
244	crude oil	clay film	<none>	NAu2_ph5_5	243	18.4	21.8	20.1	0.303	4.916
245	crude oil	clay film	<none>	NAu2_ph5_5	244	18.4	21.9	20.1	0.304	4.919
246	crude oil	clay film	<none>	NAu2_ph5_5	245	18.5	21.7	20.1	0.304	4.922
247	crude oil	clay film	<none>	NAu2_ph5_5	246	18.3	22	20.1	0.303	4.916
248	crude oil	clay film	<none>	NAu2_ph5_5	247	18.5	22	20.2	0.303	4.915
249	crude oil	clay film	<none>	NAu2_ph5_5	248	18.4	21.9	20.2	0.302	4.917
250	crude oil	clay film	<none>	NAu2_ph5_5	249	18.4	22.3	20.3	0.302	4.917
251	crude oil	clay film	<none>	NAu2_ph5_5	250	18.5	22.2	20.4	0.303	4.92

Figure B.1: Explanatory graph of contact angle average calculations, Ave_1, Ave_2, Ave_3. Reported contact angle values, standard deviations and error bars for the SSD are of the Ave_3, which includes Ave_2, while for DSD are of Ave_1

Table B.1: Standard deviation values distribution of mean contact angle (Ave_1) of left and right values, in percentages of all mean contact angle values acquired on each clay film, for crude oil and DI water. Standard deviation values are classified into four groups of <5, 5-10, 10-20, >20 degrees of angle

		Crude oil	DI water
Clay films	STD	% population	
NAu2 (reduced)	< 5	97	86
	5-10		12.6
	10-20		
	> 20	3	0.6
NAu2 (oxidised)	< 5	86	100
	5-10	9.2	
	10-20	3.7	
	> 20	0.92	
IMt2 (reduced)	< 5	85.7	96
	5-10	14.2	3
	10-20		1
	> 20		
IMt2 (oxidised)	< 5	55.4	62.6
	5-10	19.8	1.5
	10-20	17.7	9.6
	> 20	6.9	26.1

B.2 Static contact angle

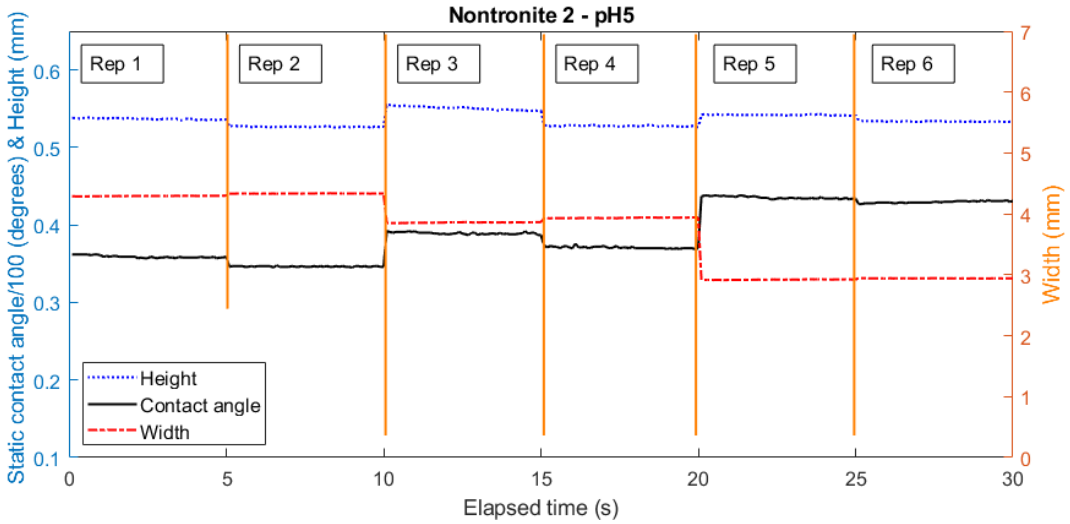

Figure B.2: Crude oil static contact angle, height and width profile against total time in seconds, of a reduced NAu2 clay film at pH 5. Each repetetion Rep, within the 5-seconds interval s correspond to a separate oil droplet.

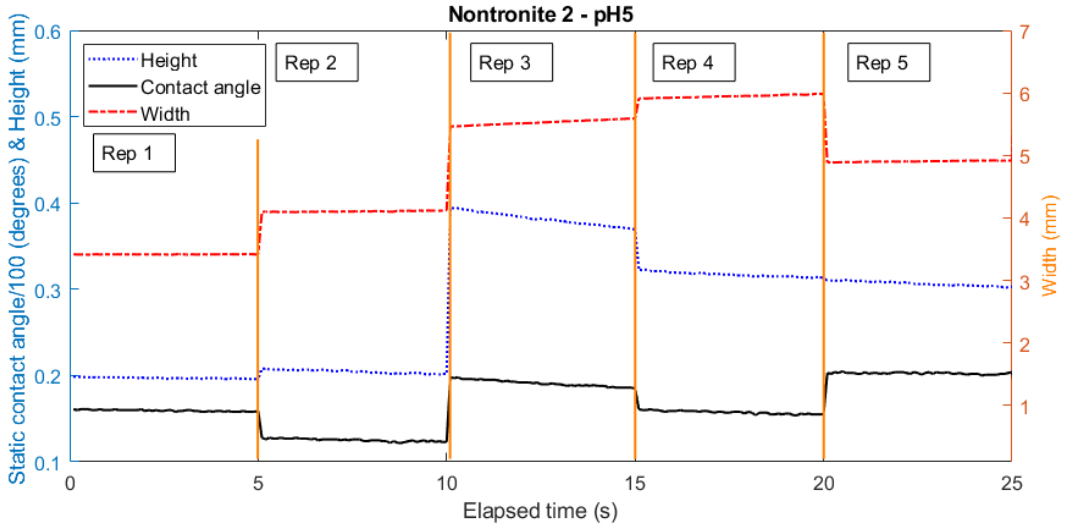

Figure B.3: Crude oil static contact angle, height and width profile against total time in seconds, of a oxidised NAu2 clay film at pH 5. Each repetition Rep, within the 5-seconds intervals correspond to a separate oil droplet.

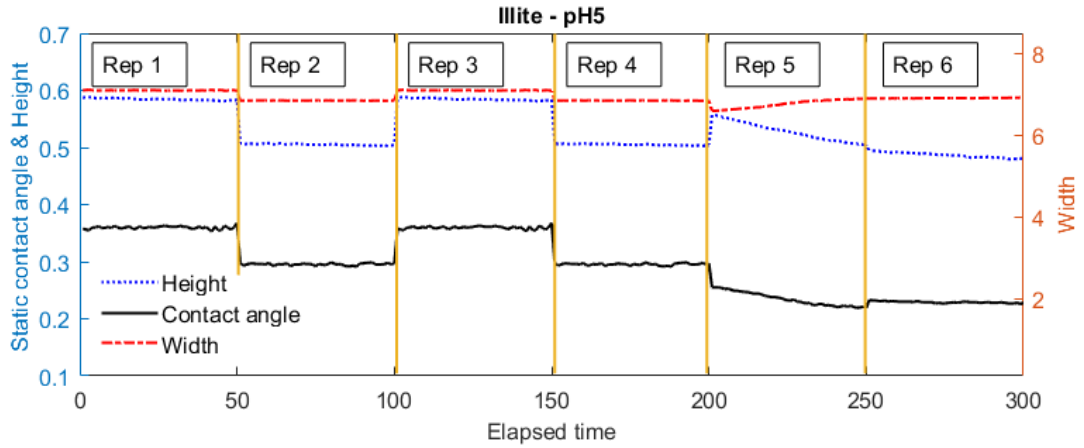

Figure B.4: Crude oil static contact angle, height and width profile against total time in seconds, of a reduced IMt2 clay film at pH 5. Each repetition Rep, within the 5-seconds intervals correspond to a separate oil droplet.

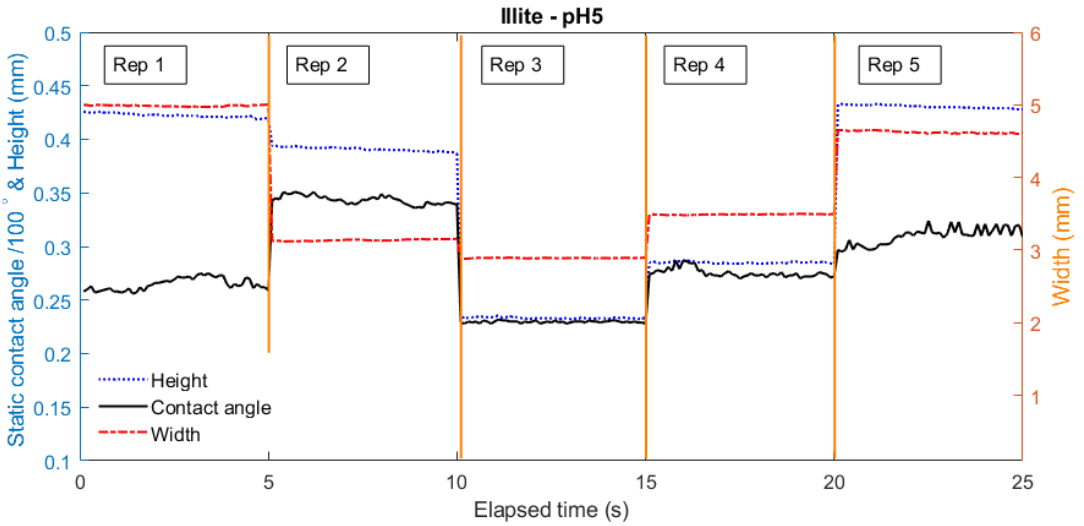

Figure B.5: Crude oil static contact angle, height and width profile against total time in seconds, of a oxidised IMt2 clay film at pH 5. Each repetetion Rep, within the 5-seconds intervals correspond to a separate oil droplet.

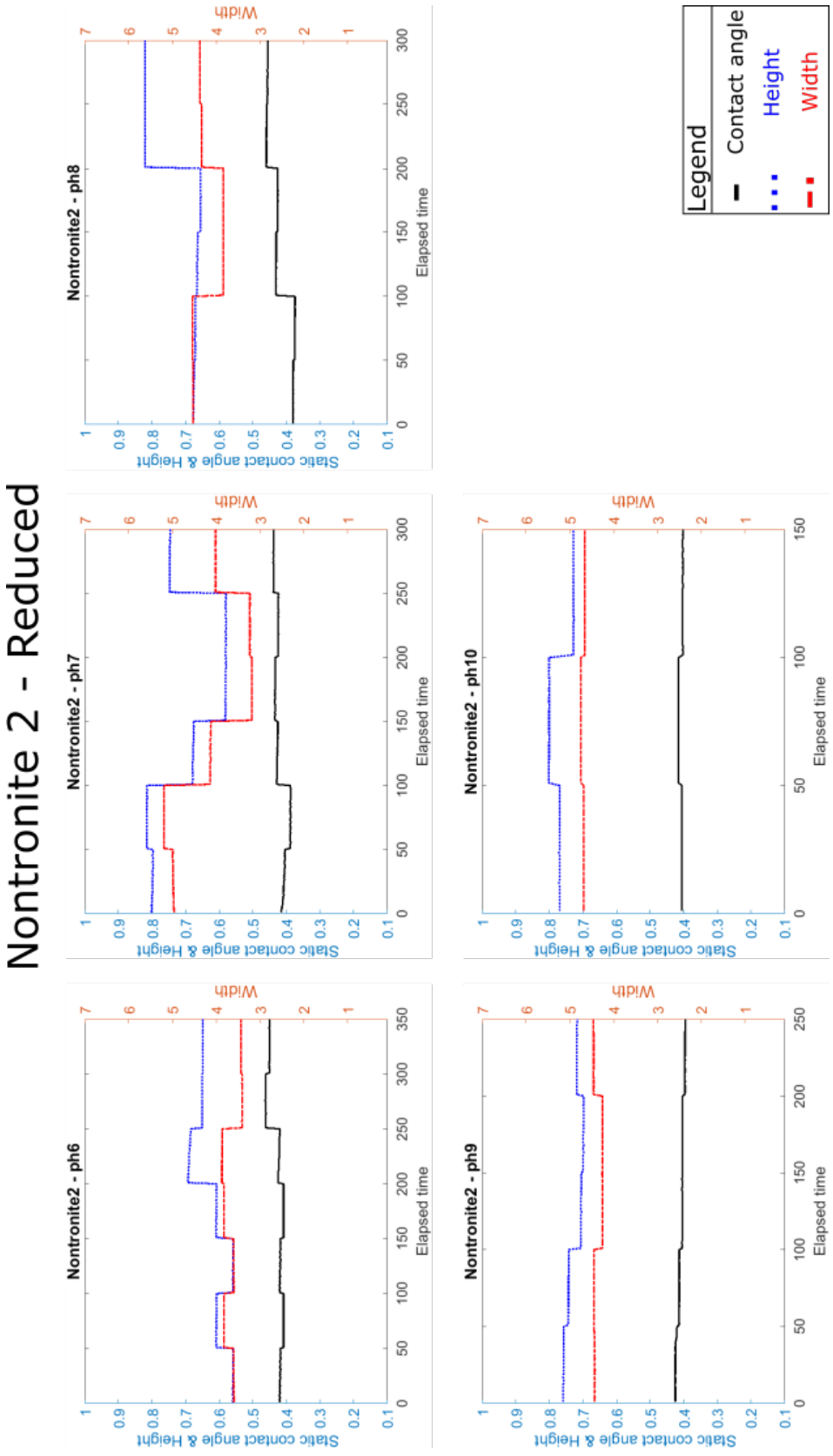

Figure B.6: Crude oil contact angle, height, and width profiles against total time for all reduced NAu2 clay films at the denoted pH values. Each repetition- Rep, within the 5-seconds intervals, correspond to one oil droplet.

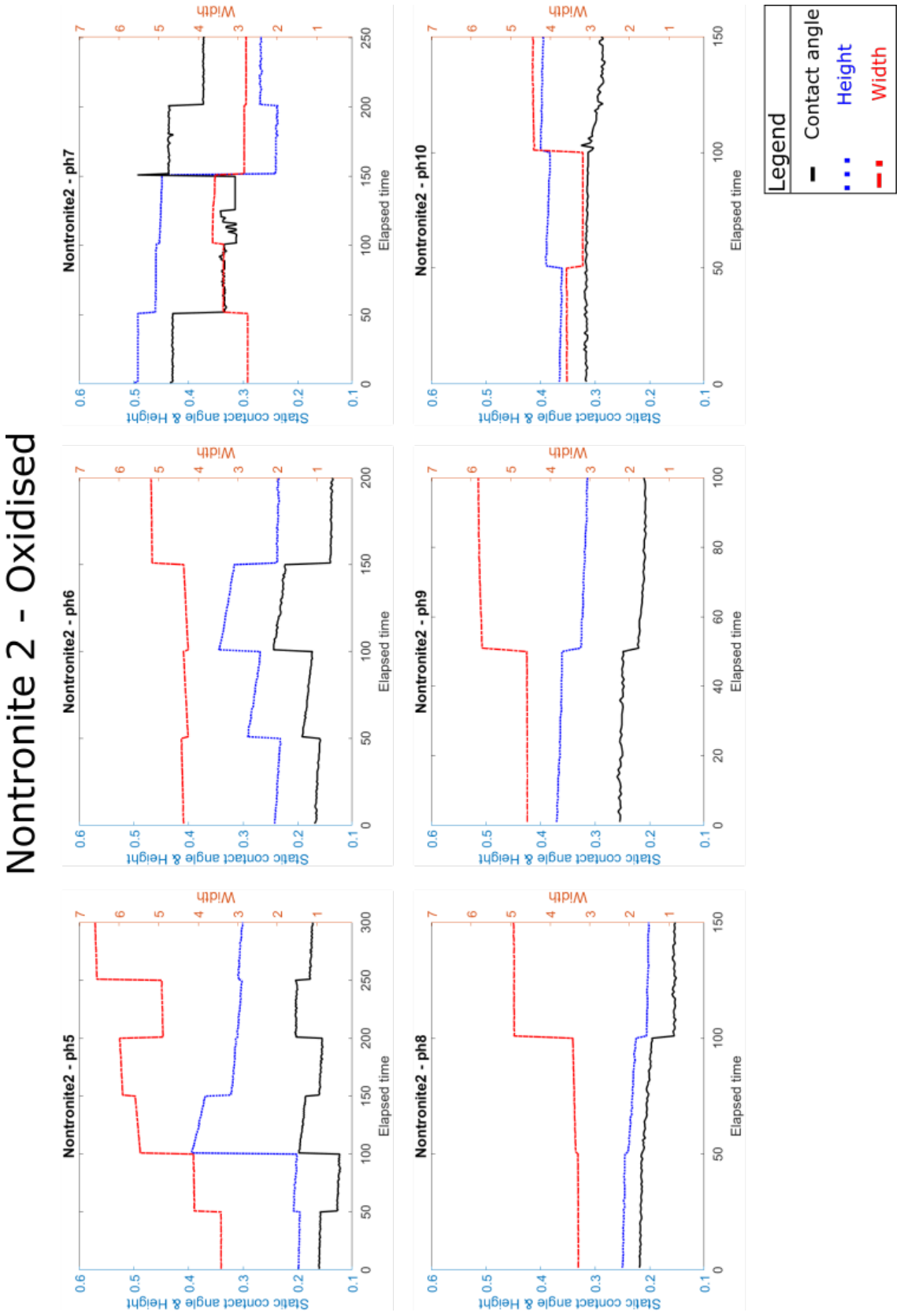

Figure B.7: Crude oil contact angle, height, and width profiles against total time for all oxidised NAu2 clay films at the denoted pH values. Each repetition- Rep, within the 5-seconds intervals, correspond to one oil droplet.

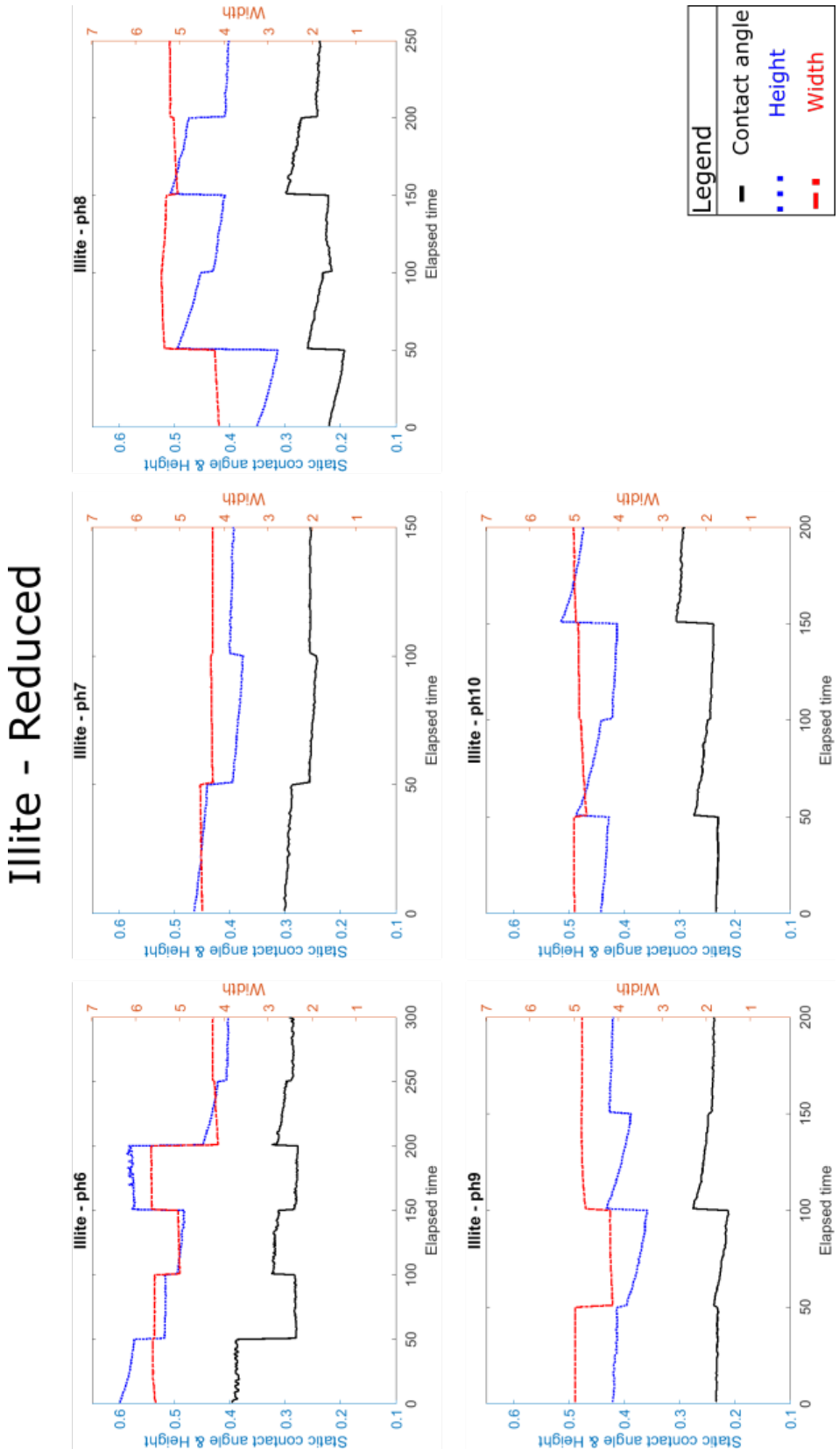

Figure B.8: Crude oil contact angle, height, and width profiles against total time for all reduced IMt2 clay films at the denoted pH values. Each repetition- Rep, within the 5-seconds intervals, correspond to one oil droplet.

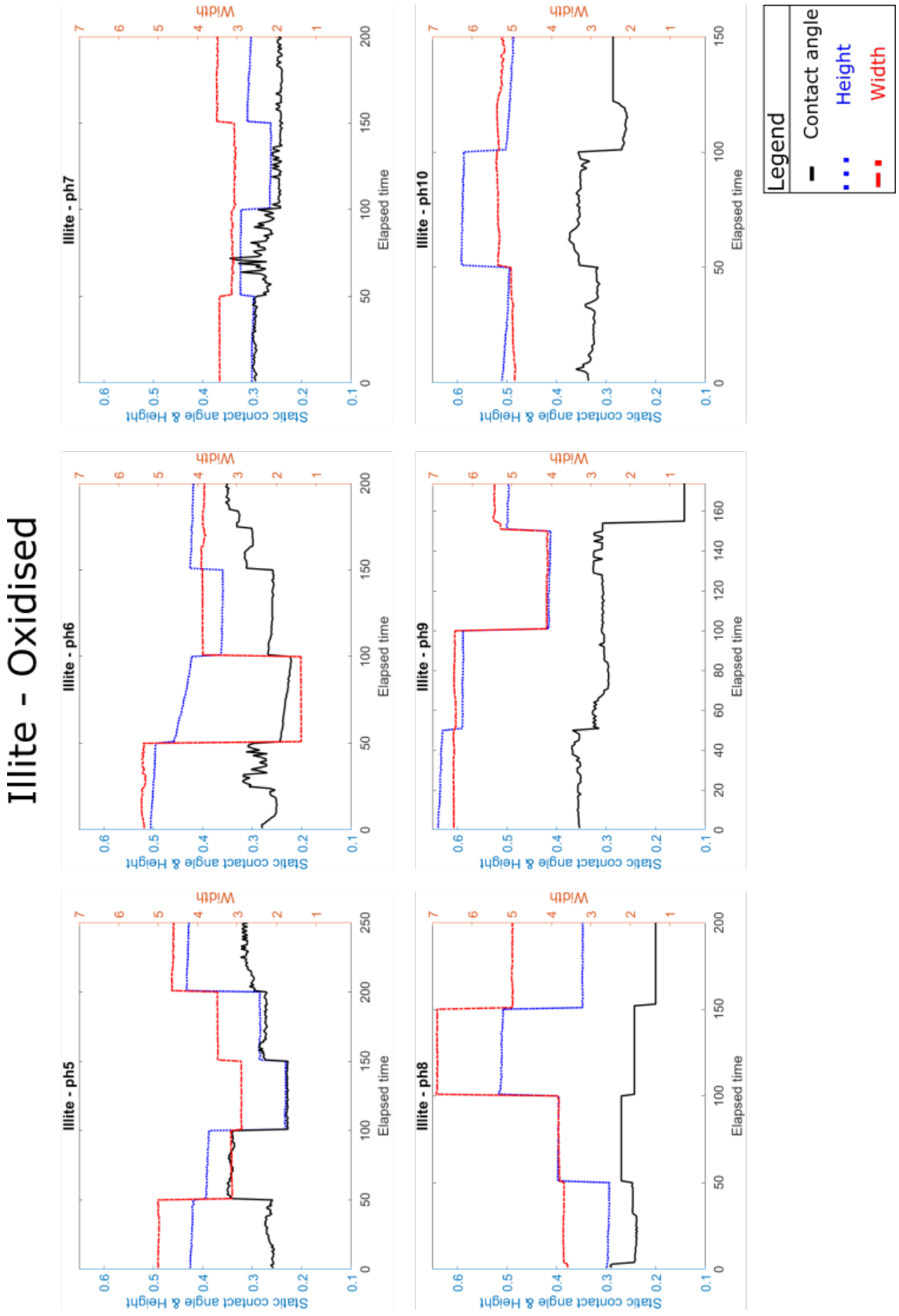

Figure B.9: Crude oil contact angle, height, and width profiles against total time for all oxidised IMt2 clay films at the denoted pH values. Each repetition- Rep, within the 5-seconds intervals, correspond to one oil droplet.

B.3 Dynamic contact angle

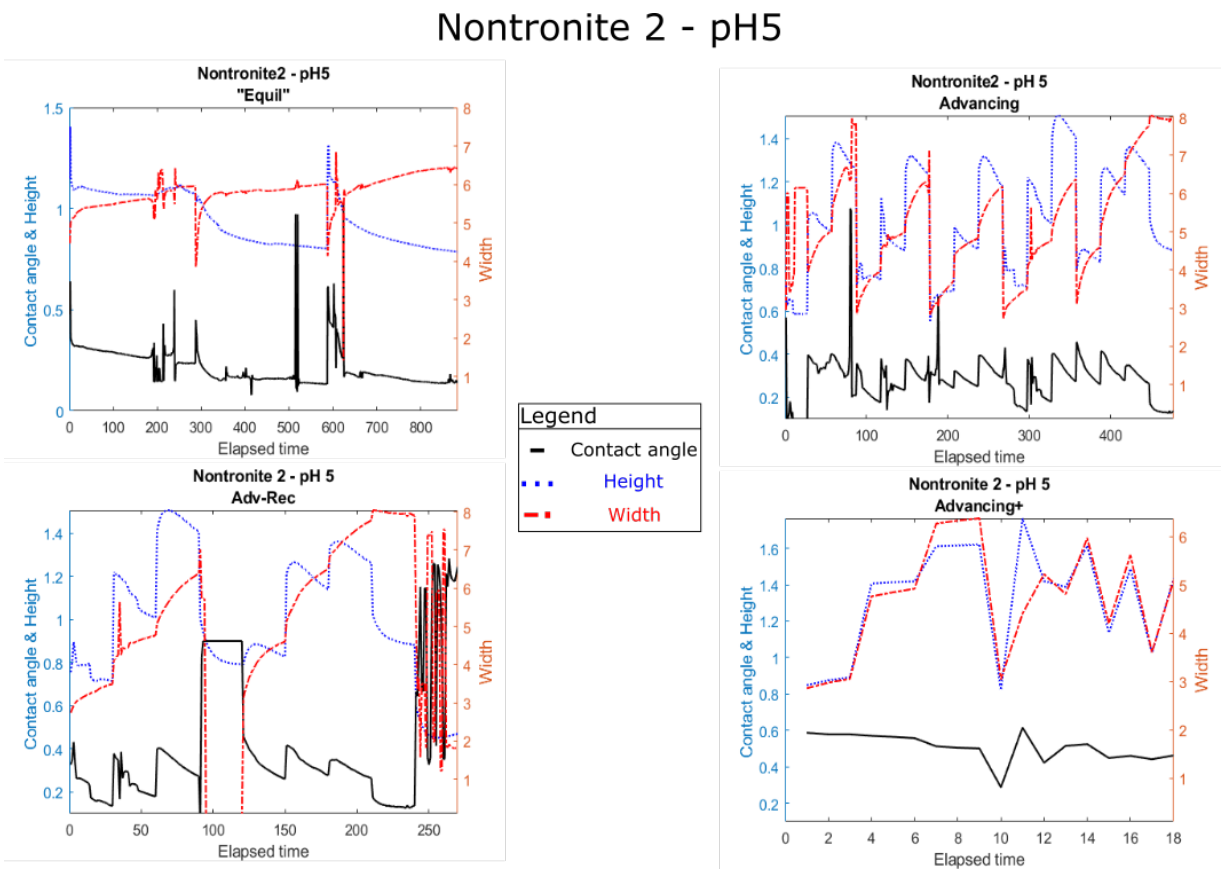

Figure B.10: Dynamic crude oil contact angle, height and width profiles against total time profiles for oxidised NAu2 at pH 5. Clay film is precipitated out of a clay solution with pH post suspension adjusted. At this case, all 4 kind of measurement are taken as described in the experimental section.

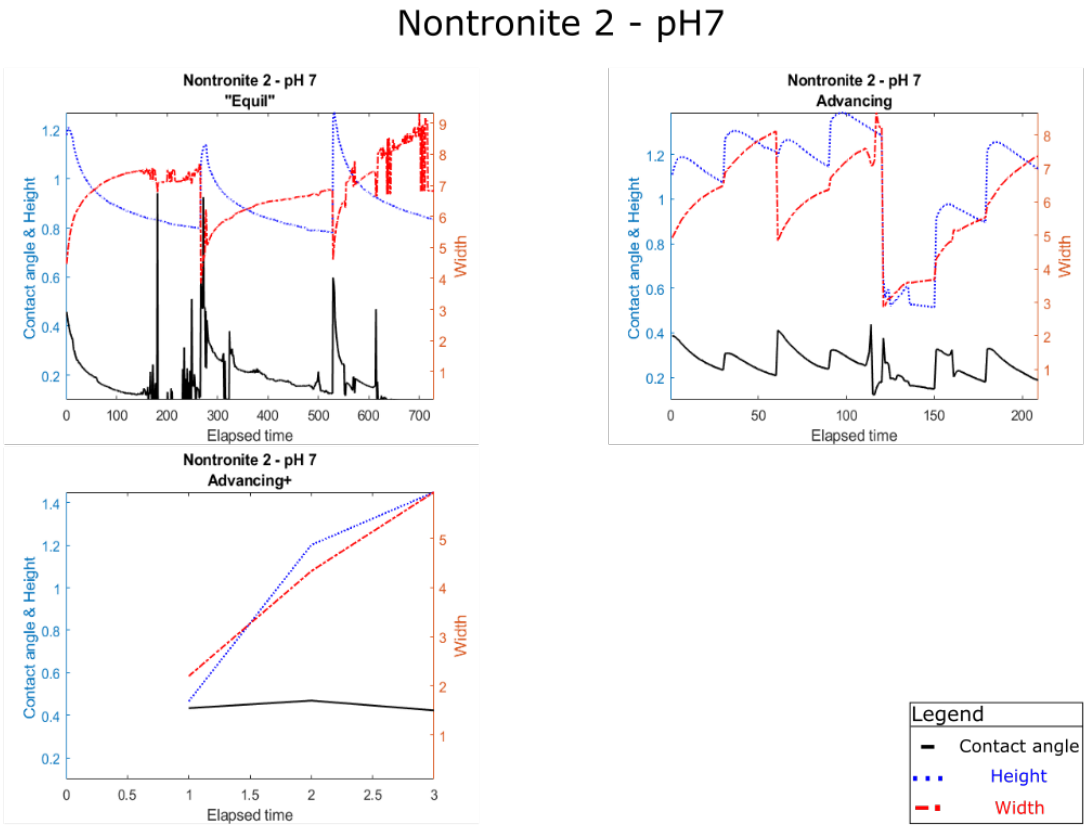

Figure B.11: Dynamic crude oil contact angle, height and width profiles against total time profiles for oxidised NAu2 at pH 7. Clay film is precipitated out of a clay solution with pH post suspension adjusted. At this case, 'Equil', Advancing and Advancing+ configurations are taken as described in the experimental section.

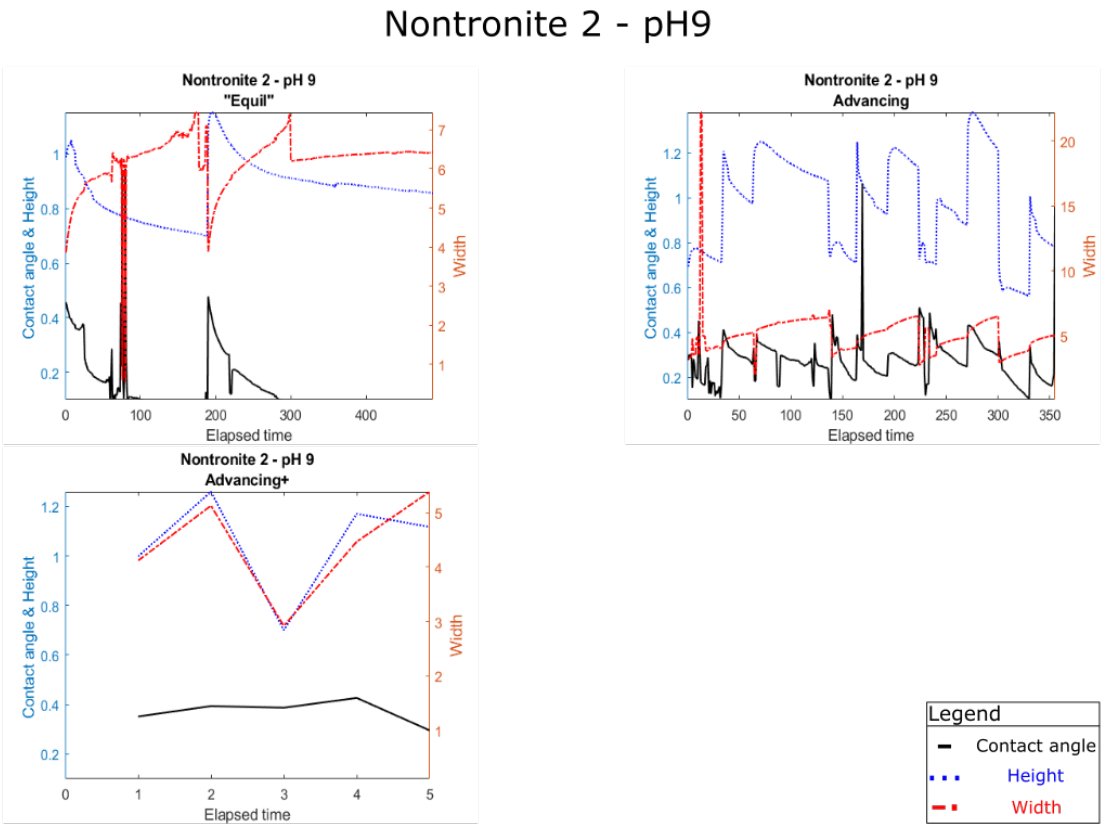

Figure B.12: Dynamic crude oil contact angle, height, and width profiles against total time profiles for oxidised NAu2 at pH 9. Clay film is precipitated out of a clay solution with pH post suspension adjusted. At this case, 'Equil', Advancing and Advancing+ configurations are taken as described in the experimental section.

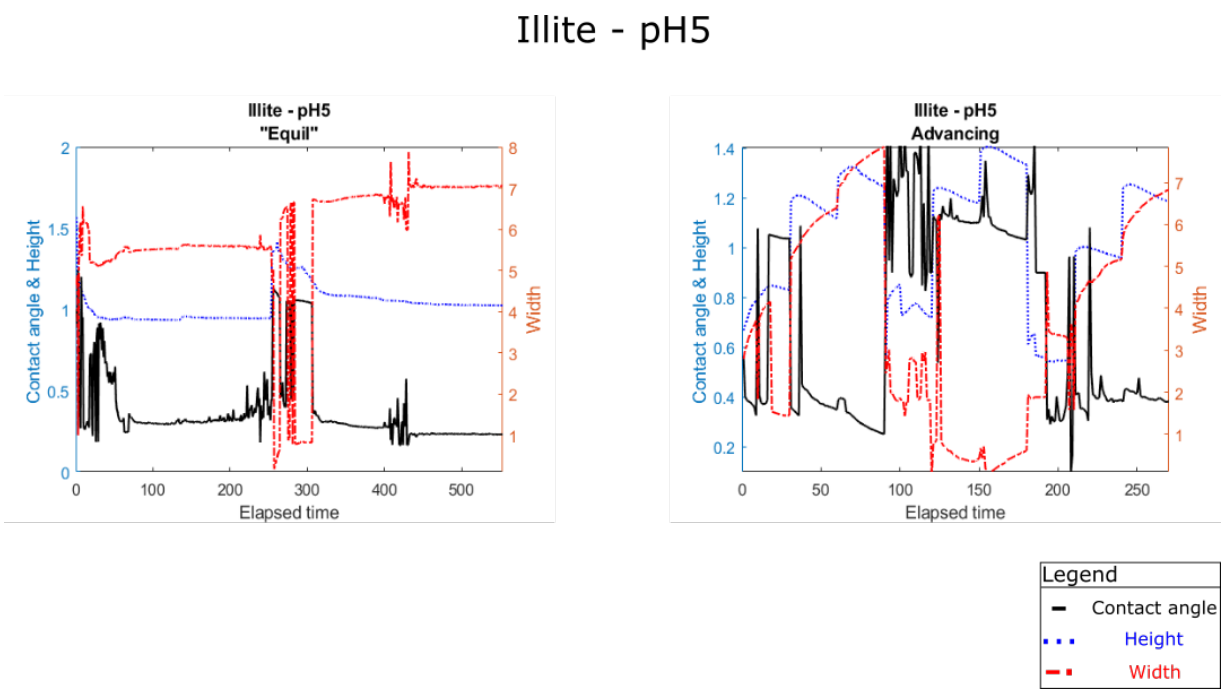

Figure B.13: Dynamic crude oil contact angle, height, and width profiles against total time profiles for oxidised IMt2 at pH 5. Clay film is precipitated out of a clay solution with pH post suspension adjusted. At this case, Equil and Advancing configurations are taken as described in the experimental section.

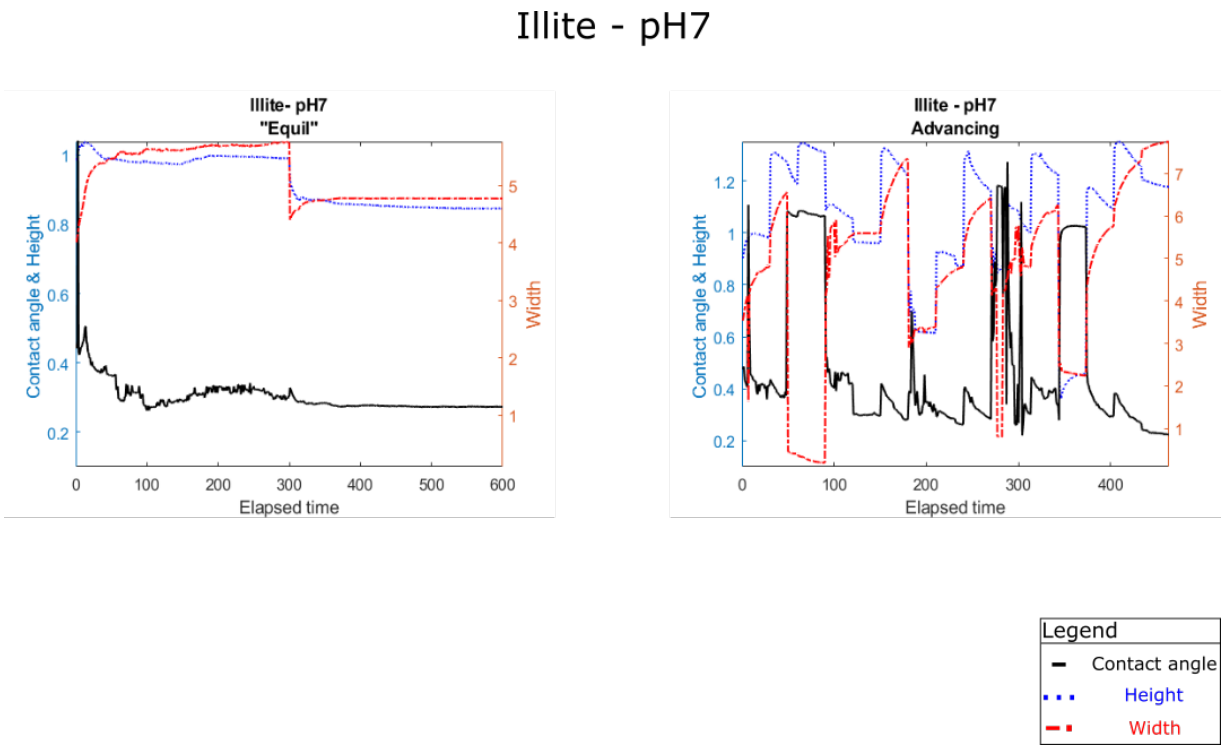

Figure B.14: Dynamic crude oil contact angle, height, and width profiles against total time profiles for oxidised IMt2 at pH 7. Clay film is precipitated out of a clay solution with pH post suspension adjusted. At this case, 'Equil' and Advancing configurations are taken as described in the experimental section.

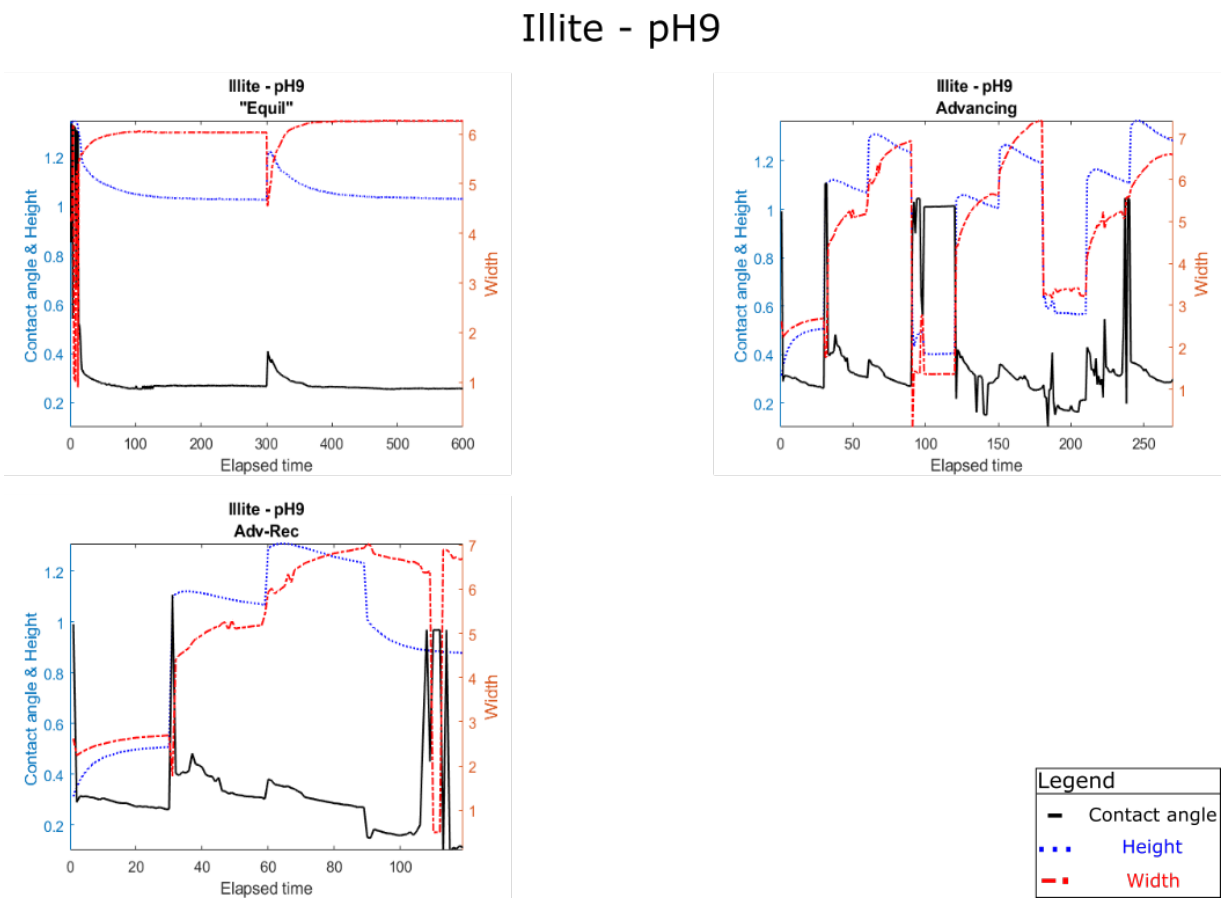

Figure B.15: Dynamic crude oil contact angle, height, and width profiles against total time profiles for oxidised IMt2 at pH 9. Clay film is precipitated out of a clay solution with pH post suspension adjusted. At this case, Equil, Advancing and Adv-Rec configurations are taken as described in the experimental section.

Appendix C

Chapter 5

C.1 M-IR

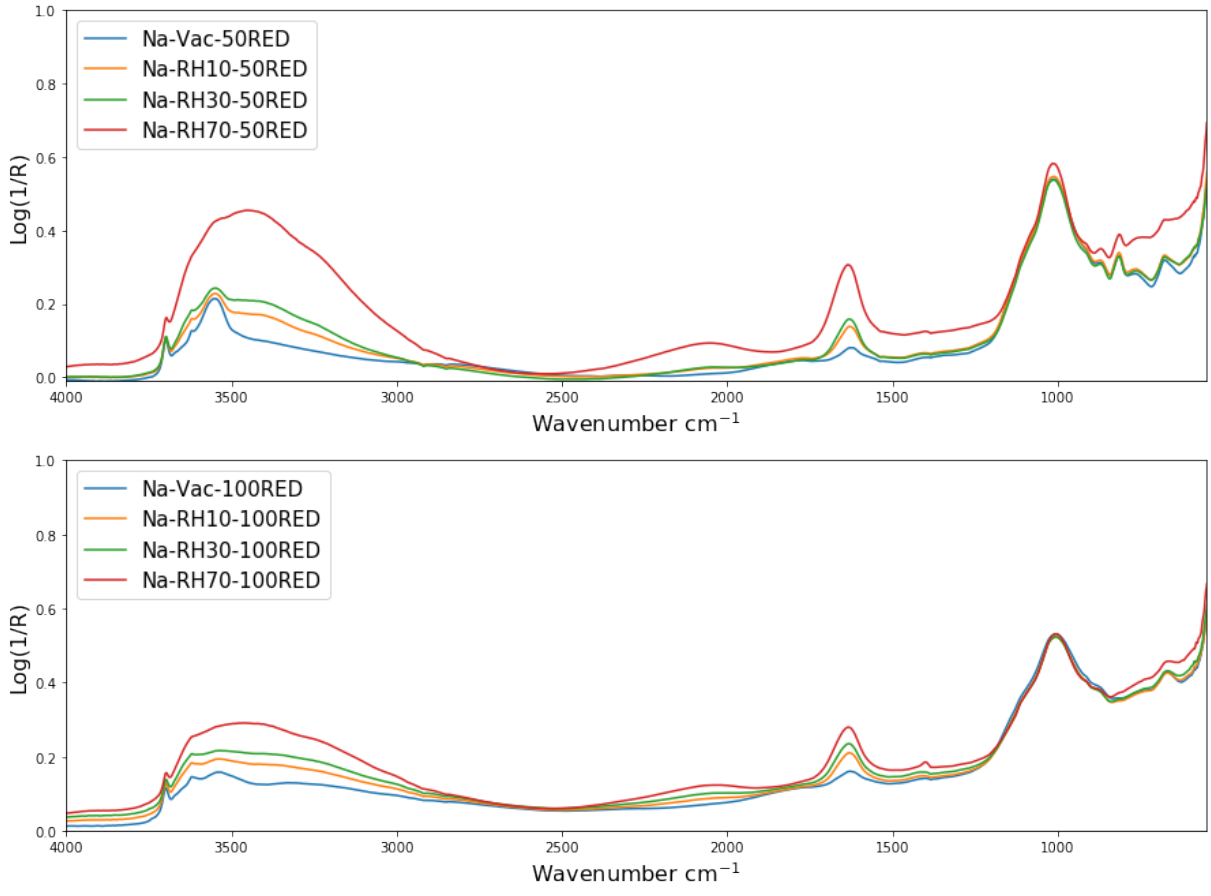

Figure C.1: NAu1-Na samples of 50% (50RED) (upper) and 100% (100RED) (lower) reduction state, showing relative humidity effects on spectra.

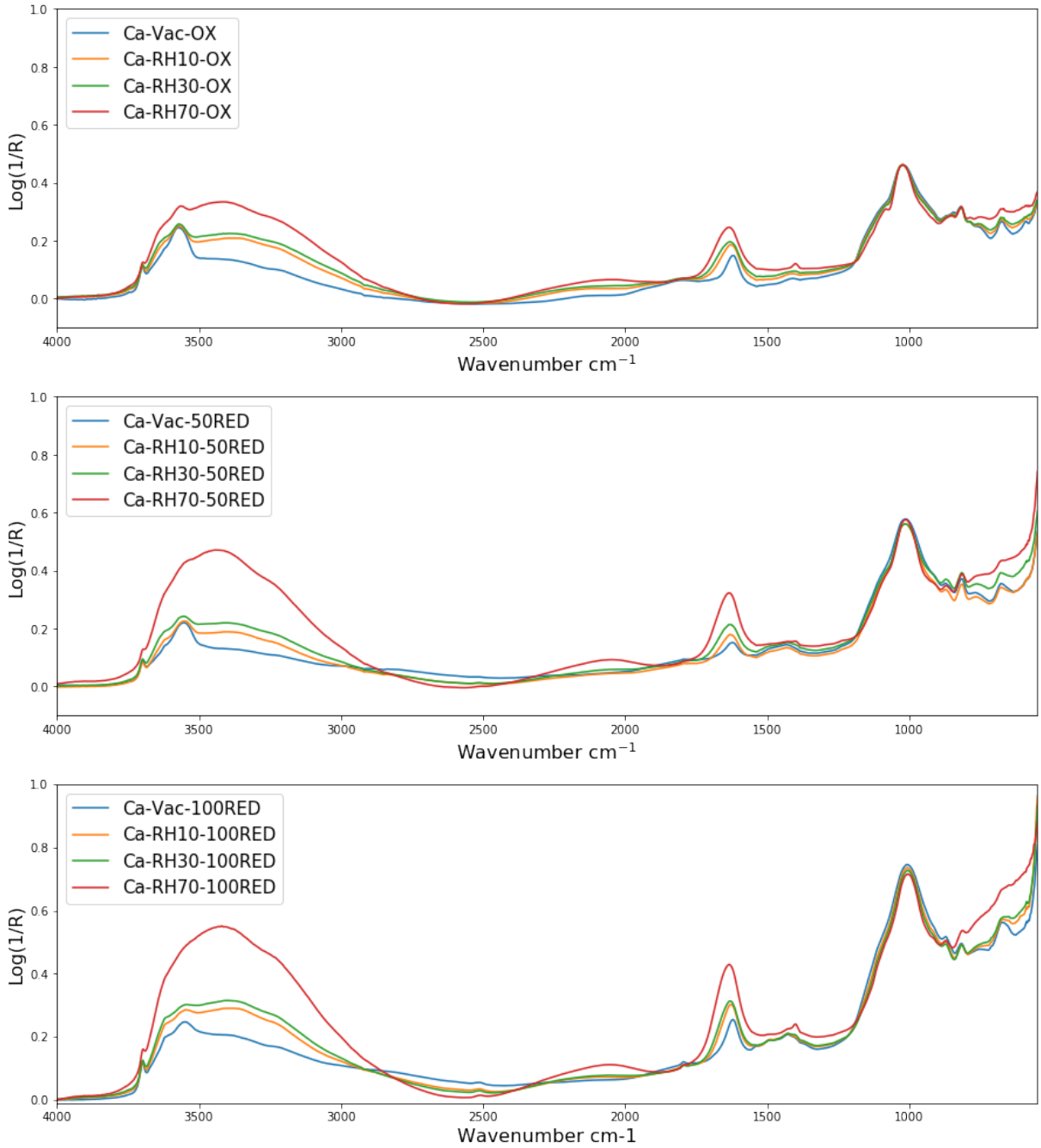

Figure C.2: NAu1-Ca samples of oxidised (upper graph), 50% (50RED) (mid graph) and 100% (100RED) (lower graph) reduction state, showing relative humidity effects on spectra.

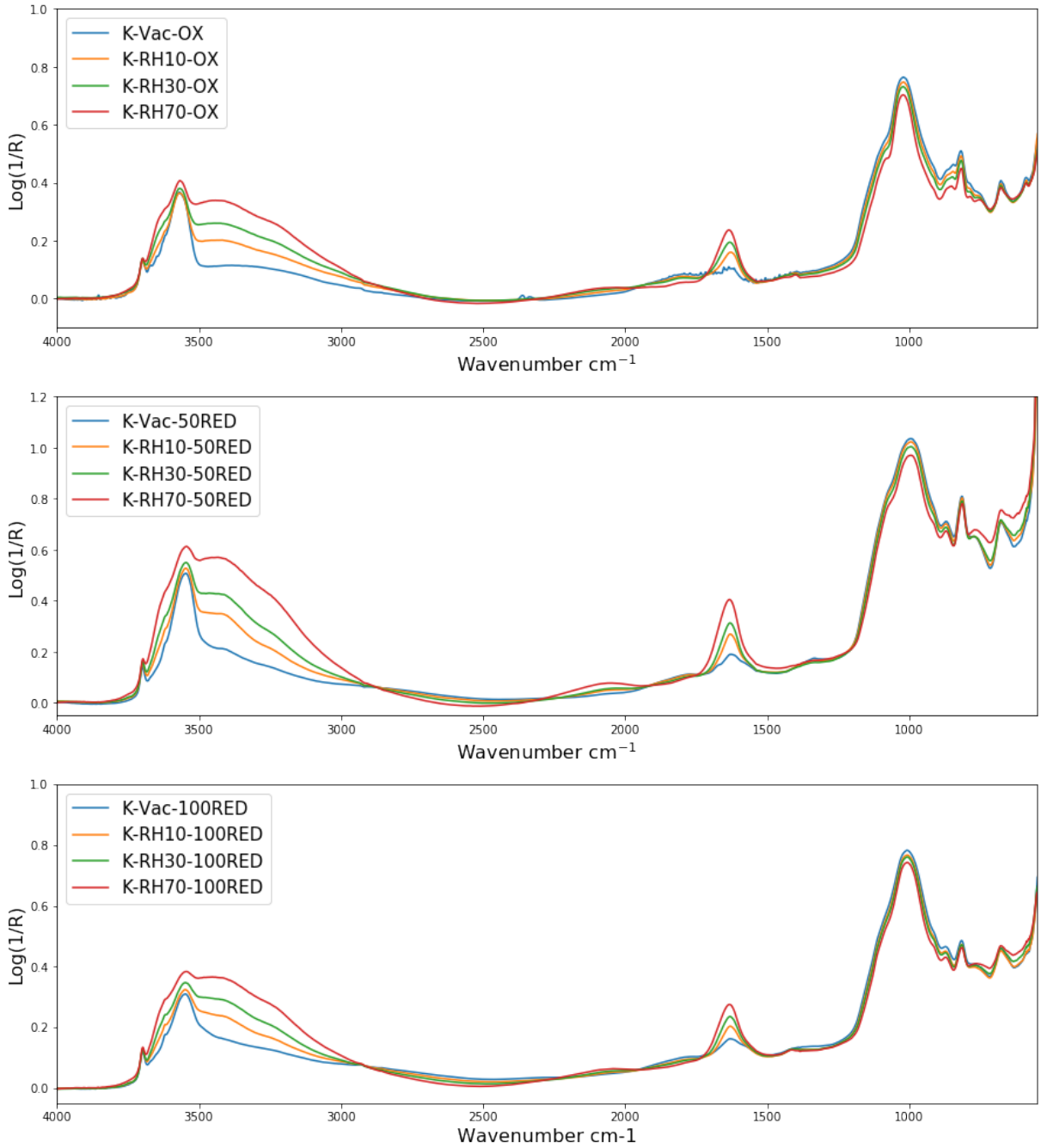

Figure C.3: NAu1-K samples of oxidised (upper graph), 50% (50RED) (mid graph) and 100% (100RED) (lower graph) reduction state, showing relative humidity effects on spectra.

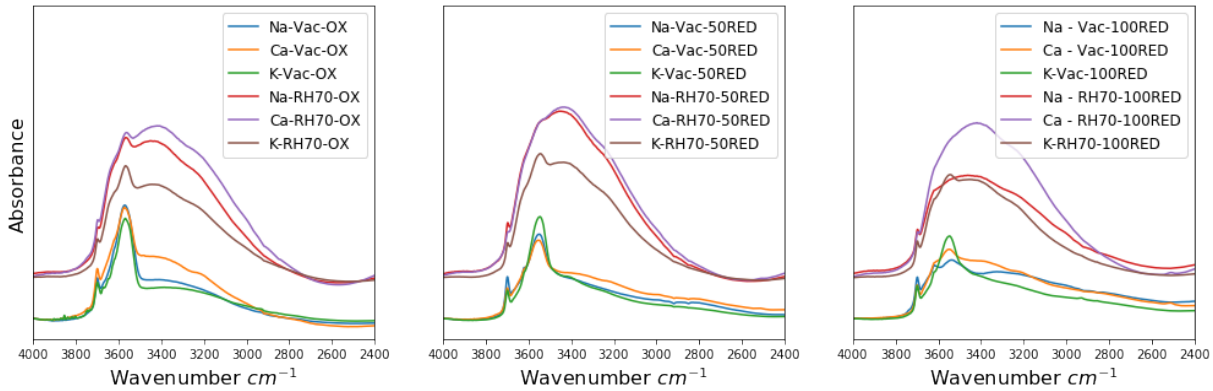

Figure C.4: NAu1-Na (Na) vs NAu1-Ca (Ca) vs NAu1-K (K) induced hydration under oxidised, 50% reduced and 100% reduced state. Higher hydration difference is observed under fully reduced conditions

C.2 N-IR

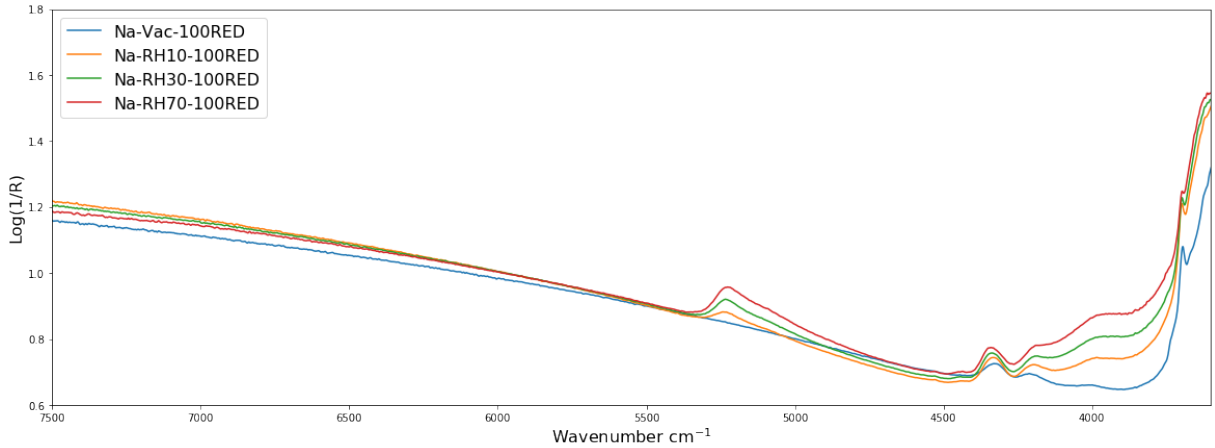

Figure C.5: NAu1-Na raw spectra at 100% (100RED) reduction state, showing relative humidity effects.

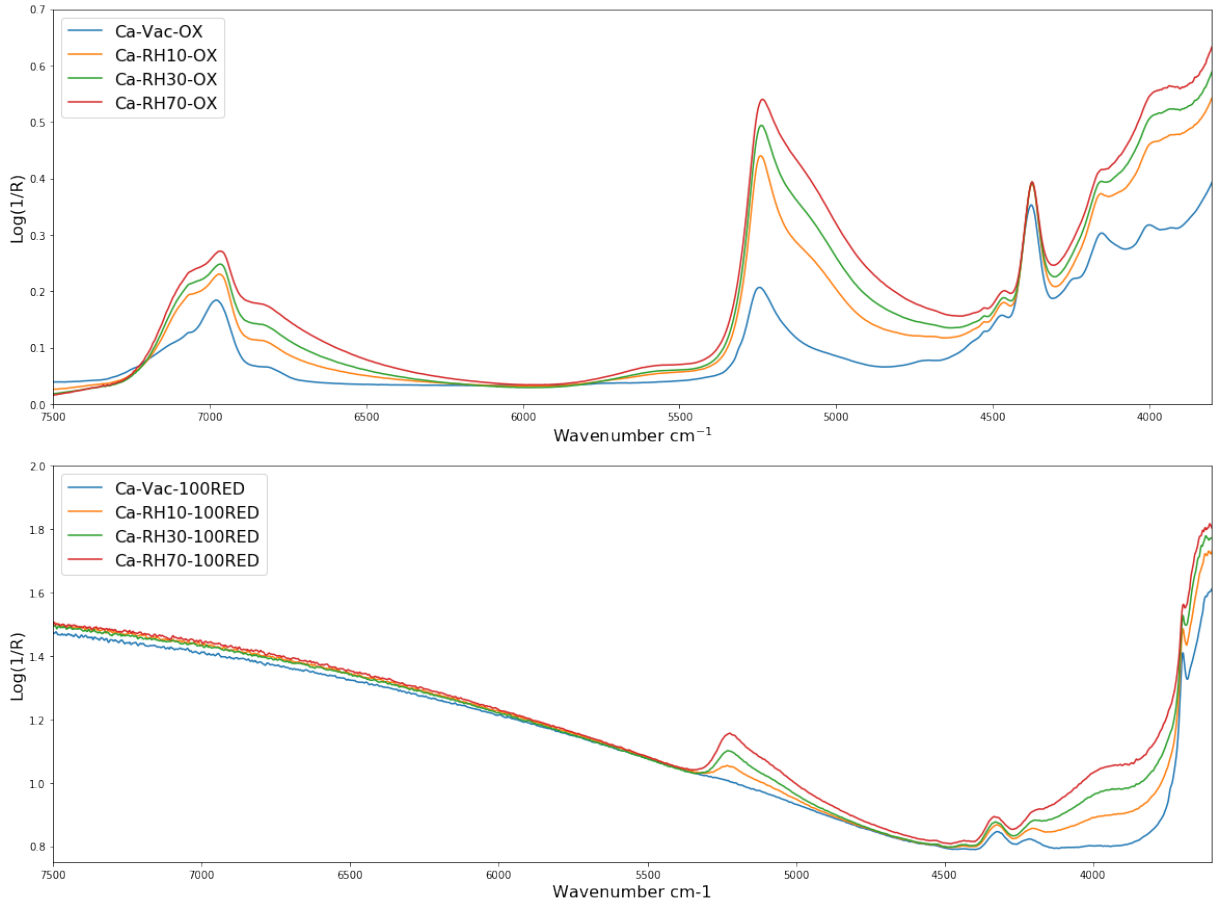

Figure C.6: NAu1-Ca raw spectra at oxidised (OX) and 100% (100RED) reduction state, showing relative humidity effects.

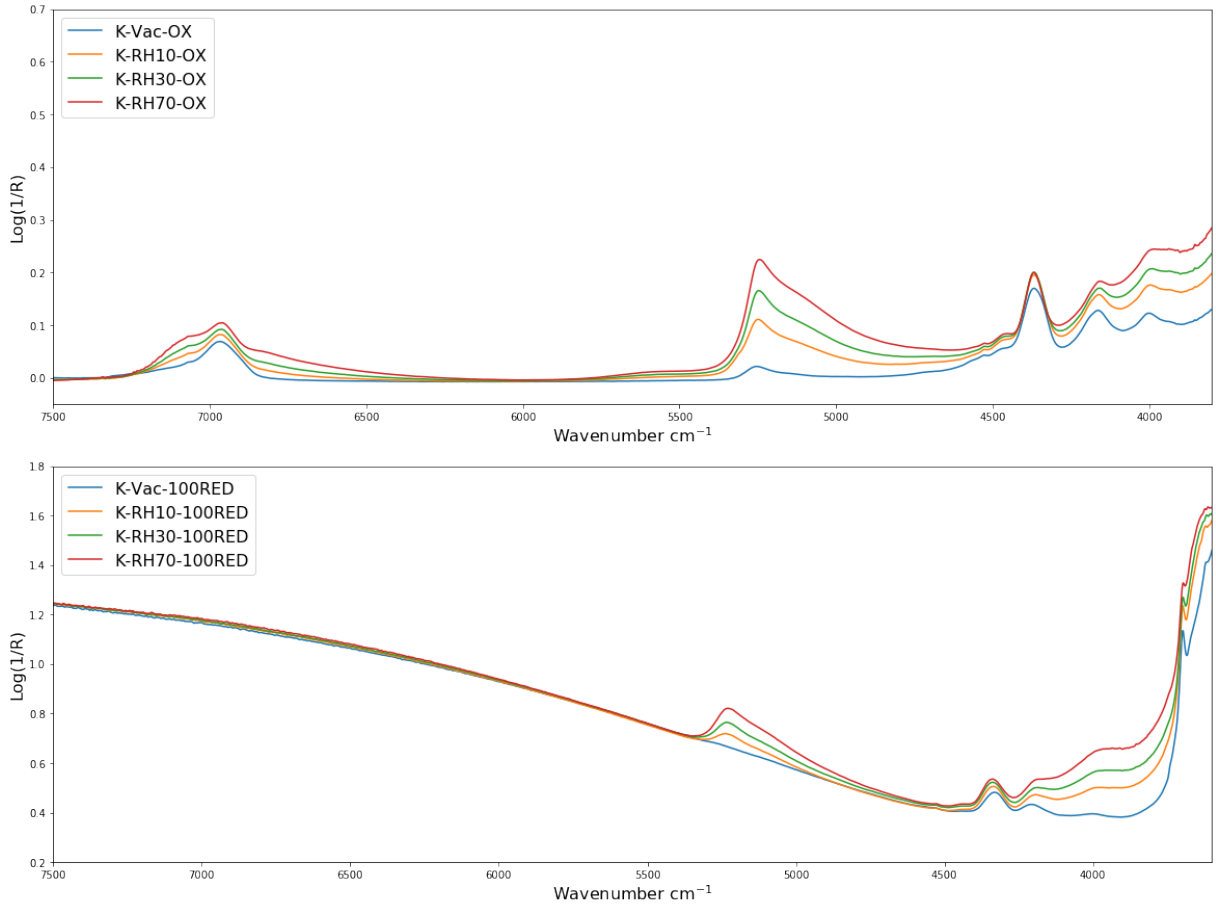

Figure C.7: NAu1-K raw spectra at oxidised (OX) and 100% (100RED) reduction state, showing relative humidity effects.

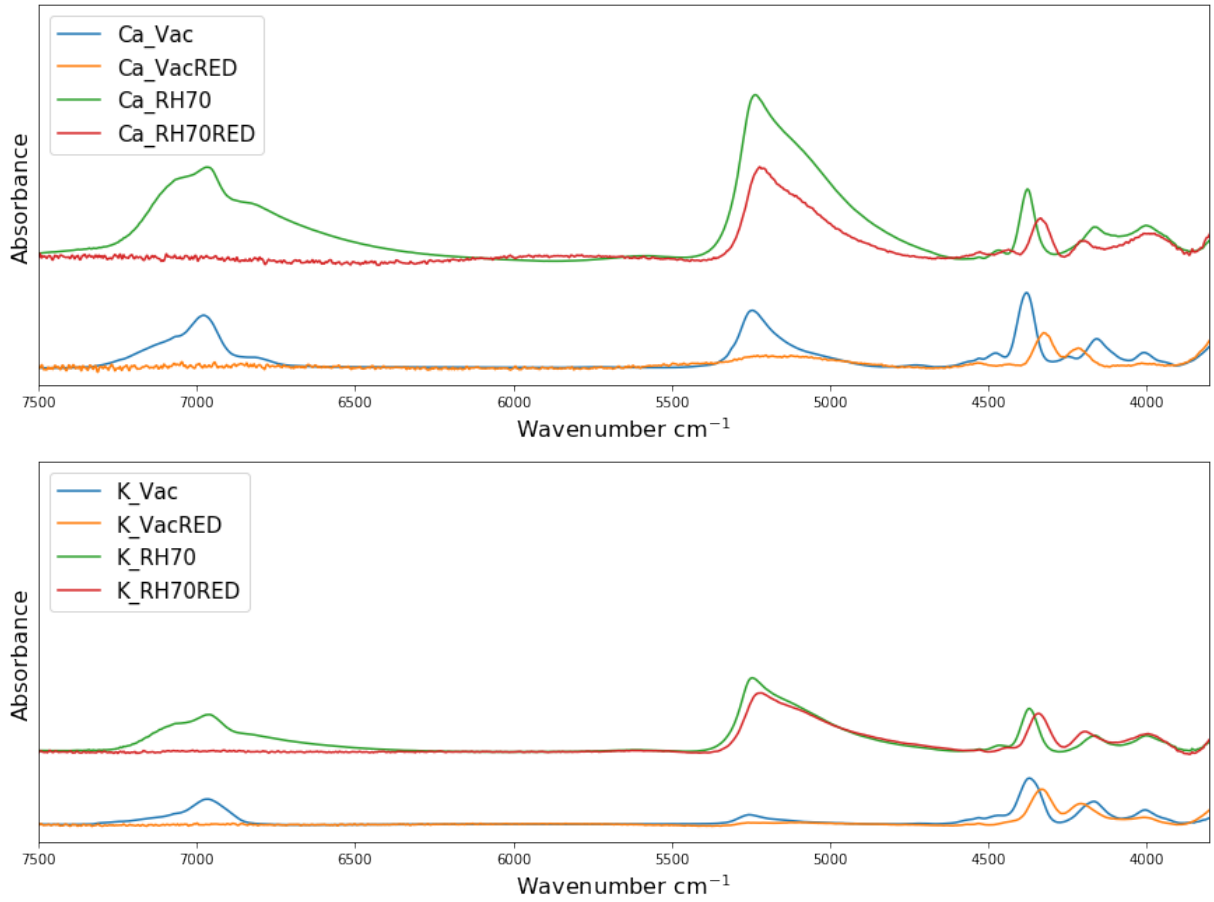

Figure C.8: NAu1-Ca (upper graph) and NAu1-K (lower graph) comparative spectra at vacuum (Vac) and reative humidity 70% at oxidised (OX) and 100% reduced conditions, showing the difference of the RH relative intensity between the two redox states. Background correction has been applied on these patterns.

C.3 Water vapour isotherms

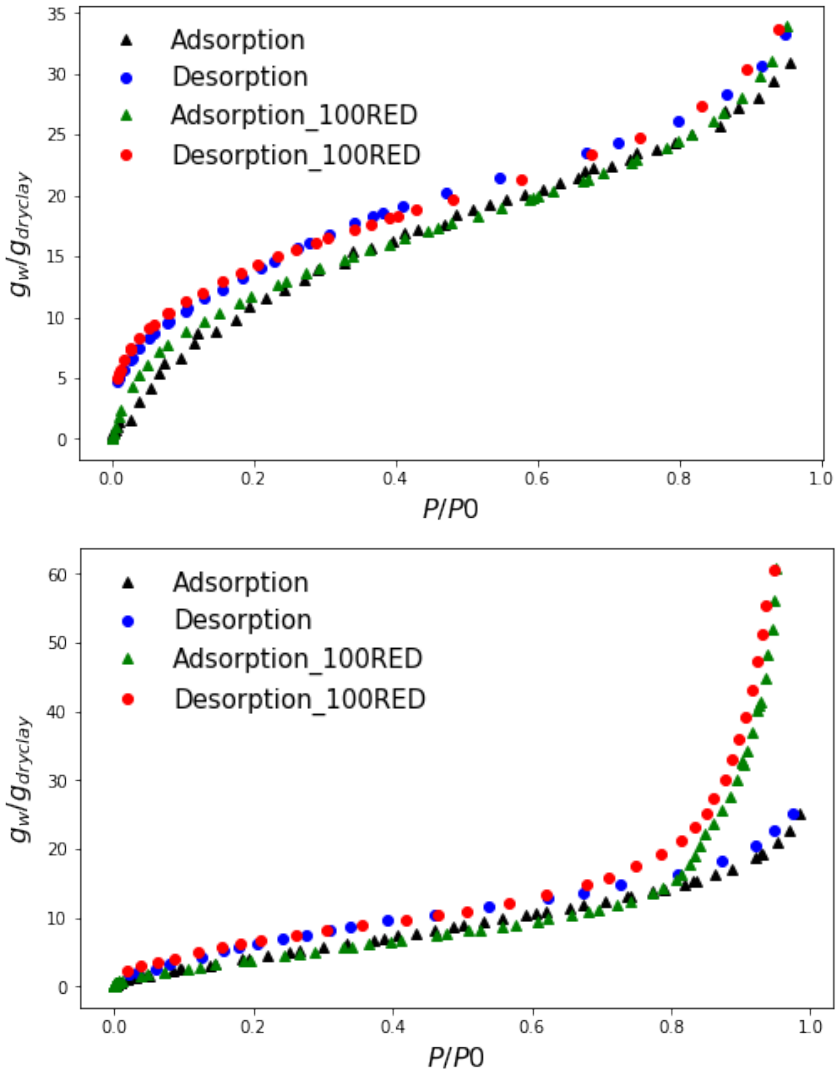

Figure C.9: NAu1-Ca (upper graph) and NAu1-K (lower graph) comparative water vapour adsorption isotherms at oxidised and 100% (100RED) reduced conditions.

Appendix D

Chapter 6

D.1 MIR Data

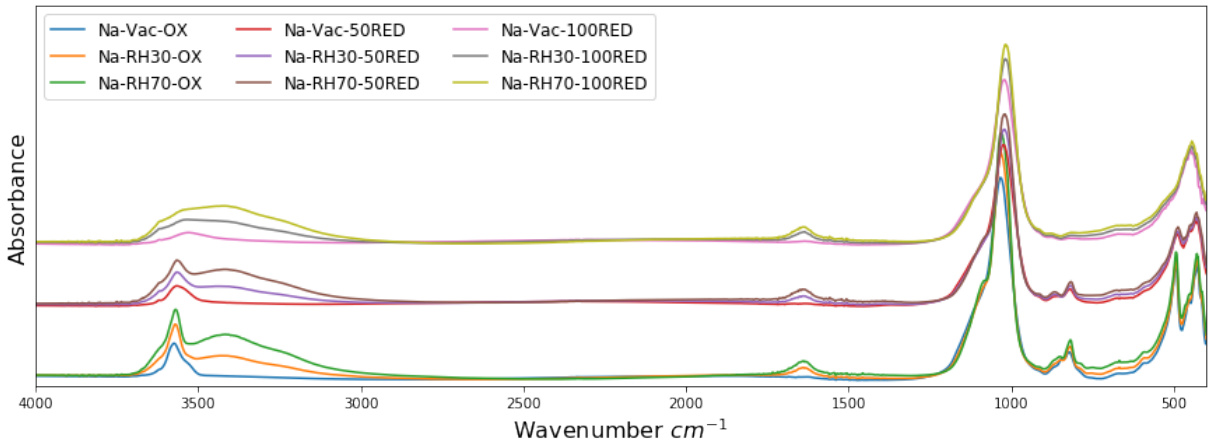

Figure D.1: Full Mid-IR spectra of NAu1-Na, under oxidized (OX), partially (50RED) and fully (100RED) reduced conditions, with different hydration extents of vacuum (Vac), and relative humidity of 30% (RH30) and 70% (RH70).

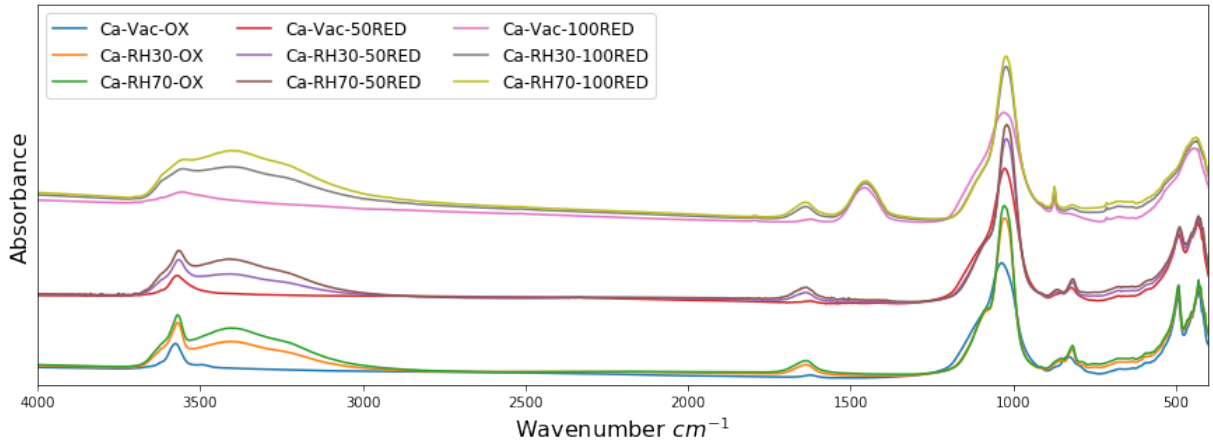

Figure D.2: Full Mid-IR spectra of NAu1-Ca, under oxidized (OX), partially (50RED) and fully (100RED) reduced conditions, with different hydration extents of vacuum (Vac), and relative humidity of 30% (RH30) and 70% (RH70). For the Ca-100RED group of spectra, an additional band was observed at/below the region of 1500 cm^{-1}, attributed to $CaCO_3$, as residues from the reduction process

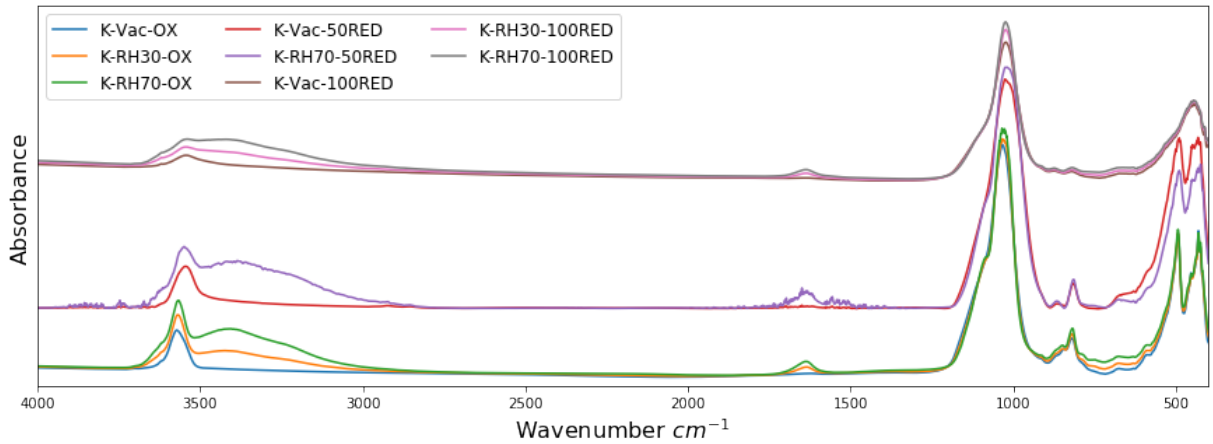

Figure D.3: Full Mid-IR spectra of NAu1-K, under oxidized (OX), partially (50RED) and fully (100RED) reduced conditions, with different hydration extents of vacuum (Vac), and relative humidity of 30% (RH30) and 70% (RH70). Only missing spectrum is the K-RH30-50RED, but should fall in-between the red (K-Vac-50RED) and purple K-RH70-50RED) spectra.

D.2 FIR Data

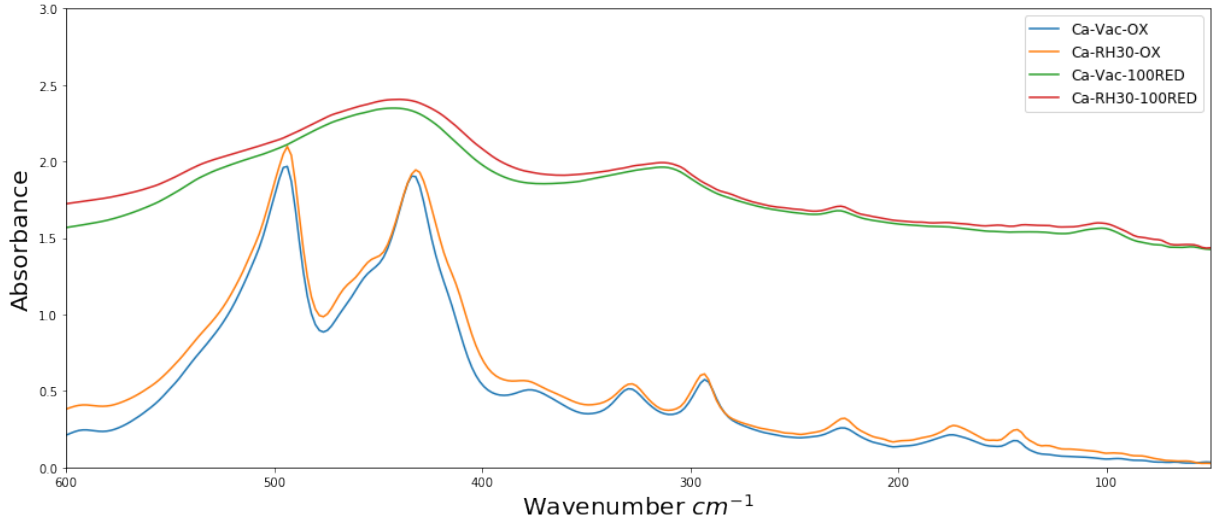

Figure D.4: F-IR spectra of NAu1-Ca under oxidized (OX) and fully reduced (100RED) condition, with different hydration extent at vacuum (Vac) and relative humidity of 30% (RH30).

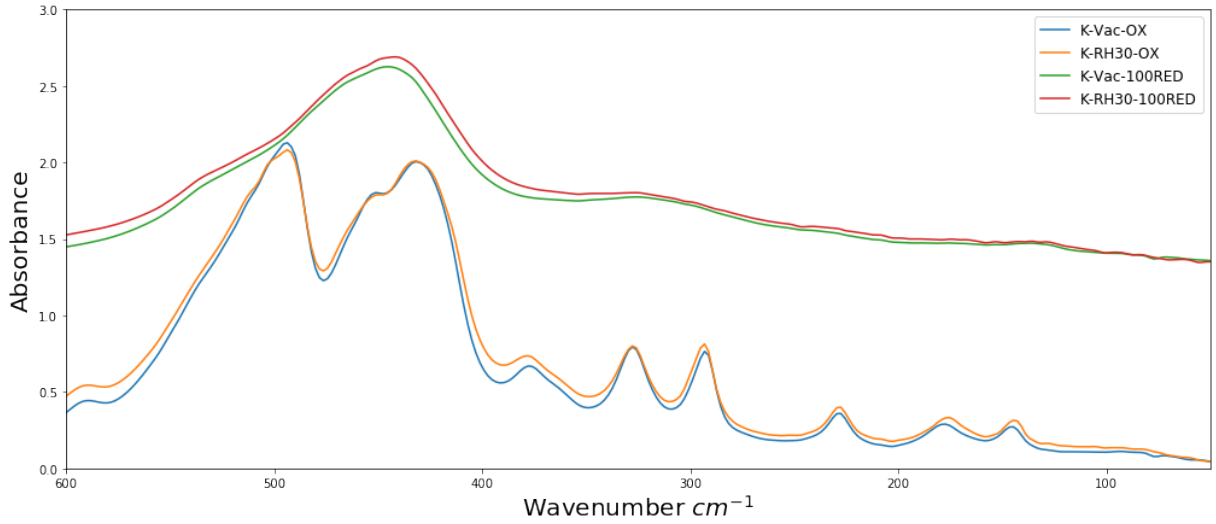

Figure D.5: F-IR spectra of NAu1-K under oxidized (OX) and fully reduced (100RED) condition, with different hydration extent at vacuum (Vac) and relative humidity of 30% (RH30).

Appendix E

Chapter 7

E.1 Thermodynamic calculations

For the determination of the values of the Equations

$$\begin{aligned} \text{(i)} \quad & lnK_{GT} = lnK_{gt} + lnf_{Ca} - lnf_{Na}^2 \\ \text{(ii)} \quad & lnf_{Ca} = -E_{Na}(1 + lnK_{gt}) + \int_0^{E_{Na}} lnK_{gt}\, dE_{Na} \\ \text{(iii)} \quad & lnf_{Na}^2 = (1 - E_{Na})(1 + lnK_{gt}) - \int_{E_{Na}}^1 lnK_{gt}\, dE_{Na} \\ \text{(iv)} \quad & lnK_{GT} = \int_0^1 lnK_{gt}\, dE_{Na} - 1 \end{aligned} \tag{E.1}$$

the following approach was followed. First all the integrals were calculated with K_{gt} being equal:

$$K_{gt} = \frac{E_{Ca}(Na^+)^2\gamma_{Na^+}^2}{E_{Na}^2(Ca^{2+})\gamma_{Ca^{2+}}} \tag{E.2}$$

Using the scipy (Python) function of integration the integrals of ln(K_{gt}) for Equation 24 (ii), (iii), (iv) can be calculated.

from scipy import integrate

n=len(ENa)

$x = lambdax : math.log((ECa[i] * (gNa2[i]) * *2 * Na1[i] * *2)/((x) * *2 * gCa2[i] * Ca1[i]))$

Fx1=[]

```
Fx2=[]
Fx3=[]
for i in range(n):
Fx1.append(integrate.quad(x,0,ENa[i]))
Fx2.append(integrate.quad(x,ENa[i],1))
Fx3.append(integrate.quad(x,0,1))
```

The values of the arrays Fx1, Fx2, and Fx3, can then be fed back to Equations 24 (ii), (iii), (iv) and the respective thermodynamic parameters be calculated, resulting to the graphs of the Figures 7.5, 7.7, 7.9, 7.11, 7.13, 7.15, and Tables 7.5, 7.6, 7.7, 7.8, 7.9, 7.10.

E.2 Results

Table E.1: Na, Ca solution concentration in the mixing, equilibrium and extracted solution, for the Na→ Ca reaction with the NAu1, as measure after ICP-OES analysis.

NAu1 Na→Ca reaction						
Mixing solution (ppm)		Equilibrium solution (ppm)		Extracted solution (ppm)		
Na	Ca	Na	Ca	Na	Ca	Total concentration in meq
26.85	351.9	53.8	551.5	3.2	109.6	0.5
50.84	303.2	91.1	442.7	3.7	99.7	0.46
114.9	200.3	187.8	275.5	5.8	110.9	0.5
168.3	104.7	353.6	132.5	11.2	10.8	0.53
200.6	41	455.7	23.18	26.5	93.81	0.52

Table E.2: Na, K solution concentration in the mixing, equilibrium and extracted solution, for the Na→ K reaction with the NAu1, as measure after ICP-OES analysis.

NAu1 Na→K reaction						
Mixing solution (ppm)		Equilibrium solution (ppm)		Extracted solution (ppm)		
Na	Ca	Na	Ca	Na	Ca	Total concentration in meq
22.71	329.6	54.69	601.7	12.47	734.3	1.74
55.56	282.1	128.5	540.5	21.69	467.2	1.16
117.8	202.2	228.2	349.4	44.69	438.2	1.18
171.2	105.9	346.5	198.6	134.3	309.1	1.24
202.0	43.17	430.7	84.33	185.3	167.0	1.11

Table E.3: Na, Ca solution concentration in the mixing, equilibrium and extracted solution, for the Na→ Ca reaction with the NAu2, as measure after ICP-OES analysis.

NAu2 Na→Ca reaction						
Mixing solution (ppm)		Equilibrium solution (ppm)		Extracted solution (ppm)		
Na	Ca	Na	Ca	Na	Ca	Total concentration in meq
26.85	351.9	69.99	827.4	2.071	78.69	0.34
50.84	303.2	155.1	926.0	4.563	89.5	0.42
114.94	200.39	272.6	416.8	6.128	51.87	0.25
151.4	94.82	277.3	131.5	8.97	71.3	0.35
193.1	40.078	382.59	35.16	14.05	63.25	0.33

Table E.4: Na, K solution concentration in the mixing, equilibrium and extracted solution, for the Na→ K reaction with the NAu2, as measure after ICP-OES analysis.

NAu2 Na→K reaction						
Mixing solution (ppm)		Equilibrium solution (ppm)		Extracted solution (ppm)		
Na	Ca	Na	Ca	Na	Ca	Total concentration in meq
22.71	329.6	120.1	1202	4.426	136.4	0.33
55.56	282.1	254.2	827	8.207	129.0	0.32
116.5	202.2	425.7	598	16.88	130.2	0.36
171.2	105.9	704.5	381	25.89	90.95	0.31
202.0	43.17	1049	236	17.12	27.7	0.13

Table E.5: Na, Ca solution concentration in the mixing, equilibrium and extracted solution, for the Na→ Ca reaction with the SWy3, as measure after ICP-OES analysis.

SWy3 Na→Ca reaction						
Mixing solution (ppm)		Equilibrium solution (ppm)		Extracted solution (ppm)		
Na	Ca	Na	Ca	Na	Ca	Total concentration in meq
26.85	351.9	39.06	475.9	0.15	25.88	0.11
50.84	303.2	166.7	273.2	0.111	17.75	0.08
111.7	207	144.0	247.6	0.28	8.195	0.03
168.3	104.7	208.9	121.1	0.265	8.268	0.03
193.1	40.07	244.8	44.33	1.63	5.148	0.02

Table E.6: Na, K solution concentration in the mixing, equilibrium and extracted solution, for the Na→ K reaction with the SWy3, as measure after ICP-OES analysis.

SWy3 Na→K reaction						
Mixing solution (ppm)		Equilibrium solution (ppm)		Extracted solution (ppm)		
Na	Ca	Na	Ca	Na	Ca	Total concentration in meq
20.64	307.8	52.1	668.3	1.94	29.18	0.07
56.95	279.6	117.2	540.3	1.71	23.3	0.06
107.69	190.2	299.20	455.0	3.26	30.24	0.08
166.4	103.5	393.8	241.1	7.96	22.62	0.08
322.5	73.09	509.7	113.9	10.9	11.97	0.07

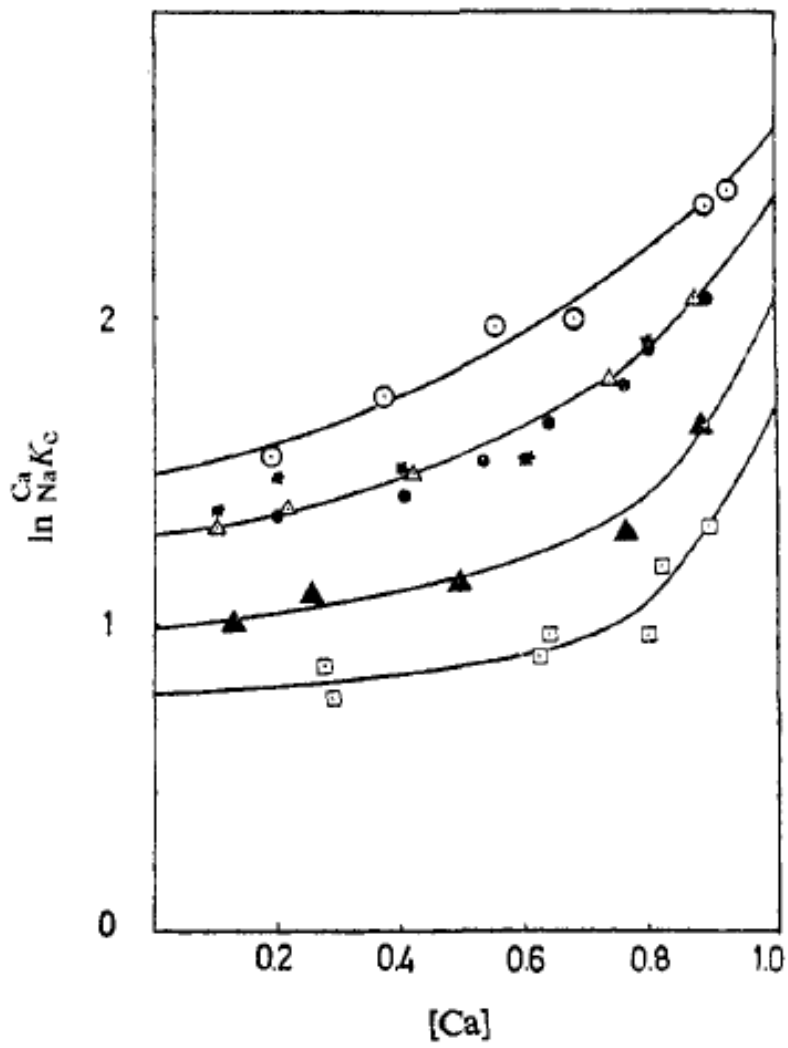

Figure E.1: Selectivity coefficient lnKc and equivalent mole fraction of Ca for the exchange reaction Na→Ca, using (O) Otay montmorillonite, and three montmoriilonitic reduced-charged samples denoted as 0.95 RCM, (Camp Berteau), 0.74 RCM (hectorite) and 0.59 RCM (Otay), for comparing charge effects on cation exchange reactions, in descending sequence. Taken from Maes, Cremers (1977). The point of this graph is to show how the same reaction can exhibit different equilibrium constant on different cation exchanger surfaces.

Bibliography

Abdallah Wael, Buckley Jill S., Canergie Andrew, Edwards John, Herorld Bernd, Fordham Edmund, Graue Arne, Habashy Tarek, Seleznev Nikita, Signer Claude, Hussain Hassan, Montaron Bernard, Ziauddin Murtaza. Fundamentals of Wettability. 2007. 44–61.

Aisawa Sumio, Ohnuma Yuuki, Hirose Kimihiro, Takahashi Satoshi, Hirahara Hidetoshi, Narita Eiichi. Intercalation of nucleotides into layered double hydroxides by ion-exchange reaction // Applied Clay Science. 2005. 28, 1. 137–145. EUROCLAY 2003.

Al-Ghouti Mohammad, Da'ana Dana. Guidelines for the use and interpretation of adsorption isotherm models: A review // Journal of Hazardous Materials. 02 2020. 393. 122383.

Al-Ibadi Hasan, Stephen Karl, Mackay Eric. Heterogeneity Effects on Low Salinity Water Flooding. Day 1 Tue, December 01, 2020. 12 2020. (SPE Europec featured at EAGE Conference and Exhibition). D011S003R003.

Altın Orhan, Özbelge H. Önder, Doğu Timur. Use of General Purpose Adsorption Isotherms for Heavy Metal-Clay Mineral Interactions // Journal of Colloid and Interface Science. II 1998. 198, 1. 130–140.

Alvarez-Silva M., Uribe-Salas A., Mirnezami M., Finch J. A. The point of zero charge of phyllosilicate minerals using the MularRoberts titration technique // Minerals Engineering. 2010. 23, 5. 383–389.

Amirian Tammy, Haghighi Manouchehr, Sun Chenhao, Armstrong Ryan T., Mostaghimi Peyman. Geochemical Modeling and Microfluidic Experiments To Analyze Impact of Clay Type and Cations on Low-Salinity Water Flooding // Energy & Fuels. 2019. 33, 4. 2888–2896.

Amonette J. E. Templeton J. C. Improvements to the Quantitative Assay of Nonrefractory Minerals for Fe(II) and Total Fe Using 1,10-Phenanthroline // Clays and Clay Minerals. I 1998. 46, 1. 51–62.

Angino Ernest E. Far infra-red spectra of montmorillonite, kaolinite and illite // Nature. 1964. 204, 4958. 569–571.

Argersinger W. J., Davidson A. W., Bonner Oscar D. Thermodynamics and Ion Exchange Phenomena // Transactions of the Kansas Academy of Science (1903-). 1950. 53, 3. 404–410.

Austad Tor, Rezaeidoust Alireza, Puntervold Tina. Chemical Mechanism of Low Salinity Water Flooding in Sandstone Reservoirs. 2010/1/1/ 2010.

Badreddine R., Dred R., Prost R. Far infrared study of K+, Rb+ and Cs+ during their exchange with Na+ and Ca2+ in vermiculite // Clay Minerals. 03 2002. 37.

Balan E., Kloprogge J.T. Chapter 2 - Theoretical Aspects of Infrared and Raman Spectroscopies // Infrared and Raman Spectroscopies of Clay Minerals. 8. 2017. 6–33. (Developments in Clay Science).

Ballah J., Chamerois M., Durand-Vidal S., Malikova N., Levitz P., Michot L.J. Effect of chemical and geometrical parameters influencing the wettability of smectite clay films // Colloids and Surfaces A: Physicochemical and Engineering Aspects. 2016. 511. 255–263.

Ballah Jamoowantee. Oil recovery by low salinity waterflooding. 2017. 1–300.

Baron Fabien, Petit Sabine, Tertre Emmanuel, Decarreau Alain. INFLUENCE OF AQUEOUS Si AND Fe SPECIATION ON TETRAHEDRAL Fe(III) SUBSTITUTIONS IN NONTRONITES: A CLAY SYNTHESIS APPROACH // Clays and Clay Minerals. 06 2016. 64, 3. 230–244.

Bartels W.-B., Mahani H., Berg S., Hassanizadeh S.M. Literature review of low salinity waterflooding from a length and time scale perspective // Fuel. 2019. 236. 338–353.

Behera Uma Sankar, Sangwai Jitendra S. Synergistic Effect of Brine System Containing Mixed Monovalent (NaCl, KCl) and Divalent (MgCl2, MgSO4) Salts on the Interfacial Tension of Pure HydrocarbonBrine System Relevant for Low Salinity Water Flooding // Energy & Fuels. 2020. 34, 4. 4201–4212.

Benson LV. A tabulation and evaluation of ion exchange data on smectites // Environmental Geology. 1982. 4, 1. 23–29.

Bernard George G. Effect of Floodwater Salinity on Recovery Of Oil from Cores Containing Clays. 1967/1/1/ 1967. 8.

Bethke Craig M. Geochemical and biogeochemical reaction modeling. 2007.

Bishop J, Madejová J, Komadel P, Fröschl H. The influence of structural Fe, Al and Mg on the infrared OH bands in spectra of dioctahedral smectites. 2002.

Blatt Harvey. Sedimentary petrology. New York: New York : Freeman, 1992. 2nd ed. 1–10.

Bleam William F. Chapter 4 - Ion Exchange // Soil and Environmental Chemistry. Boston: Academic Press, 2012. 117 – 149.

Borden D, Giese RF. Baseline studies of the clay minerals society source clays: cation exchange capacity measurements by the ammonia-electrode method // Clays and Clay Minerals. 2001. 49, 5. 444–445.

Brigatti M. F., Galan E., Theng B. K. G. Chapter 2 Structures and Mineralogy of Clay Minerals // Developments in Clay Science. Volume 1. 2006. 19–86.

Buckley J.S., Liu Y., Monsterleet S. Mechanisms of Wetting Alteration by Crude Oils // SPE Journal. 03 1998. 3, 01. 54–61.

Buckley J.S., Liu Y., Xie X., Morrow N.R. Asphaltenes and Crude Oil Wetting - The Effect of Oil Composition // SPE Journal. 06 1997. 2, 02. 107–119.

Buckley J.S., Morrow N.R. Characterization of Crude Oil Wetting Behavior by Adhesion Tests. All Days. 04 1990. 1–10. (SPE Improved Oil Recovery Conference). SPE-20263-MS.

Buckley J.S., Takamura K., Morrow N.R. Influence of Electrical Surface Charges on the Wetting Properties of Crude Oils // SPE Reservoir Engineering. 08 1989. 4, 03. 332–340.

Charlaftis Dimitrios, Jones Stuart J., Dobson Katherine J., Crouch Jonathan, Acikalin Sanem. Experimental study of chlorite authigenesis and influence on porosity maintenance in sandstones // Journal of Sedimentary Research. 03 2021. 91, 2. 197–212.

Chau T. T. A review of techniques for measurement of contact angles and their applicability on mineral surfaces // Minerals Engineering. 2009. 22, 3. 213–219.

Chen Quan, Enezi Sultan, Yousef Ali. Geochemical Modeling of Low Salinity Water Flooding EOR Mechanism. Day 2 Wed, October 30, 2019. 10 2019. (SPE Asia Pacific Oil and Gas Conference and Exhibition). D021S007R003.

Claire Fialips, Huo Dongfang, Yan Laibin, Wu Jun, Joseph . Effect of Fe oxidation state on the IR spectra of Garfield nontronite. 87. 2002. 630–641.

Dai X., Breuer P.L., Jeffrey M.I. Comparison of activated carbon and ion-exchange resins in recovering copper from cyanide leach solutions // Hydrometallurgy. 2010. 101, 1. 48–57.

Dang Cuong Thanh Quy, Nghiem Long X., Chen Zhangxin John, Nguyen Quoc Phuc. Modeling Low Salinity Waterflooding: Ion Exchange, Geochemistry and Wettability Alteration. 2013/9/30/ 2013.

De Gennes Pierre-Gilles, Brochard-Wyart Françoise, Quéré David. Capillarity and wetting phenomena: drops, bubbles, pearls, waves. 2013.

Dembicki, Jr. Harry. Chapter 1 - Introduction // Practical Petroleum Geochemistry for Exploration and Production. 2017. 1–17.

Denekas M. O., Mattax C. C., Davis G. T. Effects of Crude Oil Components on Rock Wettability. 1959/1/1/ 1959.

Deng Xiao, Kamal Muhammad Shahzad, Patil Shirish, Hussain Syed Muhammad Shakil, Zhou Xianmin. A Review on Wettability Alteration in Carbonate Rocks: Wettability Modifiers // Energy and Fuels. 2020. 34, 1. 31–54.

Derjaguin B, Landau L. Theory of the stability of strongly charged lyophobic sols and of the adhesion of strongly charged particles in solutions of electrolytes // Progress in Surface Science. 1993. 43, 1. 30–59.

Diaz M., Huard E., Prost R. Far Infrared Analysis of the Structural Environment of Interlayer K+, Nh+4, Rb+ and Cs+ Selectively Retained by Vermiculite // Clays and Clay Minerals - CLAYS CLAY MINER. 04 2002. 50. 284–293.

Dimitrov A. S., Kralchevsky P. A., Nikolov A. D., Noshi Hideaki, Matsumoto Mutsuo. Contact angle measurements with sessile drops and bubbles // Journal of Colloid and Interface Science. 1991. 145, 1. 279–282.

Dogan Meral, Dogan A. Umran, Yesilyurt F. Irem, Alaygut Dogan, Buckner Ira, Wurster Dale Eric. BASELINE STUDIES OF THE CLAY MINERALS SOCIETY SPECIAL CLAYS: SPECIFIC SURFACE AREA BY THE BRUNAUER EMMETT TELLER (BET) METHOD // Clays and Clay Minerals. 10 2007. 55, 5. 534–541.

Donaldson Erle C, Chilingarian George V, Yen Teh Fu. Enhanced oil recovery, II: Processes and operations. 1989.

Drelich Jaroslaw, Miller Jan D., Good Robert J. The Effect of Drop (Bubble) Size on Advancing and Receding Contact Angles for Heterogeneous and Rough Solid Surfaces as Observed with Sessile-Drop and Captive-Bubble Techniques // Journal of Colloid and Interface Science. 1996. 179, 1. 37–50.

Drits V.A., Manceau A. A Model for the Mechanism of Fe3+ to Fe2+ Reduction in Dioctahedral Smectites // Clays and Clay Minerals. 04 2000. 48, 2. 185–195.

Drummond Carlos, Israelachvili Jacob. Surface forces and wettability // Journal of Petroleum Science and Engineering. 2002. 33, 1. 123–133.

Du Yujing, Xu Ke, Mejia Lucas, Zhu Peixi, Balhoff Matthew T. Microfluidic Investigation of Low-Salinity Effects During Oil Recovery: A No-Clay and Time-Dependent Mechanism // SPE Journal. 12 2019. 24, 06. 2841–2858.

Dyar M. Darby, Agresti David G., Schaefer Martha W., Grant Christopher A., Sklute Elizabeth C. MSSBAUER SPECTROSCOPY OF EARTH AND PLANETARY MATERIALS // Annual Review of Earth and Planetary Sciences. 2006. 34, 1. 83–125.

Eberl Dennis D. Alkali cation selectivity and fixation by clay minerals // Clays and Clay Minerals. 1980. 28, 3. 161–172.

Eisenman George. Cation selective glass electrodes and their mode of operation // Biophysical journal. 1962. 2, 2. 259–323.

Endo Tsuneyoshi, Yamamoto S., Honna T., Eneji Anthony. Sodium-Calcium Exchange Selectivity As Influenced By Clay Minerals and Composition // Soil Science. 02 2002. 167. 117–125.

Eriksson Erik. Cation-exchange equilibria on clay minerals // Soil Science. 1952. 74, 2. 103–114.

Escudey Mauricio, Daz Patricia, Frster Juan E., Pizarro Carmen, Galindo Gerardo. Gainesthomas and rothmundkornfeld descriptions of potassiumcalcium exchange on variable surface charge soils // Communications in Soil Science and Plant Analysis. 2001. 32, 19-20. 3087–3097.

Eslinger Eric. Clay minerals for petroleum geologists and engineers. Tulsa, OK, U.S.A. (P.O. Box 4756, Tulsa, 74159-0756): Tulsa, OK, U.S.A. P.O. Box 4756, Tulsa, 74159-0756 : SEPM, 1988. (SEPM short course notes).

Farajzadeh R., Guo H., Winden J. van, Bruining J. Cation Exchange in the Presence of Oil in Porous Media // ACS Earth and Space Chemistry. 2017. 1, 2. 101–112. PMID: 28580442.

Farmer V. C. The Layer Silicates // The Infrared Spectra of Minerals. 01 1974.

Farmer VC t, Russell JD. The infra-red spectra of layer silicates // Spectrochimica Acta. 1964. 20, 7. 1149–1173.

Feng Bo, Liu Hanyi, Li Yingli, Liu Xinmin, Tian Rui, Li Rui, Li Hang. AFM measurements of Hofmeister effects on clay mineral particle interaction forces // Applied Clay Science. 2020. 186. 105443.

Fialips Claire-Isabelle, Huo Dongfang, Yan Laibin, Wu Jun, Stucki Joseph W. Effect of Fe oxidation state on the IR spectra of Garfield nontronite // American Mineralogist. 05 2002. 87, 5-6. 630–641.

Fjelde Ingebret, Asen Siv Marie, Omekeh Aruoture, Polanska Anna. Secondary and Tertiary Low Salinity Water Floods: Experiments and Modeling. 2013/6/10/ 2013.

Fjelde Ingebret, Omekeh Aruoture Voke, Haugen Preben Emil. Effect of Ferrous Ion Fe2+ on Wettability: Oxidation and Cation Bridging. 2017/6/12/ 2017.

Fogden Andrew, Kumar Munish, Morrow Norman R., Buckley Jill S. Mobilization of Fine Particles during Flooding of Sandstones and Possible Relations to Enhanced Oil Recovery // Energy & Fuels. 2011. 25, 4. 1605–1616.

Frenkel M. Surface acidity of montmorillonites // Clays Clay Miner. 1974. 22, 5-6. 435–441.

Frost Ray, Ruan Huada, Kloprogge Theo, Gates Will. Dehydration and dehydroxylation of nontronites and ferruginous smectite // Thermochimica Acta. 03 2000. 346. 63–72.

Frost Ray L, Kloprogge J.Theo. Vibrational spectroscopy of ferruginous smectite and nontronite // Spectrochimica Acta Part A: Molecular and Biomolecular Spectroscopy. 2000. 56, 11. 2177 – 2189.

Frost Ray L., Kloprogge J.Theo, Ding Zhe. Near-infrared spectroscopic study of nontronites and ferruginous smectite // Spectrochimica Acta Part A: Molecular and Biomolecular Spectroscopy. 2002. 58, 8. 1657 – 1668.

Gaines George L., Thomas Henry C. Adsorption Studies on Clay Minerals. II. A Formulation of the Thermodynamics of Exchange Adsorption // The Journal of Chemical Physics. 1953. 21, 4. 714–718.

Gaines George L., Thomas Henry C. Adsorption Studies on Clay Minerals. V. MontmorilloniteCesiumStrontium at Several Temperatures // The Journal of Chemical Physics. 1955. 23, 12. 2322–2326.

Gapon EN. On the theory of exchange adsorption in soils // J. Gen. Chem. USSR (Engl. Transl.). 1933. 3. 144–160.

Garfinkel-Shweky Diana, Yariv Shmuel. The Determination of Surface Basicity of the Oxygen Planes of Expanding Clay Minerals by Acridine Orange // Journal of Colloid and Interface Science. 1997. 188, 1. 168–175.

Gast R. G. Standard Free Energies of Exchange for Alkali Metal Cations on Wyoming Bentonite // Soil Science Society of America Journal. 1969. 33, 1. 37–41.

Gast R. G. Alkali Metal Cation Exchange on Chambers Montmorillonite // Soil Science Society of America Journal. 1972. 36, 1. 14–19.

Gates W. P., Slade P. G., Manceau A., Lanson B. Site Occupancies by Iron in Nontronites // Clays and Clay Minerals. 2002. 50, 2. 223–239.

Gates W.P. Infrared Spectroscopy and the Chemistry of Dioctahedral Smectites // The Application of Vibrational Spectroscopy to Clay Minerals and Layered Double Hydroxides. 01 2005.

Geatches D. L., Clark S. J., Greenwell H. C. Iron reduction in nontronite-type clay minerals: Modelling a complex system // Geochimica et Cosmochimica Acta. 2012. 81, Supplement C. 13–27.

Ghorbanzadeh Nasrin, Jung Woosik, Halajnia Akram, Lakzian Amir, Kabra Akhil N., Jeon Byong-Hun. Removal of arsenate and arsenite from aqueous solution by adsorption on clay minerals // Geosystem Engineering. 2015. 18, 6. 302–311.

Giles C. H., MacEwan T. H., Nakhwa S. N., Smith D. 786. Studies in adsorption. Part XI. A system of classification of solution adsorption isotherms, and its use in diagnosis of adsorption mechanisms and in measurement of specific surface areas of solids // J. Chem. Soc. 1960. 3973–3993.

Gluyas Jon G, Swarbrick Richard E. Petroleum geoscience. 2021.

Goodman B.A. Infrared methods // Clay Mineralogy: Spectroscopic and Chemical Determinative Methods. Dordrecht: Springer Netherlands, 1994. 68–119.

Goodman Bernard. A Mössbauer and I.R. Spectroscopic Study of the Structure of Nontronite // Clays and Clay Minerals - CLAYS CLAY MINER. 01 1976. 24. 53–59.

Hamon G. Low-Salinity Waterflooding: Facts, Inconsistencies and the Way Forward // Petrophysics - The SPWLA Journal of Formation Evaluation and Reservoir Description. 02 2016. 57, 01. 41–50.

Hanshaw Bruce B. Cation-exchange constants for clays from electrochemical measurements // Clays and Clay Minerals. 1963. 12, 1. 397–421.

Hassenkam T., Mitchell A.C., Pedersen C.S., Skovbjerg L.L., Bovet N., Stipp S.L.S. The low salinity effect observed on sandstone model surfaces // Colloids and Surfaces A: Physicochemical and Engineering Aspects. 2012. 403. 79–86.

Hassenkam T., Pedersen C. S., Dalby K., Austad T., Stipp S. L. S. Pore scale observation of low salinity effects on outcrop and oil reservoir sandstone // Colloids and Surfaces A: Physicochemical and Engineering Aspects. 2011. 390, 1. 179–188.

Hatch Courtney D., Wiese Jadon S., Crane Cameron C., Harris Kenneth J., Kloss Hannah G., Baltrusaitis Jonas. Water Adsorption on Clay Minerals As a Function of Relative Humidity: Application of BET and Freundlich Adsorption Models // Langmuir. 2012. 28, 3. 1790–1803. PMID: 22181675.

Heller-Kallai L. Reduction and reoxidation of nontronite: the data reassessed // Clays and Clay Minerals. 1997. 45, 3. 476–479.

Hendricks S. B., Nelson R. A., Alexander L. T. Hydration Mechanism of the Clay Mineral Montmorillonite Saturated with Various Cations1 // Journal of the American Chemical Society. 1940. 62, 6. 1457–1464.

Hirasaki G.J. Wettability: Fundamentals and Surface Forces // SPE Formation Evaluation. 06 1991. 6, 02. 217–226.

Hofmeister Franz. Zur lehre von der wirkung der salze // Archiv für experimentelle Pathologie und Pharmakologie. 1888. 24, 4-5. 247–260.

Hornibrook Edward, Longstaffe Fred. Berthierine from the Lower Cretaceous Clearwater Formation, Alberta, Canada // Clays and Clay Minerals - CLAYS CLAY MINER. 01 1996. 44. 1–21.

Hower John, Mowatt Thomas C. The mineralogy of illites and mixed-layer illite/montmorillonites // American Mineralogist. 1966. 51, 5-6.

Hunter Robert J. Zeta potential in colloid science: principles and applications. 2. 2013.

Hussain Syed Abid, Demirci ahinde, zbayolu Glhan. Zeta Potential Measurements on Three Clays from Turkey and Effects of Clays on Coal Flotation // Journal of Colloid and Interface Science. 1996. 184, 2. 535–541.

Ilgen Anastasia G., Kruichak Jessica N., Artyushkova Kateryna, Newville Matt G., Sun Chengjun. Redox Transformations of As and Se at the Surfaces of Natural and Synthetic Ferric Nontronites: Role of Structural and Adsorbed Fe(II) // Environmental Science and Technology. 2017. 51, 19. 11105–11114. PMID: 28850224.

Ilgen Anastasia G., Trainor Thomas P. Sb(III) and Sb(V) Sorption onto Al-Rich Phases: Hydrous Al Oxide and the Clay Minerals Kaolinite KGa-1b and Oxidized and Reduced Nontronite NAu-1 // Environmental Science and Technology. 2012. 46, 2. 843–851. PMID: 22136137.

Inglezakis Vassilis J. The concept of 'capacity' in zeolite ion-exchange systems // Journal of Colloid and Interface Science. 2005. 281, 1. 68–79.

Ishii M., Shimanouchi T., Nakahira M. Far infra-red absorption spectra of layer silicates // Inorganica Chimica Acta. 1967. 1. 387 – 392.

Jackson George A., Williams Peter M. Measures of net oxidant concentration in seawater // Deep Sea Research Part A. Oceanographic Research Papers. 1988. 35, 2. 209–225.

Jackson M. D., Vinogradov J., Hamon G., Chamerois M. Evidence, mechanisms and improved understanding of controlled salinity waterflooding part 1: Sandstones // Fuel. 2016. 185, Supplement C. 772–793.

Jackson M.L.R. Soil chemical analysis. 1958.

Jadhunandan P.P., Morrow N.R. Effect of Wettability on Waterflood Recovery for Crude-Oil/Brine/Rock Systems // SPE Reservoir Engineering. 02 1995. 10, 01. 40–46.

Jenny Hans. Studies on the mechanism of ionic exchange in colloidal aluminum silicates // The journal of physical chemistry. 1932. 36, 8. 2217–2258.

Jerauld Gary R., Lin C. Y., Webb Kevin J., Seccombe Jim C. Modeling Low-Salinity Waterflooding // SPE Reservoir Evaluation and Engineering. 12 2008. 11, 06. 1000–1012.

Johnston C.T. Chapter 9 - Infrared Studies of Clay Mineral-Water Interactions // Infrared and Raman Spectroscopies of Clay Minerals. 8. 2017. 288 – 309. (Developments in Clay Science).

Kareem R., Cubillas P., Gluyas J., Bowen L., Hillier S., Greenwell H. C. Multi-technique approach to the petrophysical characterization of Berea sandstone core plugs (Cleveland Quarries, USA) // Journal of Petroleum Science and Engineering. 2017. 149. 436–455. Cited By :1 Export Date: 7 December 2017.

Kareem Rikan Mohammed Ali. Nano Geochemistry of Low Salinity Enhanced Oil Recovery. 2017.

Keeling John L, Raven Mark D, Gates Will P. Geology and characterization of two hydrothermal nontronites from weathered metamorphic rocks at the Uley graphite mine, South Australia // Clays and Clay Minerals. 2000. 48, 5. 537–548.

Khaled Eid M., Stucki Joseph W. Iron Oxidation State Effects on Cation Fixation in Smectites // Soil Science Society of America Journal. 1991. 55, 2. 550–554.

Kielland Jacob. Individual activity coefficients of ions in aqueous solutions // Journal of the American Chemical Society. 1937. 59, 9. 1675–1678.

Kloprogge J.T. Chapter 6 - Raman Spectroscopy of Clay Minerals // Infrared and Raman Spectroscopies of Clay Minerals. 8. 2017. 150–199. (Developments in Clay Science).

Kopittke P. M., So H. B., Menzies N. W. Effect of ionic strength and clay mineralogy on NaCa exchange and the SARESP relationship // European Journal of Soil Science. 2006. 57, 5. 626–633.

Kumar Sanjeev, Jain Sapna. History, introduction, and kinetics of ion exchange materials // Journal of chemistry. 2013. 2013.

Kunz W., Lo Nostro P., Ninham B.W. The present state of affairs with Hofmeister effects // Current Opinion in Colloid and Interface Science. 2004. 9, 1. 1–18.

Lagaly G. Chapter 5 Colloid Clay Science // Handbook of Clay Science. 1. 2006. 141–245. (Developments in Clay Science).

Lager A., Webb K. J., Black C. J. J., Singleton M., Sorbie K. S. Low salinity oil recovery - An experimental investigation // Petrophysics. 2008. 49, 1. 28–35.

Lager Arnaud, Webb K., Seccombe J. Low Salinity Waterflood, Endicott, Alaska Geochemical Study and Field Evidence of Multicomponent Ion Exchange // 16th European Symposium on Improved Oil Recovery 2011. 04 2011. 521–541.

Laird David A, Shang Chao. Relationship between cation exchange selectivity and crystalline swelling in expanding 2: 1 phyllosilicates // Clays and Clay Minerals. 1997. 45, 5. 681–689.

Langmuir Irving. THE ADSORPTION OF GASES ON PLANE SURFACES OF GLASS, MICA AND PLATINUM. // Journal of the American Chemical Society. 1918. 40, 9. 1361–1403.

Larson Sylvia J, Pardoe GWF, Gebbie HA. The use of far infrared interferometric spectroscopy for mineral identification // American Mineralogist: Journal of Earth and Planetary Materials. 1972. 57, 5-6. 998–1002.

Lear Paul, Stucki Joseph. Role of Structural Hydrogen in the Reduction and Reoxidation of Iron in Nontronite // Clays and Clay Minerals - CLAYS CLAY MINER. 01 1985. 33. 539–545.

Lear Paul R, Stucki Joseph W. Effects of iron oxidation state on the specific surface area of nontronite // Clays and Clay Minerals. 1989. 37, 6. 547–552.

Lebedeva Evgenia V., Fogden Andrew. Wettability alteration of kaolinite exposed to crude oil in salt solutions // Colloids and Surfaces A: Physicochemical and Engineering Aspects. 2011. 377, 1. 115–122.

Lee Kangwon, Kostka Joel E., Stucki Joseph W. Comparisons of structural Fe reduction in smectites by bacteria and dithionite: an infrared spectroscopic study // Clays and Clay Minerals. 2006. 54, 2. 195–208.

Ligthelm Dick Jacob, Gronsveld Jan, Hofman Jan, Brussee Niels, Marcelis Fons, Linde Hilbert van der. Novel Waterflooding Strategy By Manipulation Of Injection Brine Composition. 2009/1/1/ 2009.

Liu Xinmin, Li Hang, Du Wei, Tian Rui, Li Rui, Jiang Xianjun. Hofmeister Effects on Cation Exchange Equilibrium: Quantification of Ion Exchange Selectivity // The Journal of Physical Chemistry C. 2013. 117, 12. 6245–6251.

López-León Teresa, Santander-Ortega Manuel J., Ortega-Vinuesa Juan L., Bastos-Gonzlez Delfi. Hofmeister Effects in Colloidal Systems: Influence of the Surface Nature // The Journal of Physical Chemistry C. 2008. 112, 41. 16060–16069.

Ma Xiangxian, Zheng Guodong, Xu Wang, Liang Minliang, Fan Qiaohui, Wu Yingzhong, Ye Conglin, Shozugawa Katsumi, Matsuo Motoyuki. Iron speciation and mineral characterization of upper Jurassic reservoir rocks in the Minhe Basin, NW China // Hyperfine Interactions. 2016. 237, 1. 77.

Macdougall G., Ockrent C., Kendall James Pickering. Surface energy relations in liquid/solid systems I. The adhesion of liquids to solids and a new method of determining the surface tension of liquids // Proceedings of the Royal Society of London. Series A. Mathematical and Physical Sciences. 1942. 180, 981. 151–173.

Madejová J., Gates W.P., Petit S. Chapter 5 - IR Spectra of Clay Minerals // Infrared and Raman Spectroscopies of Clay Minerals. 8. 2017. 107 – 149. (Developments in Clay Science).

Madejov J., Plkov H. Chapter 13 - NIR Contribution to The Study of Modified Clay Minerals // Infrared and Raman Spectroscopies of Clay Minerals. 8. 2017. 447–481. (Developments in Clay Science).

Maes Andre, Cremers Adrien. Charge density effects in ion exchange. Part 1.Heterovalent exchange equilibria // J. Chem. Soc., Faraday Trans. 1. 1977. 73. 1807–1814.

Maes Andre, Cremers Adrien. Charge density effects in ion exchange. Part 2.Homovalent exchange equilibria // J. Chem. Soc., Faraday Trans. 1. 1978. 74. 1234–1241.

Manceau A., Drits V. A., Lanson Bruno, Chateigner Daniel, Wu J., Huo D., Gates Will, Stucki Joseph. Oxidation-reduction mechanism of iron in dioctahedral smectites: II. Crystal chemistry of reduced Garfield nontronite. 85. 2000a. 153–172.

Manceau A., Lanson Bruno, Drits V. A., Chateigner Daniel, Gates Will, Wu J., Df Huo, Stucki Joseph. Oxidation-reduction mechanism of iron in dioctahedral smectites: I. Crystal chemistry of oxidized reference nontronites. 85. 2000b. 133–152.

Matott L., Rabideau A. ISOFIT - A program for fitting sorption isotherms to experimental data // Environ. Model. Softw. 2008. 23. 670–676.

McGuire P. L., Chatham J. R., Paskvan F. K., Sommer D. M., Carini F. H. Low Salinity Oil Recovery: An Exciting New EOR Opportunity for Alaska's North Slope. 2005/1/1/ 2005.

Mermut Ahmet R, Cano Angel Faz. Baseline studies of the clay minerals society source clays: chemical analyses of major elements // Clays and Clay Minerals. 2001. 49, 5. 381–386.

Mermut Ahmet R, Lagaly Gerhard. Baseline studies of the clay minerals society source clays: layer-charge determination and characteristics of those minerals containing 2: 1 layers // Clays and Clay Minerals. 2001. 49, 5. 393–397.

Michaelian K. H. The Raman spectrum of kaolinite #9 at 21C // Canadian Journal of Chemistry. 1986. 64, 2. 285–294.

Mu Nana, Schulz Hans-Martin, Fu Yunjiao, Schovsbo Niels Hemmingsen, Wirth Richard, Rhede Dieter, Berk Wolfgang van. Berthierine formation in reservoir rocks from the Siri oilfield (Danish North Sea) as result of fluidrock interactions: Part I. Characterization // Marine and Petroleum Geology. 2015. 65, Supplement C. 302–316.

Mugele Frieder, Siretanu Igor, Kumar Naveen, Bera Bijoy, Wang Lei, Maestro Armando, Duits Michel, Ende Dirk van den, Collins Ian. Charge Control And Wettability Alteration At Solid-liquid Interfaces. 2014/4/12/ 2014.

Mugele Frieder, Siretanu Igor, Kumar Naveen, Bera Bijoy, Wang Lei, Ruiter Rille de, Maestro Armando, Duits Michel, Ende Dirk van den, Collins Ian. Insights From Ion Adsorption and Contact-Angle Alteration at Mineral Surfaces for Low-Salinity Waterflooding // SPE Journal. 08 2016. 21, 04. 1204–1213.

Murray Haydn H. Chapter 2 Structure and Composition of the Clay Minerals and their Physical and Chemical Properties // Developments in Clay Science. Volume 2. 2006. 7–31.

Nakamoto Kazuo. Infrared and Raman Spectra of Inorganic and Coordination Compounds // Handbook of Vibrational Spectroscopy. 2006.

Nasralla Ramez A., Nasr-El-Din Hisham A. Coreflood Study of Low Salinity Water Injection in Sandstone Reservoirs. 2011/1/1/ 2011.

Nasralla Ramez A., Nasr-El-Din Hisham A. Double-Layer Expansion: Is It A Primary Mechanism of Improved Oil Recovery by Low-Salinity Waterflooding? 2012/1/1/ 2012.

Nasralla Ramez A., Nasr-El-Din Hisham A. Double-Layer Expansion: Is It a Primary Mechanism of Improved Oil Recovery by Low-Salinity Waterflooding? // SPE Reservoir Evaluation and Engineering. 2014. 17, 01. 49–59.

Neal C., Cooper Daniel Mark. Extended Version of Gouy-Chapman Electrostatic Theory as Applied to the Exchange Behavior of Clay in Natural Waters // Clays and Clay Minerals. 1983. 31. 367–376.

Neumann Anke, Petit Sabine, Hofstetter Thomas. Evaluation of redox-active iron sites in smectites using middle and near infrared spectroscopy // Geochimica et Cosmochimica Acta. 05 2011. 75. 2336–2355.

Nir S., Hirsch D., Navrot J., Banin A. Specific Adsorption of Lithium, Sodium, Potassium, and Strontium to Montmorillonite: Observations and Predictions // Soil Science Society of America Journal. 1986. 50, 1. 40–45.

Nir Shlomo. Specific and Nonspecific Cation Adsorption to Clays: Solution Concentrations and Surface Potentials // Soil Science Society of America Journal. 1986. 50, 1. 52–57.

Nwidee Lezorgia Nekabari, Theophilus Stephen, Barifcani Ahmed, Sarmadivaleh Mohammad, Iglauer Stefan. EOR Processes, Opportunities and Technological Advancements // Chemical Enhanced Oil Recovery (cEOR) - a Practical Overview. Rijeka: InTech, 2016. Ch. 01.

Overbeek J.Th.G, Verwey E. J. W. Theory of the Stability of Lyophobic Colloids: The Interaction of sol particles having an electric double layer. // Elsevier. 1948.

Pandey Anurag, Bera Debabrata, Shukla Anupam, Ray Lalitagauri. Studies on Cr(VI), Pb(II) and Cu(II) adsorptiondesorption using calcium alginate as biopolymer // Chemical Speciation and Bioavailability. 2007. 19, 1. 17–24.

Pilon Laurent, Wang Hainan, dEntremont Anna. Recent advances in continuum modeling of interfacial and transport phenomena in electric double layer capacitors // Journal of The Electrochemical Society. 2015. 162, 5. A5158–A5178.

Prost René, Laperche V. Far-Infrared Study of Potassium in Micas // Clays and Clay Minerals. 1990. 38. 351–355.

Pu Hui, Xie Xina, Yin Peigui, Morrow Norman R. Low-Salinity Waterflooding and Mineral Dissolution. 2010/1/1/ 2010.

Reed Brian E., Matsumoto Mark R. Modeling Cadmium Adsorption by Activated Carbon Using the Langmuir and Freundlich Isotherm Expressions // Separation Science and Technology. 1993. 28, 13-14. 2179–2195.

RezaeiDoust A., Puntervold T., Strand S., Austad T. Smart Water as Wettability Modifier in Carbonate and Sandstone: A Discussion of Similarities/Differences in the Chemical Mechanisms // Energy and Fuels. 2009. 23, 9. 4479–4485.

RezaeiDoust Alireza, Puntervold Tina, Austad Tor. Chemical Verification of the EOR Mechanism by Using Low Saline/Smart Water in Sandstone // Energy and Fuels. 2011. 25, 5. 2151–2162.

Ribeiro Fabiana R., Fabris Jos D., Kostka Joel E., Komadel Peter, Stucki Joseph W. Comparisons of structural iron reduction in smectites by bacteria and dithionite: II. A variable-temperature Mssbauer spectroscopic study of Garfield nontronite. 2009. 1499.

Rotenberg Benjamin, Morel Jean-Pierre, Marry Virginie, Turq Pierre, Morel-Desrosiers Nicole. On the driving force of cation exchange in clays: Insights from combined microcalorimetry experiments and molecular simulation // Geochimica et Cosmochimica Acta. 2009. 73, 14. 4034–4044.

Russell J. D., Fraser A. R. Infrared methods // Clay Mineralogy: Spectroscopic and Chemical Determinative Methods. Dordrecht: Springer Netherlands, 1994. 11–67.

Saadat Marzieh, Tsai Peichun A, Ho Tsai-Hsing, Øye Gisle, Dudek Marcin. Development of a microfluidic method to study enhanced oil recovery by low salinity water flooding // ACS omega. 2020. 5, 28. 17521–17530.

Sawhney BL. Selective sorption and fixation of cations by clay minerals: a review // Clays and clay minerals. 1972. 20, 2. 93–100.

Schaefer Michael V., Gorski Christopher A., Scherer Michelle M. Spectroscopic Evidence for Interfacial Fe(II)Fe(III) Electron Transfer in a Clay Mineral // Environmental Science and Technology. 2011. 45, 2. 540–545. PMID: 21138293.

Schrader Bernhard. Infrared and Raman spectroscopy: methods and applications. 2008.

Schroeder Paul. Far-Infrared Study of the Interlayer Torsional-Vibrational Mode of Mixed-Layer Illite/Smectites // Clays and Clay Minerals - CLAYS CLAY MINER. 02 1992. 40. 81–91.

Seccombe James C., Lager Arnaud, Webb Kevin John, Jerauld Gary, Fueg Esther. Improving Wateflood Recovery: LoSalTM EOR Field Evaluation. 2008/1/1/ 2008.

Seccombe Jim, Lager Arnaud, Jerauld Gary, Jhaveri Bharat, Buikema Todd, Bassler Sierra, Denis John, Webb Kevin, Cockin Andrew, Fueg Esther, Paskvan Frank. Demonstration of Low-Salinity EOR at Interwell Scale, Endicott Field, Alaska. 04 2010. SPE-129692-MS.

Shainberg I., ALPEROVITCH N., KEREN R. Charge Density and Na-K-Ca Exchange on Smectites1 // Clays and Clay Minerals - CLAYS CLAY MINER. 01 1987. 35. 68–73.

Shainberg I., Oster J. D., Wood J. D. Sodium/Calcium Exchange in Montmorillonite and Illite Suspensions // Soil Science Society of America Journal. 1980. 44, 5. 960–964.

Shang Jianying, Flury Markus, Harsh James B., Zollars Richard L. Comparison of different methods to measure contact angles of soil colloids // Journal of Colloid and Interface Science. 2008. 328, 2. 299–307.

Shang Jianying, Flury Markus, Harsh James B., Zollars Richard L. Contact angles of aluminosilicate clays as affected by relative humidity and exchangeable cations // Colloids and Surfaces A: Physicochemical and Engineering Aspects. 2010. 353, 1. 1–9.

Sharma M.M., Filoco P.R. Effect of Brine Salinity and Crude-Oil Properties on Oil Recovery and Residual Saturations // SPE Journal. 09 2000. 5, 03. 293–300.

Sheng J. J. Critical review of low-salinity waterflooding // Journal of Petroleum Science and Engineering. 2014. 120. 216–224.

Siyambalagoda Gamage Pubudu Hasanka, Thyne Geoffrey D. Comparison of Oil Recovery by Low Salinity Waterflooding in Secondary and Tertiary Recovery Modes. 2011/1/1/ 2011.

Soraya Boussour, Malick Cissokho, Philippe Cordier, Bertin Henri Jacques, Hamon Gerald. Oil Recovery by Low-Salinity Brine Injection: Laboratory Results on Outcrop and Reservoir Cores. All Days. 10 2009. (SPE Annual Technical Conference and Exhibition). SPE-124277-MS.

Speight J.G. The Chemistry and Technology of Petroleum, Fourth Edition. 2006.

Sposito G. The Thermodynamics of Soil Solutions. 1981. (Oxford science publications).

Sposito Garrison. Derivation of the Langmuir Equation for Ion Exchange Reactions in Soils // Soil Science Society of America Journal. 1979. 43, 1. 197–198.

Sposito Garrison. Derivation of the Freundlich Equation for Ion Exchange Reactions in Soils // Soil Science Society of America Journal. 1980. 44, 3. 652–654.

Sposito Garrison, others . The surface chemistry of soils. 1984.

Sripal Edison, James L. A. Application of an Optimization Method for the Restoration of Core Samples for SCAL Experiments // Petrophysics - The SPWLA Journal of Formation Evaluation and Reservoir Description. 02 2018. 59, 01. 72–81.

Stucki J. W., Golden D. C., Roth C. B. Preparation and handling of dithionite-reduced smectite suspensions // Clays and Clay Minerals. 1984a. 32, 3. 191–197. STUCKI, JW GOLDEN, DC ROTH, CB.

Stucki J. W., Roth C. B. Oxidation-reduction Mechanism for Structural Iron in Nontronite1 // Soil Science Society of America Journal. 1977. 41, 4. 808–814.

Stucki J.W. Chapter 8 Properties and Behaviour of Iron in Clay Minerals // Handbook of Clay Science. 1. 2006. 423 – 475. (Developments in Clay Science).

Stucki Joseph, C. Golden D., Roth Charles. Effects of Reduction and Reoxidation of Structural Iron on the Surface Charge and Dissolution of Dioctahedral Smectites. 32. 1984b. 350–356.

Stucki Joseph, Lee Kangwon, Zhang Lingzhi, Larson Richard. Effects of iron oxidation state on the surface and structural properties of smecites. 01 2002. 2145–2158.

Stucki Joseph, Low Philip, Roth Charles, Golden D.C. Effects of Oxidation State of Octahedral Iron on Clay Swelling // Clays and Clay Minerals. 10 1984c. 32. 357–362.

Stucki Joseph W. A review of the effects of iron redox cycles on smectite properties // Comptes Rendus Geoscience. 2011. 343, 2. 199 – 209.

Stucki Joseph W., Bailey George W., Gan Huamin. Oxidation-reduction mechanisms in iron-bearing phyllosilicates // Applied Clay Science. 1996. 10, 6. 417–430.

Stucki Joseph W., Lear Paul R. Variable Oxidation States of Iron in the Crystal Structure of Smectite Clay Minerals // Spectroscopic Characterization of Minerals and Their Surfaces. 415. 1990. Book Section 17, 330–358. (ACS Symposium Series).

Takahashi Haruka, Saito Sosuke, Morishita Ryoichi, Takahashi Kotaro, Kurihara Masanori. Development of Numerical Simulator for Predicting Oil Recovery Process of Low-Salinity Water Flooding // SPWLA 25th Formation Evaluation Symposium of Japan. 2019.

Tang Guo-Qing, Morrow Norman R. Influence of brine composition and fines migration on crude oil/brine/rock interactions and oil recovery // Journal of Petroleum Science and Engineering. 1999. 24, 2. 99–111.

Teppen Brian J, Miller David M. Hydration energy determines isovalent cation exchange selectivity by clay minerals // Soil Science Society of America Journal. 2006. 70, 1. 31–40.

Tetteh Joel T., Aryana Saman A., Barati Ghahfaorkhi Reza. An Investigation into Fluid-Fluid Interaction Phenomenon During Low Salinity Waterflooding using a Reservoir-on-a-Chip Microfluidics Model. Day 2 Tue, September 01, 2020. 08 2020. (SPE Improved Oil Recovery Conference). D021S036R001.

Thommes Matthias, Kaneko Katsumi, Neimark Alexander V, Olivier James P, Rodriguez-Reinoso Francisco, Rouquerol Jean, Sing Kenneth SW. Physisorption of gases, with special reference to the evaluation of surface area and pore size distribution (IUPAC Technical Report) // Pure and applied chemistry. 2015. 87, 9-10. 1051–1069.

Tonietto Leandro, Gonzaga Luiz, Veronez Mauricio Roberto, Souza Kazmierczak Claudio de, Arnold Daiana Cristina Metz, Costa Cristiano André da. New method for evaluating surface roughness parameters acquired by laser scanning // Scientific reports. 2019. 9, 1. 1–16.

Underwood Thomas, Erastova Valentina, Cubillas Pablo, Greenwell H. Chris. Molecular Dynamic Simulations of MontmorilloniteOrganic Interactions under Varying Salinity: An Insight into Enhanced Oil Recovery // The Journal of Physical Chemistry C. 2015. 119, 13. 7282–7294.

Underwood Thomas, Erastova Valentina, Greenwell Chris. Ion Adsorption at Clay-mineral Surfaces: the Hofmeister Series For Hydrated Smectite Minerals // Clays and Clay Minerals. 12 2016. 64.

Unsal Evren, van der Linde Hilbert, Wilson Ove B. Redox effects on relative permeability in Fe-rich clay bearing sandstones // Marine and Petroleum Geology. 2020. 115. 104251.

Vanselow Albert P. Equilibria of the Base-Exchange Reactions of Bentonites, Permutites, Soil Colloids, and Zeolites // Soil Science. II 1932. 33, 2. 95–114.

Velde B, Couty R. Far infrared spectra of hydrous layer silicates // Physics and Chemistry of Minerals. 1985. 12, 6. 347–352.

Verburg Kirsten, Baveye Philippe. Hysteresis in the Binary Exchange of Cations on 2:1 Clay Minerals: A Critical Review // Clays and Clay Minerals - CLAYS CLAY MINER. 04 1994. 42. 207–220.

Vijayalakshmi K., Devi B. Mahalakshmi, Latha Srinivasan, Gomathi Thandapani, Sudha P.N., Venkatesan Jayachandran, Anil Sukumaran. Batch adsorption and desorption studies on the removal of lead (II) from aqueous solution using nanochitosan/sodium alginate/microcrystalline cellulose beads // International Journal of Biological Macromolecules. 2017. 104. 1483–1494. 11th APCCS-2016-Chemistry, Environmental, Biotechnology and Biomedical Aspects of Chitin and Chitosan.

Wada Shin-Ichiro, Weerasooriya Janaki Deepa. Sodium-calcium, calcium-potassium, and potassium-sodium exchange equilibria on a montmorillonitic soil // Soil Science and Plant Nutrition. 1990. 36, 3. 451–459.

Wagner O. R., Leach R. O. Improving Oil Displacement Efficiency by Wettability Adjustment // Transactions of the AIME. 1959. 216, 01. 65–72.

Wang F.H.L., Guidry L.J. Effect of Oxidation-Reduction Condition on Wettability Alteration // SPE Formation Evaluation. 06 1994. 9, 02. 140–148.

Wang Junchao, Wu Yankun, Cao Yijun, Li Guosheng, Liao Yinfei. Influence of surface roughness on contact angle hysteresis and spreading work // Colloid and Polymer Science. 08 2020. 298.

Whittaker Michael L., Lammers Laura N., Carrero Sergio, Gilbert Benjamin, Banfield Jillian F. Ion exchange selectivity in clay is controlled by nanoscale chemical–mechanical coupling // Proceedings of the National Academy of Sciences. 2019. 116, 44. 22052–22057.

Winoto Winoto, Loahardjo Nina, Xie Sheena Xina, Yin Peigui, Morrow Norman R. Secondary and Tertiary Recovery of Crude Oil from Outcrop and Reservoir Rocks by Low Salinity Waterflooding. 2012.

Wu Wenju. Baseline studies of the clay minerals society source clays: colloid and surface phenomena // Clays and Clay Minerals. 2001. 49, 5. 446–452.

Yariv Shmuel, Cross Harold. Organo-clay complexes and interactions. 2001.

Yesufu-Rufai Sherifat, Marcelis Fons, Georgiadis Apostolos, Berg Steffen, Rcker Maja, van Wunnik Johannes, Luckham Paul. Atomic Force Microscopy (AFM) study of redox conditions in sandstones: Impact on wettability modification and mineral morphology // Colloids and Surfaces A: Physicochemical and Engineering Aspects. 2020. 597. 124765.

Yuan Yuehua, Lee T. Randall. Contact Angle and Wetting Properties // Surface Science Techniques. Berlin, Heidelberg: Springer Berlin Heidelberg, 2013. 3–34.

Zhang Yongsheng, Morrow Norman R. Comparison of Secondary and Tertiary Recovery With Change in Injection Brine Composition for Crude-Oil/Sandstone Combinations. 2006/1/1/ 2006.

Zhang Yongsheng, Xie Xina, Morrow Norman R. Waterflood Performance By Injection Of Brine With Different Salinity For Reservoir Cores. 2007/1/1/ 2007.

Zwinkels JC, Michaelian KH. Far-infrared diffuse reflectance spectrum of kaolinite // Infrared Physics. 1985. 25, 4. 629–632.